Aus der Klinik für Diagnostische und Interventionelle Radiologie des
Universitätsklinikums Augsburg

# Multi-Energy Reconstruction Techniques and Clinical Applications of Dual-Source Photon-Counting Detector Computed Tomography

## Kumulative Dissertation

zur Erlangung des akademischen Grades

Dr. rer. biol. hum.

eingereicht an der

Medizinischen Fakultät der Universität Augsburg

von

**Franka Risch**

Augsburg, 22.03.2024

**Eidesstattliche Versicherung und Erklärung**

Hiermit versichere ich an Eides statt, dass die vorliegende Dissertation von mir selbständig und ohne unerlaubte Hilfe angefertigt wurde. Zudem wurden keine anderen als die angegebenen Quellen verwendet. Außerdem versichere ich, dass die Dissertation keiner anderen Prüfungskommission vorgelegt wurde und ich mich nicht anderweitig einer Doktorprüfung ohne Erfolg unterzogen habe.

**Statutory declaration and statement**

I declare that I have authored this thesis independently, that I have not used other than the declared sources/resources. As well I declare that I have not submitted a dissertation without success and not passed the oral exam. The present dissertation (neither the entire dissertation nor parts) has not been presented to another examination board.

Augsburg, 22.03.2024

Dissertation eingereicht am: 22.03.2024

Erstgutachter (Hauptbetreuerin/Hauptbetreuer): Prof. Dr. Thomas Kröncke
Zweitgutachter: Prof. Dr. Constantin Lapa
Drittgutachter: Prof. Dr. Elias Wagner

Tag der mündlichen Prüfung: 28.03.2025

## Übersicht

Diese kumulative Dissertation führt in die technischen Grundlagen der spektralen Bildgebung mittels Computertomographie (CT) ein und stellt in den nachfolgenden Publikationen mögliche klinische Anwendungen von CT-Daten vor, die mittels Photonen-zählenden Detektoren erzeugt wurden. Photonen-zählende Detektoren, die 2021 in den klinischen Alltag Einzug gehalten haben, zeichnen sich unter anderem dadurch aus, dass sie die Energie jedes einfallenden Photons direkt messen können. Diese inhärente spektrale Empfindlichkeit erlaubt die einfache Anwendung diverser Nachbearbeitungen, wie der Materialzerlegung und der Simulation einer monoenergetischen Röntgenquelle, die sich in eine Vielzahl an klinischen Anwendungen übersetzen lässt. In den durchgeführten Studien konnte gezeigt werden, dass sich das Signal jodhaltiger Kontrastmittel zuverlässig aus CT-Angiographien entfernen lässt und damit zusätzliche Informationen aus dem Datensatz gewonnen werden können. Die resultierenden virtuell nativen Bildserien eigneten sich für die Quantifizierung von Koronar- und Aortenklappenverkalkungen sowie epikardialem Fettgewebe. Auf den komplementären Bildserien konnten präzise Jodkonzentrationsmessungen demonstriert werden, welche Aufschluss über die Kontrastmittelverteilung geben. Die virtuelle monoenergetische Rekonstruktion wurde auf ihren Nutzen zur Kontrastverstärkung bei der Kryoablation im niedrigen keV-Bereich sowie zur Artefaktreduktion von Dentalmaterial bei hohen keV mit vielversprechenden Ergebnissen untersucht. Zusammenfassend wurden verschiedene Fragestellungen bearbeitet, die sowohl das Potential als auch die Grenzen der photonen-zählenden Detektortechnologie analysieren und für die klinische Anwendung evaluieren.

## Abstract

This cumulative dissertation introduces the technical principles of spectral imaging using computed tomography (CT) and, in subsequent publications, presents potential clinical applications of photon-counting detector CT data. Photon-counting detectors, which became available for clinical use in 2021, are characterized in part by their ability to directly measure the energy of each incident photon. This inherent spectral sensitivity allows easy application of various post-processing techniques, such as material decomposition and virtual monoenergetic imaging, which can be translated into a variety of clinical applications. The results of the studies comprising this dissertation have shown that the signal of iodinated contrast agent can be reliably removed from CT angiography, providing additional information. The resulting virtual non-contrast image series are suitable for quantification of coronary and aortic valve calcification as well as epicardial adipose tissue. Precise contrast agent concentration measurements were demonstrated on the complementary iodine image series. Virtual monoenergetic reconstructions were evaluated for its utility in contrast enhancement for cryoablation in the low keV range and artifact reduction of dental material at high keV with promising results. In summary, several research questions have been pursued that explore the potential and limitations of the detector technology for clinical application.

# Contents

# List of Abbreviations

**AIX** artifact index

**AVCS** aortic valve calcium scoring

**BMI** body-mass-index

**CAC** coronary artery calcium

**CACS** coronary artery calcium scoring

**CCT** cardiac computed tomography

**CT** computed tomography

**CTA** computed tomography angiography

**CCTA** coronary computed tomography angiography

**CMR** cardiac magnetic resonance imaging

**CNR** contrast-to-noise ratio

**$CTDI_{vol}$** volumetric computed tomography dose index

**CX** circumflex artery

**DECT** dual-energy computed tomography

**DLP** dose length product

**DSCT** dual-source computed tomography

**EAT** epicardial adipose tissue

**ECG** electrocardiogram

**ECV** extra-cellular volume

**EID** energy-integrating detector

**FBP** filtered back projection

**FoV** field of view

**HU** Hounsfield Units

**IMAR** iterative metal artifact reduction

**IR** iterative reconstruction

**LAD** left anterior descending artery

**LM** left main coronary artery

**MAE** mean absolute error

**MPR** multiplanar reconstructions

**NECT** non-enhanced computed tomography

**PCD** photon-counting detector

**RCA** right coronary artery

**RED** relative electron density

**RSP** relative stopping power

**ROI** region of interest

**$r^2$** coefficient of determination

**SECT** single-energy computed tomography

**SD** standard deviation

**SNR** signal-to-noise ratio

**SPECT** single photon emission computed tomography

**SSDE** size-specific dose estimate

**TAVR** transcatheter aortic valve replacement

**TNC** true non-contrast

**UHR** ultra-high resolution

**VM** virtual monoenergetic

**VNC** virtual non-contrast

**VNCa** virtual non-calcium

**$VNC_{conv}$** conventional virtual non-contrast

**$VNC_{pc}$** PureCalcium virtual non-contrast

**VRT** volume rendering technique

**$Z_{eff}$** effective atomic number

PART I

# Introduction and Theoretical Background

CHAPTER 1

# Introduction

In 1979, Allan M Cormack and Godfrey Newbold Hounsfield were awarded the Nobel Prize in Physiology or Medicine by the Nobel Assembly at the Karolinska Institute for 'development of computer assisted tomography'.[1] Since then, computed tomography (CT) has evolved into one of the most important tools in medical imaging.[2] In the clinical setting, the technique provides non-invasive insight to morphological information by exploiting the different x-ray attenuation characteristics of tissues to answer pressing diagnostic questions ranging from tumor staging to bleeding detection. Spectral CT was introduced in 1971, just four years after the first machine was built. The ability to measure the energy dependence of the x-ray attenuation has opened up a much wider range of information about the object being studied.[3]

To obtain spectral CT data several techniques have been developed, either with respect to the x-ray source, such as dual-source or slow or fast kV-switching, or with respect to the detector, such as dual-layer or photon-counting detector (PCD). Each option has its own technical challenges and limitations that need to be considered depending on the application.[4] PCD-CT differs significantly from the other methods in the use of a completely new type of detector material. Current energy-integrating detector (EID) consist of a solid-state scintillator that converts the absorbed x-rays into visible light. Backside photodiodes then detect and convert the light into electrical current.[2] PCDs, however, consist of a heavy semiconductor capable of converting the photon's energy directly into a voltage pulse.[4] As well as providing inherent spectral information, this approach has a number of advantages, including the elimination of electrical noise, higher spatial resolution and improved contrast to noise ratio.[5]

Multi-energy CT data can be used to create synthetic images for key clinical applications such as material differentiation, material characterization and artifact reduction.[6] For virtual non-contrast (VNC) images the contrast media is distinguished from soft tissue and virtually subtracted. If an unenhanced scan is not available, this option not only provides a view of the hypothetical native appearance of the observed volume, but also promises to serve as a true non-contrast (TNC) substitute in multiphase contrast scans, thus reducing patient's radiation dose.[7–11] The generation of contrast media (i.e. iodine) maps can serve to differentiate contrast-staining from hemorrhage after endovascular therapy[12] or for the quantification of extracellular volume.[13] Even accurate measurement of iodine uptake itself is possible.[14] By subtracting the calcium-containing portions of each image voxel, virtual non-calcium (VNCa) series can be generated.

Applications of these images include bone removal,[3] assessing stenosis,[15] or analyzing bone marrow.[16] X-ray spectra are polychromatic with a maximum voltage corresponding to the defined potential at the x-ray tube. The spectral information allows the calculation of virtual monoenergetic (VM) images that mimic a single photon energy beam at a desired keV level. Low energy levels have the potential to improve tumor conspicuity,[6] higher levels reduce metal induced artifacts.[17]

The application of multi-energy CT data has been tested and verified to a great extent on a variety of dual-energy computed tomography (DECT) scanners. As the first CT equipped with a PCD has only recently been introduced into clinical routine in 2021,[18] the potential of this new detector technology and its intrinsic spectral sensitivity still remains to be evaluated. This thesis aims to demonstrate applications of spectral data derived from PCD-CT, starting with the explanation of the underlying technical principles, followed by the presentation of the clinical studies performed, divided into the topics of material differentiation and monoenergetic imaging.

CHAPTER 2

# Spectral Computed Tomography Fundamentals

CT has a long history of development and has been extensively covered in numerous scientific books. A comprehensive description is beyond the scope of this work. The purpose of this chapter is to explain the basic principles, combining both technical and clinical perspectives, which will facilitate the understanding of the acquisition and application of spectral data and the respective studies carried out. If not cited differently, information within the Fundamentals chapter is based on the book 'Spectral Computed Tomography' by B. Heismann, B. Schmidt and T. Flohr, published by the Society of Photo-Optical Instrumentation Engineers (SPIE) in 2012[3] and the review 'Computed tomography recent history and future perspectives' by J. Hsieh and T. Flohr published in the Journal of Medical Imaging in 2021.[2]

## 2.1 Computed Tomography from User-Side

CT is one of the most important modalities in clinical diagnostic imaging, providing volumetric, morphological information of the scanned object. Advantages include wide availability, easy handling and very short acquisition times. An entire human body can be scanned within seconds, which is of tremendous importance in emergency situations. However, each examination also involves exposure to x-rays, which have now been reduced to a minimum, but may be a disqualifier under certain circumstances, such as pregnancy.

### 2.1.1 Data Acquisition

Like conventional radiography, the setup of a CT scanner consists of a x-ray source facing a detector (see Figure 2.1). The source emits a spectrum of quanta, measured in quanta per energy [keV]. The photon energy is limited by the applied electron accelerator tube voltage [kVp], which is typically between 70 and 140 kV. As the beam passes through an object, its material-specific attenuation characteristics cause an individual reduction in x-ray signal intensity. The governing physical effects causing the attenuation are the photoelectric effect and Compton scattering. In conventional radiography, volume information is reduced to a plane in which each pixel contains the signal decreased by the superposition of specific attenuations along the beam path.

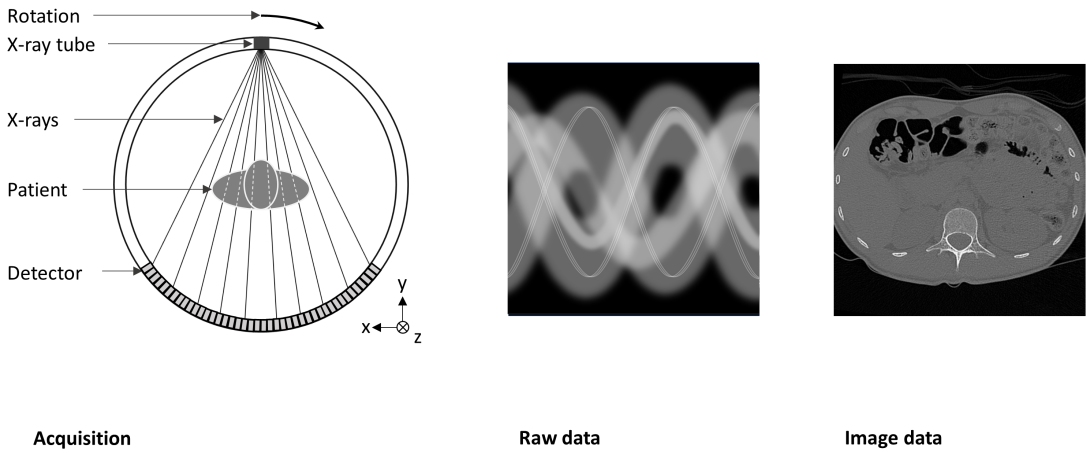


**Figure 2.1:** Demonstration of the technical principle of a CT scanner. The x-ray source and detector face each other and rotate around the object being scanned. The accumulated attenuation along the beam path from different perspectives during the rotation forms the sinogram in the raw data domain. Back-projection is used to spatially resolve the integrals to obtain the attenuation at a single image point.

In CT, a rotation of the source and detector around the longitudinal axis (z-axis) is introduced, acquiring multiple projections of the same object from different perspectives. This allows to calculate the attenuation of each voxel within the x-y-plane (axial plane) of the object at a certain position along the z-axis. The data recorded within half a gantry rotation are sufficient to reconstruct an image due to the parallel geometry. Limitations on the number of slices acquired per rotation as well as the spatial resolution of a single voxel are detector specific and provided with the detector collimation information (number of rows times their area). The patient table can be moved along the longitudinal axis to achieve greater z-coverage. Sequential acquisition mode is referred to when the table motion and scan are performed alternately, and spiral acquisition mode is referred to when the table moves linearly with the rotation of the source and detector. The pitch factor describes the table feed within one rotation divided by the collimated beam width.

Next to pitch and acquisition mode, image quality is highly dependent on the used dose. An established reference index for dose estimation is the volumetric computed tomography dose index ($CTDI_{vol}$), which gives the sum of the applied local dose estimate for each slice, taking into account the unintentional dose applied to adjacent slices, measured in [mGy]. The dose length product (DLP) additionally factors in the scan length (DLP $\approx$ $CTDI_{vol}$*scan length) and measures in [mGy*cm].

CT acquisitions often consist of multiple contrast phases, referring to different points in time before and after contrast agent injection. Used agents are usually iodine based, since iodine has a significant higher attenuation coefficient compared to soft tissue and therefore creates increased contrast. Depending on the diagnostic focus, common multi-phase scans include an unenhanced scan and one or more contrast-enhanced scans, taken in the arterial, portal venous or late venous phase, referring to the point at which the iodine reaches the respective anatomical

structure. The computed tomography angiography (CTA) usually refers to an arterial phase contrast scan.

### 2.1.2 Image Reconstruction

Reconstruction is required in order to obtain an image volume at specified settings, based on the sinogram/ raw data (refer to Figure 2.1). A standard and still widely used efficient approach is the filtered back projection (FBP). With increasing computational power, iterative reconstruction (IR) algorithms have been established which perform multiple backward and forward propagations between the raw and image domain to approximate an ideal, artifact-free image.[19,20]

Applied algorithms and their details are vendor-specific and only partially adjustable from application side. In case of IR, the iteration strength and additional processing, e.g. regarding metal artifact reduction, can be chosen. Further, the convolution kernel used can be defined which represent a compromise between image sharpness and noise. Usually the name of a kernel consists of an abbreviation describing the application it is specialized for and an index, which is a measure of the desired image resolution. Although the naming is also quite vendor-specific, a lower index will result in smoother images (soft tissue kernel) and a higher index will result in sharper and more detailed images (bone or lung kernel). Regarding volumetric settings, slice thickness and increment (z-direction) can be specified. For equal values, slices are adjacent; for an increment smaller than the thickness, slices overlap. The in-plane resolution depends on the matrix size, usually 512 x 512 pixels, and the field of view (FoV).

CT is a crossectional imaging modality, and images are typically evaluated by radiologists in axial view in the superior direction (see Figure 2.2). In addition, multiplanar reconstructions (MPR) or volume rendering technique (VRT) visualizations can be created to provide simultaneous axial, lateral and coronal views or a 3D representation. The linear attenuation coefficient of each voxel is given as a CT value measured in Hounsfield Units (HU). Distilled water (at standard pressure and temperature) represents zero, and air (at standard pressure and temperature) marks -1000 on the Hounsfield scale. Values are visualized in gray scale, whose contrast can be adjusted by selecting the center and width of the range (windowing).

## 2.2 Spectral Computed Tomography Principle

As described in the previous section, the source in CT provides a polychromatic spectrum. The absorption of the radiation by a material depends not only on the density and chemical composition of the material, but also on the individual energy of the penetrating x-ray. Different spectra result in different absorption behavior. The additional information of the materials energy dependence is of great value for various applications, allowing virtual monoenergetic and material specific imaging, as well as mapping of mass density and effective atomic number. Unlike the previous section on general CT, we will start with the imaging principle before moving on to the different acquisition approaches and detector types.

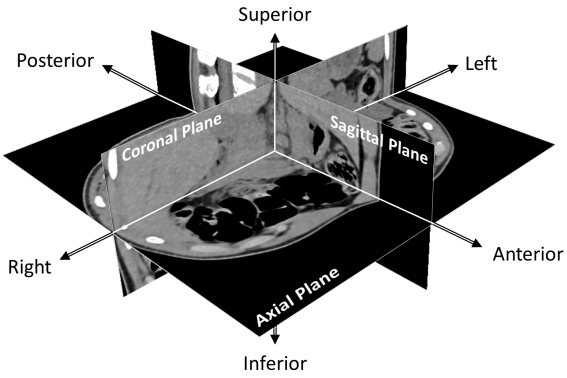


**Figure 2.2:** Demonstration of the resulting volume after image reconstruction including the medical description of planes and directions.

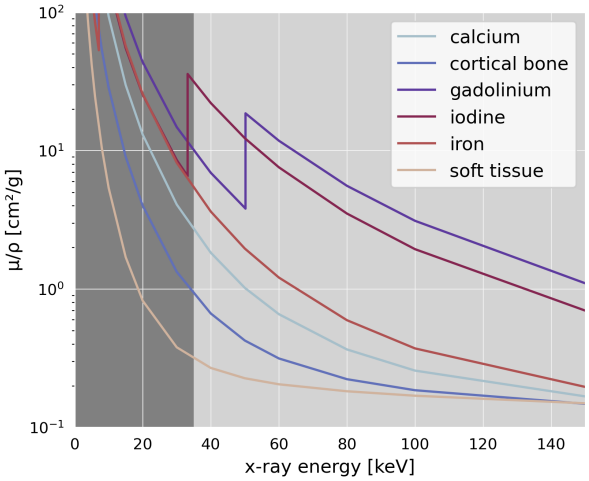


**Figure 2.3:** X-ray mass attenuation coefficients ($\frac{\mu}{\rho}$) for calcium, cortical bone, gadolinium, iodine, iron and soft tissue. Due to prefiltration, x-ray energies within the dark gray shaded area do not occur in medical CT.

### 2.2.1 Image Reconstruction

This section provides a brief overview of the principle of spectral data acquisition.

The spectral attenuation coefficient ($\mu(E)$) is the sum of the individual material densities ($\rho$) multiplied by their mass attenuation coefficients ($\frac{\mu}{\rho}$) as follows:

$$\mu(E) = \rho \left(\frac{\mu}{\rho}\right)(E) = \sum_{i=1}^{M} \rho_i \frac{\mu_i}{\rho_i}(E)$$

The characteristic function of the mass attenuation can be taken from literature for all chemical elements[21] and is visualized in Figure 2.3 for various materials.

The object x-ray attenuation ($A$) can be described as the ratio of measurements performed with ($I$) and without ($I_0$) the object. The signal intensity is dependent on the source spectrum ($S(E)$) and the detector responsivity ($D(E)$) and if present, the integrated attenuation

along the beam path ($L$) resulting in:

$$\frac{I}{I_0} = \frac{\int_E S(E)D(E)e^{-\int_L \mu(E,\vec{r})d\vec{r}}dE}{\int_E S(E)D(E)dE}$$

Single-energy computed tomography (SECT) cannot resume the energy dependence of the attenuation coefficient and assumes a monoenergetic radiation ($E = E_0$) to approximate an effective $\bar{\mu}(\vec{r})$ image by means of the inverse Radon transform. Errors related to this approximation of linear x-ray physics are known as beam-hardening artifacts, since the passage of thick or high atomic number materials will increase the energy of the detected signal, respectively harden the beam spectrum. Spectral CT algorithms require at least two energy channels per sinogram value to obtain the spectral attenuation coefficient $\mu(E, \vec{r})$ and can be divided into raw data-based, directly using sinogram data, and image-based, using reconstructed images. Basis material decomposition is the most commonly used spectral algorithm and relies on the assumption that the attenuation coefficient is a superimposition of the concentration ($c(\vec{r})$) multiplied with the attenuation function ($f(E)$) of two linearly independent materials (1 and 2):

$$\mu(E, \vec{r}) = c_1(\vec{r})f_1(E) + c_2(\vec{r})f_2(E)$$

There are three common sets of functions proposed in literature:

- one using hypothetical materials based on the physical effects of attenuation with $f_1 = \frac{1}{E^3}$ describing the photoelectric effect and $f_2 = f_{KN}(E)$ describing the Klein-Nishina formula of the Compton scattering, however, this approach was found to be limited since it does not meet the for CT required accuracy;
- another one defined by water and bone material, thus representing most of human biological tissue with $f_1 = \mu_{H_2O}(E)$ and $f_2 = \mu_{Ca_5HO_{13}P_3}(E)$;
- and the last one combining water and iodine ($f_2 = \mu_I(E)$), useful for contrast enhanced scans.

An alternative to the basis material approach is the $\rho Z$-projection algorithm that uses the density ($\rho(\vec{r})$) and the atomic number ($Z(\vec{r})$) to characterize the material attenuation:

$$\mu(E, \vec{r}) = \rho(\vec{r}) \left(\frac{\mu}{\rho}\right)(E, Z(\vec{r}))$$

In the human body, the elemental attenuation functions range from hydrogen ($Z = 1$) to bone mineral-hydroxyapatite ($Z_{eff} = 16$).

Statistical and systematic errors limit the functionality of spectral CT algorithms. Within the measurement process, statistical errors mainly imply quantum noise corresponding to the standard deviation of absorbed quanta ($\sigma(N)$) in a detector pixel within a given time, which is approximately $\sqrt{N}$, resulting in a signal-to-noise ratio (SNR) of $SNR = \frac{N}{\sqrt{N}} = \sqrt{N}$. Considering medical CT and typical attenuated signals of 50 to $10^6$ quanta and additional

electronic noise, this leads to 1-10 HU uncertainty in image data, depending on the kernel used and the object scanned.
Systematical errors include scattering, beam-hardening and limitations in the accuracy of the hardware measurement. Compton scattered primary quanta are partly already absorbed by the examined object or further reduced by the therefore existing collimator blades at the detector (see subsection 2.2.2). Because energy weighting is not constant throughout an object, spectral CT algorithms are sensitive to beam-hardening artifacts from approximate Radon transform. In case of projection-based basis material decomposition exact Radon transform equations can be obtained by energy integration and for image-based algorithms corrections can be applied to counteract beam-hardening effects. Hardware accuracy is mainly limited by the non-linearity errors of system parts, but this has been improved and is therefore a negligible contributor to systematic error.
Within the algorithmic transfer, noise and signal cannot be distinguished, leading to the transfer of statistical errors in the input data into the parameter set, which can lead to unacceptable noise gain in poorly conditioned transfer functions. Systematical errors are caused by a mismatch between the model functions used and the object ground truth. For example, decomposing into the base materials water and bone will result in elevated coefficients for an iodine-containing object and negative ones in case of high fat content.

### 2.2.2 Detector Technology

Before discussing different approaches to spectral data generation, it is worth taking a look at the two detector technologies available.

*Energy-integrating detector*
The conventional detector type used in almost every CT system is the EID (see Figure 2.4). It consists of an antiscatter collimator from tungsten material aligned with the source, which ensures that Compton scattered radiation, introduced by the scanned object, is absorbed. After passing the collimator, the primary radiation reaches the scintillator. It is made from scintillating material with a high stopping power for medical x-ray spectra, such as gadolinium oxysulfide (GdOS), structured in a pixelized array. Additional separation layers between each pixel cause optical backscattering, thus keeping the generated light energy within each pixel. With a thickness corresponding to 10-25% of the detector pixel width, these zones, which do not contribute to the measurement signal, represent a significant reduction in detector efficiency, however, are required to avoid crosstalk. Below the scintillator, similarly structured photodiodes convert the optical signal into an electrical current with an amplitude proportional to the photon's energy. At low x-ray flux, such as in low dose scans, electronic noise exceeds Poisson noise, resulting in increased image noise and CT value instability, limiting further dose reduction. An analogue-to-digital converter transforms the over a certain time period accumulated charge into a digital value. The output therefore represents the integrated quantum energy of all absorbed photons over time, in which photons with lower energy are down-weighted as they contribute less to the signal than those with higher energy ($D(E) \sim E$). Particularly in contrast-enhanced

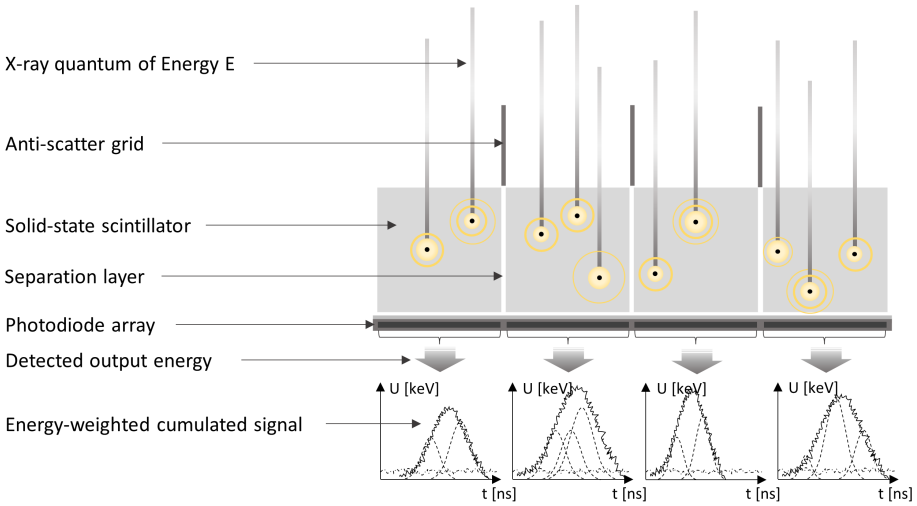


**Figure 2.4:** Demonstration of the technical principle of an EID. X-rays absorbed in the scintillator produce visible light, which is detected by the photodiodes and converted into an electric current. For each pixel of the detector array, the signal is integrated over a given period of time.

scans, this leads to a decrease in contrast-to-noise ratio (CNR), since iodine's attenuation coefficient peaks at lower energies (see Figure 2.3).

*Photon-counting detector*

PCD also use collimator blades to reduce scattering (see Figure 2.5). Underneath, instead of scintillating material, PCDs are made of semiconductors, e.g. cadmium-telluride (CdTe) or cadmium-zinc-telluride (CdZnTe), that are able to convert the absorbed photon directly, without the diversion via an optical signal, thus eliminating some of the aforementioned disadvantages of EID. Optical spacers are no longer required, which greatly improves geometric efficiency and allows for much smaller pixel dimensions compared to EID. Anti-scatter collimators separate blocks of pixels (e.g. 2 x 2) that can be resolved individually in ultra-high resolution (UHR) mode. The semiconductor layer is sandwiched between a cathode at the top and pixelated anodes at the bottom, which create a high-voltage electric field. Photons striking the semiconductor produce electron-hole pairs, and the released electrons drift towards the anodes, inducing current pulses. The short pulses of a few nanoseconds are converted into voltage by a pulse shaping circuit. The resulting peaks are proportional to the energy of the photon and are only counted if they exceed a certain threshold ($T_0$), which eliminates low-level electronic noise. In contrast to EID, all counted photons contribute individually to the measured signal without down-weighting of low energy quanta (D(E) = constant). By introducing one or more thresholds ($T_1$-$T_x$), pulses can be assigned to so-called energy bins. Images reconstructed on the basis of these bins contain only the signals with peaks between two adjacent thresholds. Two energy bins, inherently obtained from the polychromatic spectrum of a single x-ray source, are already sufficient for the application of spectral CT algorithms. With at least three energy bins, three material decompositions are possible, including one material with a K-edge, which

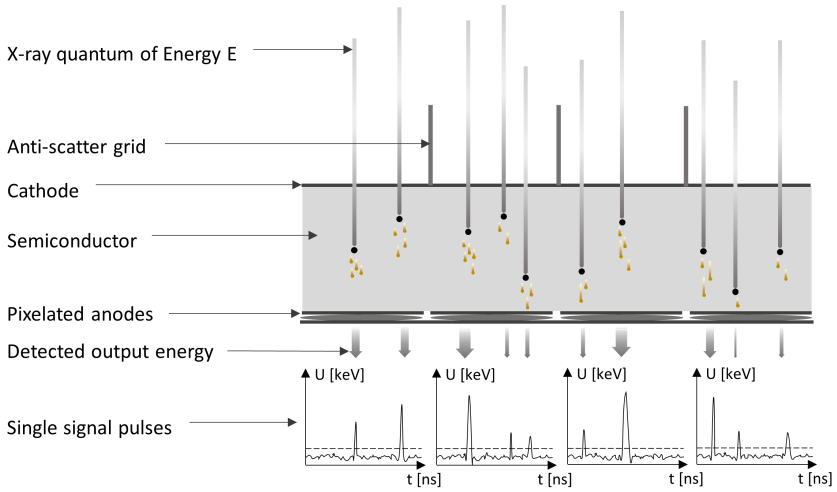


**Figure 2.5:** Demonstration of the technical principle of a PCD. X-rays absorbed by the semiconductor produce electron-hole pairs, which are separated by the applied high electric field. The current pulses induced by the electrons reaching the pixelated anodes are individually counted. Certain thresholds eliminate electronic noise and separate the signal into different energy bins.

represents an element-specific sharp jump within the otherwise continuous linear attenuation coefficients as a function of photon energy.

Limitations of the detector are charge sharing, describing the splitting of high-energy photons into two lower-energy counts due to absorption between two adjacent pixelated anodes and fluorescence, and relatedly K-escape, which means that photons absorbed in the semiconductor can eventually produce electron-hole pairs from the K-shell which are immediately replenished, releasing characteristic x-rays at fluorescence energy which can 'escape' to an adjacent detector cell.[22] Both of these unavoidable physical effects result in double counts at lower energies and therefore assignment to lower energy bins, thus decreasing spectral separation.

### 2.2.3 Data Acquisition

For the acquisition of multi-energy CT data, either source-based or detector-based techniques can be used. The overall objective is to obtain the minimum of two energy channels per sinogram value required to resolve the energy dependence of the attenuation coefficient. DECT comprise the former by performing measurements with two different source spectra. The latter include energy-resolving detector technologies, either dual-layer or photon-counting.

*Source-based technologies*

80 and 140 kV spectra are typically used as they often represent the lowest and highest possible setting with the most favorable spectral separation (compare with Figure 2.6). The acquisition of two scans with different source spectra can be achieved by switching the tube potential of the source between successive scans, also referred to as slow kV-switching (see Figure 2.7). Depending on the anatomy of interest, either wide-volume detectors are used to cover entire

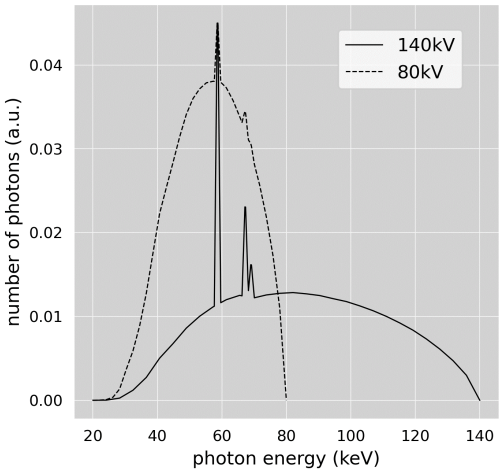


**Figure 2.6:** Demonstration of typical CT x-ray spectra with 80 and 140 kV tube potential (created with the xpecgen[23] python library).

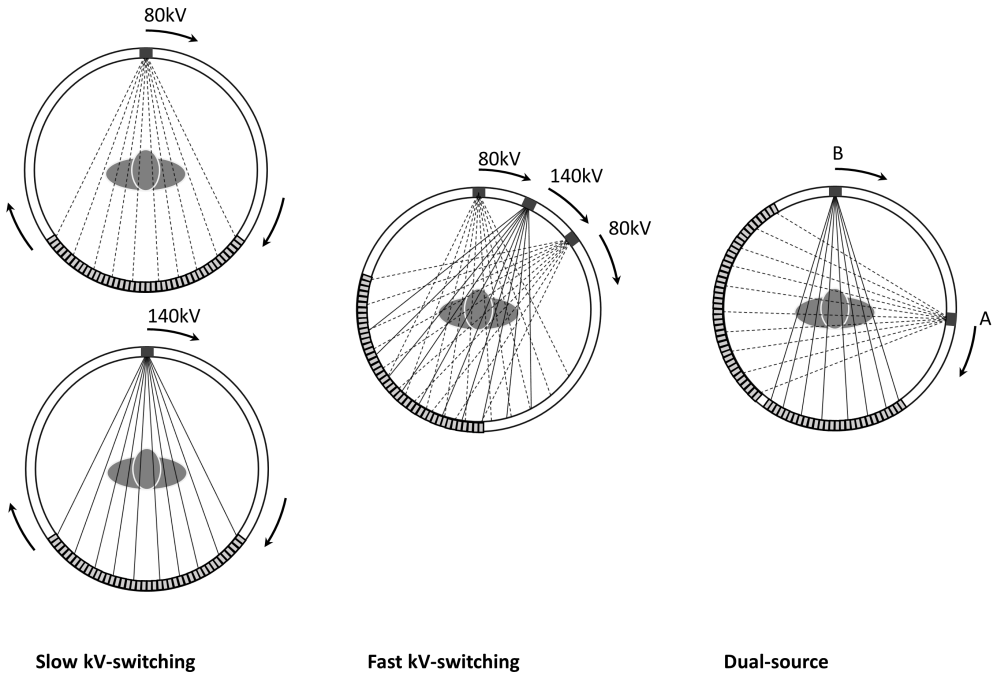


**Figure 2.7:** Demonstration of the available source-based methods to acquire spectral CT data.

organs in a single rotation, or high-pitch spiral CTs are performed for increased range in the z-direction.[6] On the plus side, beam filtration can be used during the high kV scan to improve spectral separation, and the dose of both scans can be aligned by adjusting the mA settings to match their image noise levels. The main limitation is the temporal offset, which can include movement between the two scans, e.g. patient movement or scanning of moving organs, introducing misalignment of the data sets that can only be partially reduced by non-rigid registration algorithms. In the case of contrast-enhanced CT, the rapid distribution of the contrast agent can lead to acquisition in two different phases and therefore to inconsistent CT values.

Alternatively, for fast kV-switching, the tube potential is rapidly switched between individual projections. Interpolation is used to adjust for the small variations within the resulting interleaved data of the sinogram. While this method overcomes the spatial and temporal limitations of low kV-switching, the fast switching and response time places high demands on the source and detector and therefore limits the rotation time.[6] As the adjustment of the mA settings to the tube voltage to be done at the same speed is challenging, dose adjustment is achieved either by increasing the sampling time of the 80 kV measurement by a factor of three or by taking three projections in a row alternating with one 140 kV measurement.

The final source-based method available using a single source is beam filtration. Different filters, one of tin increasing the mean energy of the spectrum and one of thin gold decreasing it, are used to split the beam longitudinally. However, the spectral separation is worse compared to the other methods presented and the filter absorbs a substantial amount of photons, requiring either strong x-ray sources or limiting it to non-obese patients.[6]

Dual-source computed tomography (DSCT) scanner are equipped with two x-ray tubes separated by an angular offset of 95°, each facing a detector. Due to the spatial limitations of the gantry, only one detector can cover the full scan FoV (detector A), while the other is restricted to the central FoV (detector B). Because both tubes can be operated individually, they can either provide the same spectrum, allowing acquisition of an image in a quarter of the gantry rotation time, or different spectra, allowing acquisition of dual-energy data. Equivalent image noise levels for both data sets can be achieved by adjusting the mA settings, improving the post-processing performance. As the data acquisition is almost simultaneous, separated only by the time required to rotate the angular offset, registration problems are largely eliminated. The spectral separation between the energy spectra used can be increased with suitable prefiltration. By moving a filter into the high kV spectrum, lower energies are absorbed and the spectrum's mean energy is raised. Cross-scattering, where radiation from one x-ray tube is detected by the detector of the other tube, is a major challenge as it potentially degrades image quality. As a countermeasure cross-scattered radiation can be subtracted. The amount can either be detected by additional detector elements outside the direct beam, or predicted from a model of the scanned object's surface.

*Detector-based technologies*

As an alternative to using multiple source spectra, it is conceivable to use energy-resolving

detectors.

With dual-layer detectors, which consist of two layers of EID on top of each other, the top layer absorbs lower-energy photons, while higher-energy photons are absorbed by the layer behind. The respective mean energy of the detected signals therefore differs between the two layers and allows for dual-energy post-processing. The advantages are manifold: Possibility to adjust the radiation exposure according to the clinical task and the individual patient, no registration problems, no cross scattering. However, as high-energy photons are also absorbed in the top layer, the two spectra have a significantly greater overlap and their doses cannot be matched than when using two different spectra.

Finally, PCD based on semiconductors rather than scintillators, as described in more detail in the subsection 2.2.2, provide energy information for each individual absorbed photon, thus fulfilling all the requirements for dual-energy post-processing.

## 2.3 Clinical Applications

As mentioned before, spectral CT algorithms can be raw data-based or image-based. The disadvantage of the former is a high sensitivity to motion, but as a plus it has an intrinsic correction for beam-hardening. The latter involves the same methods but transformed into image space and is the clinically established method. The main advantage is the handling of smaller data sizes compared to raw data. In addition, most current image reconstruction techniques, such as IR methods or automated exposure control, can be applied to generate the high and low energy CT images, that are required for subsequent spectral post-processing.

*Material-specific Imaging*
Based on the material decomposition described in the subsection 2.2.1, material-specific images can be produced in which each voxel is described by the linear contribution of that material as demonstrated in Figure 2.8. However, it should be noted that the noise is also decomposed and significantly increased for each base material image due to the small difference in slope. An alternative approach is often used for dual-energy bone removal. Similar to Figure 2.8, iodine and bone (mainly calcium) containing voxels will surround two different straight lines. Instead of decomposing the materials conventionally, a dividing line between them can be applied to identify and remove bone voxels from the image series, avoiding an increase in noise.

Calcium images can be used for accurate bone densitometry[24] or plaque evaluation.[25] Conversely, a calcium-free image allows visualization of bone marrow edema,[6,26] improved bone removal for vascular assessment in CTA acquisitions,[27] stenosis evaluation in case of calcified plaques or for improved ice ball visualization in skeletal cryoablation procedure.[28]

Differentiating between uric acid and calcium helps to classify kidney stones, providing valuable information for treatment and prevention.[29,30]

Iodine maps can be used to quantify the specific uptake of contrast agent[31,32] or to easily detect bleeding or vessel blockage. The VNC image, as a counterpart to the iodine map, has the

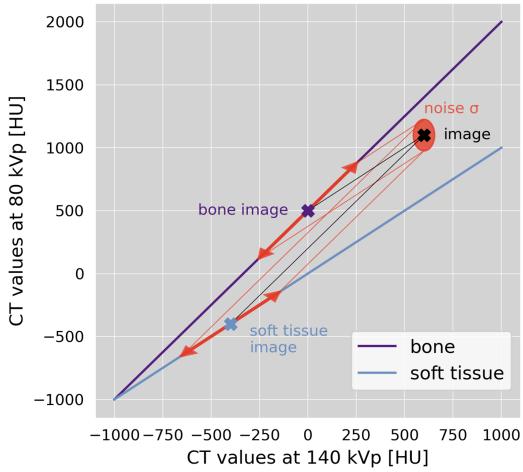


**Figure 2.8:** Demonstration of the basis material decomposition into bone and soft tissue. As the image noise is also decomposed, both base material images suffer from a significant increase in noise.

potential to replace a TNC series, the scan prior to contrast injection in multi-phase acquisitions. Applications are diverse, such as calcium quantification,[7,10,11] in patients after endovascular aneurysm repair,[9] quantification of epicardial adipose tissue.[8]

Iodine, fat and water can be distinguished in contrast-enhanced scans of fatty liver. Based on the same principle, instead of iodine, iron can be quantified on non-enhanced scans.[33]

However, it is important to remember that separating human tissue into just two materials is only an approximation and may not represent the full 'truth'.[26] An additional third dimension would be favorable and can currently be achieved by a three-material decomposition requiring at least one material being of high atomic number and therefore having a k-edge in its attenuation characteristic and three energy spectra. The k-edges of most elements in the human body are below 30 keV and therefore outside the measurable diagnostic CT range. The contrast agents iodine and gadolinium, for example, with k-edges of 33 keV and 50 keV, respectively, can be used in the setting of three-material decomposition.[34]

*Monoenergetic Imaging*

The first step in obtaining VM images is to perform a two-material decomposition. By looking up the respective attenuation coefficients at specific energies, in addition to knowing how much these two materials contribute to each individual image voxel, monoenergetic images can be synthesized at desired energy levels.

Beam-hardening and scatter artifacts induced by high-atomic material, such as metal from prostheses, are more pronounced in low-energy images and are reduced at high keVs. Therefore, high VM levels have the potential to reduce metal artifacts.[17,35] Another application is that some pathologies are more differentiable at their individual optimal VM level. For example, at low keV levels, the conspicuity of metastases in liver tissue[36] or the confidence in distinguishing between pleural empyema and non-infectious pleural effusion can be improved.[37]

However, the material decomposition induces an increase in noise for VM reconstructions, which is typically reduced by smoothing algorithms.

*Electron Density & Effective Atomic Number Imaging*
With spectral CT data it is possible to calculate maps including relative electron density (RED) and effective atomic number ($Z_{eff}$) for each tissue within the scanned object. From this, the relative stopping power (RSP) of protons to water can be estimated.[6,38] This information is of crucial importance for proton therapy, a form of tumor radiation treatment in cancer patients. Derived from SECT, high uncertainties are measured in RSP because no distinction can be made between density and composition of the material.

PART II

# Clinical Projects and Publications

CHAPTER 3

# Objectives, Materials and Methods

*Objectives*

Since PCDs have only recently become available for clinical CTs and have promising advantages over EIDs, the main goal of the research projects was to explore the performance for applications previously performed with DECT and to evaluate the benefits of inherent spectral data in a clinical scenario. A major focus has been on the reconstruction of VNC images from CTA acquisitions, as they offer the potential for radiation dose reduction in multi-phase scans including an unenhanced scan. We have investigated the image quality, particularly in terms of noise, residual calcium contrast, and their usability for routine evaluation and quantification tasks, taking into account various influencing factors such as patient characteristics, acquisition and reconstruction settings. The projects carried out on VM imaging have had the main goal of finding the most appropriate keV level for certain diagnostic questions, which allows to get the maximum information from the image.

*CT Scanner*

The CT scanner NAEOTOM Alpha from Siemens Healthcare GmbH, Erlangen, Germany, was used in all projects. It is the first approved clinical CT equipped with two PCDs and was installed at the University Hospital of Augsburg in March 2021. The CT acquires 144 slices per detector with a resolution of 0.4 mm in normal mode, which corresponds to a coverage of almost 6 cm in z-direction without patient table movement. In UHR mode, 120 slices can be resolved to 0.2 mm in z-direction and voxels of 0.11 mm in x-y-plane. Using dual-source, the scanner allows a pitch of up to 3.2 and provides a temporal resolution of up to 66 ms.

*Other Devices*

In addition to the CT scanner, the cryoablation experiments required further equipment (see subsection 5.2.1). The ICEfx cryoablation system was used in conjunction with a 17G Ice Rod 1.5 CX (Boston Scientific, Marlborough, Massachusetts, United States) and cooled with liquid argon (Linde plc, Dublin, Ireland). Temperature tracking was performed using four TS3 fiber-optic temperature sensors connected to a four-channel thermometry-system OEM-PLUS RS232 (Weidmann Technologies GmbH, Dresden, Germany).

*Patient Data*

For those studies based on patient data, CT acquisitions between July 2021 and March 2023 were considered prospectively or retrospectively and approved for use by the Institutional Review Board (Ludwig-Maximilians-University Munich). In addition to the image series already reconstructed for radiological evaluation, CT raw data was used to perform specific reconstructions as needed, e.g. to create uniform data sets or to vary settings.

*Phantom Data*

Phantom data was generated using either commercially available phantoms or experimental setups.

The Cardiac Dynamic Phantom, MODEL 008C, from Computerized Imaging Reference Systems Inc. Virginia, USA (referenced in 4.1.3), mimics a human beating heart with adjustable rate and rhythm. By providing the appropriate electrocardiogram (ECG), the scan can be triggered accordingly. At the position of the left coronary artery, individual inserts can be placed.

In a series of experiments, a coronary phantom was created that mimicked an artery with calcified plaques and a suitable lumen in terms of CT values, with or without iodinated contrast (referenced in 4.1.3). The final assembly consisted of a rigid plastic tube with an outer diameter of 5 mm to fit into the Cardiac Dynamic Phantom. Several pieces of a calcium tablet (2028.9 mg calcium carbonate each of two tablets and modified starch, Vitamaze GmbH, Heidelberg, Germany) were covered with and glued inside using a 2-component epoxy adhesive (UHU GmbH & Co. KG, Bühl/ Baden, Germany). To prepare the contrast-enhanced lumen, a mixture of 300 mg iodine per ml (Ultravist 300, Iopromide, Bayer Vital GmbH, Leverkusen, Germany) and 0.9% sodium chloride was used in a 1:20 ratio. For the lumen without contrast enhancement, iodine was not included. Agarose powder (1.4 g per 100 ml) was added to gel the solution and prevent air bubbles from moving within the tube during CT acquisition. For cleanliness, the resulting tube was sealed in a heat-shrinkable tube. To alter the lumen of the phantom, the water-soluble solution was removed and replaced.

The phantom PFO-Kalotte from Quality Assurance in Radiology and Medicine GmbH in Möhrendorf, Germany, replicates the anatomy of the human brain (referenced in 4.2.3). It is composed of brain-equivalent tissue with constant CT values and is surrounded by high x-ray absorbing structures that simulate the skull and temporal bones. Three cylindrical holes are located at the center, anterior, and lateral aspects directly beneath the skull, which allow for inserts.

Balloons have proven to be particularly useful as phantom inserts, providing sufficient volume within the holes without creating air bubbles between the insert and the phantom that could cause artifacts during CT acquisition and potentially distort quantitative measurements.

To conduct cryoablation experiments, we found that a porcine liver purchased from a local butcher was the most appropriate phantom to mimic realistic tissue characteristics as the use of cryoablation for the treatment of liver tumors and liver metastases increases.

*Reconstruction Software*

For CT image reconstruction either the scanner console (syngo, Siemens Healthcare GmbH, Erlangen, Germany) or a dedicated workstation (reconCT, not for clinical use, Siemens Healthcare GmbH, Erlangen, Germany) was used. Depending on the time of reconstruction, different versions (VA40 - VB10) were available. Settings were adjusted based on the planned analysis and kept equivalent within a study cohort. Image series reconstructed from spectral CT data can be divided into two categories: Images including spectral information, often labeld as 'spp', abbreviation for 'spectral post-processing', and images reduced to specific information, such as VM series at a particular keV level or VNC series or iodine maps.

*Analysis Software*

Various software programs were used for CT image analysis.

At the University Hospital Augsburg, DeepUnity (DH Healthcare GmbH, Bonn, Germany) is the established viewer of the Picture Archiving and Communication System (PACS). It allows multiple views, such as MPR and VRT, and simple measurements (region of interest (ROI) or distance). Within the studies, DeepUnity was most often used for general CT value assessment by placing ROIs in different tissues and, if applicable, synchronizing them to the exact same position on other reconstructions of the same study.
Another viewer, syngo.ct (Siemens Healthcare GmbH, Erlangen, Germany), allowed for more complex evaluation by utilizing the full spectral information of 'spp' image series. In 'Reading' application visualizations on demand could be created, such as adjusting keV levels of VM images, switching to iodine or VNC visualization, or varying slice thickness. The 'Dual Energy Virtual Unenhanced' application enabled simultaneous measurement of iodine density in mg/ml and CT values at VM level of 70 keV, as well as on VNC images (referenced in 4.2.3). The 'CaScoring' application segments coronary calcifications exceeding a threshold of 130 HU and allocate them to the respective artery, left main coronary artery (LM), left anterior descending artery (LAD), right coronary artery (RCA) and circumflex artery (CX) with the option of manual post-processing (referenced in 4.1.1, 4.1.2, 4.1.3 and 4.1.4). The 'Coronary Analysis' application helped to differentiate between calcified plaques and stents.

The open-source software ImageJ (https://imagej.nih.gov/ij/) was used to position ROIs and to store their coordinates and size for later automated analysis with a programmed script (referenced in 5.1.1 and 5.2.1).

Slicer3D (www.slicer.org), another open-source software, was utilized to semi-manually generate (e.g. with growing seeds) and save volume segmentation masks. (referenced in 4.1.1 and 4.1.2)

Python was utilized for all remaining analysis tasks, including automating measurement tasks, conducting statistical analyses, and visualizing numbers and graphs. The main bibliographies used were numpy, pandas, pingouin, pydicom, sklearn, and matplotlib.pyplot.

CHAPTER 4

# Differentiation of Iodinated Contrast Media

As described earlier, material differentiation has several applications (see subsection 2.3). The distinction between water and contrast agent (iodine) should be particularly emphasized, as it not only provides desirable additional information, but the water image also promises to serve as a substitute for an unenhanced scan in the presence of a subsequent CTA. Thus, all the evaluations normally performed on TNC represent potential applications of VNC, while saving radiation dose to the patient and examination time. However, it is important to remember that material differentiation divides the contribution of a variety of biological tissues into only two or possibly three materials. Accordingly, on VNC reconstructions, not only iodine is virtually subtracted, but all materials whose attenuation is more similar to that of iodine than to that of water.

The first section covers topics related to calcium scoring on VNC series and the second section deals with other applications related to with the differentiation of iodine and water as basis materials. This is followed by a discussion of applications presented.

## 4.1 Calcium Scoring on VNC

Coronary artery calcium is a measure of coronary atherosclerosis[39] and its quantification on unenhanced cardiac CT followed by CTA has become established as a non-invasive diagnostic tool for risk stratification of major adverse cardiac events.[40,41] The same applies to the prognostic value of aortic valve calcium prior to transcatheter aortic valve replacement (TAVR) procedure.[42–45] The most common method is calcium scoring according to the Agatston method, which considers voxels within the heart volume greater than 130 HU and forming a contiguous area of at least 1 $mm^2$, typically on axial slices of 3 mm thickness.[46] The score consists of the measured CT value classified into categories 1-4 multiplied with the area. In addition to the Agatston score, the calcium hydroxyapatite volume [$mm^3$] and mass [mg] were determined as parameters.

The feasibility of coronary artery calcium scoring (CACS) on VNC series derived from DECT devices has been evaluated in several studies.[47–50] With the separation into the basis materials iodine and water (refer to Figure 2.8), for each image voxel the attribution of those two materials is determined according to their high and low x-ray attenuation characteristics. This means, for

example, that calcium, which has an x-ray mass attenuation coefficient between that of iodine and that of water (see Figure 2.3), is partially attributed to both basis materials. Thus, VNC series do not contain the full calcium contrast and their use for quantification is limited. However, the correlation of CACS derived from TNC and VNC was found to be highly linear and can be used to establish a correction factor. Recently, a novel calcium-preserving VNC algorithm, further referred to as PureCalcium virtual non-contrast ($VNC_{pc}$), has been presented. In contrast to the conventional VNC (conventional virtual non-contrast ($VNC_{conv}$)) algorithm, a calcium mask is created prior to material decomposition, including all voxels at a selected monoenergetic level identified as containing calcium. This mask is used to recreate the full calcium contrast in the water image after decomposing into basis materials. The first two subsections analyze the feasibility of calcium scoring on $VNC_{pc}$ compared to $VNC_{conv}$ and reference TNC, once with the focus on coronary arteries (subsection 4.1.1) and once on the aortic valve (subsection 4.1.2).

Besides the general endeavor to reduce radiation dose in CT, imaging of the heart is particularly challenging. Technical advancements increasing temporal resolution, such as dual-source high-pitch imaging combined with prospective or retrospective ECG triggering mitigate the risk of motion artifacts.[51] Nevertheless, the heart rate should preferably be low, around 60 bpm, which can be supported by medication, e.g. beta-blockers, if recommended for the pathology present.[51] Image series from patients with higher heart rates are prone to motion artifacts, which may compromise image quality and the validity of calcium scoring. In subsection 4.1.3 the heart rate susceptibility of $VNC_{pc}$ derived calcium scores is analyzed using an ad-hoc created vessel in a cardiac motion phantom and 4.1.4 evaluates in a patient cohort the influences of heart rhythm, rate and body-mass-index (BMI) on $VNC_{pc}$ derived CACS.

### 4.1.1 Coronary Artery Calcium Scoring

## Image Characteristics of Virtual Non-Contrast Series derived from Photon-Counting Detector Coronary CT Angiography - Prerequisites for and Feasibility of Calcium Quantification

Franziska Braun*, Franka Risch*, Josua Decker, Eva Harmel, Christian Scheurig-Münkler, Emanuel Schwarz, Joseph Schöpf, Thomas Kröncke, Florian Schwarz

* = contributed equally

The study was presented by the author FR within a scientific session at the German Radiological Congress (Deutscher Röntgenkongress) in May 2022 and was published in Diagnostics in November 2023.[10] The author FR was equally involved in data collection and manuscript preparation and performed the data interpretation and statistical analysis.

### Abstract

*Objectives:* PCD-CT provides inherent spectral information which can be used for the quantification of calcium in coronary computed tomography angiography (CCTA) datasets. Typically, an intermediary dataset containing the non-iodine attenuation component is derived from the CCTA dataset which is used for calcium quantification. This intermediary dataset must satisfy certain requirements, which the literature hitherto has not explicitly addressed. This study aims to analyze the image characteristics of the VNC series derived from CCTA datasets acquired on a PCD-CT system, to compare these with the TNC in terms of efficacy of virtual iodine 'removal' and image noise and to determine whether the prerequisites for calcium quantification are satisfied.

*Materials and Methods:* This retrospective study was institutional review board approved and all patients provided written informed consent. All patients who had undergone non-enhanced CT of the heart followed by CTA prior to transcatheter aortic valve replacement on a first-generation clinical PCD-CT scanner in July and August 2021 at our clinic, were screened for study inclusion. For each patient, several VNC series with different reconstruction settings (regarding kernel, iteration level and slice thickness/ increment) and algorithms ($VNC_{conv}$, $VNC_{pc}$) were created. Histograms of the semi-automatic segmented heart volumes were used to demonstrate effective virtual iodine 'removal'. Image noise as standard deviation of CT values within the left ventricle was evaluated. Calcium was quantified on the TNC and all VNC series on a per-patient and a per-vessel level. Calcium scores and calcium volumes were correlated using linear regression and predictive accuracy was determined by 10,000-fold bootstrapping analysis.

*Results:* The final study cohort consisted of 38 patients (median age 80.0 (75.3 - 82.8) years; 22 men). Histograms showed comparable distribution of attenuation values for TNC and all VNC series, demonstrating effective iodine 'removal' from CTA (median proportion $> 130$ HU: 82% for CTA, 0.6% for TNC, 0.2% for $VNC^{1}_{conv}$ and 0.7% for $VNC^{1}_{pc}$). Image noise was significantly different for TNC compared to all VNC series (all p's $< .05$) albeit with very small

differences (4 HU to $VNC_{conv}$, 4.9 HU to $VNC_{pc}$, on average). Calcium quantities measured on $VNC_{conv}$ series showed a significant underestimation regardless of the reconstruction settings (p's $< .001$) while absolute calcium quantities on $VNC_{pc}$ were comparable to those from TNC. However, excellent correlations between TNC and both VNC reconstruction algorithms were observed ($r^2$ per-patient level $> .93$, per-vessel level $> .85$). The predictive accuracy within the bootstrapping analysis was found to be higher for $VNC_{pc}$.

*Conclusion:* Our results prove that the iodine-based attenuation component can be effectively subtracted from CCTA datasets in PCD-CT and that the remaining VNC series satisfy the requirements for calcium quantification, yielding results with excellent correlation compared with TNC scoring studies and high precision in predicting actual calcium quantities.

## Introduction

ECG-synchronized, non-enhanced computed tomography (NECT) scans of the heart are the primary non-invasive imaging modality for assessing the presence and extent of coronary artery calcification,[52] a direct measure of an individual's burden of coronary atherosclerosis.[39] CACS has substantial prognostic value for predicting major adverse cardiovascular events and even long-term mortality in both asymptomatic[40,53–55] and symptomatic individuals[56,57] and it enhances cardiovascular risk stratification beyond traditional risk factor models.[58–60] NECT for calcium scoring may be performed as a stand-alone examination in asymptomatic individuals.[61] However, in most cases, it is followed by CCTA to visualize the coronary artery lumen, including potential stenoses and non-calcified plaques.[62] Because of the introduction of DECT, VNC series can be derived from contrast-enhanced CT datasets via material decomposition using iodine and water as reference materials.[63] Several studies have validated the feasibility and accuracy of calcium scores based on VNC series derived from CCTA scans acquired with DECT.[47,48,50,64–66]

PCD-CT is a novel spectral CT technology. Over EID, PCD offers higher spatial resolution, elimination of electronic noise and increased contrast-to-noise ratio.[26] Importantly, PCD-CT data exhibit intrinsic spectral information. Recent studies have demonstrated that spectral PCD-CT information can be harnessed to estimate calcium quantities on CCTA datasets[7,67] or late enhancement cardiac scans.[68] Emrich et al. demonstrated a high correlation in CACS between VNC and the reference standard and an improved agreement for $VNC_{pc}$ derived scores.[7] In addition, Fink et al. found in their phantom study that CACS accuracy on $VNC_{pc}$ is influenced by the level of iteration and VM level during reconstruction.[67] Importantly, neither study performs image characteristic analysis of the intermediary non-iodine attenuation component dataset, which would be crucial for the validity of the argument proposed in either study. The aim of this study was therefore to close this gap by systematically investigating the image characteristics of the intermediary VNC series. To this end, the efficacy of iodine 'removal' and noise properties as well as measures of calcium (score and volume) of various VNC series derived from the CCTA scan were intraindividually compared with assimilable parameters of TNC series.

## Materials and Methods

The protocol of this retrospective, single-center study was approved by our institutional review board (project nr. 21-0773, 10/2021), which waived the necessity to obtain study-specific informed consent.

*Study Population*

We screened all patients for study inclusion who had undergone our standard scan protocol prior to TAVR in July and August 2021 on a first-generation PCD-CT scanner. The protocol includes an unenhanced scan of the heart followed by a CCTA. Exclusion criteria were defined as follows: (1) Scan protocol deviation or incompleteness; (2) Missing raw data (required for uniform image reconstruction); (3) Errors during reconstruction; (4) Severe motion artifacts of the coronary arteries that preclude correct CACS. In patients with coronary artery stents, the stent segments and all coronary segments distal to the stent were excluded from further analysis.

*Scan Protocol and Reconstruction Settings*

All scans were performed on a first-generation dual-source PCD-CT system (NAEOTOM Alpha, Siemens Healthcare GmbH, Erlangen, Germany). As a component of our CT protocol, all patients underwent a NECT of the heart followed by a contrast-enhanced CTA of the aorta and iliac arteries. The CTA scan range encompassed the internal carotid arteries to the distal common femoral artery. Scanning was ECG-triggered to ensure diastolic acquisition of the heart and coronary arteries. Both NECT and CTA examinations were performed at a tube voltage of 120 kVp, gantry rotation time of 0.25 s, high pitch of 3.2 and collimation of 144 x 0.4 $mm^2$. Patients did not receive betablockade or nitroglycerine prior to CT, in accordance with the recommendations for preprocedural CT prior to TAVR.[69] For the CTA scan, a triphasic contrast material injection protocol was used as previously described, with 90 ml of contrast material in total (Ultravist, 300 mgI/ml, Bayer Vital GmbH, Leverkusen, Germany) and an injection rate of 5 ml/s, and a 50 ml saline chaser.[70]

TNC from NECT and $VNC_{conv}$ series from CTA data were reconstructed at the scanner console (VA40, Siemens Healthcare GmbH, Erlangen, Germany), $VNC_{pc}$ series were reconstructed on a dedicated workstation (ReconCT, Version 15.0, Siemens Healthcare GmbH, Erlangen, Germany). For TNC series a regular quantitative kernel (Qr36), a slice thickness of 3.0 mm, increment of 1.5 mm and a FoV of 180 x 180 mm was used. From the CCTA dataset, several VNC series were reconstructed, again with a FoV of 180 x 180 mm covering the heart. Reconstruction settings varied in kernel (Qr36 vs. Br36), strengths of IR (Q3 vs. Q4) and slice thickness/ increment (0.4 mm/ 0.2 mm vs. 1.0 mm/ 0.4 mm). Two algorithms for virtual subtraction of contrast media were compared, the conventional $VNC_{conv}$ and the calcium preserving $VNC_{pc}$ (PureCalcium) algorithm. Detailed reconstruction parameters for each series can be taken from Table 4.1.

*Image Analysis*

A comprehensive analysis of the various VNC series and the TNC series was conducted and involved three key components: (1) Assessment of the efficacy of virtual iodine ‘removal’;

| Source | Series | Kernel | IR level | Slice thickness/ increment [mm] |
|---|---|---|---|---|
| NECT | TNC | Qr36 | no IR | 3.0/ 1.5 |
| CTA | VNC[1] | Qr36 | 4 | 0.4/ 0.2 |
| | VNC[2] | Br36 | 4 | 0.4/ 0.2 |
| | VNC[3] | Qr36 | 4 | 1.0/ 0.4 |
| | VNC[4] | Qr36 | 3 | 1.0/ 0.4 |

**Table 4.1:** Image reconstruction settings.
CTA = computed tomography angiography, NECT = non-enhanced computed tomography, IR = iterative reconstruction, TNC = true non-contrast, VNC = virtual non-contrast (including conventional and PureCalcium).

(2) Image noise measurements; And (3) quantification of coronary artery calcium.
To assess the efficacy of virtual iodine 'removal', the image volumes of each patient were transformed to obtain isotropic 1 x 1 x 1 mm voxels and registered, and a semi-manual segmentation of the whole heart was carried out with an open-source software (3D Slicer, www.slicer.org). Histograms of CT values and their proportions exceeding a threshold of 130 HU were compared between CTA, TNC, $VNC_{conv}$ and $VNC_{pc}$. As the different reconstruction settings were not expected to influence the virtual iodine 'removal', $VNC^1$ series were examined as representatives. To measure image noise, three circular ROIs with a diameter of 15 mm each were positioned in the left ventricular cavity on the CTA reconstruction of each patient, carefully avoiding papillary muscles, trabeculations and the ventricular wall. These ROIs were then automatically copied to all VNC series and to the TNC series of the same patient. The standard deviation of CT values within these ROIs served as a measure for image noise.
Quantification of coronary artery calcium was performed by a board-certified radiologist. To determine inter-reader correlation, an independent reading was performed by a second radiologist, who evaluated 10 randomly selected patients. Calcifications were quantified using Agatston score and calcium volume on a per-patient and per-vessel level. A commercially available semi-manual calcium scoring software (Syngo.CT CaScoring, VB60, Siemens Healthcare GmbH, Erlangen, Germany) was used for analysis, with a detection threshold of 130 HU. Both observers were blinded to the patients' identity, all clinical data and the reconstruction algorithms and series names. The time interval between the analyses of the TNC and VNC series was at least one week.

*Radiation Metrics*
For radiation dose estimation, the $CTDI_{vol}$ and the DLP of the NECT and CTA were retrieved from the automatically recorded dose report. Effective radiation doses of the NECT were estimated by multiplying the respective DLP with a standard conversion coefficient for adult chest CT (0.017 mSv/mGy*cm). For the CTA, we used the mean of the standard conversion coefficients of the chest (0.017 mSv/mGy*cm), abdomen (0.015 mSv/mGy*cm) and pelvis (0.019 mSv/mGy*cm) for effective dose calculation (0.017 mSv/mGy*cm).[71]

*Statistical Analysis*
Python (version 3.9) was utilized for statistical analysis in this study. Binary data are represented

| | |
|---|---|
| Total n = 38 | |
| Clinical | |
| Age [years] | 80.0 (75.3 - 82.8) |
| Male | 22 (57.9%) |
| BMI [kg/m$^2$] | 27.7 $\pm$ 5.6 |
| Cardiovascular risk factors | |
| Arterial hypertension | 27 (71.1%) |
| Current or former smoker | 4 (10.5%) |
| Diabetes | 17 (44.7%) |
| Hypercholesterolemia | 16 (42.1%) |
| Positive family history for adverse cardiovascular events | 1 (2.6%) |
| Obesity | 10 (26.3%) |
| Coronary artery calcium | |
| Total TNC Agatston Score | 934 (167 - 1991) |
| Total TNC Volume [mm$^3$] | 811 (200 - 1623) |

**Table 4.2:** Baseline study characteristics.
Values are mean $\pm$ standard deviation, median (interquartile range), or frequency (percentage). BMI = body mass index, TNC = true non-contrast.

as absolute frequencies and proportions. Continuous data were tested for normal distribution using the Shapiro-Wilk test. The paired t-test and the Wilcoxon signed-rank test were used to test for differences and the Pearson- and Spearman correlation to test for similarities for parametric and non-parametric data, respectively. Observer agreement was calculated by intraclass correlation coefficient for single fixed raters (ICC3). For all linear regression related presentations and calculations, data were square root transformed prior to analysis to approximate normal distribution and to improve homoscedasticity. The coefficient of determination ($r^2$) was used to rate the linear regression. To determine the predictive accuracy of calcium quantities on VNC series, a 10,000-fold bootstrap with a linear regression model was conducted. The mean absolute error (MAE) was calculated as the absolute difference between the predicted, back-transformed TNC value and the original TNC calcium quantity. P-values $< .05$ were considered to indicate statistical significance.

## Results

*Patient Baseline Characteristics*

A total of 50 patients were primarily enrolled, and 12 patients had to be excluded from analysis due to the predefined exclusion criteria (n(1) = 3, n(2) = 1, n(3) = 1, n(4) = 6). The final analysis included 38 patients (22 men (57.9%)) with a median age of 80.0 (75.3 - 82.8) years. Table 4.2 summarizes patient characteristics.

All patients underwent CT imaging due to aortic valve disease: 36 patients suffered from severe aortic stenosis (aortic valve area 0.7 $\pm$ 0.2 cm$^2$), one patient from severe combined aortic valve disease and one patient was planned for combined mitral and aortic valve intervention. Of the

38 patients, three presented with severe stenosis of an implanted biological aortic valve. There was no significant difference in heart rates between the NECT and CTA scans, which were 73 (62 - 83) bpm and 72 (61 - 80) bpm, respectively (p = .12). In the presence of coronary artery stents, the calcium scoring analysis excluded the coronary segment with the stent and all distal segments (LM: n = 1; LAD: n = 5; CX: n = 1; RCA: n = 4). Three of the patients showed no measurable calcium volume in the coronary arteries. Based on the TNC series, the median Agatston score and volume were 934 (167 - 1991) and 811 (200 - 1623) $mm^3$ on a per per-patient level, respectively. Representative images are provided in Figure 4.1.

*Iodine 'Removal'*

As for evaluating the effectiveness of virtual iodine 'removal' in VNC series, Figure 4.2 illustrates the method employed and the resulting histograms of the voxel CT value distribution analysis. This figure highlights the presence of three distinct CT value peaks in the CTA heart histogram, with the highest values being observed within the left ventricle, followed by the right ventricle and the myocardium. In the TNC and $VNC^1$ histograms these peaks overlap and barely any CT values exceed the threshold of 130 HU. While the median proportion of CT values $>$ 130 HU in whole heart histograms was 82.2 (77.4 - 86.4)% for CTA, this proportion significantly decreased to 0.2 (0.1 - 0.6)% for $VNC^1_{conv}$ and 0.7 (0.4 - 1.4)% for $VNC^1_{pc}$. With a median proportion of 0.6 (0.4 - 1.2)% for TNC, there was no significant difference to $VNC^1_{pc}$ (p = 0.4) but to $VNC^1_{conv}$ (p $<$ .01).

*Image Noise*

Regarding image noise, the results of the measurements are visualized in Figure 4.3. The measured noise level on TNC series was on average 26.4 $\pm$ 4.1 HU. Notably, image noise differed significantly between TNC and VNC (all p's $<$ .001) with the only exception being $VNC^4_{pc}$. The VNC reconstruction settings $VNC^1$ and $VNC^2$ resulted in rather higher noise levels ($\Delta <$ +3 HU for $VNC_{conv}{}^{1,2}$ and $\Delta <$ +7 HU for $VNC_{pc}{}^{1,2}$), the VNC reconstruction settings $VNC^3$ and $VNC^4$ in rather lower noise levels compared to TNC ($\Delta >$ -8 HU for $VNC_{conv}{}^{3,4}$ and $\Delta >$ -5 HU for $VNC^3_{pc}$).

*Calcium Scoring*

Observer agreement for calcium scores and calcium volumes was excellent for TNC and all VNC series, both on a per-patient and a per-vessel level (ICC3 $>$ .99). Analysis of the TNC series revealed three patients with a calcium score of zero. One of these patients was false positive (TNC calcium score = 0, VNC calcium score $>$ 0) in $VNC^2_{conv}$, all three patients were false positives in $VNC^2_{pc}$ and two of them were false positive in $VNC_{pc}{}^{1,3,4}$. For $VNC_{conv}$ series the discrepancies were small (Agatston score $<$ 2) and for $VNC_{pc}$ series moderate (Agatston score up to 90). False negative results (TNC calcium score $>$ 0, VNC calcium score = 0) occurred in total for four patients. Four times for $VNC^3_{conv}$, three times for $VNC^4_{conv}$ and once for $VNC^3_{pc}$. However, the respective TNC-based Agatston scores were small in all these cases (once $<$ 10, twice $<$ 80 and once $<$ 160). The boxplot in Figure 4.4A shows the results on a per-patient level. The total Agatston scores and calcium volume in TNC datasets were 934.4 (166.8 - 1990.6) and 811.4 (199.6 - 1623.4), respectively. $VNC_{conv}$ series significantly underestimated calcium

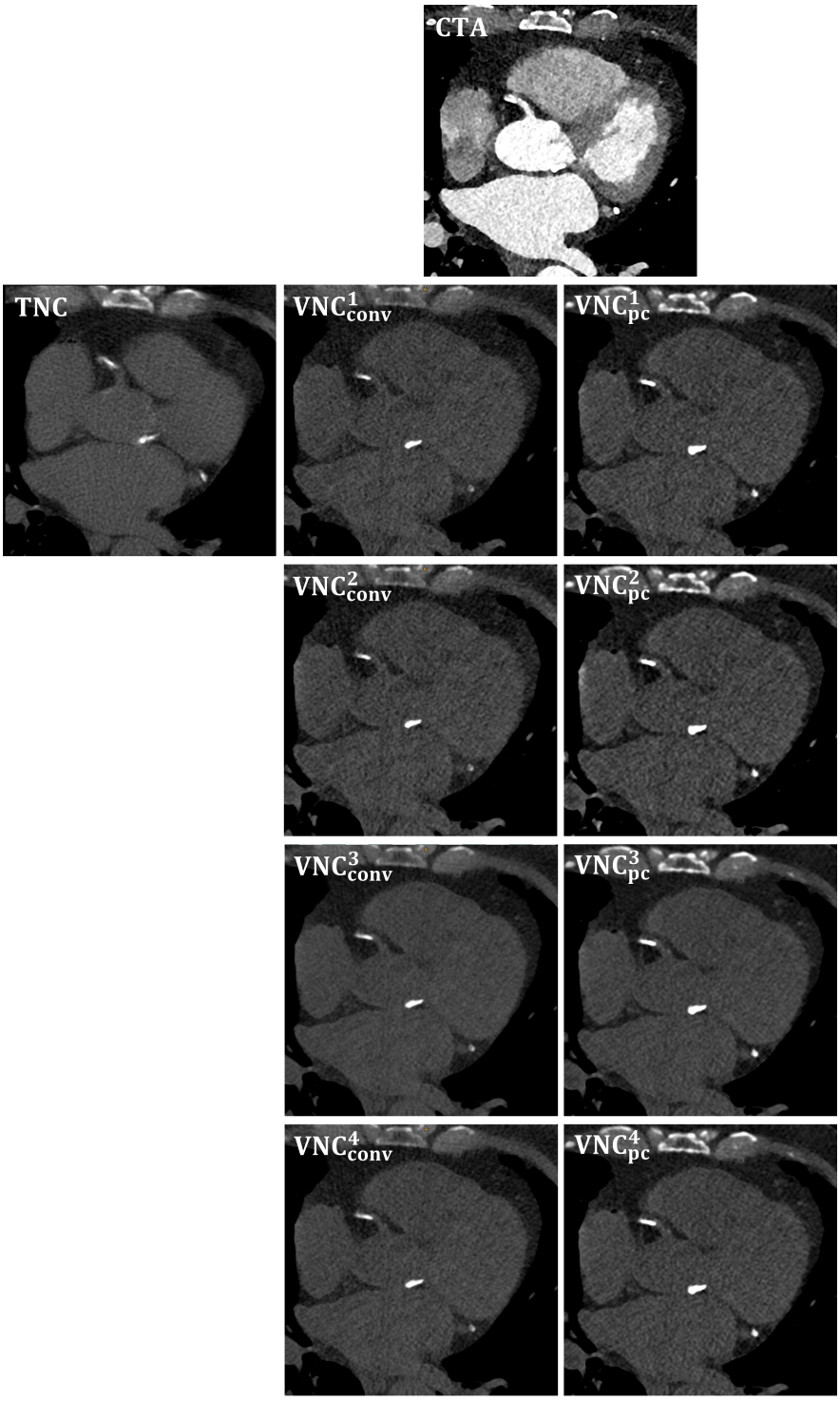


**Figure 4.1:** Corresponding image examples for TNC and all reconstructed VNC series respectively.

CTA = computed tomography angiography, TNC = true non-contrast, VNC = virtual non-contrast ($_{conv}$ = conventional, $_{pc}$ = PureCalcium).

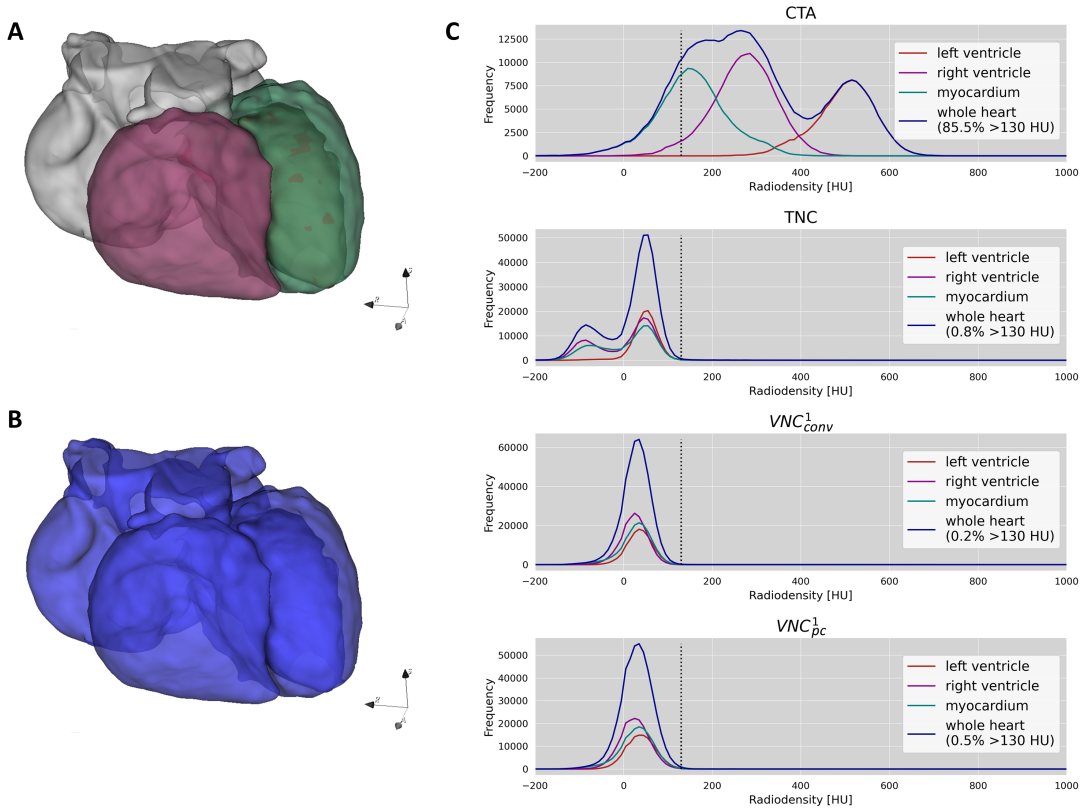


**Figure 4.2:** Effectiveness of iodine removal. **A** demonstrates the segmentation of the left ventricle, right ventricle and myocardium. **B** shows the segmentation of the whole heart including the atria. **C** exhibits the histograms based on the heart segments for CTA, TNC, $VNC^1_{conv}$ and $VNC^1_{pc}$. For the whole heart the histogram proportion exceeding 130 HU (marked by the dotted line) is given.

CTA = computed tomography angiography, TNC = true non-contrast, VNC = virtual non-contrast ($_{conv}$ = conventional, $_{pc}$ = PureCalcium).

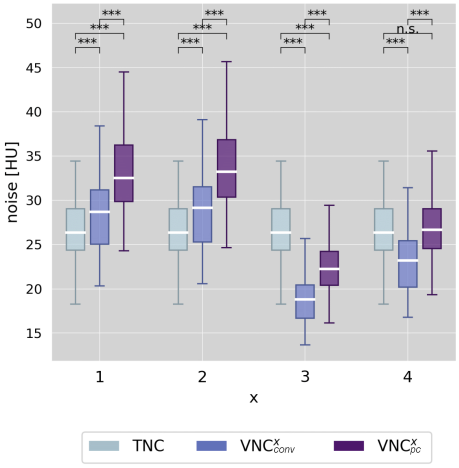


**Figure 4.3:** Boxplots of the noise levels measured as standard deviation of CT values in three circular regions of interest within the left ventricle comparing TNC and VNC series and differentiating between the different reconstruction settings of VNC$^x$ (x = 1-4). Stars mark significant differences as * = $p < .05$, ** = $p < .01$, *** = $p < .001$ and n.s. marks no significant difference.
TNC = true non-contrast, VNC = virtual non-contrast ($_{conv}$ = conventional, $_{pc}$ = PureCalcium).

quantities (all p's $< 0.001$). VNC$^2_{conv}$ showed the smallest absolute difference to TNC, with a median score of 637 and volume of 562 mm$^3$. The VNC$_{pc}$ series also differed significantly from TNC, however, to a much smaller extent. Again, VNC$^2$ achieved the best results with the smallest absolute difference of 82 (score) and 80 mm$^3$ (volume). Figure 4.4B presents the respective results on the per-vessel level for VNC$^2_{conv}$ and VNC$^2_{pc}$. Despite the differing absolute calcium quantity values, linear regression analysis showed excellent correlations between TNC and VNC, both globally ($r^2 > 0.93$), as demonstrated in Figure 4.5, and on the per-vessel level ($r^2 > 0.85$), regardless of reconstruction algorithm, reconstruction setting or calcium quantity. However, Figure 4.6 shows that the mean absolute error between the predicted calcium quantity based on VNC measurements and the true calcium quantity based on TNC measurements was significantly smaller for VNC$_{pc}$ compared to VNC$_{conv}$ for all reconstruction settings (all p's $< 0.001$). Among VNC$_{conv}$, VNC$^2_{conv}$ achieved the highest predictive accuracy with a median absolute error of 199 (162 - 238) in Agatston and 152 (127 - 179) mm$^3$ in volume score. All VNC$_{pc}$ reconstructions except VNC$^2_{pc}$ showed similar low median absolute errors of $< 138$ in Agatston and $< 110$ mm$^3$ in volume score.

*Radiation dose*

For the NECT and CTA scans, DLPs were 31.8 (24.0 - 38.7) mGy*cm and 330.0 (256.5 - 412.3) mGy*cm, with corresponding effective doses of 22.3 $\pm$ 6.8 mSv and 64.5 $\pm$18.2 mSv and CTDI$_{vol}$ of 1.5 (1.3 - 1.9) mGy and 4.4 (3.6 - 5.2) mGy, respectively.

## Discussion

Our study systematically investigated the potential of spectral data acquired during CCTA on a PCD-CT for distinguishing iodine and non-iodine attenuation components and quantifying

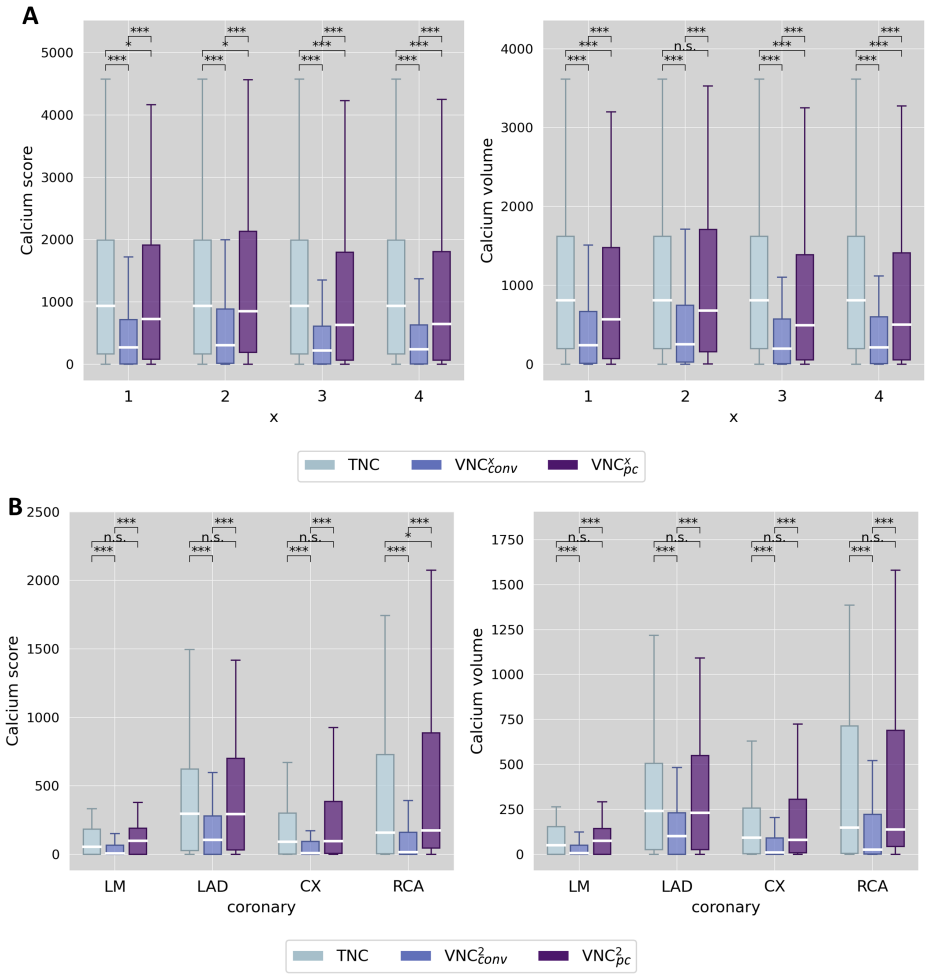


**Figure 4.4:** Boxplot of measured calcium quantities (score and volume) comparing TNC and VNC series. **A** differentiates between the different reconstruction settings of VNC$^{x}$ (x = 1-4) and **B** between the different coronary arteries considering only VNC$^{2}$ series. Stars mark significant differences as * = $p < .05$, ** = $p < .01$, *** = $p < .001$ and n.s. marks no significant difference. TNC = true non-contrast, VNC = virtual non-contrast ($_{conv}$ = conventional, $_{pc}$ = PureCalcium).

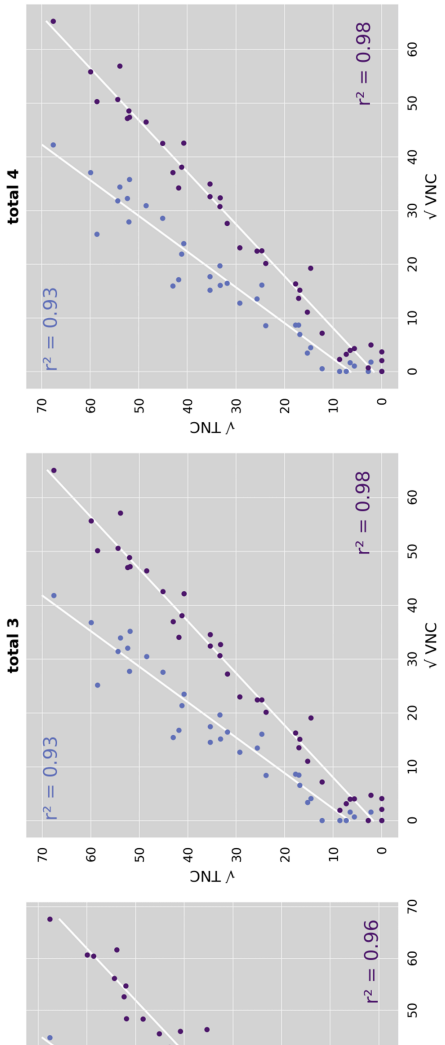


**Figure 4.5:** Linear regression analyses of TNC and VNC series shown for the Agatston score on a per-patient level for the different reconstruction settings of VNC$^x$ (x = 1-4).
$r^2$ = coefficient of determination, TNC = true non-contrast, VNC = virtual non-contrast ($_{conv}$ = conventional, $_{pc}$ = PureCalcium).

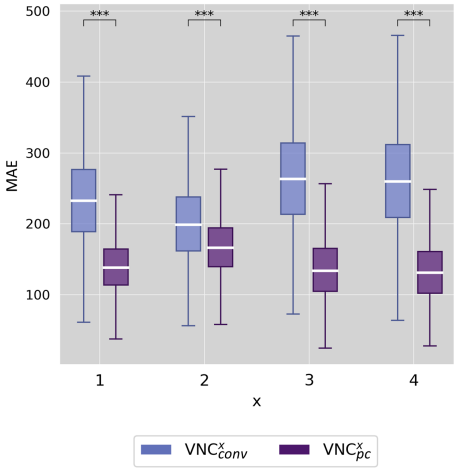


**Figure 4.6:** Boxplots of the MAE between the predicted Agatston scores based on VNC and Agatston scores derived from TNC on a per-patient level resulting from the 10,000-fold bootstrapping analysis for the different reconstruction settings of VNC$^x$ (x = 1-4). Stars mark significant differences as * = $p < .05$, ** = $p < .01$, *** = $p < .001$ and n.s. marks no significant difference.

MAE = mean absolute error, TNC = true non-contrast, VNC = virtual non-contrast ($_{conv}$ = conventional, $_{pc}$ = PureCalcium).

calcium in CTA datasets. Our main findings are as follows: (1) VNC series derived from CTA datasets exhibit a highly effective subtraction of the iodine attenuation component (i.e. contrast material); (2) The resulting VNC series have suitable noise properties for a HU-threshold based calcium quantification; (3) The absolute calcium quantities derived from VNC series differ significantly from the absolute values measured on TNC scans but show excellent correlation with the reference standard; (4) The calcium-preserving algorithm $VNC_{pc}$ outperforms the conventional $VNC_{conv}$ algorithm by achieving comparable absolute scores to the ground truth on TNC and yielding a higher predictive accuracy.

Due to their distinct mechanistic properties, PCD systems generate spectral information about the tissue examined. Similar to earlier work on DECT, this can be utilized to derive VNC series from contrast-enhanced scans, such as CTA studies, by material decomposition. In VNC series, CT values represent the non-iodine attenuation component of each voxel, with values $> 130$ HU primarily attributable to calcium. This permits calcium quantification, akin to earlier work on DECT.[47,48,50,64–66,72] Employing such a technique in the workup of coronary artery disease would have the advantage of eliminating the need for a dedicated non-enhanced acquisition, thereby reducing procedure time and overall radiation dose.

Presently, there remains a scarcity of literature regarding the implementation of this method on spectral PCD-CT data. Emrich et al.[7] and Fink et al.[73] have demonstrated a strong correlation between calcium quantities obtained from CCTA-derived VNC series and actual calcium quantities obtained from TNC series. In addition, utilizing a novel algorithm that produces $VNC_{pc}$ series by selectively subtracting the iodine attenuation component, calcium quantities measured on CTA datasets exhibited a high degree of concordance with actual calcium quantities. Despite

the remarkable findings of these studies, neither one convincingly addressed the image features of VNC series, which must satisfy specific requirements for the validity of the aforementioned correlation or agreement to be unambiguously demonstrated. Our study closes this gap in knowledge.

VNC series, that are suitable for calcium quantification and interchangeable with TNC series, must satisfy at least three requirements: (1) Effective virtual 'removal' of the iodine attenuation component to generate a VNC dataset; (2) Noise properties within the VNC dataset that permit HU-threshold-based calcium quantification, which necessitates low standard deviation (SD) in CT values in normal soft tissue; And (3) preservation of calcium. Failure to fulfill requirements (1) and (2) could result in false positives or inappropriately high calcium scores, while failure to meet requirement (3) could lead to false negatives or inaccurately low calcium scores.

To assess the fulfillment of requirement (1), we performed an extensive three-dimensional comparative analysis of the CT value distribution for the entire heart in all relevant series (CTA, TNC, $VNC^{1}_{conv}$ and $VNC^{1}_{pc}$ series). As anticipated, the CT value histograms of the CTA datasets displayed mostly trimodal distribution (left ventricle, right ventricle, myocardium). Conversely, VNC series exhibited unimodal distributions closely resembling TNC series. These stark similarities in CT value distribution, both qualitatively and quantitatively, between TNC and VNC series strongly indicate a highly efficacious removal of the iodine attenuation component. To assess the fulfillment of requirement (2), we evaluated the distribution of CT values within ROIs located in the left ventricle on the TNC and all VNC series. Calcium scoring is traditionally performed on 3 mm slices as this provides an optimal balance between image noise and calcium sensitivity.[46] Our reference standard TNC was acquired accordingly. Since VNC series are derived from underlying CCTA datasets at a significantly higher $CTDI_{vol}$, we expected image noise to be comparable at much lower slice thicknesses, and thus employed either 0.4 mm or 1.0 mm. Using additional variations in reconstruction kernels and strengths of IR, we derived four distinct series from CCTA dataset for each VNC algorithm. Our analysis of image noise revealed significant differences between TNC and all VNC series. Notably, despite the low slice thickness of 0.4 mm, $VNC^{1,2}$ series demonstrated only marginally higher image noise than TNC series. In $VNC^{3,4}$ series (1.0 mm slice thickness), noise was even lower than in TNC series. In summary, these findings highlight that, with the appropriate selection of VNC settings, requirement (2) can be easily met. To evaluate the fulfillment of requirement (3), we used an indirect method of proof by comparing calcium quantities obtained from VNC series with those derived from TNC series, the reference standard. Our results, consistent with prior research on DECT, demonstrate that calcium quantities on $VNC_{conv}$ series consistently underestimate references values, whereas $VNC_{pc}$ results in comparable absolute values. Notably, only few cases of false negatives or false positives were found. We observed that $VNC_{conv}$ rather produces false negatives while $VNC_{pc}$ rather produces false positives, which can be explained by the different VNC reconstruction algorithm. However, both algorithms exhibit excellent correlation for both the entire coronary tree, as well as individual coronary arteries and for calcium scores and volumes. Nonetheless, the 10,000-fold bootstrap cross-validation shows a higher predictive accuracy of $VNC_{pc}$ for actual TNC calcium quantities.

Summarizing our results on the VNC-dataset characteristics, the most favorable approach was the use of 0.4 mm reconstructions in combination with a high level of IR (level 4). Surprisingly, a regular body kernel (Br36) yielded slightly superior results to the dedicated quantitative kernel (Qr36).
In essence, our findings corroborate the conclusions drawn by Emrich et al. regarding the remarkable correlation and strong predictive value of calcium quantities measured on VNC series with actual calcium quantities. However, we go a step further in filling the remaining gap in knowledge by demonstrating that VNC series employed for this purpose are nearly indistinguishable from NECT regarding the presence of contrast material and exhibit optimal noise characteristics for HU-based calcium quantification. It is only when these requirements are met that the correlation of calcium quantities attains the logical validity as suggested.
Some limitations of our study merit consideration. First, with 38 patients, our study cohort was relatively small, and further studies with a larger study group should follow to confirm our results. Another limitation might be that our study cohort was examined using a high pitch acquisition mode irrespective of the individual heart rate. Patients did not receive betablockade or nitroglycerine. Theoretically, one could expect higher proportions of CT scans affected by motion artifacts. To address this potential objection, patients with marked motion artifacts of the coronary arteries were excluded from further analysis.

## Conclusion

In conclusion, our results show that the iodine-based attenuation component can be effectively subtracted from PCD-CTA datasets, and that the remaining non-iodine attenuation component satisfies all the mentioned requirements for calcium quantification, yielding coronary artery calcium quantities with excellent correlation to the reference standard TNC. For the conventional $VNC_{conv}$ algorithm, the best results were obtained by the use of ultra-thin-slice reconstructions (0.4 mm) in combination with a high level of iteration (QIR4). The calcium-preserving $VNC_{pc}$ algorithm was not influenced by the reconstruction settings tested in this study, and it even outperformed $VNC_{conv}$. Therefore, CACS on $VNC_{pc}$ raises the prospect of substituting TNC scans with a VNC reconstruction to save radiation dose, time, and cost.

### 4.1.2 Aortic Valve Calcium Scoring

## Virtual Non-Contrast Series of Photon-Counting Detector Computed Tomography Angiography for Aortic Valve Calcium Scoring

Franka Risch*, Eva Harmel*, Katharina Rippel, Bastian Wein, Philip Raake, Evaldas Girdauskas, Sebastien Elvinger, Tamer Owais, Christian Scheurig-Münkler, Thomas Kröncke, Florian Schwarz, Franziska Braun*, Josua Decker*

* = contributed equally

The study was published in The International Journal for Cardiovascular Imaging in January 2024.[11] The author FR performed the data collection, interpretation and statistical analysis and revised the manuscript.

### Abstract

*Background:* The prognostic value of aortic valve calcium scoring (AVCS) in patients prior to TAVR is well established. Its reliable quantification usually requires a TNC CT scan of the heart. With inherently acquired spectral data of PCD-CT, VNC reconstructions based on CTA acquisitions can be derived. The aim of our study was to evaluate two different VNC algorithms in terms of noise, effectiveness of contrast media subtraction and AVCS compared to TNC based results.

*Methods:* Consecutive patients underwent TAVR planning examination on a PCD-CT comprising a TNC scan, followed by a CTA of the heart. Eight VNC series were reconstructed using a conventional ($VNC_{conv}$) and a novel calcium-preserving algorithm ($VNC_{pc}$), with different reconstruction settings regarding kernel, IR strength or slice thickness. Noise was analyzed by means of the SD of CT values within ROIs placed in the left ventricle. To assess the effectiveness of contrast media removal, whole heart volumes were segmented and the proportion of their histograms greater than 130 HU was taken. AVCS was measured by Agatston score and volume.

*Results:* 41 patients (41.46% female) were included in the study. Comparable noise levels to TNC were achieved with all reconstruction settings and VNC algorithms. Contrast media was effectively virtually removed and histogram proportions exceeding 130 HU were significantly reduced in VNC compared to CTA. Median calcium scores derived from $VNC_{conv}$ underestimated TNC-based scores by up to 74%. The most comparable results were obtained with ultra thin (0.4 mm) $VNC_{pc}$ reconstructions with a regular soft tissue body kernel (Br36, IR strength 4), but they still resulted in a significant underestimation of 29% in the median. However, both VNC algorithms showed perfect correlation in AVCS with TNC, with negligible differences between reconstruction settings.

*Conclusion:* Thin-slice VNC reconstructions derived from PCD-CTA provide equivalent noise levels to standard thick-slice TNC series and effective virtual removal of iodinated contrast. AVCS was shown to be feasible on both $VNC_{conv}$ and $VNC_{pc}$ series, with values showing near-perfect correlation, but with significant underestimation. $VNC_{pc}$ with 0.4 mm slices and Br36 kernel at IR strength 4 gave the most comparable results and could be a promising replacement

for additional TNC scans, reducing patient radiation dose and examination time.

## Introduction

The prognostic value of AVCS in patients prior to TAVR is well established.[42–45,74] In 2021, the European Society of Cardiology/ European Association for Cardio-Thoracic Surgery guidelines for the management of valvular heart disease further emphasized the importance of AVCS on cardiac computed tomography (CCT) images for class IIa indications prior to aortic valve replacement. To assess the feasibility of a TAVR procedure by evaluating anatomical details of the aortic valve and vascular access, as well as to calculate annular dimensions, CTA is considered the gold standard in the diagnostic workup.[69,75] However, accurate AVCS in TAVR patients requires an additional TNC scan, which naturally increases radiation exposure to the patient.

CT systems capable of acquiring spectral data allow virtual subtraction of iodine contrast from CTA series. The resulting VNC series promises to eliminate the need for separate TNC series, reducing patient's radiation dose and acquisition time.[9,76] In addition to the well-known techniques, such as dual-energy, kV-switching or dual-layer based on EIDs, novel PCDs inherently provide spectral information for each scan performed. Recent studies have demonstrated the reliability of VNC-measured coronary calcium scores, with excellent correlation to TNC-measured scores.[7,50,72,73,77] Because calcium and iodine have similar attenuation characteristics, conventional VNC algorithms ($VNC_{conv}$) partially subtract the calcium contrast, resulting in an underestimation of the score. A novel calcium-preserving VNC algorithm (PureCalcium, $VNC_{pc}$) performs additional steps to differentiate between iodine and calcium prior to contrast subtraction and restores calcium contrast subsequently.[7]

The study objective was to evaluate the feasibility of AVCS on both conventional and calcium-preserving VNC series, derived from PCD-CTA datasets compared to reference TNC values. Furthermore, we investigated the influence of different reconstruction settings on noise, effectiveness of iodine removal and tested the acquired VNC calcium scores for their predictive accuracy compared to TNC.

## Materials and Methods

This retrospective single-center study at the University Hospital Augsburg was approved by the institutional review board with a waiver for written informed consent. The trial was reviewed and cleared by local ethics committee of the Ludwig Maximilian University of Munich (project number 22-0456).

*Study Population*

Consecutive patients who followed the institution's standard pre-TAVR scanning protocol between June and September 2021 were included in the study cohort and allowed for further processing and analysis of CT images. Patients with status post aortic valve replacement or non-measurable massive calcification, e.g. severe calcification including the aortomitral continuity, were excluded from the analysis.

| Series | Kernel | IR level | Slice thickness/ increment [mm] |
|---|---|---|---|
| TNC | Qr36 | no IR | 3.0/ 1.5 |
| $VNC^1_{conv}$/ $VNC^1_{pc}$ | Qr36 | 4 | 0.4/ 0.2 |
| $VNC^2_{conv}$/ $VNC^2_{pc}$ | Br36 | 4 | 0.4/ 0.2 |
| $VNC^3_{conv}$/ $VNC^3_{pc}$ | Qr36 | 4 | 1.0/ 0.4 |
| $VNC^4_{conv}$/ $VNC^4_{pc}$ | Qr36 | 3 | 1.0/ 0.4 |

**Table 4.3:** Image reconstruction settings for TNC and VNC.
IR = iterative reconstruction, TNC = true non-contrast, VNC = virtual non-contrast ($_{conv}$ = conventional, $_{pc}$ = Pure-Calcium).

*Data Acquisition*

All scans were performed on a first generation, dual-source PCD-CT (NAEOTOM Alpha, Siemens Healthcare GmbH, Erlangen, Germany). The scan protocol included two contrast phases, first, a pre-contrast acquisition of the heart (TNC) and second a CTA of the heart, aorta, and iliac arteries. Both scans were performed with a high pitch of 3.2 and ECG-triggered. The tube voltage was 120 kVp and the detector collimation 144 x 0.4 $mm^2$. By setting the image quality level to 19 and 64 for TNC and CTA, respectively, the reference tube current time product was adjusted. For the CTA a triphasic contrast injection protocol with bolus tracking was used, following institutional standard. In the first phase 60 ml of undiluted contrast material (Iopromide Ultravist 300 mgI/ml, Bayer Vital, Leverkusen, Germany) was injected followed by a mixture of 30 ml contrast material and 30 ml 0.9% saline solution and chased with 20 ml 0.9% saline solution. A flow of 5 ml/s was used in all three phases.

*Image Reconstruction*

TNC from pre-contrast and $VNC_{conv}$ series from CTA raw data were directly reconstructed on the scanner console (VA40, Siemens Healthcare GmbH, Erlangen, Germany). $VNC_{pc}$ reconstructions were performed on a dedicated workstation (ReconCT, Version 15.0, Siemens Healthcare GmbH, Erlangen, Germany), both using the best diastole. Only one TNC series was reconstructed as ground truth with standard settings, using a quantitative regular kernel (Qr36), VM level of 70 keV, the quantum IR off and slice thickness and increment of 3.0 and 1.5 mm. For reconstructions based on CTA, the approach of thin slices/ increments (0.4/ 0.2 mm and 1.0/ 0.4 mm) was followed, as they were expected to reveal even very small calcifications and to max out the resolution capabilities of the CT detectors. To compensate for an increase in image noise, the IR levels were increased (Q3 and Q4). In addition to the proposed quantitative kernel (Qr36), a body kernel (Br36) was also used. All settings were combined with both VNC algorithms (conventional and PureCalcium at VM level of 70 keV). A detailed description of the settings resulting in four reconstructions for each VNC algorithm is given in Table 4.3. The FoV was set for all series equivalently to 180 x 180 $mm^2$, covering the whole heart. The main difference between the VNC algorithms used, is in the handling of calcium. Since the attenuation properties of iodinated contrast media and calcium are similar, subtraction of iodine alone will also result in partial removal of the calcium component as in $VNC_{conv}$. By differen-

tiating between iodine and calcium prior to the iodine subtraction step, the $VNC_{pc}$ algorithm reconstructs the calcium contrast afterwards.

*Image Analysis*

Image analysis was divided into three parts including noise analysis, effective iodine subtraction assessment and AVCS. Noise was measured by positioning a 15 mm diameter ROI within the left ventricle on three different slices of the CTA series using commercial imaging software (DeepUnity, Dedalus HealthCare Group AG, Bonn, Germany). ROIs were automatically transferred to the TNC and VNC reconstructions and the mean and SD of the CT values were recorded. The SD averaged over the three slice positions was used as a measure of image noise. To assess effective virtual iodine subtraction, for each patient the series were transformed to obtain isotropic 1 $mm^3$ voxels, registered and a semi-manual segmentation of the whole heart was performed using open-source software (Slicer3D, www.slicer.org). CT value distributions were compared between CTA, TNC and VNC series. $VNC^1_{conv}$ and $VNC^1_{pc}$ reconstructions were used as representative for each algorithm.

AVCS was measured semi-manually with a commercially available software (syngo.CT, CaScoring workflow, Siemens Healthcare GmbH, Erlangen, Germany) considering contiguous voxels with a CT value above a threshold of 130 HU. Both, Agatston score and volume of the aortic valve were analyzed for all, TNC and VNC series.

*Statistical Analysis*

Statistical analyses were performed using python (version 3.8.1). The Shapiro-Wilk test was applied to assess value distribution. The paired t-test and the Wilcoxon signed-rank test were used to test for differences in parametric and non-parametric data respectively. For all linear regression related presentations and calculations, data were square root transformed prior to analyses to improve homoscedasticity. To obtain the predictive accuracy of calcium quantities in VNC series, a 10,000-fold bootstrap was performed on a linear regression model. The mean absolute error was calculated as the absolute difference between the predicted, back-transformed and the TNC measured calcium quantity. Binary data are presented in frequencies (proportions) and continuous data with mean $\pm$ SD or as median with interquartile range, as individually indicated. P-values $< .05$ were considered to indicate statistical significance.

## Results

*Baseline Study Characteristics*

A total of 45 patients were primarily enrolled. Four patients were excluded due to status post aortic valve replacement (n = 3) and non-segmentable massive calcification of the aortic valve and aortomitral continuity (n = 1) according to the exclusion criteria. The other patients (n = 41), thereof 17 (41.5%) women, were included in the study. Regarding CT radiation dose, median $CTDI_{vol}$ and DLP were 1.5 mGy and 31.8 mGy*cm for the pre-contrast, and 4.4 mGy and 330.0 mGy*cm for CTA scans, respectively. Mean AVCS on TNC series was 2829 and 2242 $mm^3$ for Agatston score and volume, respectively. Further baseline characteristics of the study cohort are shown in Table 4.4. Figure 4.7 visualizes all reconstructions considered at

| | | |
|---|---|---|
| Total n = 41 | | |
| Clinical | | |
| Age [years] | 80.0 (75.0 - 83.0) | |
| Male | 24 (58.5%) | |
| BMI [kg/m$^2$] | 25.9 (23.6 - 32.4) | |
| Aortic valve area [cm$^2$] | 0.72 $\pm$ 0.22 | |
| TNC calcium Agatston score | 2829 $\pm$ 1618 | |
| TNC calcium volume [mm$^3$] | 2242 $\pm$ 1253 | |
| Cardiovascular risk factors | | |
| Arterial hypertension | 30 (73.2%) | |
| Current or former smoker | 10 (24.4%) | |
| Diabetes | 18 (43.9%) | |
| Hypercholesterolemia | 15 (36.6%) | |
| Positive family history for adverse cardiovascular events | 1 (2.4%) | |
| Obesity | 11 (26.8%) | |
| CT radiation dose | Pre-contrast | CTA |
| $CTDI_{vol}$ [mGy] | 1.5 (1.2 - 1.9) | 4.4 (3.6 - 5.2) |
| DLP [mGy*cm] | 31.8 (23.5 - 38.8) | 330.0 (270 - 410) |
| Effective mAs [mAs] | 21 (17 - 26) | 62 (52 - 77) |
| SSDE [mGy] | 2.0 (1.7 - 2.2) | 5.4 (4.8 - 6.1) |

**Table 4.4:** Baseline study characteristics.

Values are mean $\pm$ SD, median (interquartile range), or frequency (percentage). BMI = body mass index, $CTDI_{vol}$ = volumetric CT dose index, DLP = dose length product, SSDE = size specific dose estimate, TNC = true non-contrast.

the same axial slice position. All results of the evaluations performed for noise, virtual iodine subtraction and aortic valve calcification are summarized in Table 4.5.

*Image Noise*

Image noise levels, assessed as SD of CT values in ROIs in the left ventricular cavity, showed significant differences between TNC (27 $\pm$ 4 HU) and all $VNC_{conv}$ and most $VNC_{pc}$ series ($p < .001$) as demonstrated in the boxplot in Figure 4.8. For reconstruction settings x = 1, 2 noise on VNC was on average higher ($VNC_{conv}^{1,2}$ = 28 $\pm$ 5, 29 $\pm$ 5 HU and $VNC_{pc}^{1,2}$ = 33 $\pm$ 5, 33 $\pm$ 5 HU) and for x = 3, 4 noise was lower compared to TNC ($VNC_{conv}^{3,4}$ = 19 $\pm$ 4, 23 $\pm$ 4 HU and $VNC_{pc}^{3}$ = 22 $\pm$ 4 HU). However, differences were small (on average $<$ 6 HU). Only $VNC_{pc}^{4}$ showed no significant difference in noise level ($VNC_{pc}^{4}$ = 27 $\pm$ 4 HU).

*Virtual Iodine Subtraction*

Figure 4.9 shows the principle of how the effectiveness of virtual iodine subtraction was measured. The CT value histograms of the whole heart volume were compared between CTA, TNC, conventional and PureCalcium VNC. As representatives only reconstructions x = 1 were used. Median proportions exceeding 130 HU were 81%, 0.5%, 0.2% and 0.6% for CTA, TNC, $VNC_{conv}^{1}$ and $VNC_{pc}^{1}$, respectively. Differences were significant between CTA and all non-contrast series ($p < .001$). The proportions of TNC greater than 130 HU were also significantly different from $VNC_{conv}^{1}$ ($p < .001$) but not from $VNC_{pc}^{1}$ (p = 1.0).

*Calcium quantification*

Median calcium quantities were 2800 and 2206 $mm^3$ on TNC. Mean percentage differences of $VNC_{conv}^{1\text{-}4}$ to TNC were -69%, -69%, -71%, -70% and -69%, -69%, -71%, -70% and of $VNC_{pc}^{1\text{-}4}$ to TNC -25%, -25%, -32%, -31% and -28%, -28%, -35%, -34%, for score and volume respectively (see Figure 4.10). Measurements on all VNC reconstructions significantly underestimated calcium quantities with TNC as ground truth ($p < .001$). However, the underestimation in the score was more than twice as high for $VNC_{conv}$ compared to $VNC_{pc}$. The differences between the individual reconstruction settings x = 1 - 4 were relatively small, but x = 2 (body kernel, maximum IR level, super thin slices) gave the best results with the smallest average underestimation. Two patients had no calcium and an equivalent score of zero for TNC and all VNC reconstructions. Linear correlation of TNC and all VNC-based calcium quantities was excellent (all $r^2 > 0.9$) without striking differences between the two VNC algorithms or reconstruction settings. In Figure 4.11A a linear regression is demonstrated for Agatston scores of series x = 2. However, the results of the bootstrap analysis showed a small trend towards higher absolute mean errors in predicting calcium scores based on a linear regression model for $VNC_{pc}$ compared to $VNC_{conv}$. The median MAE was 405, 378, 404, 398 and 316, 296, 308, 301 $mm^3$ for $VNC_{conv}^{1\text{-}4}$ and 448, 426, 392, 394 and 357, 341, 305, 309 $mm^3$ for $VNC_{pc}^{1\text{-}4}$ for score and volume, respectively. Figure 4.11B shows the results for the Agatston score and all series x = 1 - 4.

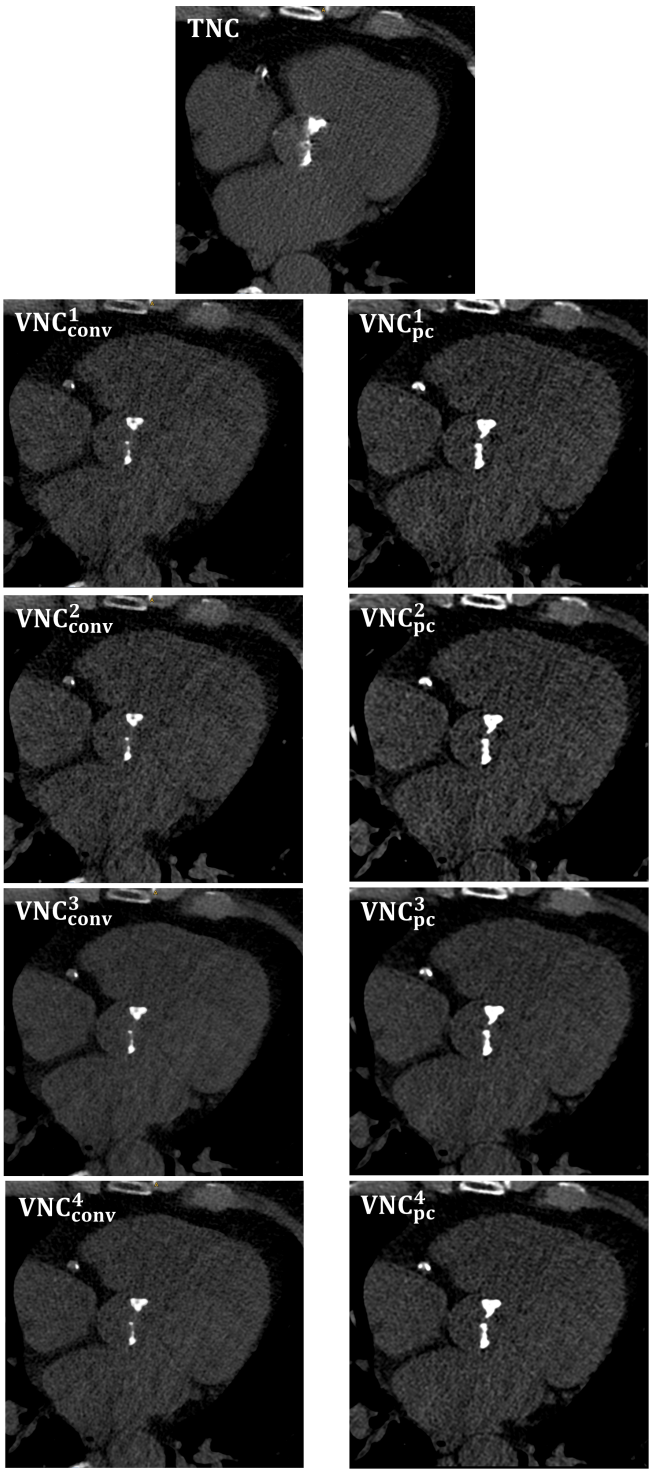


**Figure 4.7:** Demonstration of the aortic calcification in an axial slice for TNC and both VNC series, conventional and PureCalcium, and all $VNC^x$ reconstruction settings (x = 1 - 4).
TNC = true non-contrast, VNC = virtual non-contrast ($_{conv}$ = conventional, $_{pc}$ = PureCalcium).

| | Noise SD [HU] | p-value | Virtual Iodine Subtraction Histogram > 130 HU | p-value | Aortic Valve Calcification Total Agatston score Volume score [$mm^3$] | Percentage difference In Agatston score In Volume score | p-value | $r^2$ | MAE |
|---|---|---|---|---|---|---|---|---|---|
| TNC | 27 ± 4 | | 0.5 (0.4 - 1.2)% | | 2800 (2075 - 3682)<br>2206 (1645 - 2895) | | | | |
| $VNC^1_{conv}$ | 28 ± 5 | p<.001 | 0.2 (0.1 - 0.5)% | p<.001 | 752 (390 - 1357) | -69 ± 11% | p<.001 | 0.91 | 405 (351 - 475) |
| | | | | | 653 (320 - 1052) | -69 ± 11% | p<.001 | 0.91 | 316 (276 - 369) |
| $VNC^1_{pc}$ | 33 ± 5 | p<.001 | 0.6 (0.4 - 1.3)% | p = 1.0 | 1986 (1270 - 3278) | -25 ± 20% | p<.001 | 0.91 | 448 (388 - 520) |
| | | | | | 1515 (971 - 2480) | -28 ± 20% | p<.001 | 0.91 | 357 (308 - 416) |
| $VNC^2_{conv}$ | 29 ± 5 | p<.001 | | | 777 (408 - 1381) | -69 ± 11% | p<.001 | 0.92 | 378 (328 - 441) |
| | | | | | 652 (333 - 1064) | -69 ± 11% | p<.001 | 0.92 | 296 (257 - 344) |
| $VNC^2_{pc}$ | 33 ± 5 | p<.001 | | | 2023 (1320 - 3282) | -25 ± 19% | p<.001 | 0.92 | 426 (368 - 493) |
| | | | | | 1536 (1009 - 2479) | -28 ± 19% | p<.001 | 0.91 | 341 (294 - 396) |
| $VNC^3_{conv}$ | 19 ± 4 | p<.001 | | | 731 (383 - 1279) | -71 ± 11% | p<.001 | 0.91 | 404 (348 - 478) |
| | | | | | 591 (316 - 980) | -71 ± 11% | p<.001 | 0.92 | 308 (267 - 363) |
| $VNC^3_{pc}$ | 22 ± 4 | p<.001 | | | 1760 (1180 - 3082) | -32 ± 19% | p<.001 | 0.93 | 392 (339 - 453) |
| | | | | | 1351 (900 - 2341) | -35 ± 19% | p<.001 | 0.93 | 305 (263 - 353) |
| $VNC^4_{conv}$ | 23 ± 4 | p<.001 | | | 757 (391 - 1302) | -70 ± 11% | p<.001 | 0.92 | 393 (338 - 468) |
| | | | | | 610 (323 - 1022) | -70 ± 11% | p<.001 | 0.92 | 301 (261 - 356) |
| $VNC^4_{pc}$ | 27 ± 4 | p = 1.0 | | | 1808 (1183 - 3121) | -31 ± 19% | p<.001 | 0.93 | 394 (339 - 456) |
| | | | | | 1396 (907 - 2374) | -34 ± 19% | p<.001 | 0.92 | 309 (265 - 358) |

**Table 4.5:** Summarized results of the evaluations performed for noise, virtual iodine subtraction and aortic valve calcification.

Values are mean ± SD or median (interquartile range), MAE = mean absolute error, TNC = true non-contrast, VNC = virtual non-contrast ($_{conv}$ = conventional, $_{pc}$ = PureCalcium). P-values refer to comparison with ground truth (TNC) and are corrected using the Bonferroni method.

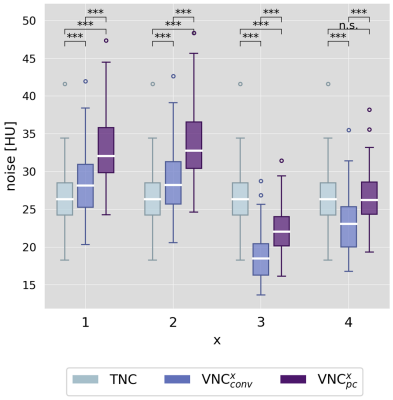


**Figure 4.8:** Box plots of image noise analyses. Noise is assessed as ROI in the left ventricular cavity and compared between TNC, $VNC_{conv}^{x}$ and $VNC_{pc}^{x}$ series for all reconstruction settings (x = 1 - 4). Stars mark significant differences as * = $p < .05$, ** = $p < .01$, *** = $p < .001$ and n.s. marks no significant difference.

TNC = true non-contrast, VNC = virtual non-contrast ($_{conv}$ = conventional, $_{pc}$ = PureCalcium).

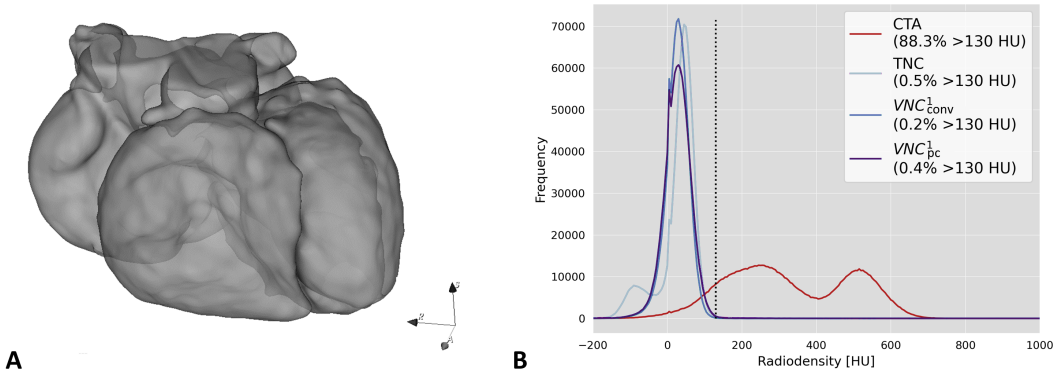


**Figure 4.9:** Effectiveness of iodine removal. A demonstrates the segmentation of the whole heart and B shows the histograms based on the respective reconstruction. The histogram proportion exceeding 130 HU (marked by the dotted line) is given in the legend.

CTA = CT angiography, TNC = true non-contrast, VNC = virtual non-contrast ($_{conv}$ = conventional, $_{pc}$ = PureCalcium).

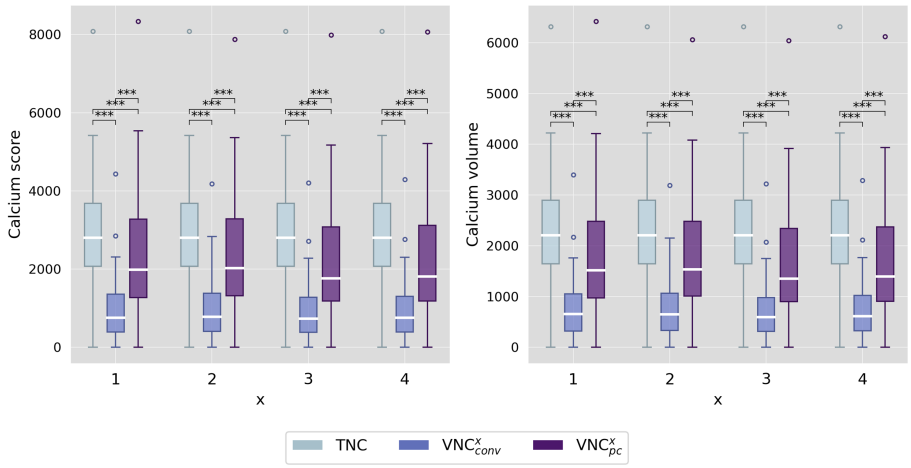


**Figure 4.10:** Boxplot of measured calcium quantities comparing TNC and VNC series for each different reconstruction setting of VNC$^x$ (x = 1 - 4). Stars mark significant differences as * = $p < .05$, ** = $p < .01$, *** = $p < .001$ and n.s. marks no significant difference.
CTA = CT angiography, TNC = true non-contrast, VNC = virtual non-contrast ($_{conv}$ = conventional, $_{pc}$ = PureCalcium).

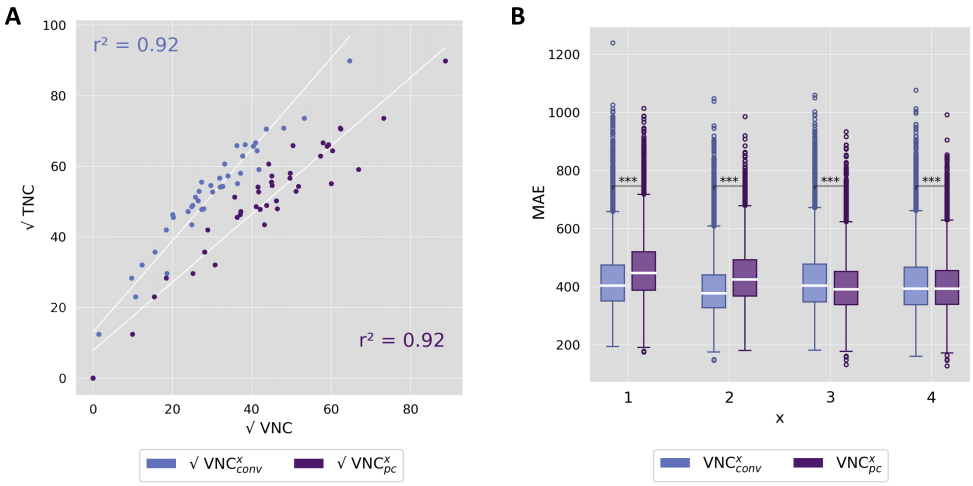


**Figure 4.11:** **A** shows the linear regression analyses of square root transformed Agatston scores derived from TNC vs. VNC for reconstruction setting x = 2. **B** shows the calculated mean absolute error from 10,000-fold bootstrapping analysis for the Agatston score and all reconstruction settings of VNC$^x$ (x = 1 - 4). Stars mark significant differences as * = $p < .05$, ** = $p < .01$, *** = $p < .001$ and n.s. marks no significant difference.
$r^2$ = coefficient of determination, TNC = true non-contrast, VNC = virtual non-contrast ($_{conv}$ = conventional, $_{pc}$ = PureCalcium).

## Discussion

This study evaluated the performance of different VNC algorithms and reconstruction parameters for virtual AVCS on PCD-CTA series. The main findings of this study are: (1) Iodine contrast was effectively removed in all VNC series; (2) AVCS values were significantly underestimated on all VNC reconstructions, with little effect of the reconstruction setting, however, differences to TNC-based values were more than twice as large for $VNC_{conv}$ compared to $VNC_{pc}$; (3) Although the linear correlation was excellent for all VNC to TNC-based AVCS measures, the prediction error was negligibly higher for $VNC_{pc}$ reconstructions than for $VNC_{conv}$ reconstructions.

In the spreading field of catheter-based procedures, aortic stenosis remains the most important indication for catheter-based valve replacement.[78] Various CT derived parameters, e.g. AVCS quantity, play a tremendous role in procedure planning, patient selection and medical indication for treatment.[69,79] The precise quantification of AVCS in TAVR patients hitherto relies on a TNC scan, acquired prior to CTA for TAVR planning. Substituting the TNC scan with a VNC series derived from the CTA may reduce both radiation and examination time. As been described for dual-energy CTAs, CACS derived from PCD-CTA series using the $VNC_{conv}$ algorithm were approximately 50% lower but showed excellent linear correlation with TNC calcium quantities.[47,50,72] Thus, a correction factor can be applied to allow comparability with TNC series. A possible reason for the 70% discrepancy between TNC and $VNC_{conv}$ in this study may be the extent of calcification. While CACS quantities are predominantly $< 1000$ in Agatston score, the interquartile range in this study was from 2000 up to 3700. The novel calcium-preserving $VNC_{pc}$ algorithm promised to eliminate the additional transformation step by providing full calcium contrast, however, the study situation is sparse. CACS on $VNC_{pc}$ derived from PCD-CT showed a reduced underestimation of the ground truth results of approximately 26% in the median.[7] Our results are consistent with this, with calcium scores on $VNC_{pc}$ reconstructions more than twice as high as those on $VNC_{conv}$ ones. However, scores were still significantly underestimated compared to TNC and no superiority of $VNC_{pc}$ was observed in terms of linear correlation to TNC. The question is, how much variation in AVCS score is acceptable? Most commonly, patients are divided into high and low AVCS according to thresholds. Using an Agatston score of 1200 for women and 2000 for men,[80] the best-rated reconstruction algorithm, $VNC^2_{pc}$, correctly classifies 14 out of 15 patients in women and 14 out of 18 in men into the high AVCS group. In contrast, $VNC^2_{conv}$ only correctly matches 4 and 2 for women and men. Even better results might be obtained by adjusting the monoenergetic level, which is possible for the $VNC_{pc}$ algorithm. Recently Fink et al. found that 60 keV $VNC_{pc}$ to best match TNC results regarding CACS[73] and Mergen et al. additionally applied high IR level and showed that 80 keV $VNC_{pc}$ combined with IR level 4 works best vor AVCS.

In the context of TAVR planning and also follow-up, PCD-CT was already described as a promising technique[81] that could be further enhanced by using the inherent spectral data for calcium quantification. As radiation reduction and time efficiency play an important role in modern CT diagnostics, PCD-based VNC reconstructions are an alternative with the potential

to replace dedicated TNC studies for AVCS quantification.
Besides its retrospective design and being conducted on a single center, this study has several limitations. First, our cohort includes a rather small sample size, which seems justified by the extensive reconstructions using several parameters and the quantitative analyses of all series. Second, further studies are needed to confirm our findings and to assess the impact on related clinical decisions. Third, the choice of reconstruction settings should be extended to include different virtual monenergetic levels, as they seem to significantly affect the performance of AVCS quantification on $VNC_{pc}$. Finally, this study focuses only on quantitative parameters. A subjective evaluation and comparison of the reconstructed series could add more comprehensive information.

## Conclusion

In conclusion this study proved the feasibility of AVCS on VNC reconstructions derived from PCD-CTA. Comparable noise levels and an effective virtual removal of iodinated contrast media could be demonstrated. In contrast to $VNC_{conv}$ the novel calcium sensitive $VNC_{pc}$ algorithm provides an improved calcium contrast and more comparable AVCS scores to TNC but with a persistent significant underestimation. With further algorithmic advances $VNC_{pc}$ promises to be an adequate replacement for an additional TNC scan, minimizing radiation dose and examination time.

### 4.1.3 Heart Rate Sensitivity of Coronary Artery Calcium Scores

## Heart Rate Sensitivity of Virtual Non-Contrast Calcium Scores Derived from Photon Counting Detector CT Data: A Phantom Study

Franka Risch, Florian Schwarz, Thomas Kröncke, Josua Decker

The study was published in La Radiologia Medica in February 2024. The author FR was equally involved in the design of the coronary phantom and the experiments, performed the data collection, the interpretation, the statistical analysis and wrote the manuscript.

### Abstract

*Objective*: To assess the reliability of VNC derived coronary artery calcium scores in relation to heart rate and the VNC algorithm used compared to reference TNC, considering several clinically established acquisition modes.

*Methods*: An ad hoc built coronary phantom containing four calcified lesions and an iodinated lumen was scanned using three different acquisition modes (flash, spiral, sequence) three times within an anthropomorphic cardiac motion phantom simulating different heart rates (0, 60, 80, 100 bpm) and reconstructed with a conventional ($VNC_{conv}$) and a calcium-sensitive ($VNC_{pc}$) VNC algorithm. As TNC reference, experiments were repeated with the same phantom but with non-iodinated lumen and scanned only at 0 bpm. Calcium scores were assessed in terms of number of lesions detected, Agatston and volume scores. Global noise was measured for the dynamic heart and the static background region. Paired t-test and Wilcoxon test were performed to test measurements for significant difference for parametric and non-parametric data, respectively. Differences from TNC were visualized in Bland-Altman plots and percentage differences were calculated.

*Results*: For both VNC algorithms used, calcium levels or noise were not significantly affected by heart rate. Measurements on $VNC_{pc}$ reconstructions best reproduced TNC results, but with increased variability, indicating poorer reproducibility and dependence on scan mode compared to TNC (Agatston scores at 0 bpm for TNC, $VNC_{conv}$, and $VNC_{pc}$ were $47.1 \pm 1.1$, $6.7 \pm 2.8$ ($p < .001$), and $45.3 \pm 7.6$ ($p > .05$), respectively). Although the same radiation dose was used for all scans, VNC reconstructions showed lower noise levels compared to TNC, especially for $VNC_{pc}$ ($noise_{heart}$ on TNC, $VNC_{conv}$ and $VNC_{pc}$ at 0 bpm was $5.0 \pm 0.4$, $4.5 \pm 0.2$, $4.2 \pm 0.2$).

*Conclusions*: No significant heart rate dependence of VNC-based calcium scores was observed in an intra-reconstruction comparison. $VNC_{pc}$ reproduces TNC scores better than $VNC_{conv}$ without significant differences and decreased noise, however, with an increasing average deviation with rising heart rates. VNC-based CACS should be used with caution as the measures show higher variability compared to reference TNC and therefore hold the potential of incorrect risk categorization.

## Introduction

The appearance and extent of coronary artery calcium (CAC) is a reliable indicator for coronary artery disease and coronary atherosclerosis, and an established predictor of cardiovascular risk.[82,83] By means of the radiopacity of calcified plaques, CT can provide a fast and non-invasive evaluation of CAC.[84] Usually, the extent of calcium in coronary arteries is quantified on non-enhanced CT scans, followed by an angiography for stenosis evaluation.[85] Spectral CT information, provided by dual-energy or PCD-CT acquisitions, allow post-processing steps including the virtual removal of the iodinated contrast medium resulting in VNC images.[3] Many studies investigated the possibility of calcium scoring on VNC reconstructions and found excellent correlations which promise to reduce the radiation exposure to solely the CT angiography and omitting an additional unenhanced scan.[7,48,50,72] A relevant challenge in cardiac imaging is motion which might lead to artifacts and corresponding misinterpretation of the CAC. Werf et al. found in their multi-manufacturer system phantom study a significant influence of heart rate on measured calcium quantities.[86] To transfer such analyses on VNC reconstructions, there is a limited availability of suitable coronary phantoms. So far, phantoms either provide calcified plaques in combination with blood equivalent lumen, the focus is on stenosis analysis and non-calcified plaques are simulated, or comparison to reference TNC is lacking.[86–89]
For this study, a coronary vessel phantom including calcifications embedded in iodinated agarose was built to fit within an anthropomorphic cardiac motion phantom. Different heart rates were simulated and clinical coronary angiography CT scans were performed on a photon-counting detector system. Calcium scores were measured on VNC reconstructions and compared to TNC reconstructions.

## Materials and Methods

Because the study uses only phantom data, an ethics approval was not required.

*Phantom*

The phantom setup consists of two parts: The dynamic cardiac phantom and the coronary vessel phantom.
Former is an anthropomorphic heart inside a thorax body from tissue equivalent materials (MODEL 008C, Computerized Imaging Reference Systems Inc., Virginia, USA). A cylindric part containing the heart can be controlled to perform motions of variable heart rate combining translation and rotation with the possibility to read out the correlating electrocardiographic profile. Three 5 mm-diameter accessible cutouts in the heart simulate the left coronary artery and can be individually filled with inserts.
In the absence of commercially available inserts simulating coronary arteries with calcified plaques and the ability to alternate the lumen, a suitable phantom was developed. A rigid plastic tube with an outer diameter of 5 mm was cut lengthwise and pieces mimicking common sizes of coronary calcified plaques, ranging from 0.3 mm to 0.7 mm as the longest diameter of the same calcium tablet (2028.9 mg calcium carbonate each of two tablets and modified starch, Vitamaze

| Phantom | With iodine | Without iodine |
|---|---|---|
| Heart rate [bpm] | 0/ 60/ 80/ 100 | 0 |
| Scan mode | Flash/ spiral/ sequence | Flash/ spiral/ sequence |
| Tube voltage [kVp] | 120 | 120 |
| Repetitions | 3 | 3 |
| Kernel, iteration | Qr36, Q3 | Qr36, Q3 |
| Slice thickness, increment [mm] | 3.0, 1.5 | 3.0, 1.5 |
| Post-processing | $VNC_{conv}$/ $VNC_{pc}$ 65 keV | VM 65 keV |

**Table 4.6:** Phantom and image acquisition and reconstruction settings.
Qr = quantitative regular kernel, VM = virtual monoenergetic, VNC = virtual non-contrast ($_{conv}$ = conventional, $_{pc}$ = PureCalcium).

GmbH, Heidelberg, Germany) were placed and glued inside. Agarose powder (1.4 g for 100 ml solution) was dissolved in a mixture of iodine (Ultravist 300, Iopromide, Bayer Vital GmbH, Leverkusen, Germany) and sodium chloride (0.9%) (ratio 1:20). The plastic tube was embedded in the solution and cooled in a refrigerator to gel. The surrounding agarose was removed, and the filled plastic tube was placed in a heat-shrinkable tube and sealed on both sides. For reference TNC scans, the shrink tube was removed and the iodinated agar was washed out. All steps of embedding the tube were repeated without adding iodine.

*CT Protocol*

The phantom including the iodinated vessel was scanned at heart rates of 0, 60, 80, and 100 bpm (see Table 4.6). Without iodine the phantom was only scanned at 0 bpm as reference. All scans were performed on a PCD-CT system (NAEOTOM Alpha, Siemens Healthcare GmbH, Erlangen, Germany) in December 2022. All three available scan modes for cardiac imaging, flash (corresponds to high-pitch spiral), spiral, and sequence were used at a tube voltage of 120 kVp with a constant image quality level of 70 to adjust the tube current-time product and repeated three times. The spiral and sequence acquisition modes were electrocardiographically triggered, using the best diastole. An acquisition mode with spectral information readout (Quantum Plus, Siemens Healthcare GmbH, Erlangen, Germany) was used and the collimation was 144 x 0.4 mm.

*Image Reconstruction*

All scans were reconstructed at the scanner console (syngo, VA50, Siemens Healthcare GmbH, Erlangen, Germany) using the quantitative regular kernel Qr36 with an iteration strength of three. Slice thickness and increment were 3.0 mm and 1.5 mm, respectively, and the field of view 180 x 180 $mm^2$, covering the heart. CT data of the iodinated vessel phantom were processed using two virtual non-contrast algorithms, the conventional $VNC_{conv}$ and the calcium-preserving $VNC_{pc}$. TNC scans of the phantom without iodine were reconstructed at a virtual monoenergetic level of 65 keV.

*Image Analyses*

Calcium quantities, number of recognized lesions ($CAC_{Number}$), volume ($CAC_{Volume}$) and Agatston ($CAC_{Agatston}$) score, were acquired semi-manually on a dedicated workstation (syngo.via, version VB60A, Siemens Healthcare GmbH, Erlangen, Germany), considering contiguous voxels with an attenuation above a threshold of 130 HUs. Measurements were taken for each reconstructed series and exported in tabular form.

For noise analysis, volumes were cropped to 50 slices in axial direction to cover only the heart. Three slices, approximately equidistant from each other and from the range boundaries (slice 13, 26, 39) (see supplemental Figure 4.12A), were selected and their noise map calculated. Following Christianson et al.,[90] a filter of 6 mm size, referring to 17 pixels (512 pixel in rows and columns with a FoV of 180 result in a pixel size of 0.352 mm) was used to calculate the standard deviation of CT values for each image pixel (see supplemental Figure 4.12B). A rectangular ROI covering the moving cylinder (the heart) of the phantom was used to distinguish between the dynamic heart and the static background. Histograms of the noise map allow the detection of the most frequent occurring standard deviation within one axial slice, which was used as a measure for global noise, in both regions, heart and background, respectively (see supplemental Figure 4.12C). The global noise values were averaged over the three slices considered, resulting in two global noise values, for heart ($noise_{heart}$) and background ($noise_{background}$), for each reconstruction.

*Statistical Analyses*

Statistical analyses were performed using Python (version 3.9). The Shapiro-Wilk test was used to assess the distribution of the data. The paired t-test and the Wilcoxon signed-rank test were used to test for differences, for parametric and non-parametric data, respectively. For multiple comparisons, p-values were corrected using the Bonferroni method and considered to indicate statistical significance if $< .05$. CAC and noise were once compared between different heart rates within each reconstruction and once between different reconstructions within each heart rate, visualized in box plots. Percentage deviations were calculated as $\frac{X_{VNC}-X_{TNC}}{X_{TNC}} * 100\%$, with $X_{VNC}$ representing CAC or noise derived from a VNC series (either conventional or Pure-Calcium) and $X_{TNC}$ derived from ground truth. Differences due to scan modes (flash, spiral, sequence) were not evaluated. However, each mode is used in clinical practice and therefore represented in equal proportions in this study (see CT protocol and image reconstruction section).

## Results

*Coronary Phantom*

Figure 4.13A shows the different stages of development of the coronary phantom insert. Embedded in iodinated agar, as shown in the second image, the mean measured CT values of the calcifications ranged from 790 $\pm$ 50 HU for the smallest to 1120 $\pm$ 110 HU for the largest volume. The contrast within the tube was measured to be 500 $\pm$ 25 HU. Figure 4.13B shows the reconstructions of TNC and VNC of the cardiac motion phantom including the coronary insert are shown as maximum intensity projections at 0 bpm and the same scan and reconstruction

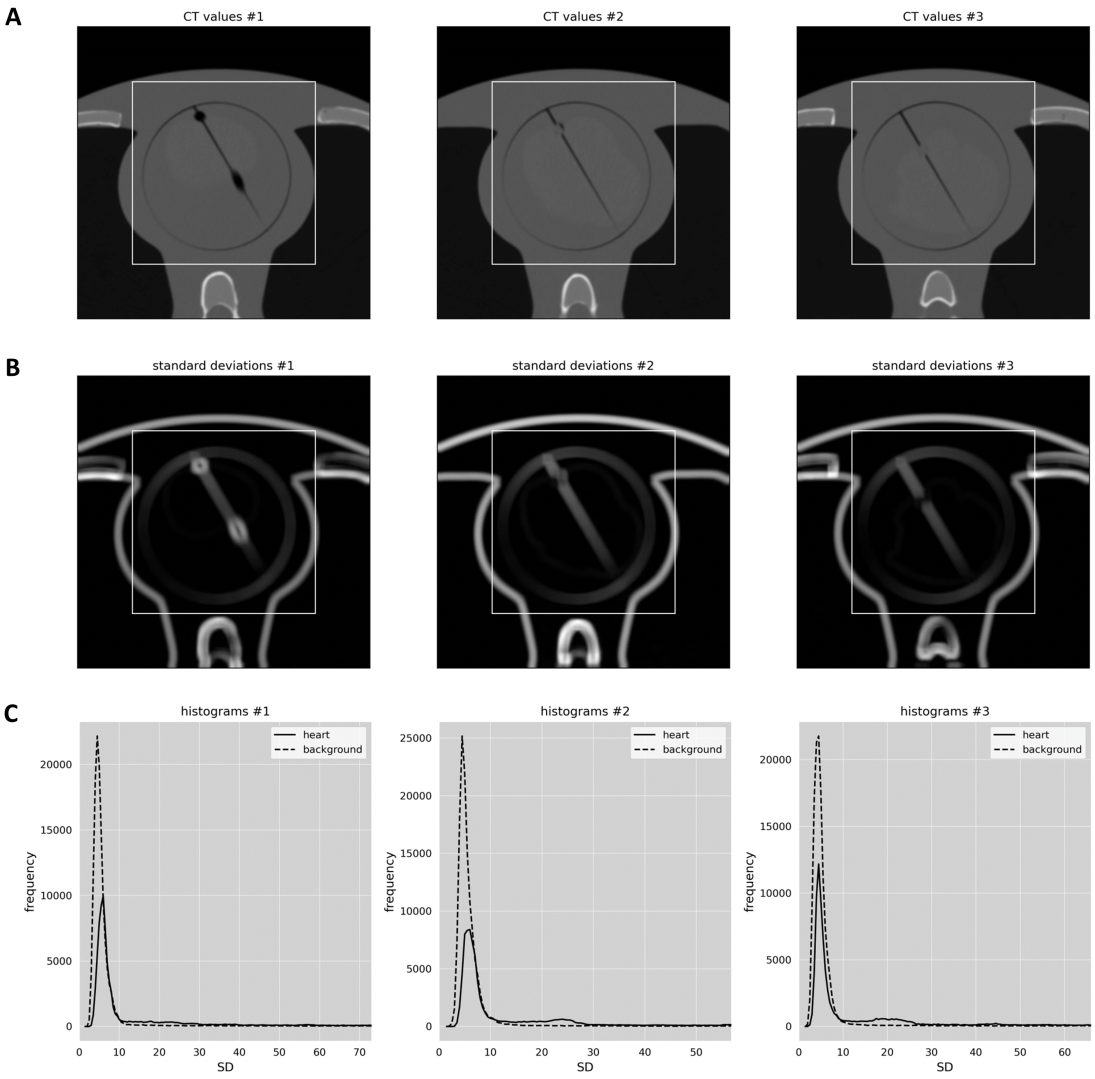


**Figure 4.12:** Demonstration of the performed global noise measurements. **A** shows the three selected slices within the heart volume and **B** their respective noise maps. The rectangular boarder marked in red differentiates between the moving heart cylinder and the static background of the phantom. In **C** for both regions the histograms are plotted which most frequent standard deviation in HU was taken as global noise measure.

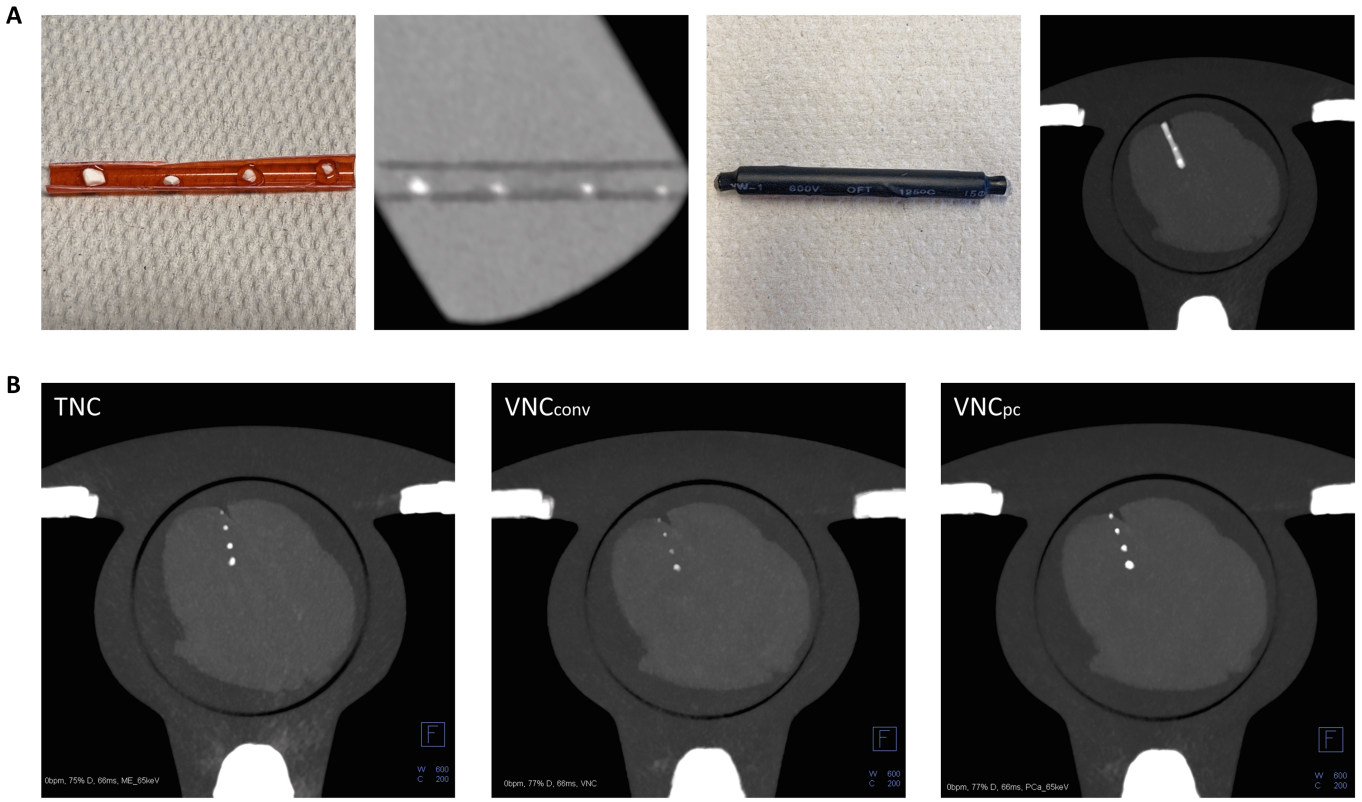


**Figure 4.13:** **A** shows the development of the coronary vessel phantom from gluing the pieces of the calcium tablet into the tube, to embedding the phantom in iodinated agarose, to the final phantom covered and sealed in a heat-shrinkable tube inside the cardiac phantom. **B** shows a maximum intensity projection of the reconstruction modes for the TNC, the conventional and PureCalcium VNC reconstruction at equal heart rate, scan and reconstruction settings.
TNC = true non-contrast, VNC = virtual non-contrast ($_{conv}$ = conventional, $_{pc}$ = PureCalcium).

| Phantom | With iodine | | | | Without iodine |
|---|---|---|---|---|---|
| Heart rates | 0 bpm | 60 bpm | 80 bpm | 100 bpm | 0 bpm |
| Pitch factor | 0.8 (0.2-3.2) | 0.8 (0.2-3.2) | 0.8 (0.3-3.2) | 0.8 (0.3-3.2) | 0.8 (0.2-3.2) |
| Eff. mAs | 38 | 38 | 38 | 38 | 38 |
| $CTDI_{vol}$ | 5.9 | 6.2 | 6.2 | 6.1 | 6.1 |
| [mGy] | (2.7-13.7) | (2.8-43.8) | (2.7-33.7) | (2.7-27.4) | (2.8-43.8) |
| DLP | 55.8 | 86.9 | 86.9 | 86.5 | 86.6 |
| [mGy*cm] | (47.8-176.0) | (48.0-480.0) | (47.9-507.0) | (47.9-415.0) | (61.3-652.0) |
| SSDE [mGy] | 9.7 | 10.1 | 10.1 | 10.1 | 10.1 |
| | (4.4-24.3) | (4.4-70.1) | (4.4-53.9) | (4.4-43.8) | (4.5-69.9) |

**Table 4.7:** Measured dose parameters for the coronary vessel scanning with and without iodinated lumen, including three repetitions and three scan modes per heart rate.
Values are median (interquartile range). $CTDI_{vol}$ = volumetric CT dose index, DLP = dose length product, SSDE = size specific dose estimate.

settings. The four placed calcifications are clearly visible in all reconstructions.

*Dose*

Pitch and dose parameters, including $CTDI_{vol}$, DLP, and size-specific dose estimate (SSDE), are listed in Table 4.7. Since the acquisition settings were kept identical, equivalent doses were used for TNC and CTA scans. Small deviations are due to variations in the manual selection of the scan area.

*Calcium Scoring*

Detailed CAC measurements, including the percentage differences from TNC results, are shown in Table 4.8. There is a trend for both VNC algorithms, yet more pronounced for $VNC_{pc}$, to have similar CAC measurements at 60 bpm, lower at 80 bpm, and higher at 100 bpm compared to each algorithm's measurement at 0 bpm. However, as shown in Figure 4.14A, the difference caused by heart rate is not significant for either the CAC measurement or the VNC algorithm (almost all p-values $> .05$, p-value for $VNC_{conv}$ 0 vs. 80 bpm = 0.047). Focusing on the differences between the reconstructions, as in Figure 4.14B, only TNC at 0 bpm was able to detect all four calcium lesions (median of 3 (3 - 4) lesions). With $VNC_{conv}$, for most of the heart rates, there were two lesions with a median of more than 130 HU that could be counted, and only one lesion at 60 bpm. In general, more lesions were found on $VNC_{pc}$ reconstructions (e.g. at 0 bpm 2 (2 - 2) on $VNC_{conv}$ and 3 (2 - 3) on $VNC_{pc}$) and the percentage difference to TNC was smaller compared to the conventional VNC algorithm (e.g. at 0 bpm -40% for $VNC_{conv}$ and -21% for $VNC_{pc}$), however, differences between $VNC_{conv}$ and $VNC_{pc}$ were not significant. At least one calcification was detected at all heart rates.

The $VNC_{pc}$ derived Agatston scores did not differ significantly from reference (TNC at 0 bpm), but the interquartile range and standard deviation were greater (e.g at 0 bpm Agatston score on TNC of $47 \pm 1$ and on $VNC_{conv}$ of $45 \pm 8$). The percentage difference was smallest at 0 bpm with an underestimation of TNC Agatston scores about -4%, increasing to -17% at 80 bpm. At

| Heart rate [bpm] | Recon | Coronary artery calcification | | | Percentage difference to TNC [%] | | |
|---|---|---|---|---|---|---|---|
| | | Number | Agatston | Volume [$mm^3$] | Number | Agatston | Volume [$mm^3$] |
| 0 | TNC | 3 (3 - 4) | 47.1 ± 1.1 | 41.8 ± 1.3 | | | |
| | $VNC_{conv}$ | 2 (2 - 2) | 6.7 ± 2.8 | 9.7 ± 3.3 | -40 ± 24 | -86 ± 6 | -77 ± 8 |
| | $VNC_{pc}$ | 3 (2 - 3) | 45.3 ± 7.6 | 39.9 ± 6.1 | -21 ± 18 | -4 ± 17 | -4 ± 16 |
| 60 | $VNC_{conv}$ | 1 (1 - 3) | 7.5 ± 4.0 | 10.1 ± 4.4 | -49 ± 26 | -84 ± 8 | -76 ± 10 |
| | $VNC_{pc}$ | 2 (2 - 3) | 44.4 ± 16.2 | 38.8 ± 13.5 | -35 ± 19 | -6 ± 34 | -8 ± 32 |
| 80 | $VNC_{conv}$ | 2 (1 - 2) | 4.4 ± 2.0 | 6.8 ± 3.2 | -46 ± 24 | -91 ± 4 | -84 ± 8 |
| | $VNC_{pc}$ | 2 (2 - 3) | 38.8 ± 10.2 | 33.4 ± 9.3 | -38 ± 23 | -17 ± 22 | -20 ± 24 |
| 100 | $VNC_{conv}$ | 2 (2 - 3) | 7.7 ± 6.1 | 10.3 ± 6.8 | -37 ± 26 | -84 ± 13 | -75 ± 16 |
| | $VNC_{pc}$ | 3 (2 - 3) | 54.3 ± 18.8 | 48.2 ± 15.2 | -27 ± 25 | 15 ± 38 | 15 ± 35 |

**Table 4.8:** Measured calcified lesions in number, Agatston and volume score at heart rates of 0, 60, 80, 100 bpm in TNC and VNC, conventional and PureCalcium, series.

Values are median (interquartile range) or mean ± standard deviation. TNC = true non-contrast, VNC = virtual non-contrast ($_{conv}$ = conventional, $_{pc}$ = PureCalcium).

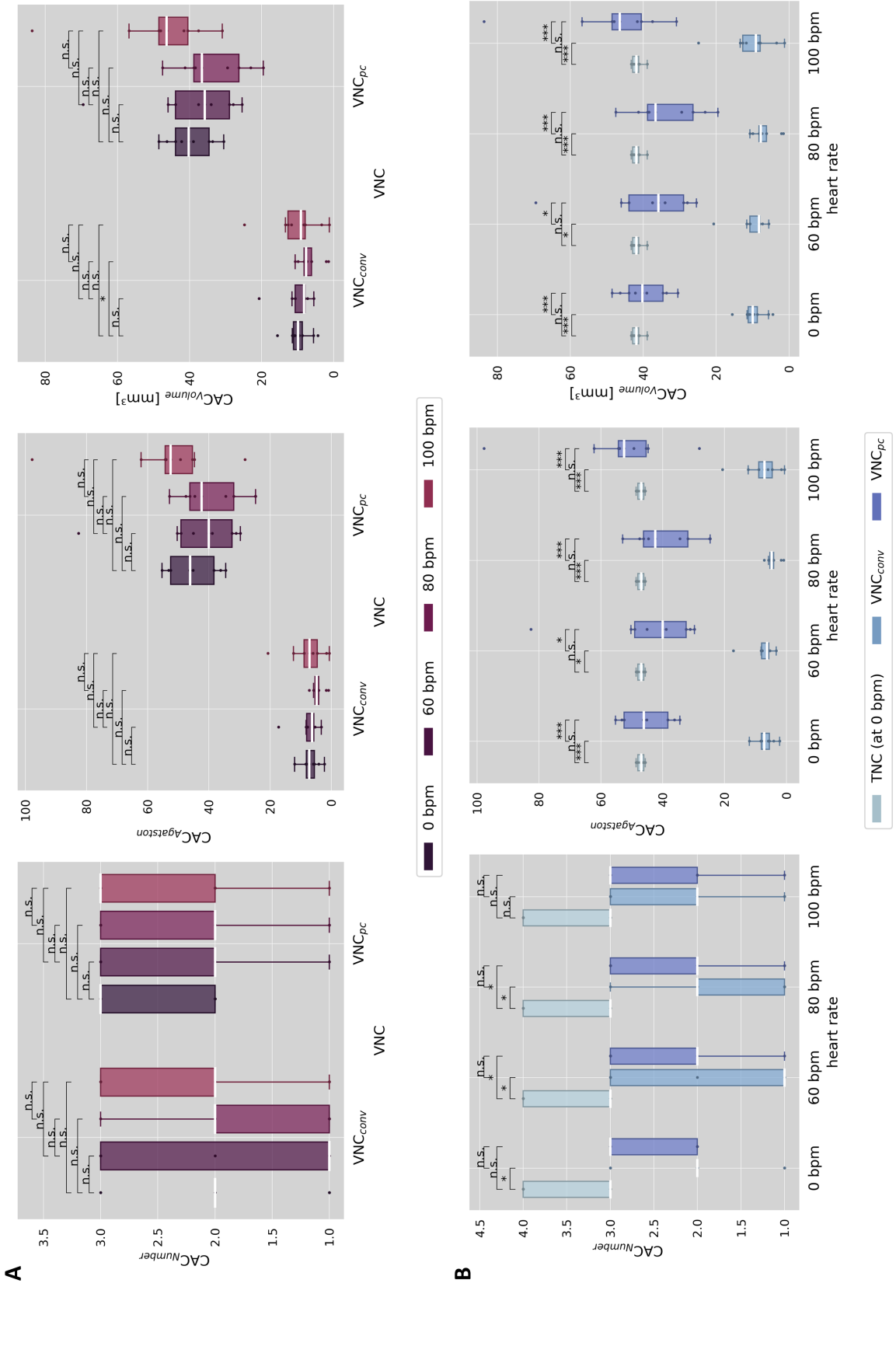


**Figure 4.14:** Measured number of calcified lesions ($CAC_{Number}$), the Agatston score ($CAC_{Agatston}$) and the volume ($CAC_{Volume}$) in **A** comparing the heart rates within the respective reconstructions of conventional and PureCalcium VNC and **B** comparing the reconstructions TNC at 0 bpm vs. VNC at heart rates 0, 60, 80 and 100 bpm. Stars mark significant differences as * = $p < .05$, ** = $p < .01$, *** = $p < .001$ and n.s. marks no significant difference.
TNC = true non-contrast, VNC = virtual non-contrast ($_{conv}$ = conventional, $_{pc}$ = PureCalcium).

| Heart rate [bpm] | Recon | Global noise level [HU] | | Percentage difference to TNC [%] | |
|---|---|---|---|---|---|
| | | Heart | Background | Heart | Background |
| 0 | TNC | $5.0 \pm 0.4$ | $4.1 \pm 0.3$ | | |
| | $VNC_{conv}$ | $4.5 \pm 0.2$ | $3.6 \pm 0.1$ | $-9 \pm 6$ | $-13 \pm 4$ |
| | $VNC_{pc}$ | $4.2 \pm 0.2$ | $3.5 \pm 0.2$ | $-16 \pm 3$ | $-15 \pm 7$ |
| 60 | $VNC_{conv}$ | $4.4 \pm 0.4$ | $3.4 \pm 0.3$ | $-12 \pm 6$ | $-18 \pm 5$ |
| | $VNC_{pc}$ | $4.1 \pm 0.4$ | $3.3 \pm 0.2$ | $-18 \pm 7$ | $-19 \pm 5$ |
| 80 | $VNC_{conv}$ | $4.5 \pm 0.4$ | $3.4 \pm 0.2$ | $-10 \pm 4$ | $-17 \pm 3$ |
| | $VNC_{pc}$ | $4.2 \pm 0.3$ | $3.3 \pm 0.2$ | $-17 \pm 3$ | $-19 \pm 3$ |
| 100 | $VNC_{conv}$ | $4.5 \pm 0.4$ | $3.4 \pm 0.1$ | $-10 \pm 4$ | $-16 \pm 4$ |
| | $VNC_{pc}$ | $4.1 \pm 0.3$ | $3.5 \pm 0.2$ | $-18 \pm 5$ | $-17 \pm 2$ |

**Table 4.9:** Measured global noise levels for heart and background at heart rates of 0, 60, 80, 100 bpm in TNC and VNC, conventional and PureCalcium, series.
Values are mean $\pm$ standard deviation. TNC = true non-contrast, VNC = virtual non-contrast ($_{conv}$ = conventional, $_{pc}$ = PureCalcium).

100 bpm Agatston scores were overestimated by 15%. For $VNC_{conv}$, the highest underestimation of scores was observed for 80 bpm with -91%. For the heart rates 0, 60 and 100 bpm, the underestimations was about -85%. The Bland-Altman plot in Figure 4.15 shows the difference VNC - TNC over the respective means. It is noticeable that for $VNC_{conv}$ (Figure 4.15A) the distribution appears unstructured, resulting in a constant bias across heart rates. However, for $VNC_{pc}$ (Figure 4.15B) the distribution appears linear, with smaller differences at lower means and larger differences at higher means.
Similar results are found for CAC volume score measurements. Interestingly, compared to corresponding Agatston scores the percentage difference to TNC is smaller for $VNC_{conv}$ (percentage difference to reference at 80 bpm: Agatston score -91%, volume score -84%) and greater for $VNC_{pc}$ (Agatston score-17%, volume score -20%).
It should to be noted that although the variability seems to be more pronounced for $VNC_{pc}$ measurements compared to $VNC_{conv}$ ones, a transformation based on linear correlation includes an intercept and a slope and would naturally also increase the range, especially regarding the outliers. However, a valid observation is that at 0 bpm heart rate, TNC showed the least variability compared to VNC derived CACS.

*Noise*
Detailed global noise level measurements, including the percentage differences from TNC results, are shown in Table 4.9. In Figure 4.16A, the heart rates within each VNC algorithm are the focus of comparison. Neither for $VNC_{conv}$ nor for $VNC_{pc}$ did the heart rates cause significant differences in noise levels (all p-values $> .05$). Focusing on the different reconstruction methods, as shown in Figure 4.16B, TNC at 0 bpm has the highest noise level ($5.0 \pm 0.4$ HU and $4.1 \pm 0.3$ HU in heart and background), which differs significantly from both VNC recon-

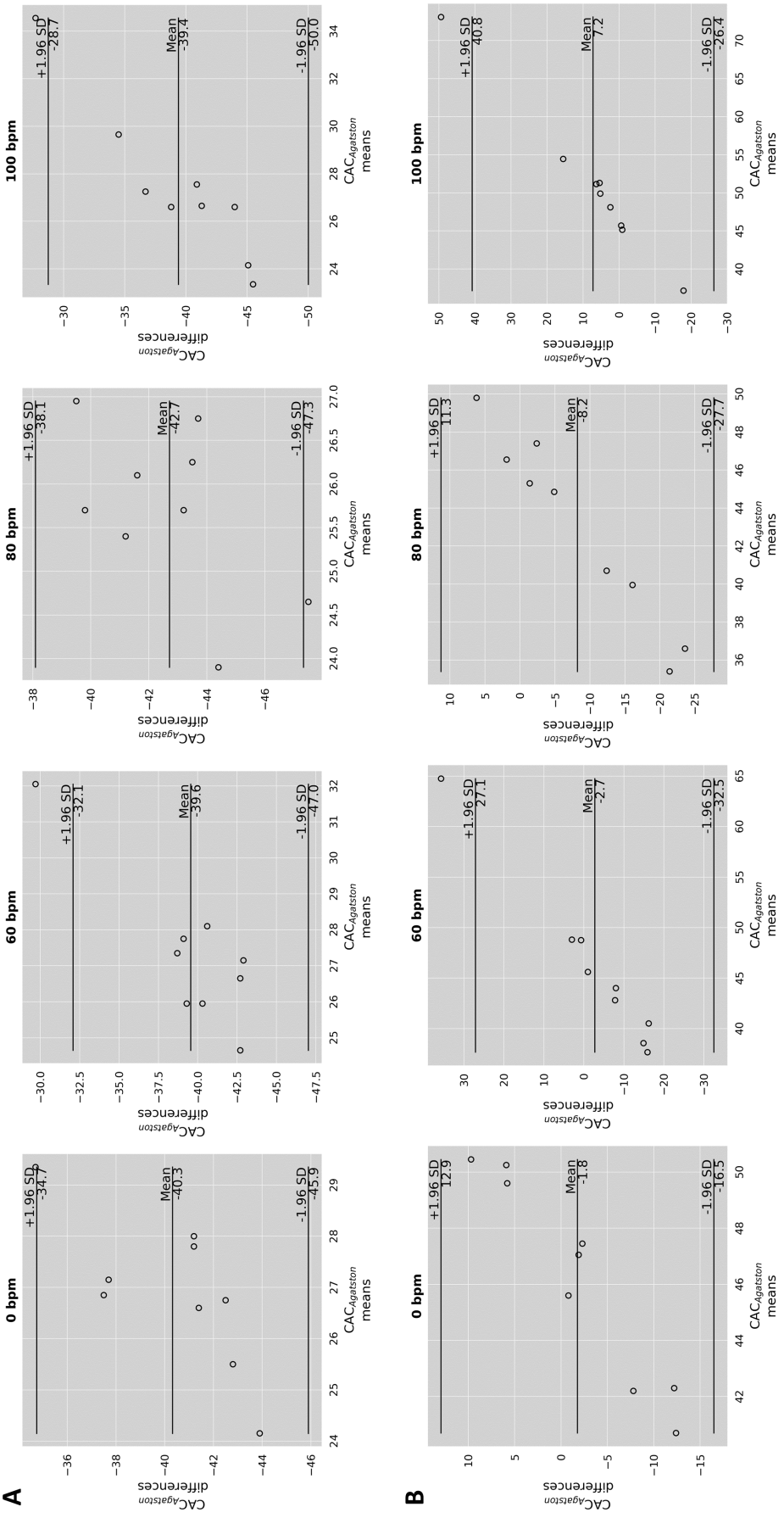


**Figure 4.15:** Bland Altman plots showing the means and differences of the Agatston scores measured in **A** $VNC_{conv}$ and **B** $VNC_{pc}$ at 0, 60, 80 and 100 bpm vs. measured in TNC at 0 bpm.

TNC = true non-contrast, VNC = virtual non-contrast ($_{conv}$ = conventional, $_{pc}$ = PureCalcium).

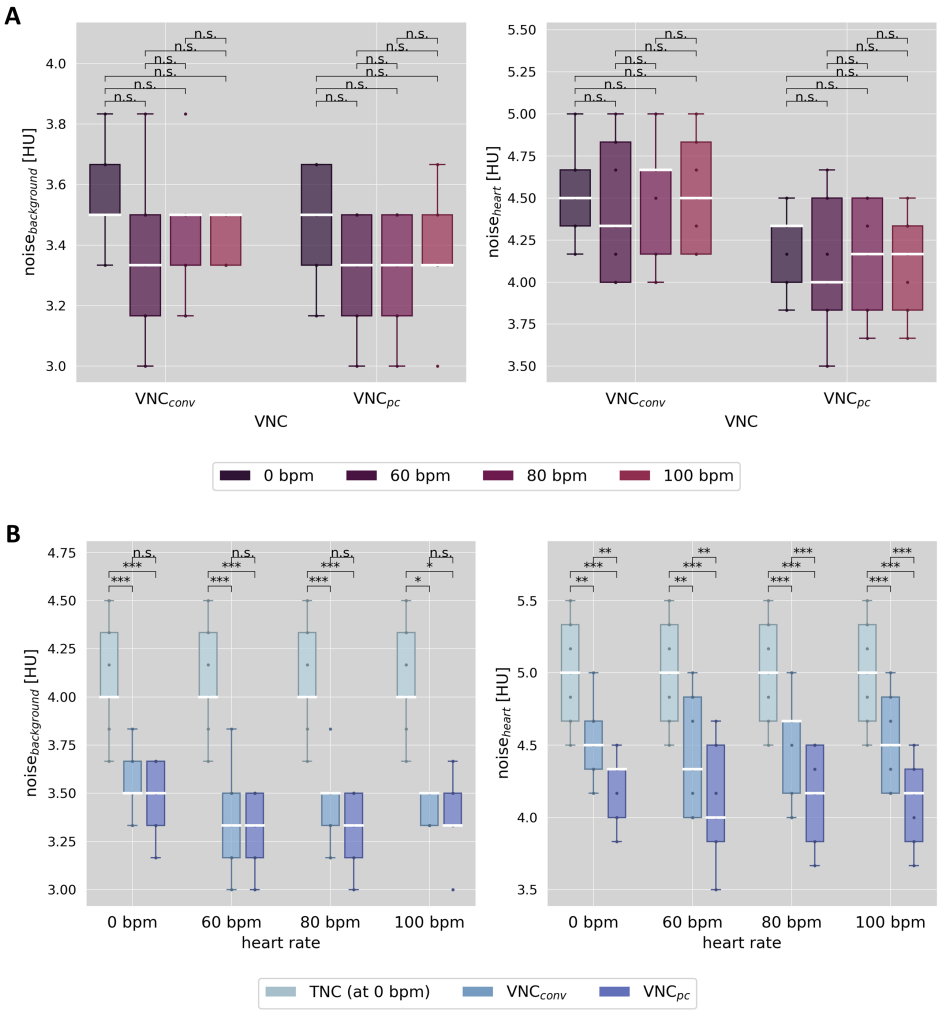


**Figure 4.16:** Measured number of calcified lesions ($CAC_{Number}$), the Agatston score ($CAC_{Agatston}$) and the volume ($CAC_{Volume}$) in **A** comparing the heart rates within the respective reconstructions of conventional and PureCalcium VNC and **B** comparing the reconstructions TNC at 0 bpm vs. VNC at heart rates 0, 60, 80 and 100 bpm. Stars mark significant differences as * = $p < .05$, ** = $p < .01$, *** = $p < .001$ and n.s. marks no significant difference.

TNC = true non-contrast, VNC = virtual non-contrast ($_{conv}$ = conventional, $_{pc}$ = PureCalcium).

structions for all heart rates and ROIs (p-values $< .05$ or $< .001$). Within the static background, $VNC_{conv}$ showed a lower noise level compared to TNC with a reduction from a minimum of 13% at 0 bpm to a maximum of 18% at 60 bpm. For $VNC_{pc}$ the reduction was slightly higher, ranging from 15% to 19%. However, there was no significant difference in noise between the VNC algorithms. Noise in the dynamic heart region generally exceeded background measurements by approximately 1 HU. Although here the VNC algorithms barely differed in absolute global noise level (approximately 0.3 HU difference, but all p-values $< .05$) the percentage reduction compared to TNC was higher for $VNC_{pc}$ with up to 18% less noise than for $VNC_{conv}$ with a maximum of 12% less noise.

## Discussion

For this study, we scanned an ad hoc coronary vessel in a cardiac motion phantom at various heart rates using standard cardiac protocols. Calcification and image noise were quantified on VNC images derived from the dynamic contrast-enhanced phantom scans and on TNC reference, reconstructed from static unenhanced scans. The focus of the evaluation was on the heart rate sensitivity of the two used VNC reconstruction algorithms, and on their performance against each other and against the reference TNC. Our main important findings are: (1) $VNC_{pc}$ reproduces TNC better than $VNC_{conv}$ in terms of found calcium lesions, Agatston and volume score, with predominantly no significant differences; (2) The average discrepancy, however, increases with higher heart rates; (3) A high variability of measured calcium quantities on VNC reconstructions indicates a poorer reproducibility and dependence on the scan modes used compared to TNC, which carries the potential for incorrect risk classification; (4) Noise is reduced in VNC reconstructions compared to TNC, equally for the static background and more pronounced for $VNC_{pc}$ within the dynamic cardiac region.

VNC reconstructions, especially in combination with the calcium-preserving algorithm ($VNC_{pc}$), have proven their clinical relevance as a replacement for TNC in several applications. Recent studies have investigated, for example, the evaluation of patients after EVAR,[9] quantification of epicardial adipose tissue[8] or the quantification of coronary artery calcium[7,68,73] based on $VNC_{pc}$ reconstructions with promising results. Regarding the latter, the calcium sensitivity of $VNC_{pc}$ provides TNC-equivalent values without the need for transformation, as previously required for $VNC_{conv}$-based calcium assessment.[48–50,72,77] Moving organs are always a challenge in medical imaging, because they are prone to artifacts. The same is true for cardiac imaging, which is why beta-blockers are often used to reduce heart rate.[91] However, there are patients, with contraindications to the use of beta-blockers who must be scanned at higher heart rates.[92] In their phantom study, Werf et al. found heart rate-induced variations in CAC extent measured on TNC for both high-end energy-integrating[86] and photon-counting detector[93] CT systems. Higher heart rates decrease the reproducibility of CAC measurements, as found in phantom[94] and in patient cohort[95] studies. In this study, no significant heart rate-related differences were found for either $VNC_{conv}$- or $VNC_{pc}$-based CAC quantities or global noise levels, when considering only intra-reconstruction comparisons. These results are consistent with Brodoefel et

al, who found heart rate-independent image quality in dual-source CTA compared to invasive angiography, but instead found a correlation with heart rate variability and calcification extent.[96] Another study concluded that dual-source CTA provides high diagnostic accuracy independent of the heart rate.[97] However, this study compared higher and lower heart rates according to a single threshold.

Focusing on differences between reconstructions, the reproducibility of VNC-based CAC scores was found to be much lower compared to ground truth with a higher variability in measured quantities. Again, it should be noted that the apparently smaller interquartile ranges of $VNC_{conv}$ would naturally increase to a range similar to that of $VNC_{pc}$ if the transformation were applied. The percentage deviation from the reference TNC values increased with rising heart rate. Given a greater calcification burden than simulated with the phantom insert, this discrepancy may enlarge accordingly, leading to misclassification in risk categorization.

Noise, on the other hand, was significantly reduced on VNC reconstructions compared to TNC. Jungblut et al. measured noise in the lung parenchyma using a technique similar to that used in this study and compared TNC to $VNC_{conv}$ both derived from PCD-CT, without reporting significant or large differences.[37] These discrepant results may be due to reconstruction with a sharp lung kernel compared to the soft tissue kernel used in our study.

This study has several limitations. First, the ad hoc phantom was created manually, so there is a possibility that the differences between TNC and VNC are not entirely algorithmic. Second, the comparisons are based on small sample sizes (9 vs. 9 measurements each), which limits their power, especially for tests of significance. Third, ideal heart movements were simulated without taking into account heart rate variations or arrhythmias. Fourth, all evaluations are entirely objective and based on quantitative measurements. Further studies should assess the subjective image perception.

## Conclusion

In conclusion, VNC-based calcium quantification and noise assessment showed no dependence on heart rate in an intra-reconstruction comparison. Although the difference between the calcium-sensitive $VNC_{pc}$ and the ground truth was not significant in the assessment of lesion number, Agatston score, and calcium volume, the average deviation increased with higher heartrates in the mean. The high variability of measured CACS on VNC reconstructions indicates poor reproducibility and holds the potential for incorrect risk classification.

### 4.1.4 Impact of BMI, Heart Rhythm and Heart Rate on Coronary Artery Calcium Scores

## Impact of BMI, Heart Rhythm, and Heart Rate on Photon-Counting Detector Virtual Coronary Calcium Scoring

Judith Becker, Josua Decker, Stefanie Bette, Franziska Braun, Luca Canalini, Claudia Wollny, Christian Scheurig-Münkler, Thomas Kröncke, Florian Schwarz, Franka Risch

The study is submitted for publication in a journal. The author FR was equally involved in the data collection, performed the interpretation and statsitical analysis and revised the manuscript.

### Abstract

*Background:* Virtual non-contrast reconstructions derived from spectral CT angiography data can be used for coronary artery calcium scoring.

*Objectives:* To investigate the reliability of calcium sensitive $VNC_{pc}$ reconstructions for CACS regarding BMI, heart rhythm, and heart rate compared to true non-contrast series.

*Methods:* This prospective study included consecutive patients who underwent cardiac imaging including TNC and CTA on a PCD-CT system. The Agatston score was measured on TNC and $VNC_{pc}$ series. Analyses were performed within subgroups according to patient characteristics. Distributions were tested for differences (t-test, Wilcoxon) and linear correlation ($r^2$). Percentage deviation of absolute values and agreement in CACS category were calculated.

*Results:* The final cohort consisted of 88 patients (52 women, median of 79 years). Agatston scores on $VNC_{pc}$ showed a significant underestimation of TNC derived values (TNC = 542 (200 - 1294), on $VNC_{pc}$ = 449 (130 - 1183), $p < 0.001$, -11%). However, linear correlation was high ($r^2$ = 0.95), and the CACS was categorized equivalent in 80%. In approximately 11% a falsified treatment due to misclassification was considered possible. Subgroup analysis revealed impact on the significance and extent of the percentage difference for BMI $>$ 28 kg/m$^2$ and heart rates $>$ 69 bpm, but correlation as well as category agreement remained unaffected.

*Conclusions:* $VNC_{pc}$ reconstructions from PCD-CT provide a reliable estimate of TNC CACS for BMI $\leq$ 28 kg/m$^2$ and heart rate $\leq$ 69 bpm in patients with severe coronary artery disease. However, the potential underestimation of severity, especially with increased BMI and heart rate, must be considered for clinical decision making.

### Introduction

According to the World Health Organization, cardiovascular diseases are the leading cause of death worldwide.[98] CCTA and CACS have become established as non-invasive diagnostic tools for risk stratification of major adverse cardiac events.[39–41] CACS is performed on TNC series and allows a categorization into no, mild, moderate and high risk calcification with a high prognostic value regarding the clinical outcome.[39] An increasing number of studies have shown

that VNC reconstructions, which virtually subtract the iodinated contrast agent from spectral CTA studies by means of material differentiation, are also suitable for CACS and promise to reduce radiation dose and examination time by eliminating the need for a separate unenhanced scan.[47–50] However, studies criticized the accuracy of CT values depending on the patient's BMI, heart rate, and degree of coronary sclerosis.[99–101] Since PCD-CT scanners have been introduced, the inherently acquired spectral data allow for the routinely reconstruction of VNC images providing a high diagnostic utility.[7–9,73] Next to the conventional $VNC_{conv}$ algorithm, a novel calcium sensitive algorithm, namely PureCalcium ($VNC_{pc}$), has been made available. This algorithm creates a mask of calcium containing voxels prior to the material decomposition into iodine and water, which is then used to restore the original calcium contrast. In terms of CACS, higher calcium scores can be measured that do not necessarily require a conversion factor to approximate scores derived from TNC series, as is usual with $VNC_{conv}$.[7]
Nevertheless, the stability and reliability of CACS on $VNC_{pc}$ images derived from PCD-CT with respect to patient characteristics remains unclear. The aim of this study was to investigate the influence of BMI, heart rhythm and heart rate on the reliability of $VNC_{pc}$ series-based calcium scores compared to TNC series as ground truth.

## Materials and Methods

*Patients*

This prospective single-center study was approved by the institutional review board (Ludwig-Maximilians-University Munich, clinical trials NCT04996693) and all participants provided written informed consent. For the study cohort, consecutive patients with a PCD-CT scan of the heart as part of the preliminary examination to TAVR between January 2022 and March 2023 were considered. This cohort of patients was chosen because they are usually examined uniformly and without medication (e.g. beta-blockers) and often have concomitant coronary artery disease. Inclusion criteria were: (1) Minimum age of 18 years; (2) Completeness of scan protocol and consistency of scan settings; (3) Availability of raw data for uniform image reconstruction. Patients with coronary stents or bypasses were excluded from analysis. Patient characteristics including sex, age, and BMI were obtained from electronic medical records.

*CT Protocol*

Scans were performed on a dual-source PCD-CT (NAEOTOM Alpha, Siemens Healthcare GmbH, Erlangen, Germany), including an unenhanced scan and a CTA of the heart. For this study only spiral acquisitions with a high pitch factor for TNC and a low pitch factor for CTA and a constant tube voltage of 120 kVp were considered with a scan range covering the heart. The CTA was ECG-triggered. Reference tube current time product was adjusted by setting the image quality level to 19 for TNC and 50 for CTA. For the readout of spectral information, the dedicated acquisition mode Quantum Plus (Siemens Healthcare GmbH, Erlangen, Germany, with the following detector-based energy thresholds: 20, 35, 65 and 70 keV) was used. Collimation was 144 x 0.4 mm. Heart rhythm and heart rate were obtained from the automatically generated ECGs. As no beta-blockers were administered, only minor differences between scans

were expected, and statistical analyses refer to the heart rhythm and heart rate measured during the TNC scan. For the CTA a triphasic contrast injection protocol with bolus tracking was used. In the first phase 60 ml of undiluted contrast material (Ultravist, Iopromid 300 mgI/ml, Bayer Vital GmbH, Leverkusen, Germany) was injected followed by a mixture of 30 ml contrast material and 30 ml normal saline solution and finalized with 20 ml saline solution. A flow of 5 ml/s was used in all three phases. Dose information, including DLP, $CTDI_{vol}$, and SSDE were extracted from the automatically generated structured dose report.

*Image Reconstruction*

All reconstructions were performed on the scanner console (VA50A, Siemens Healthcare GmbH, Erlangen, Germany) using the quantitative regular kernel (Qr36) optimized for quantitative analyses and spectral post-processing with the quantum IR algorithm at strength 3. TNC images were generated from the unenhanced scan, and $VNC_{pc}$ images from the CTA using an iodine subtracting and calcium preserving VNC post-processing algorithm, both at a virtual monoenergetic image impression of 70 keV. Slice thickness and increment were consistently 3.0 mm and 1.5 mm. FoV with a matrix size of 512 pixels and number of slices were adjusted to cover the whole heart.

*Image Analysis*

Noise analyses were performed using Python (version 3.9). As a measure of quantitative image quality, the global noise level was calculated. Of each patient and reconstruction three slices, approximately equidistant to each other and the scan range margins, were selected and their noise map generated. As described previously by Christianson et al., a noise map consists of the standard deviation of CT values for each pixel within one image calculated using a filter of 6 mm size.[90] The histogram of the noise map reveals the most frequent SD of CT values within the respective slice. The average of the most frequent SD of the three slices was taken as global noise level representing the whole image volume (Supplemental Figure 4.17). Calcium quantities were determined using commercially available software on a dedicated workstation (Syngo.via, version VB60A, Siemens Healthcare GmbH, Erlangen, Germany). Contiguous voxels with an attenuation above a threshold of 130 HU were detected and semi-manually assigned to the respective coronary artery. The Agatston score was quantitatively exported on a per-patient level (Figure 4.18).

*Statistical analysis*

Statistical analyses were performed using Python (version 3.9). Patients were categorized by BMI into normal weight, with a BMI less than 24 $kg/m^2$ ($BMI_{<24}$), mild obesity with a BMI between 24 and 28 $kg/m^2$ ($BMI_{24\text{-}28}$) and obesity with a BMI greater than 28 $kg/m^2$ ($BMI_{>28}$). Regarding heart rhythm, no sinus ($HRh_{no\_sin}$) and sinus rhythm ($HRh_{sin}$) were differentiated. Patients' heart rates were categorized from 60 to 90 bpm in 10 bpm increments, $HR_{<60}$, $HR_{60\text{-}69}$, $HR_{70\text{-}79}$, $HR_{80\text{-}89}$ and $HR_{>89}$. Both, heart rhythm and heart rate refer to measurements during TNC acquisition. All data were tested for normal distribution using the Shapiro-Wilk test. Continuous parametric data are presented as mean $\pm$ SD, non-parametric data as median with interquartile range, and binary data as frequencies with proportions. Differences between TNC and

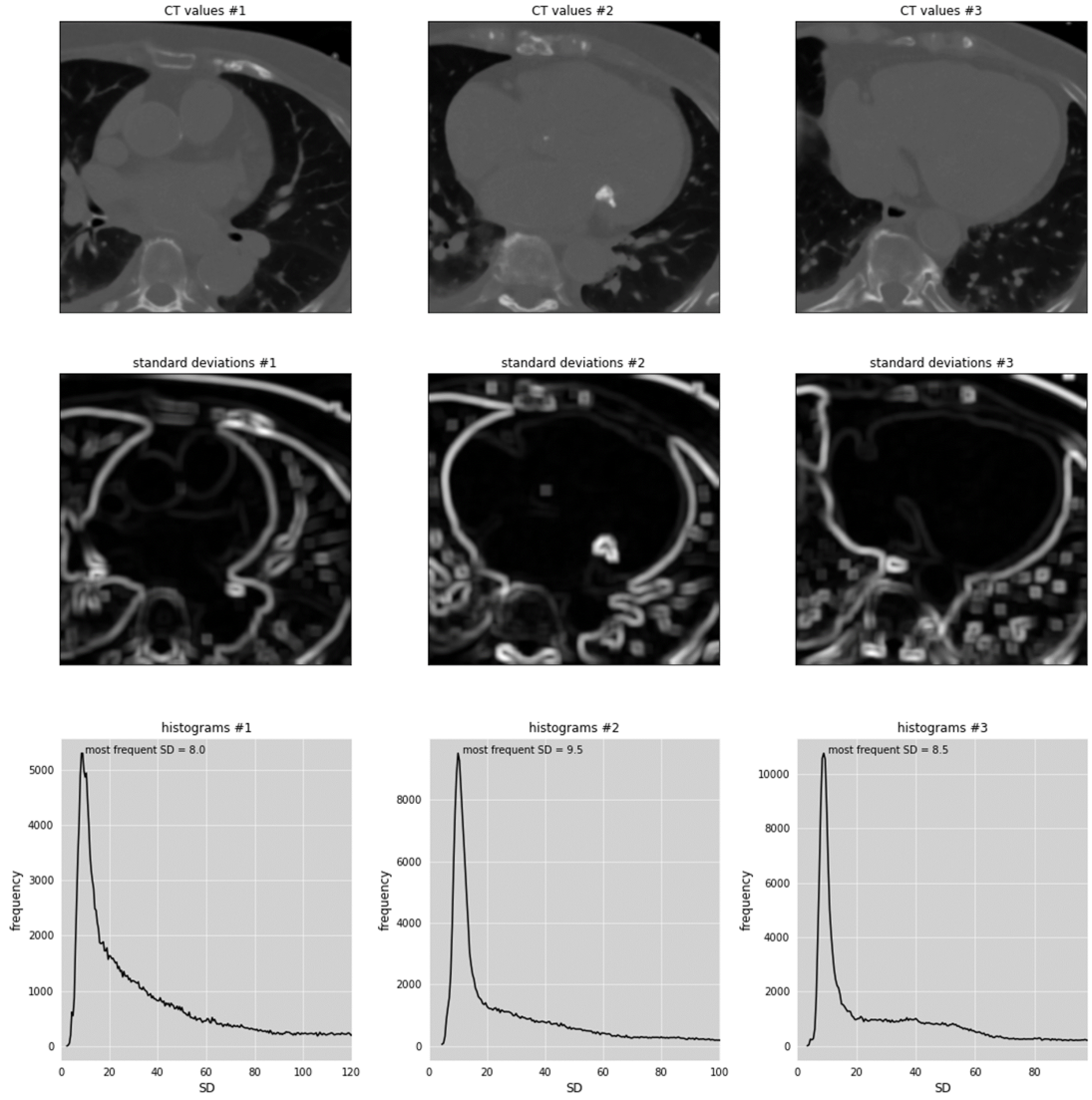


**Figure 4.17:** Demonstration of global noise calculation for one image volume. **A** shows the three selected slices equally distributed on the x-axis and **B** their SDs after filtering. The histogram in **C** shows the most frequent SD that was averaged over the three slices and used as global noise level.

SD = standard deviation.

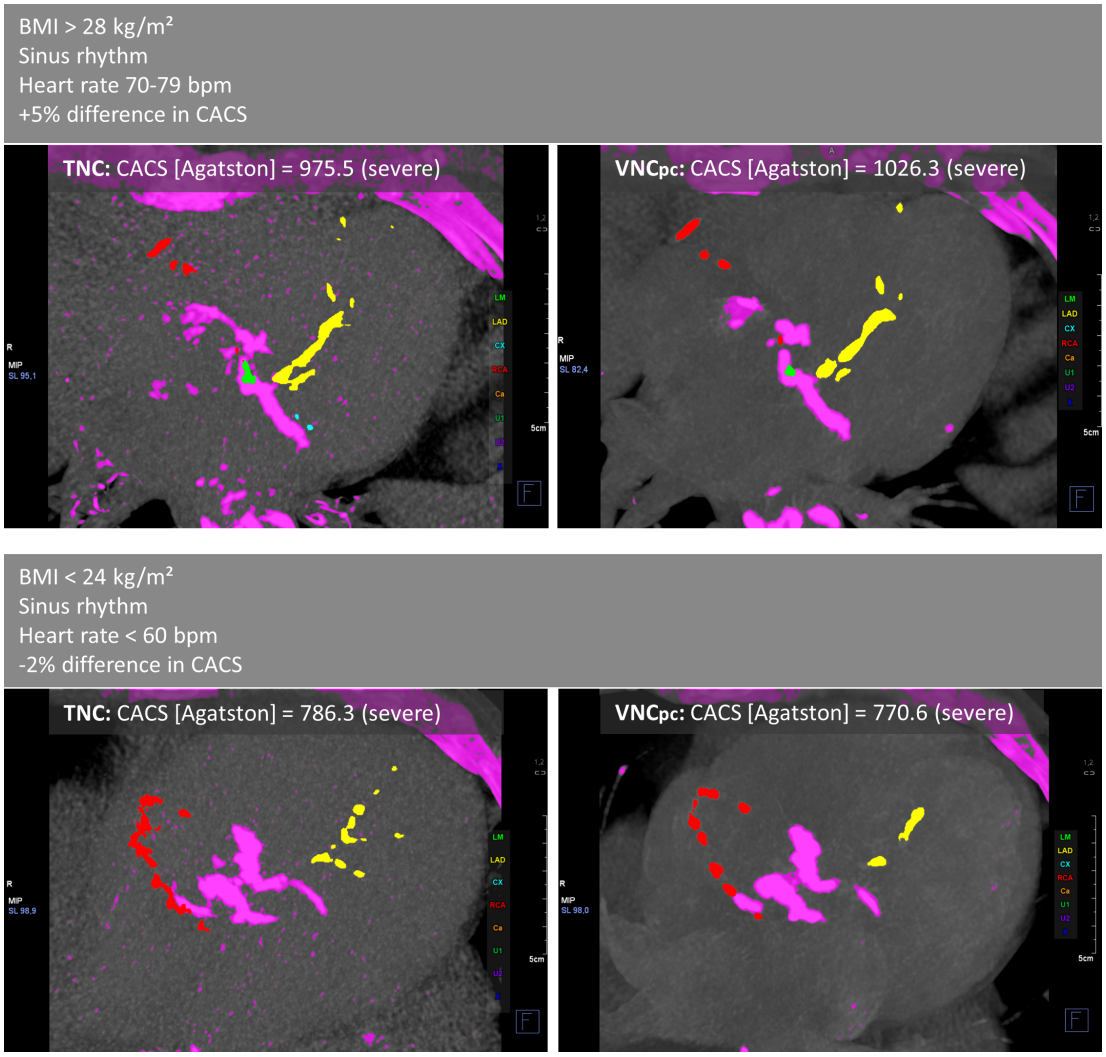


**Figure 4.18:** Demonstration of CACS for two examples. Images show maximum intensity projections of axial slices for TNC and $VNC_{pc}$ reconstructions. Voxels with CT values exceeding 130 HU are considered to represent calcifications (marked purple) and can be allocated semi-manually to single coronary arteries.

BMI = body-mass-index, CACS = coronary artery calcium scoring, TNC = true non-contrast, $VNC_{pc}$ = PureCalcium virtual non-contrast.

| | | |
|---|---|---|
| Total n = 88 | | |
| Clinical | | |
| Age [years] | 78.9 ± 6.1 | |
| Female | 52 (59%) | |
| BMI [kg/m$^2$] | 27.1 ± 5.1 | |
| Sinusrhythm | 62 (70.5%) | |
| Heat rate [bpm] | 75 (62.8 - 86.3) | |
| CT protocol | Unenhanced | CTA |
| Image quality level | 19 | 50 |
| Pitch factor | 3.2 | 0.21 (0.17 - 0.24) |
| CT radiation dose | | |
| Mean CTDI$_{vol}$ [mGy] | 1.4 (1.1 - 1.7) | 28.3 (18.7 - 38.3) |
| DLP [mGy*cm] | 27.9 (22.6 - 34.3) | 437.5 (299.5 - 666.3) |
| SSDE [mGy] | 1.8 (1.6 - 2.1) | 36.4 (27.6 - 50.5) |
| Coronary artery calcification | TNC | VNC$_{pc}$ |
| Total score [Agatston] | 541.7 (200.2 - 1293.9) | 449.3 (129.6 - 1182.5) |

**Table 4.10:** Study baseline characteristics. Including clinical and CT protocol and radiation dose parameters for the unenhanced scan and the angiography.

Values are mean ± standard deviation, median (interquartile range), or frequency (percentage). BMI = body-mass-index, CTA = computed tomography angiography, CTDI$_{vol}$ = volumetric CT dose index, DLP = dose length product, SSDE = size specific dose estimate.

VNC$_{pc}$ distributions were tested for their significance using the paired t-test or Wilcoxon signed-rank test for parametric and non-parametric data, respectively. P-values of multiple comparisons were corrected with Bonferroni method and considered to indicate statistically significant differences if $\leq .050$. Percentage difference was calculated as follows: $\frac{VNC_{pc}-TNC}{TNC} * 100\%$. For linear regression analyses, data was square root transformed to approximate normal distribution and to improve homoscedasticity. To evaluate the linear model's predictive value, the coefficient of determination ($r^2$) was calculated. CACS risk category agreement between TNC and VNC$_{pc}$ was calculated using the categorization into no, mild, moderate, and severe calcification with an Agatston score of 0, 1 - 100, 101 - 400 and $> 400$.

## Results

*Patient Baseline Characteristics*

In total, 112 patients were enrolled in this study. Thereof, 24 were excluded due to coronary stents (n = 23) or bypass (n = 1). The final study cohort consisted of 88 patients, 52 women and 36 men, with a mean age of 79 years. Table 4.10 lists all values concerning clinical parameters, scan protocol and dose parameters, as well as total CACS. Defining the total radiation exposure as sum of the unenhanced and CTA scan, the share of the unenhanced scan is about 6% (median proportions CTDI$_{vol}$ = 5.1%, DLP = 6.2%, SSDE = 5.0%).

*Image Noise*

The global noise level on TNC series with an average of 22 $\pm$ 4 HU was significantly higher ($p < .001$) compared with $VNC_{pc}$ series with an average of 10 $\pm$ 2 HU.

*Calcium Scoring*

In Table 4.11 total and subgroup results are listed. Overall, CACS measured on $VNC_{pc}$ differed significantly from TNC-based scores (see Figure 4.19A) by a median of -11%. However, there was excellent correlation ($r^2 = 0.95$) (see Figure 4.19B) and 80% agreement in risk categorization (see Figure 4.19C).

The BMI groups contained 23, 30 and 30 patients for $BMI_{<24}$, $BMI_{24\text{-}28}$ and $BMI_{>28}$ respectively. Due to missing weight or height information, 5 patients were not considered for BMI subgroup analysis. The scores differed significantly between TNC and $VNC_{pc}$ only for obese patients ($BMI_{>28}$, $p < .001$). Furthermore, the median underestimation was twice as high compared to patients with a lower BMI ($BMI_{<24}$: -10%, $BMI_{24\text{-}18}$: -8%, $BMI_{>28}$: -20%). The correlation remained high for all subgroups ($r^2 > 0.9$), but the category agreement between TNC and $VNC_{pc}$ was lowest for $BMI_{24\text{-}28}$ at 'only' 77%, although the percentage difference was the smallest.

62 patients showed a sinus ($HRh_{sin}$), and 26 showed no sinus heart rhythm ($HRh_{no\_sin}$). Both groups showed similar results. Scores differed significantly between TNC and $VNC_{pc}$ with a median percentage of -12% and -13% for $HRh_{sin}$ and $HRh_{no\_sin}$. The correlation for $HRh_{sin}$ slightly exceeded the one of $HRh_{no\_sin}$ ($r^2 = 0.96$ vs. 0.91), however, the category agreement was equivalent (79% vs. 81%).

In terms of heart rate, the results began to differ significantly between TNC and $VNC_{pc}$ from 70 bpm onwards. $HR_{<60}$ and $HR_{60\text{-}69}$ showed only small median percentage difference of -5% and -6%, a consistent high correlation ($r^2 = 0.93$ and 0.98) and an agreement in risk category of 83% and 77%. $HR_{70\text{-}79}$ showed an increase in underestimation of scores on $VNC_{pc}$ with a median difference of -15% to TNC derived scores. Although the correlation was high with $r^2$ of 0.94, the risk agreement was lowest at only 63%. For both heart rate groups above 79 bpm, the median difference reached -26%, but the first quartile was the most extreme at -330% for the group of $HR_{>89}$. Correlation and risk category agreement was similarly high for both groups ($r^2 = 0.95$ and 0.91, agreement of 89% and 88% for $HR_{80\text{-}89}$ and $HR_{>89}$).

Table 4.12 allows a more detailed examination of risk category agreement and shows the difference between $VNC_{pc} - TNC$ in the absolute number of patients classified as no, mild, moderate, and severe CACS (see also Figure 4.19C). As demonstrated, according to TNC derived scores most (54 out of 88) patients suffered from severe CACS, thereof 10 were misclassified into lower risk category based on $VNC_{pc}$ scores, 2 into mild and 8 into moderate. Although most of the misclassified patients were in higher BMI groups, more than half showed sinus rhythm and all heart rate groups were represented. 21 patients had moderate CACS, with $VNC_{pc}$ showing deviating results in 5 cases, with 1 patient classified as having no, 3 patients as having mild and one patient as having severe CACS. Misclassified patients were mildly obese or obese but showed all sinus rhythm and rather low heart rates below 80 bpm. TNC

| Group | | n | Absolute CACS TNC | $VNC_{pc}$ | p-value | Difference ($VNC_{pc}$−TNC)/TNC | Correlation $r^2$ | Category TNC = $VNC_{pc}$ |
|---|---|---|---|---|---|---|---|---|
| Total | | 88 | 542 (200-1294) | 449 (130-1183) | 0.000 | -11 (-36 - 2)% | 0.95 | 80% |
| BMI [kg/m$^2$] | < 24 | 23 | 400 (172-1224) | 354 (141-1144) | 0.520 | -10 (-25 - 4)% | 0.97 | 87% |
| | 24 - 28 | 30 | 603 (290-1713) | 563 (195-1819) | 0.205 | -8 (-28 - 9)% | 0.93 | 77% |
| | > 28 | 30 | 659 (362-1238) | 476 (140-1083) | 0.000 | -20 (-47- -6)% | 0.96 | 83% |
| Heart rhythm | No sinus | 26 | 700 (354-2098) | 633 (234-1820) | 0.033 | -13 (-29 - 8)% | 0.91 | 81% |
| | Sinus | 62 | 477 (138-1194) | 399 (88-1086) | 0.005 | -12 (-48 - 1)% | 0.96 | 79% |
| Heart rate [bpm] | < 60 | 12 | 888 (732-1254) | 971 (650-1305) | 0.366 | -5 (-19 - 10)% | 0.93 | 83% |
| | 60 - 69 | 22 | 601 (361-1723) | 552 (266-1953) | 0.824 | -6 (-21 - 9)% | 0.98 | 77% |
| | 70 - 79 | 19 | 471 (166-1226) | 301 (160-1101) | 0.036 | -15 (-40 - -5)% | 0.94 | 63% |
| | 80 - 89 | 18 | 395 (107-1088) | 167 (63-1005) | 0.043 | -26 (-54 - -5)% | 0.95 | 89% |
| | > 89 | 17 | 532 (190-1232) | 491 (102-1008) | 0.003 | -26 (-330 - -6)% | 0.91 | 88% |

**Table 4.11:** Coronary artery calcification. Derived from TNC vs. derived from $VNC_{pc}$ grouped by BMI, heart rhythm and heart rate. Columns include the number of patients, the absolute measured calcification each series and the p-value of their distribution differences, their percentage difference, the coefficient of determination of their linear correlation and their agreement in risk category.

BMI = body-mass index, n = absolute number of patients, $r^2$ = coefficient of determination, TNC = true non-contrast, $VNC_{pc}$ = PureCalcium virtual non-contrast.

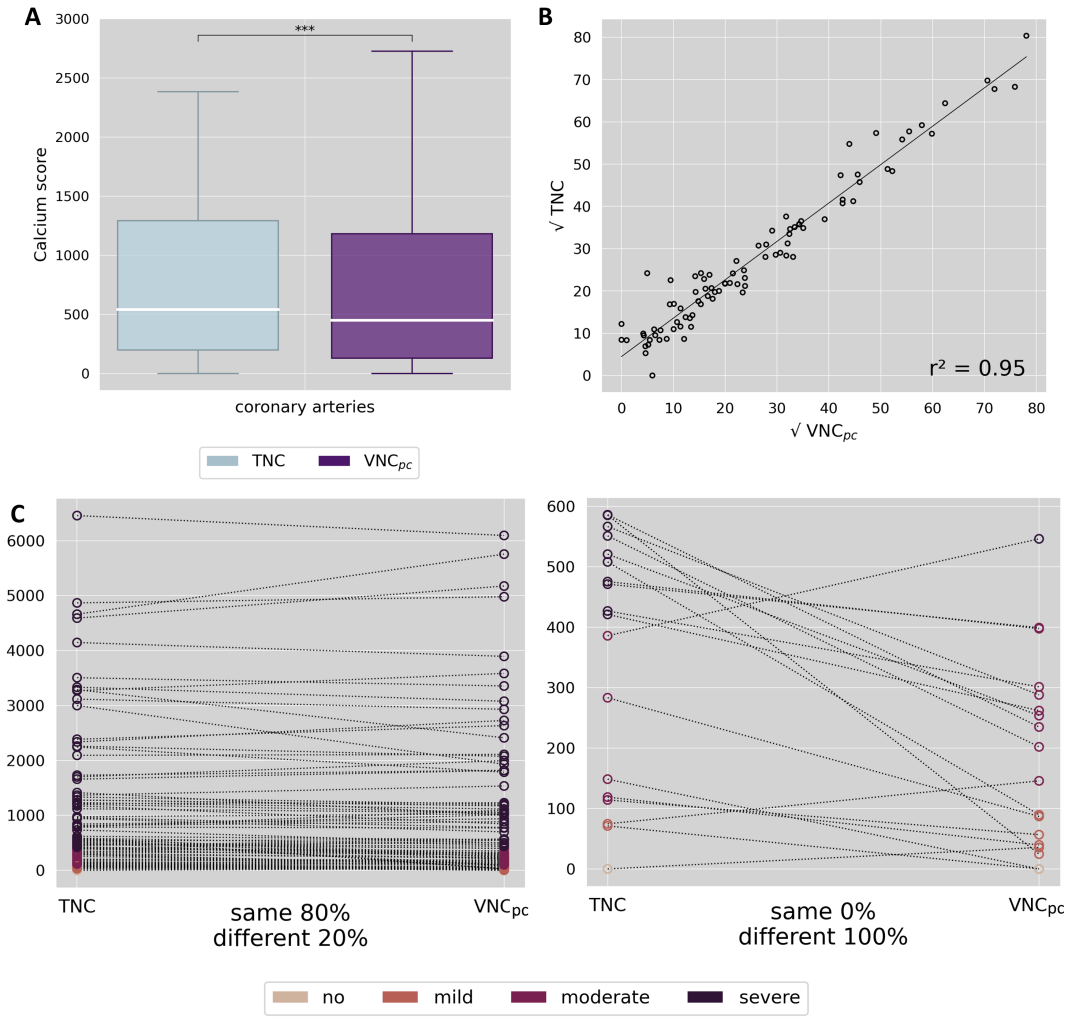


**Figure 4.19:** Comparison of the total calcium scores derived from TNC and $VNC_{pc}$ reconstructions. In **A** the absolute measurements are compared in a box plot (*** = $p < 0.001$), in **B** the linear regression of the square root transformed values are demonstrated and in **C** the agreement in risk categorization is shown for all patients on the left and only for the misclassified patients on the right.

$r^2$ = coefficient of determination, TNC = true non-contrast, $VNC_{pc}$ = PureCalcium virtual non-contrast.

| | | n | Agreement in Risk Category [n] | | | | | | | | | | | | | | | |
|---|---|---|---|---|---|---|---|---|---|---|---|---|---|---|---|---|---|---|
| | | | No ($CACS_{TNC}$ = 0) | | | | Mild ($CACS_{TNC}$ = 1-100) | | | | Moderate ($CACS_{TNC}$ = 101-400) | | | | Severe ($CACS_{TNC} > 400$) | | | |
| | | | 0 | 1 | 2 | 3 | -1 | 0 | 1 | 2 | -2 | -1 | 0 | 1 | -3 | -2 | -1 | 0 |
| Total | | 88 | 0 | 1 | 0 | 0 | 1 | 10 | 1 | 0 | 1 | 3 | 16 | 1 | 0 | 2 | 8 | 44 |
| BMI [kg/m$^2$] | $< 24$ | 23 | 0 | 0 | 0 | 0 | 1 | 2 | 0 | 0 | 0 | 0 | 8 | 1 | 0 | 0 | 1 | 10 |
| | 24 - 28 | 30 | 0 | 1 | 0 | 0 | 0 | 1 | 0 | 0 | 1 | 2 | 5 | 0 | 0 | 1 | 2 | 17 |
| | $> 28$ | 30 | 0 | 0 | 0 | 0 | 0 | 5 | 0 | 0 | 0 | 1 | 3 | 0 | 0 | 1 | 3 | 17 |
| Heart rhythm | No sinus | 26 | 0 | 0 | 0 | 0 | 0 | 0 | 1 | 0 | 0 | 0 | 6 | 0 | 0 | 1 | 3 | 15 |
| | Sinus | 62 | 0 | 1 | 0 | 0 | 1 | 10 | 0 | 0 | 1 | 3 | 10 | 1 | 0 | 1 | 5 | 29 |
| Heart rate [bpm] | $< 60$ | 12 | 0 | 1 | 0 | 0 | 0 | 1 | 0 | 0 | 0 | 0 | 0 | 0 | 0 | 0 | 1 | 9 |
| | 60 - 69 | 22 | 0 | 0 | 0 | 0 | 0 | 1 | 0 | 0 | 0 | 2 | 3 | 1 | 0 | 0 | 2 | 13 |
| | 70 - 79 | 19 | 0 | 0 | 0 | 0 | 0 | 1 | 1 | 0 | 1 | 1 | 4 | 0 | 0 | 0 | 4 | 7 |
| | 80 - 89 | 18 | 0 | 0 | 0 | 0 | 0 | 5 | 0 | 0 | 0 | 0 | 5 | 0 | 0 | 1 | 1 | 6 |
| | $> 89$ | 17 | 0 | 0 | 0 | 0 | 1 | 2 | 0 | 0 | 0 | 0 | 4 | 0 | 0 | 1 | 0 | 9 |

**Table 4.12:** Agreement in risk category. Grouped by BMI, heart rhythm and heart rate. Columns contain the classification into no, mild, moderate and severe calcification according to Agatston scores derived from TNC and the respective difference to the $VNC_{pc}$-based categorization in range -3 to 3 (underestimation to overestimation of maximum three categories).

BMI = body-mass index, n = absolute number of patients, TNC = true non-contrast, $VNC_{pc}$ = PureCalcium virtual non-contrast.

Agatston scores showed mild CACS in 12 patients and no CACS in 1 patient. Within the mild category, $VNC_{pc}$ agreed with 10 patients and categorized one as no and one as moderate. The one patient with no CACS on TNC was categorized as mild by $VNC_{pc}$. Again, there is no clear trend in the cohort in terms of BMI, heart rhythm or heart rate causing the misclassification.

## Discussion

In this study we performed CACS in a large cohort and evaluated the influence of BMI, heart rhythm and heart rate, on the accuracy of $VNC_{pc}$ compared to TNC derived calcium scores on PCD-CT data. Main findings of our study are: 1) CACS on $VNC_{pc}$ significantly underestimates TNC-based scores. In 80% of the evaluated cases categorization of CACS severity matched for $VNC_{pc}$ and TNC derived scores. Of the 20% misclassified patients, in approximately 11% a falsified treatment was considered possible. 2) For non-obese patients (BMI $< 28$ kg/m$^2$) with normal pulse ($< 69$ bpm) CACS based on $VNC_{pc}$ did not significantly differ from TNC. Differences increased for obese and tachycardic patients, however, correlation and the CACS risk categorization remained unaffected.

CCTA has a class 1 indication for the diagnosis of coronary artery disease according to current European Society of Cardiology guidelines.[61] In Germany, an admission as a health insurance service is soon expected.[102] The possibility of a reliable CACS on CTA-derived $VNC_{pc}$ reconstructions promises a reduction in patient radiation dose and acquisition time to a minimum. Several studies analyzing dual-energy[47,48,50,72,103] and photon-counting[7,73] CT data have demonstrated feasibility based on excellent correlation of calcium scores. However, the stability and reliability of calcium quantification based on $VNC_{pc}$ images in terms of BMI, heart rhythm and heart rate remain unclear.

This study provides a structured analysis of the potential influence of patient characteristics. Calcium scores were determined on $VNC_{pc}$ and TNC reconstructions derived from PCD-CT data and contrasted within the subgroups of each characteristic. Differences including their significance, correlation, and agreement in CACS severity were evaluated.

Overall, a significant underestimation of CACS was observed, which, in contrast to conventional $VNC_{conv}$ derived scores, does not require a general correction factor.[47,49] The effect is probably due to an underestimation of plaque density and volume.[47] However, the agreement in severity categorization was high and the correlation was excellent.

Previously, BMI has been shown to have a negative impact on image quality with respect to CACS in VNC images.[99,104,105] Evaluation of the accuracy within BMI groups showed no significant differences in calcium scores for normal weight and mildly obese patients, whereas in obese patients scores differed significantly and the percentage underestimation was doubled. Interestingly, this observation was not reflected regarding high correlation and categorization of CACS severity, which both remained stable even for BMIs exceeding 28 kg/m$^2$. Extreme misinterpretation of scores occurred mainly within one category, especially the severe category, and not across categories. Improved independence of CT values in VNC images from PCD-CT systems from patient BMI has already been demonstrated in other anatomical regions.[36,106]

Cardiac arrhythmias can lead to poor image quality in cardiac imaging.[107–109] One third of the patients included lacked a sinus rhythm. However, the percentage difference, correlation as well as risk categorization agreement comparing TNC and $VNC_{pc}$ was equivalent for both groups.
Similar to arrhythmia, an increased heart rate can decrease the quality of CT imaging due to myocardial contractility.[110] Therefore, decreasing the heart rate to $< 65$ bpm has been recommended in cardiac imaging for quite some time.[111–113] This study's subgroup analysis revealed no significant, and in the percentage median minor differences in CACS for heart rates $< 80$ bpm. For higher heart rates, the underestimation extremely enlarged. However, the correlation and the agreement in risk category was comparable for all categories, except for the middle one, which included heart rates from 70 to 79 bpm, and an agreement of only just two-thirds.
CACS is an independent risk factor for cardiovascular disease.[114] According to guidelines, the quantification can be used to make treatment decisions in patients with elevated cholesterol, especially in those patients in whom statin therapy is still uncertain. Patients with an Agatston score of $> 100$ have a 7.5% risk of a cardiovascular event within 10 years[114] and therapy with statins is recommended for patients $> 40$ years.[115] If, on the other hand, the Agatston score is 0, this may indicate a wait-and-see approach to statin therapy in patients at low risk for a cardiovascular events.[115] In this study 6 patients (referring to 7% of the study cohort) were erroneously classified to risk category $< 100$ according to $VNC_{pc}$ based Agatston scores and two patients (referring to 2% of the study cohort) showed no measurable CACS on $VNC_{pc}$ series. If they were considered low or no risk patients, they may have been mistakenly not treated. Vice versa, one patient was erroneously categorized into groups $> 100$ and one $> 0$ according to $VNC_{pc}$ based Agatston scores which would potentially lead to unnecessary therapy.
This study has several limitations. First, although the total number of patients in this study was high, creating subgroups reduces the number within each and therefore the informative values of the results. Larger or even multi-centric studies are needed to confirm the results regarding the influence of patient characteristics on CACS. Second, this study lacks an actual assessment of the differences in clinical decision-making according to the different CACS. However, this would be the consequent next step following the analysis of severity agreement. Third, all results are solely on a quantitative basis analyzing differences, correlation, and severity agreement. Qualitative evaluations and/ or further quantitative measures should be considered in future studies. Fourth, the study cohort had predominantly severe coronary artery disease, so the conclusions for low CACS need to be verified.

## Conclusion

In conclusion, this study proved $VNC_{pc}$ to provide a reliable estimate of TNC-based CACS for non-obese patients ($< 28$ kg/m$^2$) with normal pulse ($< 69$ bpm) in patients with severe coronary artery disease. For obese or tachycardic patients the possibility of significant underestimation of TNC CACS must be considered for clinical decision making. Further improvements in $VNC_{pc}$ algorithm might soon allow the substitution of additional TNC scans for CACS.

## 4.2 Other Applications

Although the topic of calcium scoring on virtual non-contrast series occupies a large part of this dissertation, the applications for VNC reconstructions, as well as its counterpart, iodine maps, are far more versatile. For example, our research group found a strong positive correlation between CT values measured in blood on VNC reconstructions with serum hemoglobin and hematocrit, allowing the detection of the presence and differentiation of the severity of anemia[116,117] or demonstrated the usefulness of $VNC_{pc}$ for patients who underwent endovascular aneurysm repair with a subjective assessment of image quality and stent visibility.[9]
Staying with cardiac imaging, as in the previous section, the paper presented within the first subsection (4.2.1) analyses the feasibility of epicardial adipose tissue (EAT) volume quantification on VNC images. As an indicator of several pathologies, fat volume has gained attention and is usually evaluated on TNC. Attempts have been made to obtain the same information from CTA, with the aim of eliminating the need for additional unenhanced scans of the heart. In this study we evaluate measurements performed on two in algorithm different VNC series and compare them with two previously reported CTA-based approaches and reference TNC results.
If acute bleeding is suspected, multiple contrast phases are usually acquired including an unenhanced scan followed by at least one CTA in arterial, portal venous or late phase.[118] The TNC series is necessary as a reference in case a hyper dense finding cannot be clearly identified as hemorrhage on CTA, but may represent calcification. If the finding shows equivalent contrast on TNC, then the latter is true, otherwise acute hemorrhage is likely. This incident of several contrast phases plus an unenhanced scan provides perfect prerequisite to evaluate the optimal VNC reconstruction in terms of CTA contrast phase combined with VNC algorithm as discussed in subsection 4.2.2.
As a counterpart to the virtual subtraction of iodine proportions, the reliable quantification of its concentration can be of immense importance, e.g. after intracranial interventions. After procedures such as recanalisation or embolization, an unenhanced CT is performed to rule out possible bleeding. However, contrast media is used during the intervention, which may have crossed the blood-brain barrier, complicating differentiation between emerging bleeding or contrast media extravasation and affecting patient management. In subsection 4.2.3 we performed a phantom study analyzing the potential of blood and iodine discrimination including the precise quantification of the latter.

### 4.2.1 Fat Quantification on VNC

## Assessment of Epicardial Adipose Tissue on Virtual non-Contrast Images derived from Photon-Counting CT Datasets

Franka Risch, Florian Schwarz, Franziska Braun, Stefanie Bette, Judith Becker, Christian Scheurig-Münkler, Thomas Kröncke, Josua Decker

The study was published in European Radiology in December 2022.[8] The author FR performed the data interpretation and statsitical analysis and wrote the manuscript.

### Abstract

*Objectives:* To assess EAT volume and attenuation of different VNC reconstructions derived from CCTA datasets of a PCD-CT system to replace TNC series.

*Methods:* Consecutive patients (n = 42) with clinically indicated CCTA and coronary TNC were included. Two VNC series were reconstructed, using a conventional ($VNC_{conv}$) and a novel calcium-preserving ($VNC_{pc}$) algorithm. EAT was segmented on TNC, $VNC_{conv}$, $VNC_{pc}$ and CCTA series using thresholds of -190 to -30 HU ($CTA_{-30}$) and an additional segmentation on the CCTA series with an upper threshold of 0 HU ($CTA_0$). EAT-volumes and their histograms were assessed for each series. Linear regression was used to correlate EAT-volumes, and the Euclidian distance for histograms. The paired t-test and the Wilcoxon signed-rank test were used to assess differences for parametric and non-parametric data.

*Results:* EAT-volumes from VNC and CCTA series showed significant differences compared to TNC (all $p < .05$), but excellent correlation (all $r^2 > 0.9$). Measurements on the novel $VNC_{pc}$ series showed the best correlation ($r^2 = 0.99$) and only minor absolute differences compared to TNC values. Mean volume differences were -12%, -3%, -13%, +10% for $VNC_{conv}$, $VNC_{pc}$, $CTA_{-30}$, $CTA_0$ compared to TNC. Distribution of CT values on $VNC_{pc}$ showed less difference to TNC than on $VNC_{conv}$ (mean attenuation difference +7% vs. +2%; Euclidean distance of histograms 0.029 vs. 0.016).

*Conclusions:* $VNC_{pc}$-reconstructions of PCD-CCTA datasets can be used to reliably assess EAT-volume with a high accuracy and only minor differences in CT values compared to TNC. Substitution of TNC would significantly decrease patient's radiation dose.

### Introduction

EAT is the visceral fat located between the myocardial surface and the visceral layer of the pericardium.[119] Its extent and density are directly associated with the development and severity of a variety of cardiovascular and metabolic diseases, such as coronary artery disease, myocardial infarction, atrial fibrillation or obesity-related insulin resistance.[120–126]
EAT volume has been shown to be the most accurate measure to obtain EAT quantity, over thickness or area.[125] Echocardiography, cardiac magnetic resonance imaging (CMR) imaging

and CCT allow the non-invasive assessment of EAT quantity.[127,128] However, echocardiography can only provide EAT-thickness and CMR is time consuming with limited availability in clinical routine.[129] CT is already used for a wide range of cardiac examinations and provides highly reproducible, rapid EAT volume measurements on ECG triggered TNC series.[119] Furthermore, not only the extent but also CT attenuation values within EAT volume were found to correlate with local and systemic inflammatory markers.[130–132] EAT volumetry is based on CT value thresholds, varying from -250 to -190 HU and -50 to -30 HU, for the lower and upper threshold, respectively. By raising the upper threshold, EAT volumes can also be approximated on CCTA series.[133] Here it has been shown that an adjustment of the upper threshold from -30 to 0 HU on CCTA series provides more accurate EAT volumes compared to TNC values.[134,135]
The recent introduction of PCD-CT systems with inherent spectral information on clinical scans, now routinely enables several post-processing steps after data acquisition, including iodine removal from contrast-enhanced CT scans.[7,9,13,22] By now, two algorithms are available to create VNC series, conventional ($VNC_{conv}$) and PureCalcium ($VNC_{pc}$), that share a basic material differentiation into water and iodine. The $VNC_{pc}$ algorithm additionally performs a decomposition into iodine and calcium beforehand and was specifically developed to obtain full calcium contrast within the final image. Since none of the VNC algorithms specifically focus on decomposition into fat, adipose tissue is partly attributed to all base materials, and the attenuation values are expected to slightly differ from those of TNC.[6] The performance of the novel $VNC_{pc}$ algorithm on EAT quantification from CCTA scans has not yet been investigated. In this study, we therefore sought to analyze VNC reconstructions derived from PCD-CCTA datasets for the assessment of EAT in comparison to reference TNC and CCTA series.

## Materials and Methods

*Study population*
The protocol for this retrospective single-center study was approved by the institutional review board (Ludwig-Maximilian-University Munich, project number 22-0456) with a waiver for written informed consent. Consecutive patients with a clinically indicated ECG-gated CT scan of the heart on the PCD-CT (NAEOTOM Alpha, Siemens Healthineers) between 01/2022 and 04/2022 were included. Inclusion criteria were: (1) Age $>$ 18 years; (2) Pre-contrast TNC series for calcium scoring and contrast-enhanced CCTA series; (3) Availability of raw CT-data for image reconstructions.

*Data acquisition*
All patients received a pre-contrast scan for calcium scoring followed by a CCTA, both at 120 kVp and a collimation of 144 x 0.4 mm. Reference tube current time product was adjusted by setting the image quality level to 19 for TNC and 60 for CTA. For the CTA, a triphasic contrast injection protocol with bolus tracking was used. In the first phase, 60 ml of nonionic iodinated contrast material (Iopromide 300 mgI/ml, Ultravist, Bayer) was injected followed by a 50% diluted mixture of 30 ml contrast material and 30 ml normal saline solution and a saline chaser (25 ml). A flow of 5 ml/s was used in all three phases. By placing a region of interest

in the descending aorta, bolus tracking was performed, and the scan was initiated 8 seconds after the enhancement reached 150 HU. If there was no clinical contraindication, 0.4 mg of nitroglycerin was administered sublingually 5 minutes prior to the scan and 5 mg of metoprolol was administered intravenously in patients with a heart rate of more than 70 bpm.

*Image reconstruction*

All reconstructions were performed on a dedicated research workstation (ReconCT, Version 15.0.58331.0, Siemens Healthineers). For all patients, a true non-contrast (TNC) series based on the pre-contrast raw data, and a regular, a $VNC_{conv}$ and $VNC_{pc}$ series based on the CTA were reconstructed, all at a virtual monochromatic level of 70 keV. For all reconstructions, a quantitative kernel Qr36 with a quantum IR algorithm with strength level 3 and a slice thickness/ increment of 3.0/ 1.5 mm was used. The VNC image series differ in the iodine removal algorithm. In both alternatives, a material decomposition into water and iodine is performed but the $VNC_{pc}$ algorithm takes some further steps beforehand to preserve the full calcium contrast in the final image. Emrich et al. recently provided a detailed description of the $VNC_{pc}$ algorithm.[7]

*Image analysis*

Image analyses were performed on a dedicated workstation (syngo.via version VB70A, Siemens Healthineers, using the CT Cardiac Risk Assessment application). For each patient and series, the fat volume in ml and the histogram of the attenuation values in HU within the semi-automatically segmented pericardial adipose tissue were measured. For all series, the lower threshold was set to -190 HU and the upper threshold to -30 HU.[136–138] To assess a potential underestimation of EAT volume on CTA series with a range of -190 to -30 HU ($CTA_{-30}$), an additional measurement with an adapted upper threshold of 0 HU ($CTA_0$) was performed.[134,135] Figure 4.20 exemplarily shows a comparison of the segmentations, their volumes, and corresponding histograms. Only series with equal threshold range were considered in the analysis of the histograms, so $CTA_0$ was excluded for reasons of inter-series comparability and similarity between $CTA_0$ and $CTA_{-30}$. Image noise was defined as SD of CT values within the whole segmented EAT volume of the respective series.

*Statistical analyses*

Statistical analyses were performed using python (version 3.9.7). The Shapiro-Wilk test was used to test for normal distribution. The paired t-test and the Wilcoxon signed-rank test were used to assess differences for parametric and non-parametric data, respectively. In multiple comparisons, p-values were adjusted using the Bonferroni method. Binary data are presented in frequencies (proportions) and continuous data with mean $\pm$ SD or as median with interquartile range for parametric or non-parametric data, respectively. The coefficient of determination $r^2$ was used to assess the accuracy of the linear regression predictions to approximate TNC measurements and serves as a correlation measure. Euclidean distance was used for quantitative comparison of the histograms, which is calculated as follows:

$$\|q - p\|_2 = \sqrt{\sum_{i-1}^{n} (q_i - p_i)^2}$$

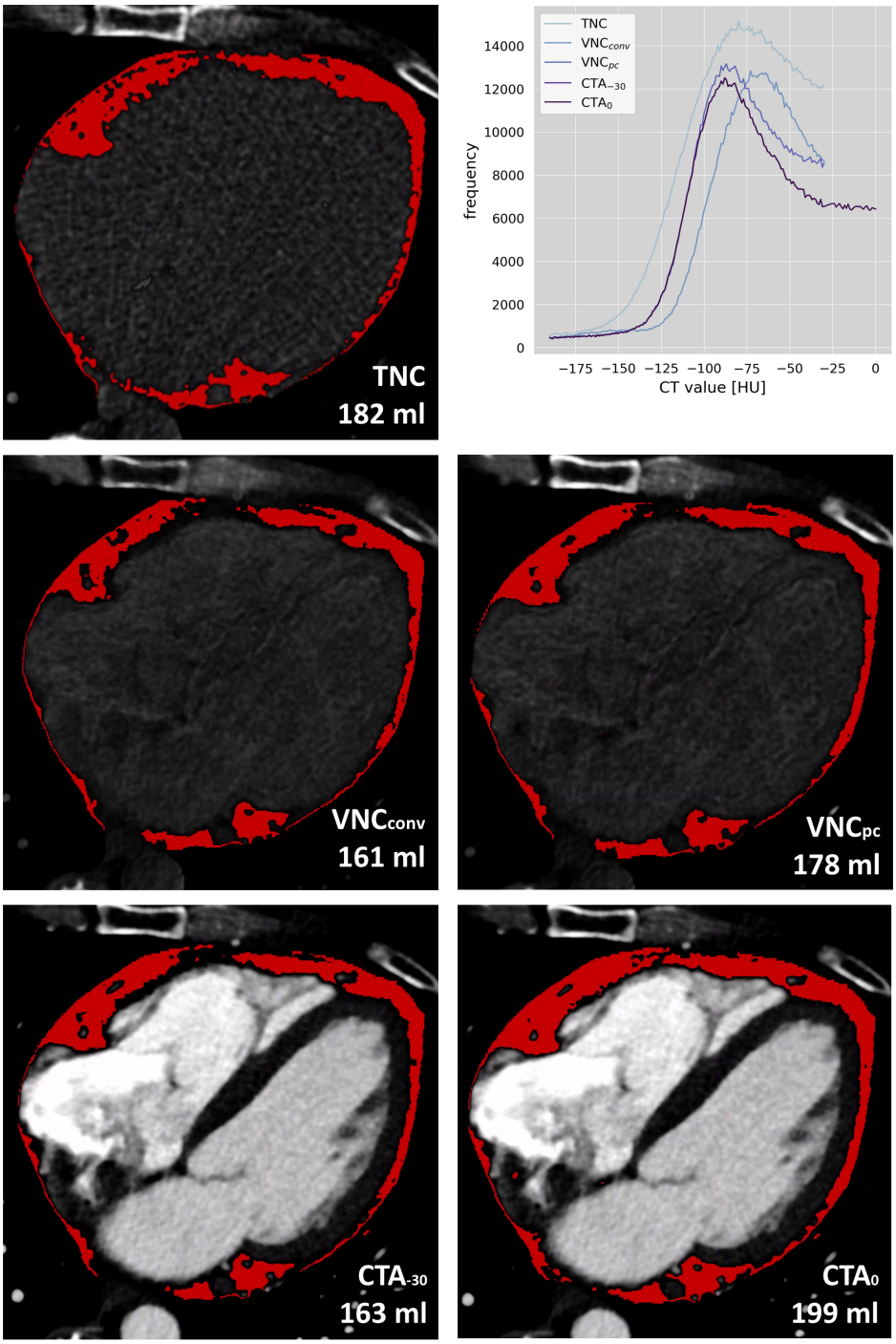


**Figure 4.20:** Demonstration of EAT segmentations, their volumes, and histograms.
EAT = epicardial adipose tissue, $CTA_0$ = CT angiography with an upper threshold of 0 HU, $CTA_{-30}$ = CT angiography with an upper threshold of -30 HU, TNC = true non-contrast, VNC = virtual non-contrast ($_{conv}$ = conventional, $_{pc}$ = PureCalcium).

| Total n = 42 | | |
|---|---|---|
| Clinical | | |
| Age [years] | 72.0 ± 9.5 | |
| Sex [female] | 20 (47.6%) | |
| CT radiation dose | TNC | CTA |
| $CTDI_{vol}$ [mGy] | 1.7 (1.3 - 2.7) | 15.3 (5.4 - 33.5) |
| DLP [mGy*cm] | 34.3 (27.3 - 50.2) | 262.5 (95.4 - 503.5) |
| SSDE [mGy] | 2.2 (1.9 - 3.3) | 22.0 (6.4 - 27.8) |
| Effective mAs | 22 (18 - 26) | 37 (29.3 - 47) |

**Table 4.13:** Baseline study characteristics.
Values are mean ± standard deviation, median (interquartile range), or frequency (percentage). $CTDI_{vol}$ = volumetric CT dose index, DLP = dose length product, SSDE = size specific dose estimate.

Where q and p are the equal sized histograms with bin size 1 HU, n is the total number of bins (-190 to -30 HU = 161 bins) and i the respective bin at a certain CT value. P-values $< 0.05$ were considered to indicate statistically significant differences.

## Results

*Patient Baseline Characteristics*

66 patients were primarily enrolled. Of these, 24 had to be excluded due to following reasons: Missing non-contrast series (n = 12); Missing CCTA series (n = 10); Missing raw data (n = 2). The final study cohort comprised 42 patients (mean age 72 ± 10 years, 20 females). In non-contrast series, DLP and $CTDI_{vol}$ were 34.3 (27.3 - 50.2) mGy*cm and 1.7 (1.3 - 2.7) mGy. In CCTA, DLP and $CTDI_{vol}$ were 262.5 (95.4 - 503.5) mGy*cm and 15.3 (5.3 - 33.5) mGy, respectively. The dose proportion of the pre-contrast scan corresponds to 12.9 (7.6 - 28.6)% and 13.1 (6.5 - 31.6)% of the total DLP and $CTDI_{vol}$ in all three phases. Table 4.13 summarizes the baseline study characteristics.

*EAT Volume*

Median EAT volume was measured 195.6 (122.6 - 268.4) ml on TNC series. Except for $CTA_0$ measurements with a mean difference of +14.8 ml, corresponding to +10% of the TNC volume, the volumes were significantly underestimated compared to TNC (Table 4.14 and Figure 4.21). The mean differences were -26.9 ml and -29.1 ml in $VNC_{conv}$ and $CTA_{-30}$, respectively, corresponding to -12% and -13% of the TNC volume. The most accurate measurement with the smallest difference in mean and standard deviation compared to volumes measured on TNC series was observed in $VNC_{pc}$ series with a mean difference of -5.7 ml, corresponding to a mean deviation of -3% to the TNC volume (Figure 4.22). EAT volumes of $CTA_{-30}$ and $VNC_{conv}$ did not significantly differ from each other (p-value = 0.2).

In linear regression analyses, EAT volumes from all reconstructed series showed a strong positive correlation to the ground truth in TNC series (all $r^2 > 0.9$). A near-perfect predictive

| | | Δ EAT volume [ml] p-value | | | |
|---|---|---|---|---|---|
| Series | EAT volume [ml] | TNC | $VNC_{conv}$ | $VNC_{pc}$ | $CTA_{-30}$ |
| TNC | 195.6 (122.6-268.4) | | | | |
| $VNC_{conv}$ | 177.6 (112.8-247.2) | -26.9 (-12%) $< 0.001$ | | | |
| $VNC_{pc}$ | 189.5 (103.2-229.3) | -5.7 (-3%) 0.001 | -21.2 (-12%) <0.001 | | |
| $CTA_{-30}$ | 180.9 (103.2-229.2) | -29.1 (-13%) <0.001 | -4.2 (-1%) 0.2 | -23.4 (-11%) <0.001 | |
| $CTA_0$ | 223.5 (131.6-306.6) | +14.8 (+10%) 0.001 | +40.5 (+24%) <0.001 | +20.5 (+12%) <0.001 | +43.9 (+26%) <0.001 |

**Table 4.14:** EAT volumes in ml on the respective image series and subgroup analyses including median differences in ml (and %), as well as the pairwise Wilcoxon p-value.
Volumes are median (interquartile range) and differences are mean (%). EAT = epicardial adipose tissue, $CTA_0$ = CT angiography with an upper threshold of 0 HU, $CTA_{-30}$ = CT angiography with an upper threshold of -30 HU, TNC = true non-contrast, VNC = virtual non-contrast ($_{conv}$ = conventional, $_{pc}$ = PureCalcium).

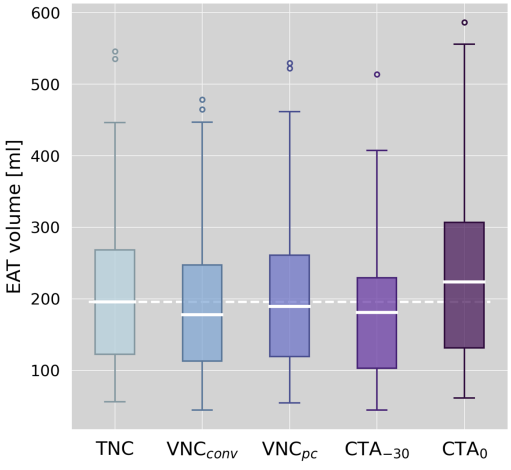


**Figure 4.21:** Boxplot of the measured epicardial adipose tissue volume in ml.
EAT = epicardial adipose tissue, $CTA_0$ = CT angiography with an upper threshold of 0 HU, $CTA_{-30}$ = CT angiography with an upper threshold of -30 HU, TNC = true non-contrast, VNC = virtual non-contrast ($_{conv}$ = conventional, $_{pc}$ = PureCalcium).

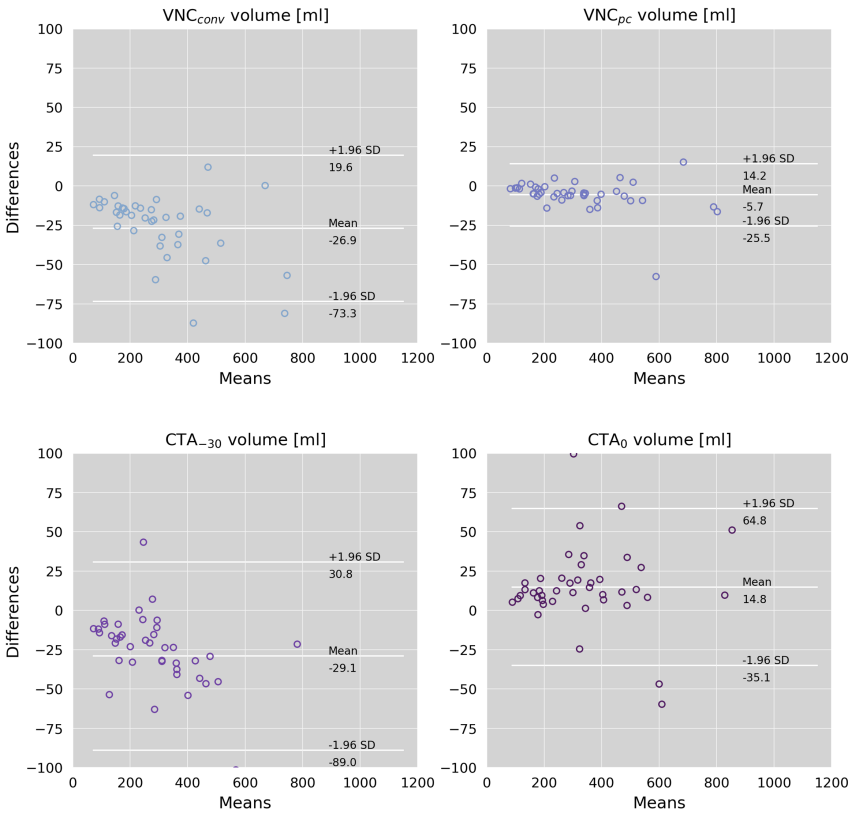


**Figure 4.22:** Mean difference plots between the EAT volumes in ml measured on TNC and the respective volumes measured on CTA and VNC.

EAT = epicardial adipose tissue, $CTA_0$ = CT angiography with an upper threshold of 0 HU, $CTA_{-30}$ = CT angiography with an upper threshold of -30 HU, TNC = true non-contrast, VNC = virtual non-contrast ($_{conv}$ = conventional, $_{pc}$ = PureCalcium).

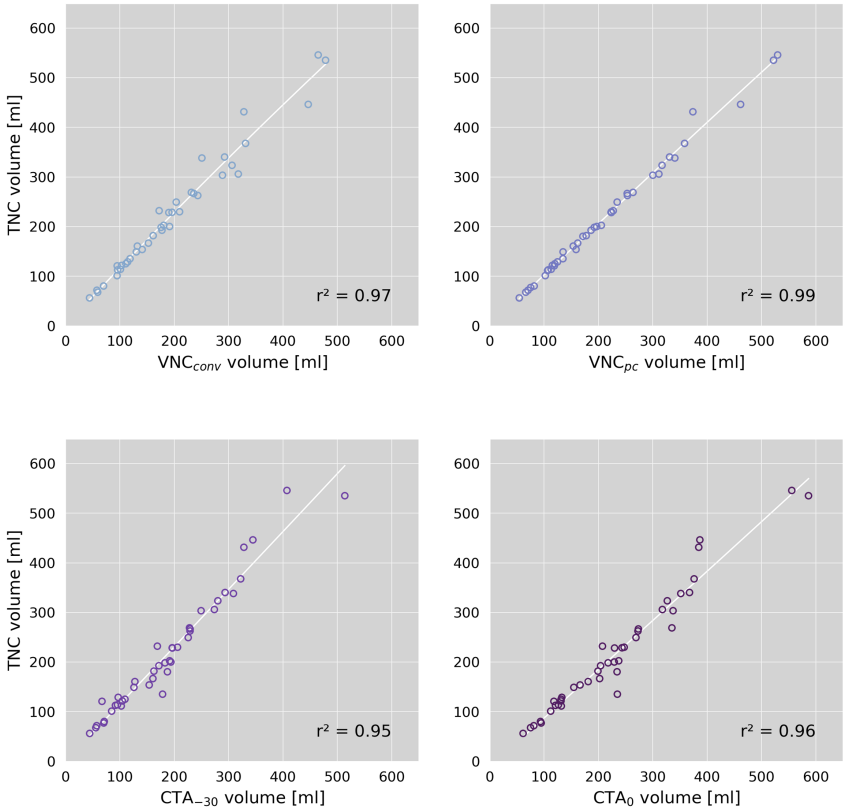


**Figure 4.23:** Linear regression plots between the EAT volumes in ml measured on TNC and the respective volumes measured on CTA and VNC.
EAT = epicardial adipose tissue, $CTA_0$ = CT angiography with an upper threshold of 0 HU, $CTA_{-30}$ = CT angiography with an upper threshold of -30 HU, TNC = true non-contrast, VNC = virtual non-contrast ($_{conv}$ = conventional, $_{pc}$ = PureCalcium).

accuracy was observed for EAT volumes measured on $VNC_{pc}$ series ($r^2$ = 0.99) (Figure 4.23).

*EAT Attenuation*

Mean attenuation within the EAT segmentation was -81.1 $\pm$ 5.8 HU, -75.4 $\pm$ 4.4 HU, -79.1 $\pm$ 5.9 HU, and -83.1 $\pm$ 8.3 HU for TNC, $VNC_{conv}$, $VNC_{pc}$ and $CTA_{-30}$, respectively (Figure 4.24). Compared to TNC, CT values were significant higher on VNC series (+6.6% and +2.3% for $VNC_{conv}$ and $VNC_{pc}$) and lower on $CTA_{-30}$ series (-2.1%). The noise level was 32.5 $\pm$ 2.0 HU, 31.0 $\pm$ 4.4 HU, 30.3 $\pm$ 2.4 HU, and 32.3 $\pm$ 3.6 HU for TNC, $VNC_{conv}$, $VNC_{pc}$ and $CTA_{-30}$, respectively. Significant differences existed only between noise measured on $VNC_{pc}$ to TNC and $CTA_{-30}$ (Table 4.15). Figure 4.25A shows the attenuation values within the segmented EAT volume divided by the total of voxel counts and averaged over all patients. The differences of the histograms represented by the Euclidean distance was greatest between TNC and $VNC_{conv}$ (0.029 $\pm$ 0.013) (Figure 4.25B). Both distances, TNC$-VNC_{pc}$ and TNC$-CTA_{-30}$ were significantly smaller (0.016 $\pm$ 0.007 and 0.017 $\pm$ 0.008, p's $< .05$, for TNC$-VNC_{pc}$ and TNC$-CTA_{-30}$, respectively) (Table 4.16).

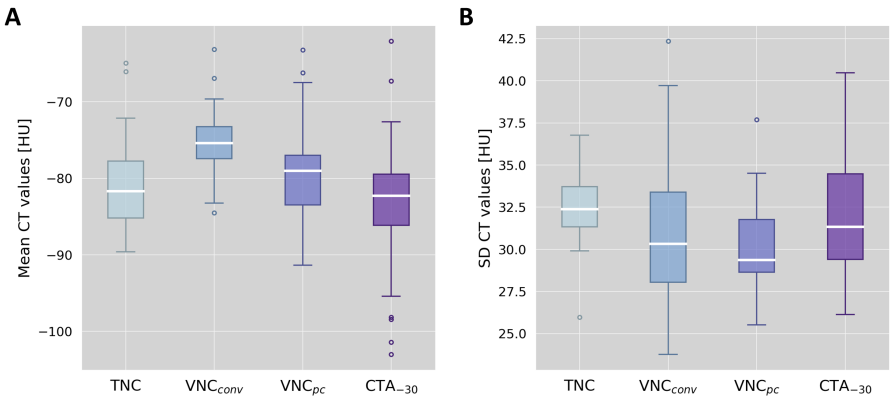


**Figure 4.24:** Boxplot of **A** the mean and **B** the SD of CT values measured within the segmented EAT volumes.

EAT = epicardial adipose tissue, CTA$_{-30}$ = CT angiography with an upper threshold of -30 HU, SD = standard deviation, TNC = true non-contrast, VNC = virtual non-contrast ($_{conv}$ = conventional, $_{pc}$ = PureCalcium).

| | | | p-value | |
|---|---|---|---|---|
| Series | Noise [HU] | VNC$_{conv}$ | VNC$_{pc}$ | CTA$_{-30}$ |
| TNC | $32.5 \pm 2.0$ | 0.082 | $< 0.001$ | 0.54 |
| VNC$_{conv}$ | $31.0 \pm 4.4$ | | 0.13 | 0.32 |
| VNC$_{pc}$ | $30.3 \pm 2.4$ | | | 0.015 |
| CTA$_{-30}$ | $32.3 \pm 3.6$ | | | |

**Table 4.15:** Image noise as standard deviation of the CT values in HU, measured within the segmented EAT volumes as well as p-values of the pairwise t-test.

Values are mean $\pm$ standard deviation. EAT = epicardial adipose tissue, CTA$_{-30}$ = CT angiography with an upper threshold of -30 HU, TNC = true non-contrast, VNC = virtual non-contrast ($_{conv}$ = conventional, $_{pc}$ = PureCalcium).

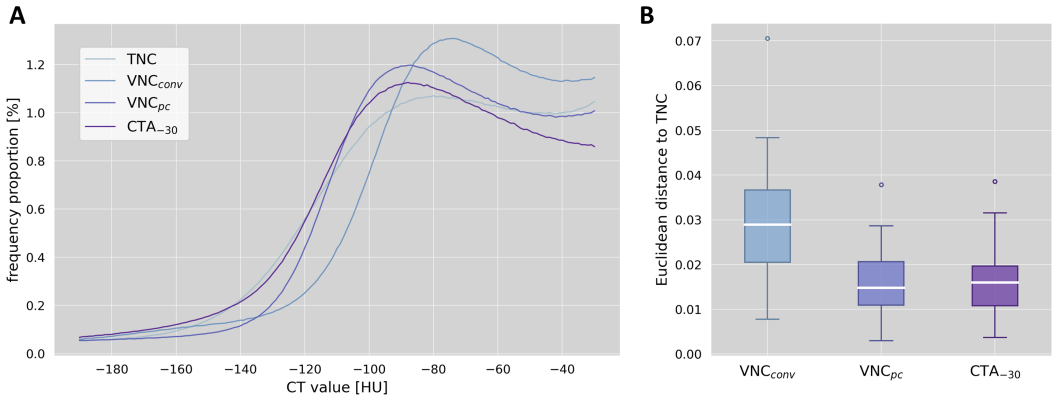


**Figure 4.25:** **A** Plots of the histograms divided by their total number of voxels and averaged over all patients for the respective image series and **B** boxplots of the Euclidean distance between the histograms of TNC and the respective histograms of CTA$_{-30}$ and VNC.

CTA$_{-30}$ = CT angiography with an upper threshold of -30 HU, TNC = true non-contrast, VNC = virtual non-contrast ($_{conv}$ = conventional, $_{pc}$ = PureCalcium).

| Series | Euclidean distance | p-value $\|VNC_{conv}-TNC\|_2$ | p-value $\|VNC_{pc}-TNC\|_2$ |
|---|---|---|---|
| $\|VNC_{conv}-TNC\|_2$ | $0.029 \pm 0.013$ | | |
| $\|VNC_{pc}-TNC\|_2$ | $0.016 \pm 0.007$ | $< 0.001$ | |
| $\|CTA_{-30}-TNC\|_2$ | $0.017 \pm 0.008$ | 0.002 | 0.54 |

**Table 4.16:** Euclidean distances between the normalized histograms of attenuation values within the EAT volumes and p-values of the pairwise t-test.
Values are mean ± standard deviation. EAT = epicardial adipose tissue, $CTA_{-30}$ = CT angiography with an upper threshold of -30 HU, TNC = true non-contrast, VNC = virtual non-contrast ($_{conv}$ = conventional, $_{pc}$ = PureCalcium).

## Discussion

This retrospective study evaluates the potential of substituting TNC series by VNC reconstructions derived from PCD-CCTA datasets for the quantification of EAT volume and its CT values. The main findings of this study are: (1) VNC series derived from PCD-CT CCTA datasets enable consistent EAT volume measurements in comparison to reference TNC; (2) With TNC as ground truth, $VNC_{pc}$ shows superior and more consistent results for EAT volume compared to $VNC_{conv}$, $CTA_{-30}$ or $CTA_0$; (3) the distribution of EAT attenuation values measured on VNC and CTA series significantly differs in comparison to TNC but the best agreement was observed for $VNC_{pc}$.

Epicardial adipose tissue has gained attention as it has been associated with numerous pathologies. Correlations of EAT volume to atrial fibrillation, coronary artery disease and sleep apnea syndrome have been reported as well as its ability to predict clinical coronary outcomes.[120–126,129] CT can provide a rapid, reliable, and highly reproducible non-invasive assessment of EAT. Usually, cardiac CT already includes several series, of which the pre-contrast phase for calcium scoring is used to quantify EAT.[119,129] The radiation exposure in CT-acquisitions is a non-negligible disadvantage. To reduce radiation dose to a necessary minimum, there are a variety of approaches, one of which is to substitute the pre-contrast phase with a virtual non-contrast reconstruction based on the coronary CTA. With the introduction of a PCD-CT system that inherently provides spectral information for every scan, VNC series can be routinely reconstructed from every contrast-enhanced scan.[5] Studies have shown the suitability of VNC reconstructions for several applications, such as diagnosis of acute bleedings,[139] coronary calcium quantification[7,50] or in patients after endovascular aneurysm repair.[9]

Our results show that EAT volume measurements for both the conventional and the novel VNC reconstructions have excellent correlation with the ground truth TNC, but also systematically underestimate. However, for $VNC_{pc}$, the difference to TNC is negligibly small (-3%). Further studies should be performed to investigate how this affects individual risk stratification by the application of specific volume thresholds. The underestimation can be attributed to the material differentiation into water and iodine which is performed to create VNC images. Since adipose tissue is partly split into both base materials, the CT values on the water image are systematically higher compared to TNC.[6] This effect can be seen especially in the positive shift

of the $VNC_{conv}$ histogram. Nevertheless, many studies showed that VNC images mimic TNC very well for the vast majority of tissues examined. Sauter et al. found an absolute difference of less than 10 HU for ROIs in aorta, liver, renal cortex, muscle, fluid and also fat, measured on VNC images obtained from a dual layer detector CT system.[140] With photon-counting detector CT systems, similar results were found with a high quantitative and qualitative agreement of VNC and TNC.[13,141] Although Choi et al. observed an underestimation of fatty liver density on VNC, they did not find a significant diagnostic difference to TNC.[142] In general, the results of our study show that differences between the VNC algorithms have a measurable impact on EAT volume and attenuation, with a clearly superior assessment on $VNC_{pc}$ series.

Regarding EAT volumes obtained from CTA, an upper threshold of -30 HU resulted, as expected, in an underestimation compared to TNC. Xu et al. found that an adapted upper threshold of -3 HU for measurements on CTAs result in statistical equivalent EAT volumes compared to TNC.[135] In this study we tested an upper threshold of 0 HU for CTA (according to Marwan et al.[134]), and could not reproduce EAT volumes on TNC but overestimated them. One conceivable explanation could be that different contrast injection protocols lead to different CT value intervals between non-contrast and contrast scans. These intervals need to be analyzed individually and the threshold adjusted accordingly.

Using VNC or CTA for EAT volume measurement both pursue the same goal: To obviate the pre-contrast phase and thus reduce radiation dose, acquisition time, and cost. In our study, TNC on average accounted for 13% of $CTDI_{vol}$ and DLP of the combined TNC and CCTA study, according to which a radiation dose reduction of approximately this percentage might be possible using the CTA or VNC approach. Processing of spectral CTA data promises the possibility for comprehensive diagnostic with minimal effort. The inherent enormous potential for many applications, such as monoenergetic imaging for artifact reduction, VNC series for calcium scoring, pure lumen for stenosis analysis or iodine maps to measure iodine concentration, just to name a few, has already been evaluated for the most part in a number of studies.[50,143,144] This study shows that $VNC_{pc}$ reconstructions derived from PCD-CCTA datasets can reliably be used as a substitute for TNC to quantify EAT volume. In summary, the inherent spectral information obtained from PCD-CT scans should be used to the maximum extent to optimize each examination for the best possible diagnostic performance in each individual patient.

Of course, this study has its limitations: First, this study was carried out retrospectively and single-centered. Its findings must be confirmed by larger multi-centric studies. Second, only the two currently at our CT scanner available VNC algorithms were evaluated and future adjustments of the algorithms (e.g. by implementing the differentiation of water and fat) might lead to even more accurate results. Third, the possibility to adjust the upper threshold for quantifying the EAT volume on VNC or CCTA series was not fully exploited and might yield more consistent measurements.

## Conclusion

In conclusion, novel $VNC_{pc}$ series derived from PCD-CCTA datasets can be used to assess

EAT with consistent results with only minimal deviations to reference TNC and superior results compared to conventional $VNC_{conv}$ or CCTA series. Using $VNC_{pc}$ as a substitute for TNC might significantly reduce the applied radiation dose for the individual patient.

### 4.2.2 Optimal Contrast Phase for VNC Reconstruction

**Multiphase photon counting detector CT data sets - which combination of contrast phase and virtual non-contrast algorithm is best suited to replace true non-contrast series in the assessment of active bleeding?**

Franka Risch*, Stefanie Bette*, Andrea Sinzinger, Katharina Rippel, Christian Scheurig-Münkler, Thomas Kröncke, Josua Decker

* = contributed equally

The study was published in the European Journal of Radiology in September 2023.[145] The author FR carried out the data collection and interviews, performed the interpretation and statistical analysis of the data, and was equally involved in writing the manuscript.

#### Abstract

*Objectives:* Aim of this study was to determine which VNC reconstruction algorithm, applied to which contrast phase of CTA, best matches TNC images in the assessment of active bleeding.

*Methods:* Patients who underwent a triphasic scan (pre-contrast, arterial and portal venous contrast phase) on a PCD-CT (120 kV, image quality level of 68) with suspected active (tumor, postoperative, spontaneous or other) bleeding were retrospectively included in this study. Conventional ($VNC_{conv}$) and a novel calcium-preserving VNC ($VNC_{pc}$) algorithm were derived from both arterial ($^{art}$) and portal venous ($^{pv}$) contrasted scans, and analyzed quantitatively and qualitatively by two independent and blinded raters.

*Results:* 40 patients (22 female, mean age 76 years) were retrospectively included. Measurements of CT values showed significant albeit small differences between TNC and VNC for most analyzed tissue regions without clear superiority of a VNC algorithm or CTA contrast phase (e.g. $\Delta$HU in fat between TNC and $VNC_{pc}^{pv}$ 3.1 HU). However, qualitative analysis showed a preference to VNC reconstructions derived from portal venous phase with the calcium sensitive reconstruction algorithm ($VNC_{pc}^{pv}$) in terms of image quality (on a 5-point Likert scale $VNC_{conv}^{art}$ = 3.5 $\pm$ 0.8, $VNC_{pc}^{art}$ = 3.7 $\pm$ 0.7, $VNC_{conv}^{pv}$ = 3.7 $\pm$ 0.7, $VNC_{pc}^{pv}$ = 3.8 $\pm$ 0.7) and residual calcium contrast ($VNC_{conv}^{art}$ = 3.0 $\pm$ 0.8, $VNC_{pc}^{art}$ = 3.5 $\pm$ 0.7, $VNC_{conv}^{pv}$ = 3.6 $\pm$ 0.7, $VNC_{pc}^{pv}$ = 3.9 $\pm$ 0.6).

*Conclusions:* When multiple post-contrast phases are available (e.g. in the setting of active bleeding), $VNC_{pc}$ series based on portal venous CTA are the most suitable replacement for an additional pre-contrast scan, with the prospect of a significant reduction in patient radiation dose.

#### Introduction

Active bleeding is an emergency that requires immediate action.[146,147] Causes and locations can vary, but active bleeding is suspected because of a drop in hemoglobin or circulatory symptoms.[148,149] A fast and reliable diagnosis is essential, not only to locate the bleeding site but to evaluate potential therapy options.[150] Therefore, imaging must be rapidly available and

accurate.[151] CT fulfills all requirements, especially in emergency setting, and is non-invasive. Several studies proved the usefulness and accuracy of CTA for hemorrhage detection.[147, 151–154] Multiphase protocols are recommended, with at least one arterial phase after contrast injection, often supplemented by a portal venous or even late phase.[118] A pre-contrast phase is needed to avoid false positive findings due to pre-existing hyperdense material, such as calcifications, sutures, or other foreign bodies.[151, 155]

CT as imaging modality always comes with the disadvantage of radiation dose exposure which must be kept as low as reasonably achievable. Common approaches for dose reduction include (ultra) low-dose scans, automated tube potential adaption or IR methods.[156–158] Particularly for multiphase scan protocols, the obvious suggestion is to reduce the number of phases. Using spectral CT data, which are inherently provided by PCD technology, several post-processing possibilities have become feasible, including the reconstruction of VNC images from contrast-enhanced series.[7–9, 13, 22, 116] By now, our institute has two algorithms available for creating VNC series, the conventional ($VNC_{conv}$) and the PureCalcium ($VNC_{pc}$). Both perform a material differentiation into water and iodine to create the non-contrast perception in the water image. Since calcium shares a similar attenuation behavior with iodine, it is partly removed from the water image resulting in reduced calcium contrast. $VNC_{pc}$ was specifically designed to counteract and therefore creates a calcium mask before water-iodine material differentiation to prevent from incorrect subtraction and preserve full calcium contrast.

This study sought to analyze the possibility of substituting a pre-contrast phase in case of suspected acute bleeding with a virtual non-contrast series reconstructed from PCD-CT raw data. Therefore, the suitability of both, arterial and portal venous phases, and the two different algorithms for VNC reconstruction were quantitatively and qualitatively analyzed and evaluated to identify the most suitable combination.

## Materials and Methods

*Study Population*

The institutional review board approved the protocol for this retrospective single-center study (Ludwig-Maximilian-University Munich, project number 22-0456) with a waiver for written informed consent. Consecutive patients with a clinically indicated CT scan for the detection of a suspected acute thoracoabdominal bleeding on a novel PCD-CT (NAEOTOM Alpha, Siemens Healthcare GmbH, Erlangen, Germany) between 07/2021 and 05/2022 were retrospectively included. Inclusion criteria were: (1) Age $>$ 18 years; (2) Triphasic CT-scan, including pre-contrast, arterial and portal venous contrast phase; (3) Availability of the respective raw CT-data for image reconstruction.

*Data Acquisition*

The PCD has a collimation of 144 x 0.4 mm. All patients received a pre-contrast scan followed by two contrast-enhanced scans at arterial (bolus tracking aorta +10 s) and portal venous (+75 s) phases. In all phases, scans were performed with a pitch of 0.8 and a tube voltage of 120 kVp. The reference tube current time product was automatically adjusted by setting the image quality

level to 68 for all phases. The contrast injection protocol included 120 ml nonionic iodinated contrast material (Ultravist 300 mgI/ml, Bayer Vital GmbH, Leverkusen, Germany), followed by 20 ml of saline chaser, both at a flow rate of 5.0 ml/s.

*Image Reconstruction*

Image reconstructions were performed on a dedicated workstation (ReconCT, Version 15.0.58331.0, Siemens Healthcare GmbH, Erlangen, Germany). Virtual monoenergetic images at 70 keV were reconstructed from pre-contrast (TNC), arterial ($CTA^{art}$) and portal venous ($CTA^{pv}$) phases. Virtual non-contrast series were reconstructed from both CTA contrast phases, by means of two different algorithm mechanisms ($VNC_{conv}$ and $VNC_{pc}$). Both algorithms perform a material decomposition into water and iodine to achieve the non-contrast impression, but the PureCalcium algorithm ($VNC_{pc}$) takes further measures to preserve full calcium contrast within the water image. A more detailed description of the new $VNC_{pc}$ algorithm has been described previously.[7] The quantitative kernel Qr40 with a quantum IR algorithm at strength 3 and a slice thickness/ increment of 1.5/ 1.0 mm was used throughout for all series.

*Image analyses*

Image analyses were performed on a dedicated workstation (Deep Unity version 1.1.0.1, Dedalus Healthcare GmbH, Bonn, Germany). For quantitative evaluation, ROIs with 15 mm diameter were placed in the abdominal aorta, liver, spleen, subcutaneous fat and muscle on $CTA^{art}$ and synchronized on $CTA^{pv}$, TNC and VNC series. The mean CT value and its SD in HU were measured for each ROI and series. As different scan ranges were considered, not all measurements could be collected for each patient. For qualitative analyses two experienced radiologists (C.SM. and K.R.) with 16 and 6 years of experience in emergency CT and endovascular treatment of acute bleeding were presented with three non-contrast series, the TNC and the two VNC series ($VNC_{conv}$ and $VNC_{pc}$), and two CTA series in arterial and the portal venous phase ($CTA^{art}$ and $CTA^{pv}$). The non-contrast series were in random order and all identifying labels, concerning patient or reconstruction, were removed. Each rater evaluated every patient of the cohort twice, once with the two virtual non-contrast series derived from arterial ($VNC^{art}$) and once from portal venous ($VNC^{pv}$) phase. The questionnaire included questions about the effective contrast media subtraction, general image quality and residual calcium contrast of the non-contrast image series (compare with Table 4.17). Answers were assessed in a five-point Likert scale, ranging from 1 - poor to 5 - excellent. All questions were posed for each of the randomly ordered non-contrast series (TNC, $VNC_{conv}$, $VNC_{pc}$) and for both CTA contrast phases from which the VNC series ($VNC^{art}$, $VNC^{pv}$) were derived.

*Statistical Analyses*

Python (version 3.9.7) was used for statistical analyses. Normal distribution was tested with the Shapiro Wilk test. According to the results, the paired t-test or the Wilcoxon signed rank test was used to assess differences in parametric or non-parametric data respectively. In case of multiple comparisons, p-values were adjusted with the Bonferroni method. Binary data are presented in frequency (proportions) and continuous data as mean $\pm$ SD or median (interquartile range) for parametric and non-parametric data, respectively. P-values $< .05$ were considered to

| Question | Answer Possibilities |
|---|---|
| Contrast medium subtraction | 1 = no contrast medium subtraction<br>2 = large portions of residual contrast medium<br>3 = moderate residual contrast medium<br>4 = minimal focal contrast medium spots<br>5 = no residual contrast medium |
| Overall image quality | 1 = no diagnostic quality<br>2 = significantly limited diagnostic quality<br>3 = slightly limited diagnostic quality<br>4 = no significant limitation in diagnostic quality<br>5 = highest diagnostic quality |
| Residual calcium contrast | 1 = no preservation of calcium contrast<br>2 = minimal preservation of calcium contrast<br>3 = moderate preservation of calcium contrast<br>4 = predominantly preservation of calcium contrast<br>5 = complete preservation of calcium contrast |

**Table 4.17:** Subjective analysis questionnaire. Answers were assessed in a five-point Likert scale, ranging from 1 - poor to 5 - excellent.

indicate statistical significance.

## Results

*Patient Baseline Characteristics*

49 patients were preliminarily enrolled. Thereof 8 patients lacked either the pre-contrast, the arterial or the portal-venous phase, and for one patient the raw data for image reconstruction was not available. The final cohort consisted of 40 patients (22 female, mean age 76 years) with suspected acute bleeding, of whom 10 (25%) were diagnosed positive. Indications were postoperative/ interventional (n = 17 (42.5%)), tumor (n = 9 (22.5%)), spontaneous bleeding (n = 9 (22.5%)), or other (n = 5 (12.5%)). Scan ranges covered chest (n = 9 (22.5%)), chest/ abdomen (n = 2 (5%)), abdomen (n = 17 (42.5%)), abdomen/ pelvis (n = 12 (30%)). $CTDI_{vol}$ and DLP for the pre-contrast scan was 265 (184 - 356) mGy and 5.4 (4.6 - 7.1) mGy*cm, corresponding to a proportion of 39 (33 - 42)% and 41 (33 - 42)% of all three phases. For arterial and portal venous phase $CTDI_{vol}$ was measured to 174 (113 - 257) mGy and 245 (157 - 325) mGy and DLP to 4.4 (2.9 - 5.4) mGy*cm and 5.7 (3.8 - 7.1) mGy*cm. Table 4.18 summarizes the baseline study characteristics.

*Quantitative Series Comparison*

Table 4.19 gives an overview of the measured mean CT values of the ROIs within the different tissue types on the various reconstruction series. Almost all measurements on VNC reconstructions differed significant from TNC (p-values $< .05$), regardless of the contrast phase of the underlying CTA or the applied algorithm. Absolute differences to corresponding CTA and TNC are visualized in Figure 4.26. The graph in A demonstrating VNC$-$CTA measurements, shows

| | | | |
|---|---|---|---|
| Total n = 40 | | | |
| Patient characteristics | | | |
| Age [years] | 76 (69 - 82) | | |
| Sex [female] | 22 (55%) | | |
| BMI [kg/m$^2$] | 25.4 $\pm$ 5.3 | | |
| CT radiation dose | TNC | CTA$^{art}$ | CTA$^{pv}$ |
| $CTDI_{vol}$ [mGy] | 5.4 (4.6 - 7.0) | 4.4 (2.9 - 5.4) | 5.7 (3.8 - 7.1) |
| DLP [mGy*cm] | 265 (184 - 356) | 174 (113 - 257) | 245 (157 - 325) |
| SSDE [mGy] | 6.9 (6.1 - 9.0) | 5.5 (3.9 - 7.2) | 7.1 (5.3 - 9.7) |
| Effective mAs | 69 (59 - 90) | 55 (36 - 68) | 72 (47 - 90) |

**Table 4.18:** Baseline study characteristics.

Values are mean $\pm$ SD, median (interquartile range), or frequency (percentage). $^{art}$ = derived from arterial phase, CTA = computed tomography angiography, $CTDI_{vol}$ = volumetric CT dose index, DLP = dose length product, $^{pv}$ = derived from portal venous phase, SSDE = size specific dose estimate.

| | | liver (29) | aorta (35) | spleen (25) | fat (39) | muscle (40) |
|---|---|---|---|---|---|---|
| Mean CT values | TNC | 57.1 $\pm$ 8.7 | 37.3 $\pm$ 9.4 | 51.5 $\pm$ 5.5 | -91.2 $\pm$ 15.4 | 43.2 $\pm$ 11.9 |
| | CTA$^{art}$ | 70.4 $\pm$ 11.3 | 394.9 $\pm$ 122.4 | 99.1 $\pm$ 27.1 | -90.7 $\pm$ 14.0 | 46.4 $\pm$ 12.8 |
| | $VNC^{art}_{conv}$ | 53.2 $\pm$ 7.7 | 22.9 $\pm$ 10.9 | 47.4 $\pm$ 7.1 | -75.2 $\pm$ 12.3 | 45.5 $\pm$ 11.4 |
| | | p = 0.04 | p $<$ 0.01 | p = 0.07 | p $<$ 0.01 | p = 0.05 |
| | $VNC^{art}_{pc}$ | 50.6 $\pm$ 7.4 | 23.2 $\pm$ 10.4 | 46.2 $\pm$ 6.9 | -91.3 $\pm$ 13.4 | 38.7 $\pm$ 12.1 |
| | | p $<$ 0.01 | p $<$ 0.01 | p = 0.01 | p = 1 | p $<$ 0.01 |
| | CTA$^{pv}$ | 116.0 $\pm$ 25.8 | 179.6 $\pm$ 34.5 | 125.6 $\pm$ 22.8 | -87.5 $\pm$ 15.1 | 54.0 $\pm$ 13.3 |
| | $VNC^{pv}_{conv}$ | 52.9 $\pm$ 8.7 | 24.1 $\pm$ 6.5 | 47.2 $\pm$ 7.8 | -74.1 $\pm$ 12.9 | 46 $\pm$ 11.9 |
| | | p = 0.09 | p $<$ 0.01 | p = 0.05 | p $<$ 0.01 | p = 0.06 |
| | $VNC^{pv}_{pc}$ | 52.5 $\pm$ 8.7 | 24.2 $\pm$ 6.6 | 47.1 $\pm$ 8.0 | -88.1 $\pm$ 14.6 | 41.9 $\pm$ 12.3 |
| | | p = 0.04 | p $<$ 0.01 | p = 0.06 | p $<$ 0.01 | p = 0.76 |

**Table 4.19:** Measured mean CT values within the different organs and tissue types on the respective reconstruction. The number of possible measurements, limited by availability within the scan area, is given in parentheses for each tissue type. The Bonferroni corrected p-values given for VNC series refer to the differences to the TNC series.

Values are shown as mean $\pm$ SD. $^{art}$ = derived from arterial phase, CTA = computed tomography angiography, $^{pv}$ = derived from portal venous phase, TNC = true non-contrast, VNC = virtual non-contrast ($_{conv}$ = conventional, $_{pc}$ = PureCalcium).

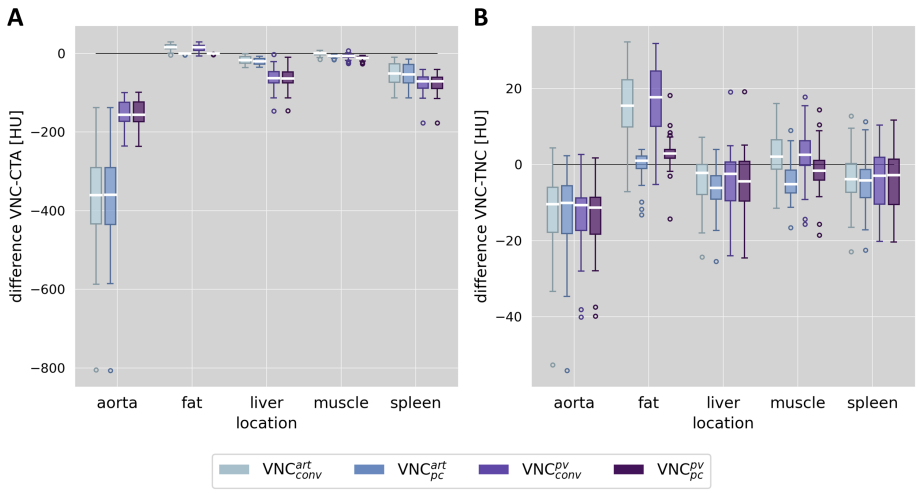


**Figure 4.26:** Boxplots of the differences in CT values comparing the VNC with **A** the corresponding CTA (VNC−CTA) and **B** the TNC reconstruction (VNC−TNC).
$^{art}$ = derived from arterial phase, CTA = CT angiography, $^{pv}$ = derived from portal venous phase, TNC = true non-contrast, VNC = virtual non-contrast ($_{conv}$ = conventional, $_{pc}$ = PureCalcium).

the expected influence of the contrast phases on the amount of virtually subtracted contrast agent, and only a minor influence of the VNC algorithm used. In B differences VNC−TNC are visualized. The greatest differences were observed within fat for $VNC_{conv}$ with an overestimation of mean CT values compared to TNC of approximately 16 HU. For the aorta both algorithms showed lower mean CT values than TNC in both contrast phases (approximately -11 HU on average). For all other measurement sites (liver, muscle, spleen) only minor differences to TNC were observed.
SD in CT values, as an indicator for image noise is presented in Table 4.20. Noise was reduced on VNC reconstructions compared to the underlying CTA, reaching levels similar to TNC.

*Qualitative Series Comparison*
Qualitative series ratings are visualized in Figure 4.27. Regarding virtual subtraction of contrast media $VNC^{art}$ reconstructions were preferred to $VNC^{pv}$ reconstructions and achieved 'excellent' assessment in 74% of the cases. In terms of image quality, there was a slight preference for $VNC^{pv}_{pc}$ reconstruction ('adequate' or better in 99%) over the other VNC algorithm ('adequate' or better in 97%) or the other CTA contrast phase ('adequate' or better in 90% for $VNC^{art}_{conv}$ and 96% for $VNC^{art}_{pc}$). More distinct differences between VNC algorithms and CTA contrast phases can be observed with respect to residual calcium contrast. $VNC^{art}_{conv}$ reconstructions were rated 'insufficient' or even 'poor' in 25% of cases, whereas $VNC^{pv}_{pc}$ reconstructions were rated 'good' or 'excellent' in 80% of cases.
Figure 4.28 shows an example of a patient with abdominal bleeding and illustrates the value of $VNC_{conv}$ and $VNC_{pc}$ reconstructions derived from arterial, and portal venous phase compared to TNC.

| | | liver (29) | aorta (35) | spleen (25) | fat (39) | muscle (40) |
|---|---|---|---|---|---|---|
| SD CT values | TNC | 16.5 ± 2.3 | 19.2 ± 4.2 | 16.8 ± 1.8 | 16.6 ± 4.7 | 19.0 ± 4.9 |
| | $CTA^{art}$ | 19.3 ± 3.0 | 27.9 ± 11.3 | 22.2 ± 4.0 | 17.8 ± 3.5 | 20.2 ± 4.3 |
| | $VNC^{art}_{conv}$ | 16.9 ± 2.5 | 20.6 ± 3.7 | 16.6 ± 2.0 | 18.6 ± 3.6 | 17.1 ± 3.2 |
| | | p = 1 | p = 0.08 | p = 1 | p = 0.01 | p < 0.01 |
| | $VNC^{art}_{pc}$ | 17.3 ± 2.2 | 22.5 ± 4.1 | 17.9 ± 2.1 | 17.3 ± 3.1 | 18.0 ± 3.7 |
| | | p = 0.11 | p < 0.01 | p = 0.03 | p = 0.79 | p = 0.2 |
| | $CTA^{pv}$ | 19.5 ± 4.1 | 22.1 ± 6.0 | 20.0 ± 4.2 | 17.4 ± 4.0 | 19.7 ± 4.4 |
| | $VNC^{pv}_{conv}$ | 15.9 ± 2.9 | 17.8 ± 3.3 | 16.0 ± 3.0 | 17.8 ± 4.2 | 16.0 ± 3.7 |
| | | p = 1 | p = 0.22 | p = 0.69 | p = 0.21 | p < 0.01 |
| | $VNC^{pv}_{pc}$ | 17.3 ± 3.2 | 19.8 ± 4.4 | 17.6 ± 3.1 | 16.9 ± 3.7 | 16.8 ± 3.8 |
| | | p = 0.63 | p = 1 | p = 0.63 | p = 1 | p < 0.01 |

**Table 4.20:** Measured SD of CT values within the different organs and tissue types on the respective reconstruction. The number of possible measurements, limited by availability within the scan area, is given in parentheses for each tissue type. The Bonferroni corrected p-values given for VNC series refer to the differences to the TNC series.

Values are shown as mean ± SD. $^{art}$ = derived from arterial phase, CTA = computed tomography angiography, $^{pv}$ = derived from portal venous phase, TNC = true non-contrast, VNC = virtual non-contrast ($_{conv}$ = conventional, $_{pc}$ = PureCalcium).

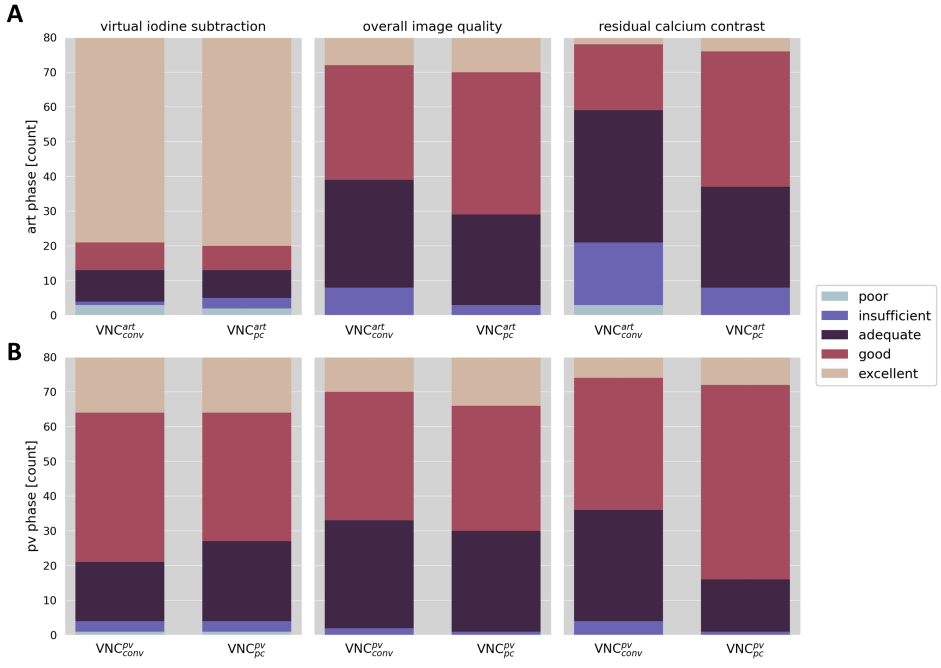


**Figure 4.27:** Subjective image analysis regarding the effectiveness of virtual iodine subtraction, overall image quality and residual calcium contrast in TNC, $VNC_{conv}$ and $VNC_{pc}$ images reconstructed from CTA of both, **A** arterial and **B** portal venous contrast phases.

$^{art}$ = derived from arterial phase, CTA = CT angiography, $^{pv}$ = derived from portal venous phase, TNC = true non-contrast, VNC = virtual non-contrast ($_{conv}$ = conventional, $_{pc}$ = PureCalcium).

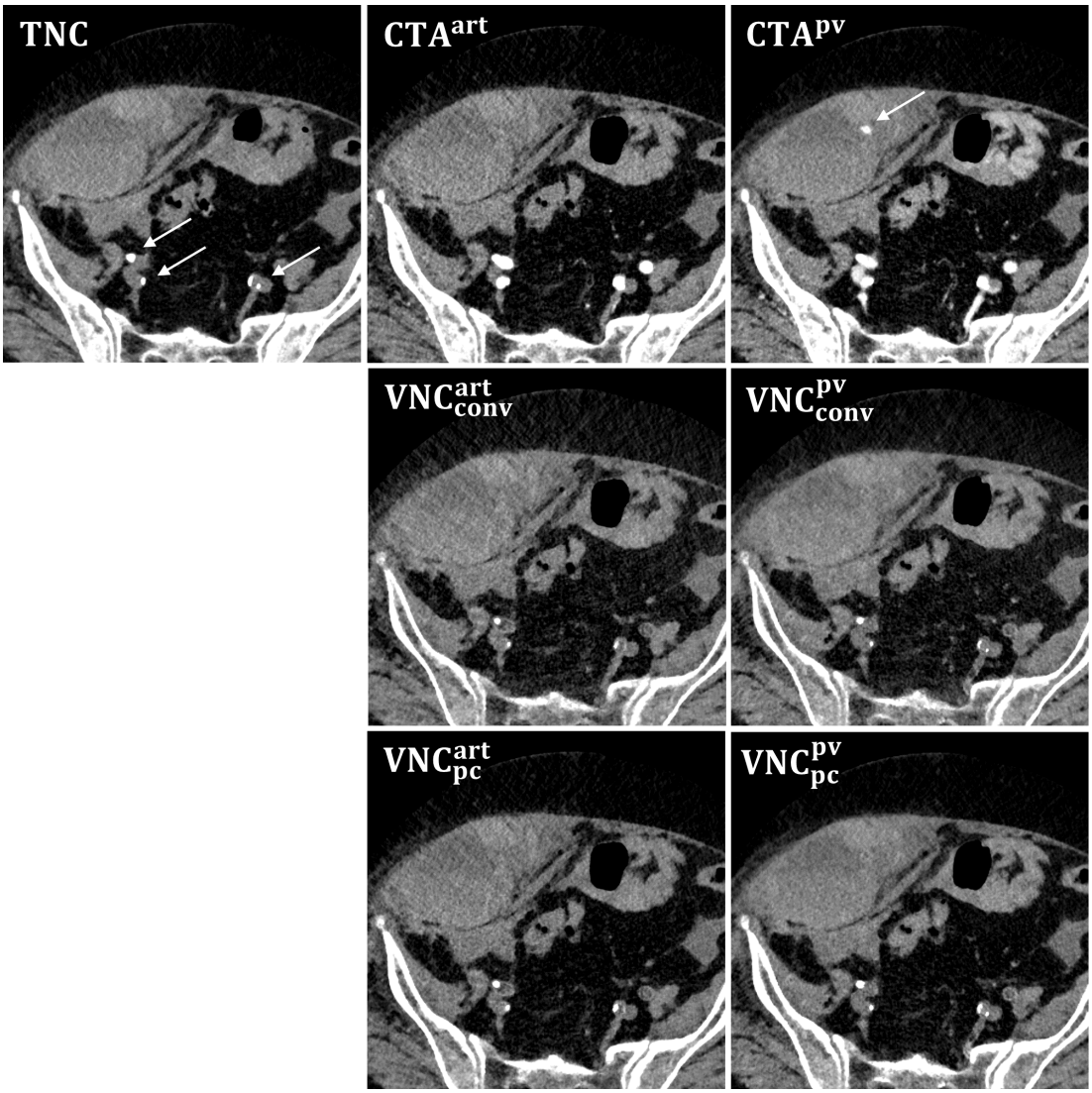


**Figure 4.28:** Example of a patient with active bleeding (shown as contrast extravasation in portal venous phase) in the right abdominal wall. TNC as well as $VNC_{conv}$ and $VNC_{pc}$ images reconstructed from CTA of both, arterial and portal venous contrast phases. Calcium (shown in TNC) was not subtracted in all VNC reconstructions.

$^{art}$ = derived from arterial phase, CTA = CT angiography, $^{pv}$ = derived from portal venous phase, TNC = true non-contrast, VNC = virtual non-contrast ($_{conv}$ = conventional, $_{pc}$ = PureCalcium).

## Discussion

In this retrospective study, two different algorithms for generating VNC series from spectral CTA data derived from PCD-CT in two contrast phases were analyzed for their suitability to replace the TNC series in the setting of assessment of acute hemorrhage. Our main finding is that VNC series from portal venous scans using the calcium-sensitive PureCalcium algorithm are best suited to replace the TNC scan. These reconstructions were superior in both qualitative and quantitative analysis. Replacing the TNC series with $VNC_{pc}^{pv}$ has the potential to reduce the applied radiation by more than a third.

For the diagnosis of active bleeding, multiphasic CT is recommended and includes a pre-contrast scan and post-contrast scans in arterial and portal venous contrast phases (sometimes also later contrast phases).[118] These three or even four CT scans imply a high radiation dose.[159,160] Therefore, it is important to find ways to reduce radiation dose without degrading image quality and diagnostic confidence in an emergency setting. Previous studies on DECT showed that VNC can safely replace TNC in the setting of active gastrointestinal bleeding and pointed out the dose-saving potential.[139,161,162] Recently, PCD-CT has been introduced into clinical routine, which inherently acquires spectral data with each scan. Similar to dual-energy-based methods, this allows several post-processing steps such as virtual subtraction of iodinated contrast agents with the detector-dependent advantage of eliminated electronic noise and improved spatial resolution.[22] In addition, unlike dual-source solutions, PCD-CT is not restricted in FoV, which is especially important for obese, as has been demonstrated in oncology imaging.[163] Recent studies assessed the value of VNC and the accuracy and image quality on a PCD-CT.[13] Studies showed a benefit for abdominal imaging,[141,164] for cardiac and vascular imaging[7–9] and for lung imaging.[165] To our knowledge, there are no previous studies on PCD-CT that have quantitatively and qualitatively analyzed the most appropriate contrast phase or VNC reconstruction algorithm in the setting of active bleeding.

In the present study, we analyzed the value of $VNC_{conv}$ and $VNC_{pc}$, derived from both, arterial and portal venous contrast phase CTA quantitatively and qualitatively compared to TNC. Quantitative analyses showed significant differences between TNC and VNC for almost all analyzed CTA contrast phases and VNC algorithms. For most sites (aorta, liver, spleen) both algorithms performed similarly, except for fat where $VNC_{conv}$ overestimated CT values six times more than $VNC_{pc}$. Overall, however, there was no clear superiority of one algorithm or one CTA contrast phase over the other. Image noise was reduced in the VNC reconstructions compared to the CTA originals, reaching levels equivalent to TNC noise.

While $VNC^{art}$ was rated 'excellent' regarding the virtual iodine subtraction more often, $VNC^{pv}$ received more positive agreement for overall image quality and residual calcium contrast. This goes in line with a previous study performed on dual-energy CT, which showed that VNC derived from portal venous contrast phase represents TNC scans more accurately than VNC from arterial contrast phase.[166] Furthermore, when comparing the VNC algorithms, $VNC_{pc}$ tended to be rated better. A previous study pointed out the benefit of this novel calcium-preserving

algorithm in the analysis of vessels after endovascular aneurysm repair.[9] The results therefore suggest $VNC_{pc}$ as a promising new algorithm. Thus, $VNC_{pc}^{pv}$ seems the most adequate replacement for TNC in the context of acute bleeding assessment.
This study has limitations. First, its retrospective single-center study design. Second, this study includes a relatively small cohort - further multicenter studies with larger cohorts should be performed to confirm these findings. Third, the different scan ranges limited the number of possible quantitative measurement sites. Fourth, the scan ranges of the arterial and portal-venous acquisitions were smaller than those of the TNC series because they were adjusted after the initial evaluation. Therefore, the exact dose that could be saved by omitting the TNC series cannot be calculated with the data used. Fifth, as only 25% (n = 10) of patients showed visible contrast extravasation, we did not evaluate the diagnostic performance in the assessment of active bleeding.

## Conclusion

When both arterial and portal venous phases are available, VNC reconstructions using the Pure-Calcium algorithm derived from the portal venous contrast CTA are most suitable for replacing TNC in the assessment of active bleeding. Replacing the TNC has the potential to reduce the applied dose by up to one-third. Further (prospective) studies are needed to prove the diagnostic accuracy and applicability of this method in clinical routine.

### 4.2.3 Discrimination of Hemorrhage and Iodinated Contrast Media

## Discrimination of Hemorrhage and Contrast Media in a Head Phantom on Photon-Counting Detector CT Data

Franka Risch, Ansgar Berlis, Thomas Kröncke, Florian Schwarz*, Christoph Maurer*

* = contributed equally

The study was published in the American Journal of Neuroradiology in December 2023.[14] The author FR was equally involved in the experiments for data generation, performed data collection, interpretation and statistical analyses and wrote the manuscript.

### Abstract

*Objective:* Evaluation of the potential of PCD-CT for the discrimination of hemorrhage and contrast media at various concentrations and the determination of the contrast media density.

*Methods:* Samples including blood, glucose, sodium chloride and contrast media with concentrations from 0 to 6 mg iodine per ml were placed at the center, anterior and lateral aspects of an anthropomorphic head phantom. Additionally, another set of samples without blood was analyzed for reference. Scans were performed with a standard clinical cranial CT protocol on a PCD-CT and spectral thin sliced image series were reconstructed using a quantitative regular kernel (Qr40). Measurements, including the iodine concentration, as well as mean and standard deviation of CT values for the contrast media map (CM), virtual monoenergetic image at 70 keV (ME70) and virtual non-contrast image (VNC), were taken by placing regions of interest within the samples on several different slices.

*Results:* Measurements showed precise discrimination of contrast media and blood with rising CT values on CM and ME70 and constant CT values on VNC for increasing iodine concentrations. Linear regression analysis showed perfect correlation of intended to measured iodine concentration ($r^2$ = 1.0), albeit with an underestimation for high contrast media densities (slope = 0.9, max underestimation of -0.6 mg/ml at 6 mg/ml intended iodine concentration).

*Conclusions:* This in-vitro study demonstrated that PCD-CT allows for reliable discrimination of hemorrhage and contrast media including the density determination of the latter for various iodine concentrations. The technology promises to add value in several applications within neuroimaging.

### Introduction

In recent years the field of intracranial endovascular intervention has gained expertise and application due to the therapeutic benefit the minimally invasive treatment provides.[167] Intracranial interventions, such as recanalization or embolization procedures usually require an unenhanced control CT scan to rule out possible bleeding. However, distinguishing hemorrhage from contrast enhancement that may have passed the blood-brain barrier during the intervention

is challenging due to their similar x-ray attenuation.[168,169]
PCD-CT is a promising technology that has the potential to facilitate the differentiation between contrast media enhancement and hemorrhage following neurointerventional procedures in clinical routine. This scanner inherently acquires spectral information that allow for post-processing steps including material differentiation.[22] Accordingly, a CT scan can be separated into the attenuation resulting from remaining iodine and soft tissue, generating contrast media (CM) maps and VNC series. The instant availability of this information promises to improve the diagnostic confidence and the associated therapeutic decision.
The purpose of this in-vitro study was to evaluate the ability of PCD-CT to precisely distinguish between blood and iodine at various iodine concentrations including the accurate determination of the contrast media density within an anthropomorphic head phantom.

## Materials and Methods

*Phantom*
The phantom used in this study replicates the human brain anatomy and comprises brain-equivalent tissue with constant CT values, surrounded by high x-ray absorbing structures that simulate the skull and temporal bones (PFO-Kalotte, Quality assurance in Radiology and Medicine GmbH, Möhrendorf, Germany). Additionally, three cylindric holes at the center, anterior and lateral aspects, directly beneath the skull, allow for inserts.

*Insert Composition*
Iodine concentrations from 0 to 6 mg/ml with 1 mg/ml increments were included in this study. As a reference, one series of concentrations consisted solely of iodine (30 mg/ml) and sodium chloride (0.9%). The second series was designed to represent the actual clinical scenario of iodine mixed with blood. To simulate blood, red cells from an outdated blood donation were diluted with glucose (40%) and mixed with iodine and sodium chloride in a constant ratio (two shares of blood, one share of glucose, one share of iodine diluted with sodium chloride). All solutions were adjusted to a total volume of 120 ml to fill the whole of the phantom with a stand-off on both sides.

*CT Protocol*
All samples were scanned on a novel PCD-CT (NAEOTOM Alpha, Siemens Healthcare GmbH, Erlangen, Germany) with a standard clinical cranial CT protocol at all three phantom insert positions, respectively. Scans were acquired single source at a tube voltage of 120 kVp in spiral mode with a pitch of 0.55. The image quality level was set to 280 and the single/ total collimation was 0.4/ 38.4 mm.

*Image Reconstruction*
Images were iteratively reconstructed (Q2, quantum iterative reconstruction, QIR, Siemens Healthcare GmbH) on the scanner console (version VA50A) using a quantitative regular kernel (Qr40). Spectral post-processing (SPP) series were generated to fully preserve spectral image information for further analyses. Slice thickness/ increment were set to 1.0/ 0.4 mm.

*Image Analysis*

Image analysis was performed on a dedicated workstation (syngo.via, version VB70A, Siemens Healthcare GmbH) in dual-energy workflow (virtual unenhanced application profile). Four different axial slice positions were considered, two within and two out of the temporal bone section, approximately equally distributed from cranial to caudal direction (see Figure 4.29). Circular ROIs with a constant area of 3.5 $cm^2$ were positioned centrally within the inserts excluding possible air bubbles. Next to the positions anterior (A), central (C) and left (L), two further reference measurements were taken, posterior ($R_{posteriror}$) and right ($R_{right}$), which were placed symmetrically to the rotation axis. The calculated iodine concentration in mg/ml, as well as mean and SD of CT values in HU for the contrast media map (CM), the virtual monoenergetic image at 70 keV (ME70) and the virtual non-contrast (VNC) image were recorded. The noise level was defined as the SD of CT values measured within the reference ROIs ($R_{posteriror}$ and $R_{right}$).

*Statistical Analyses*

Statistical analyses were conducted using python (version 3.9). Data were tested for normal distribution using the Shapiro-Wilk test. To assess differences, the paired t-test and the Wilcoxon signed-rank test were used for parametric and non-parametric data, respectively. In case of multiple comparisons, p-values were adjusted using the Bonferroni method. Continuous data are given as mean $\pm$ SD or as median (interquartile range) for parametric or non-parametric data. The accuracy of linear regression analysis was assessed using the coefficient of determination ($r^2$). Statistical significance was set at p-values $< .05$.

## Results

The effective mAs, $CTDI_{vol}$ and DLP were 170 mAs, 30.6 mGy and 533 mGy*cm for each scan respectively.

The general noise level was 3.5 (3.3 - 3.7) HU. All measurements of CT values within the reference and the blood samples are demonstrated in Figure 4.30. The reference probes without blood show low CT values for an intended iodine density of 0 mg/ml of mean 3.8, 13.7 and 9.9 for CM, ME70 and VNC, respectively. With increasing iodine concentrations Hounsfield units of CM and ME70 rise accordingly in  22 HU steps with a significant (all p's $< 0.01$) albeit small constant distance of $< 10$ HU to each other, attributable to the attenuation of the sodium chloride. Meanwhile VNC CT values remain constant around 9 HU. Results from blood-containing probes were even more accurate. At zero iodine concentration, ME70 and VNC showed no significant difference (p = 0.12) and mean CT values on CM were close to 0 HU (-0.9 $\pm$ 1.6 HU). A linear rise of CT values of ME70 and CM was observed with increasing iodine density, but with a larger distance in measurement to each other ( 67 HU) due to the blood attenuation. On VNC, CT values were consistent with smaller standard deviations compared to the non-blood samples.

Figure 4.31 shows the regression analysis between the intended and measured iodine concentrations of the reference samples without blood and the samples with blood and glucose. The

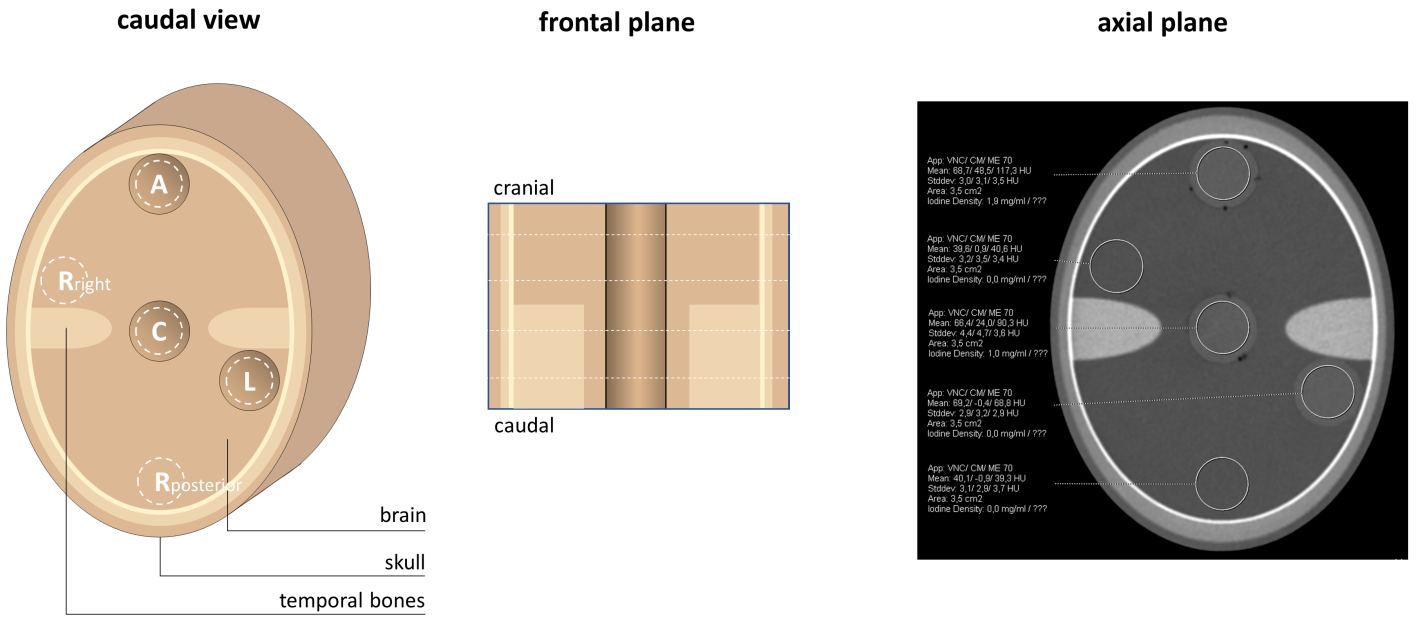


**Figure 4.29:** The schematic structure of the phantom and the respective positions of measurement.
A = anterior, C = central, L = left, $R_{posterior}$ = posterior reference, $R_{right}$ = right reference.

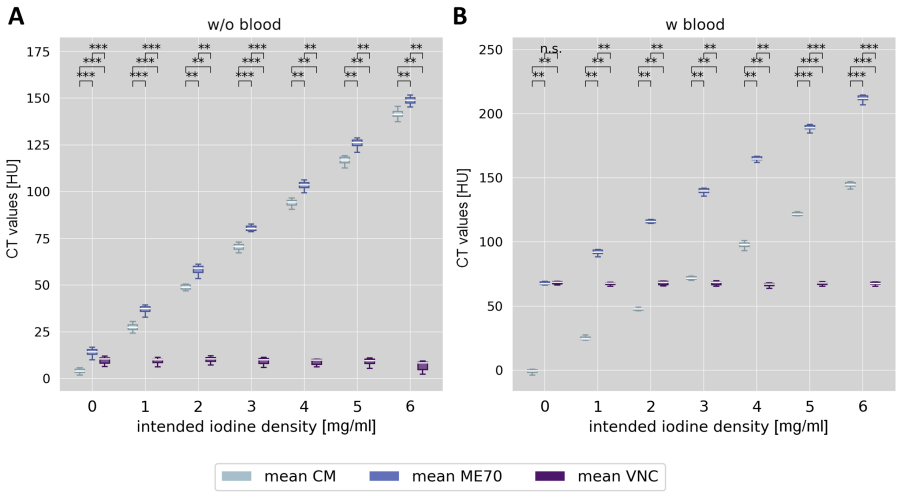


**Figure 4.30:** Measured CT values within the samples on **A** w/o and **B** with blood, at all positions (anterior, center, left) and on all slices (next and above the temporal bone structures) presented in boxplots. CT values are compared between virtual monoenergetic, contrast media map, and virtual non-contrast. Stars mark significant differences as * = $p < .05$, ** = $p < .01$, *** = $p < .001$ and n.s. marks no significant difference.

ME70 = virtual monoenergetic at 70 keV, CM = contrast media, VNC = virtual non-contrast.

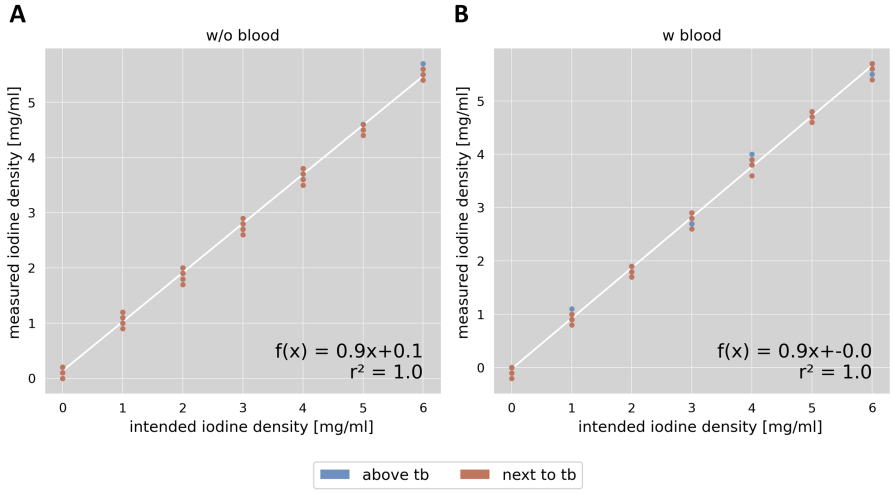


**Figure 4.31:** Linear regression of initial and measured iodine concentration of the samples. On **A** for reference samples w/o and on **B** for samples with blood including all positions (anterior, center, left) and the compared between sections above and next to temporal bone structures.

tb = temporal bone.

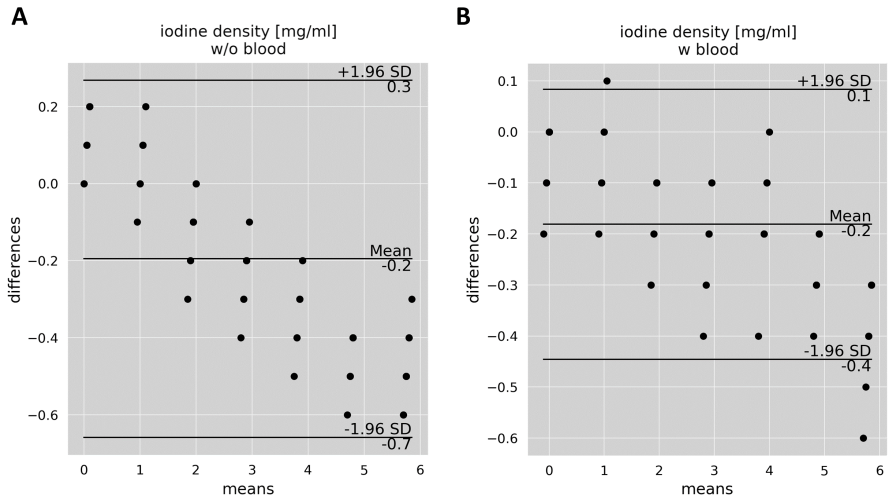


**Figure 4.32:** Bland-Altman plot showing the means and differences between the measured and intended iodine concentration in samples **A** w/o blood and **B** with blood. All positions (anterior, center and left) and sections (above and next to temporal bone structures) are considered.

regression lines demonstrate a perfect linear relationship with an $r^2$ value of 1.0. However, the measured iodine concentrations are slightly underestimated with increasing intended concentration, indicated by the slope of 0.9. ROI positioning above or next to the temporal bone structures showed no influence on the measurement. Figure 4.32 shows that the mean difference between the intended and measured iodine concentrations is of -0.2 mg/ml, which is consistent for both, reference and the blood samples.

## Discussion

In this study, we analyzed several blood samples with iodine concentrations ranging from 0 to 6 mg/ml in an anthropomorphic head phantom and tested the ability of PCD-CT to discriminate contrast media and to determine its exact concentration. We found that the spectral data of PCD-CT provide reliable differentiation between iodine and non-iodine caused attenuation, regardless of the presence of blood or the height of contrast media concentration. Moreover, we demonstrated the feasibility of iodine concentration determination using PCD-CT.

In patients with acute ischemic stroke, the blood-brain barrier disruption can lead to contrast enhancement of the infarcted area in the first few hours following mechanical thrombectomy. Distinguishing between contrast pooling and subarachnoid or parenchymal hemorrhage is crucial for patient management and outcome.[170,171] Additionally, this differentiation is important for other neuro-interventions, such as embolization procedures for aneurysms, arteriovenous malformations, dural arteriovenous fistulas, and, more recently, embolization of the middle meningeal artery for treatment of chronic subdural hematomas.[172–174] During these interventions, hemorrhages can easily occur and must be distinguished from extravasation of contrast media or contrast enhancement.

Computed tomography is the imaging modality of choice since it is widely available and allows for rapid and accurate diagnosis. With conventional single energy CT, however, a differentiation

of blood and contrast media is extremely difficult due to the similar attenuation behavior of x-rays.[12] Spectral information, such as provided by dual-energy CT, allows to perform material decomposition into attenuation shares caused by contrast and non-contrast media[3] and therefore has a wide range of application in neuroradiological interventions.[172] The introduction of photon-counting detector CT into clinical routine provides inherently spectral information and simultaneously overcomes limitations of conventional energy-integrating detectors with higher spatial resolution and absence of electronic noise.[22]

This study used the standard cranial CT protocol for the anthropomorphic head phantom, to achieve dose results comparable to clinical in vivo scans. Analysis of Hounsfield units showed that iodine and blood is clearly distinguishable regardless of the underlying iodine density. Furthermore, material decomposition of iodine and non-iodine shares appears to be more accurate in samples with blood than in reference samples with only sodium chloride. Further, differences of 1 mg/ml in iodine concentration can clearly be differentiated in CT values. The automated calculation of the underlying iodine density shows a perfect linear correlation to the intended one, albeit with an increasing underestimation for higher concentrations. However, these inaccuracies may be partly due to several limitations. First, the accuracy of the instruments used, and possible human error could affect the samples and their intended iodine concentration. Second, a homogeneous distribution of contrast media within the sample's volume could not be guaranteed which might have led to local variation and therefore measurement errors. Third, the experiment is of in-vitro nature and further studies are necessary to translate the results into clinical benefits for patient care.

## Conclusion

In conclusion, PCD-CT demonstrated to be a reliable tool for differentiating between blood and iodine, and accurately determining several iodine concentrations in an anthropomorphic head phantom. These findings suggest the potential of PCD-CT for various applications in neuroimaging. Further studies should investigate the use of PCD-CT for imaging of brain hemorrhage with differentiation between calcification and hemorrhage, prediction of hematoma expansion on unenhanced CT and CT angiography[175] as well as the identification of hemorrhagic tumors in hemorrhages of unknown origin.[176]

## 4.3 Discussion

In this chapter several applications of the reconstructions obtained by the differentiation of iodine and water as basis materials of PCD-CT derived spectral data are presented. The first part deals with the feasibility and influencing factors, such as the patient's BMI, heart rhythm and heart rate, of calcium quantification on VNC series, while the second part examines the quantification of epicardial adipose tissue on VNC, the best TNC substitute in terms of VNC algorithm and CTA contrast phase, and the accurate quantification of iodine concentration. The aim of this discussion is to find common ground between the projects carried out and to incorporate new findings from other studies.

We were able to demonstrate that iodinated contrast was effectively and sufficiently removed from VNC image series. Histogram evaluation of total heart volumes as well as comparison of CT values within different tissues showed significant differences to the original CTA (refer to subsection 4.1.1 and 4.1.2) with tissue dependent small differences to the TNC reconstructions (refer to subsection 4.2.2). Adipose tissue makes a good example to explain the deviations. The material differentiation models into iodine and water which is why fat erroneously results in negative CT values on the iodine map and systematically higher CT values on the water (VNC) image. Our studies showed that this effect is more pronounced for $VNC_{conv}$ than for $VNC_{pc}$ (refer to subsection 4.2.1). Prior studies analyzing VNC reconstructions from the arterial and portal venous phases of PCD-CTA reported similar results (e.g. for spleen and muscle tissue) and in some cases even smaller differences in CT values compared to TNC (e.g. for aorta and liver tissue) and concluded an accurate attenuation and good image quality of VNC reconstructions.[13] However, it was noted that the algorithm requires adjustment and should be used cautiously in clinical practice.[141] In a phantom study it was shown that the error in CT values VNC−TNC was significantly reduced for PCD compared to EID-CT data.[177] Regarding the most appropriate contrast phase of CTA to be used when available, we observed only a slight trend towards the portal venous phase in combination with $VNC_{pc}$ (refer to study in subsection 4.2.2). Rather, the subjective analysis revealed that the suitability of VNC as a TNC substitute depends on the diagnostic question. In the case of active bleeding, in most cases the radiologist is able to detect the bleeding and exclude a possible calcification on the basis of the appearance on CTA. The rare cases where uncertainty remains, require unenhanced series that are 100% reliable.

In all our studies we quantified the noise, partly by analyzing the SD of CT values within specifically placed ROIs, and partly by using the most frequent SD of CT values ('global noise') derived from multiple slices. The latter promises a more comparable and stable approach with less dependence on the reader.[90] Compared to EID-CT, the PCD technology was shown to significantly reduce noise (up to 47%)[5] for several reasons, which are explained in more detail in the Fundamentals section. Apart from the technical details of the acquisition, noise is highly dependent on the settings for radiation dose and reconstruction.[178] In cardiac scans, unenhanced acquisition is mainly used for calcium quantification and therefore has limited

diagnostic use and does not require optimal image quality. At our institute, the unenhanced scan is acquired in flash mode (high pitch spiral), which is associated with a significant reduction in dose compared to (lower pitch) spiral or sequential mode, which is usually used for CTA (compare with e.g. subsection 4.1.4). The differences in dose are reflected in higher noise levels in the TNC series, which we attempted to compensate for by reducing the slice thickness of the VNC reconstructions (in the first two studies presented). For equivalent dose levels, we measured comparable noise on TNC and VNC. Although the SD of CT values as a quantifier of noise is easy to collect, it has limited informative value. Another study, on the other hand, looked at a more meaningful parameter, the noise power spectrum, in which VNC showed a 33% increased noise magnitude and a higher amplitude at low spatial frequencies compared to TNC.[13] Regarding reconstruction settings, we found that a raise in IR strength to result in lower noise levels (kernel Qr36 IR strength 3 vs. 4, refer to subsection 4.1.1). Another study analyzing (non-VNC) abdominal scans even achieved a noise reduction of $> 40\%$ and an improvement of CNR of $> 65\%$ using high levels of IR.[179]

Regarding calcium quantification, an early phantom study on PCD-CT showed that VM reconstructions (e.g. at 70 keV and IR off) resulted in equivalent scores compared to EID scanner reconstructions and further found that the scores were independent of radiation dose (image quality level 20 vs. 80).[180] Our studies are based solely on in-scanner comparisons, focusing on multi-contrast phase acquisitions and the potential of VNC reconstructions as a substitute for additional TNC scans. Therefore, unenhanced examinations reconstructed as VM images were used as reference. Consistent with previous DECT studies, we found a strong linear correlation between VNC-based calcium measures and TNC.[50] As a decisive difference between the two evaluated VNC algorithms, $\text{VNC}_{\text{pc}}$ additionally restores the original calcium contrast. With appropriate reconstruction settings (0.4 mm, Br36, IR level 4, refer to subsection 4.1.1), we achieved CAC values equivalent to TNC on per vessel level with only minor underestimation on a per patient level which is in line with similar studies analyzing the potential of $\text{VNC}_{\text{pc}}$ on PCD-CT.[7] It should be noted that the software version of the scanner console used in this study (VA40) was later updated (to VA50), which further reduced the discrepancies.[68] In terms of heart rate sensitivity, we found no significant dependence of CACS on VNC in our phantom study (refer to subsection 4.1.3). Fink et al. performed a very similar study, differing only in the phantom used and the lack of reference TNC scans.[67] They observed a significant decrease in calcium with increasing heart rate compared to the static VNC-based quantity for their high density insert. However, their results are based on three measurements per heart rate with a single acquisition mode, which limits the value of statistical analysis. Again, comparing VNC to TNC derived Agatston scores, our patient study showed an increased underestimation for heart rates above 69 bpm (refer to subsection 4.1.4). But the reference was naturally also acquired in motion, suggesting that higher discrepancies may result from general increase in variability. Previous studies on TNC-based calcium scores found strong dependencies on heart rate, calcification density and reconstruction settings,[94] others even discourage the use of Agatston scores as they are less reproducible compared to mass scores.[95,181] Obesity is another known

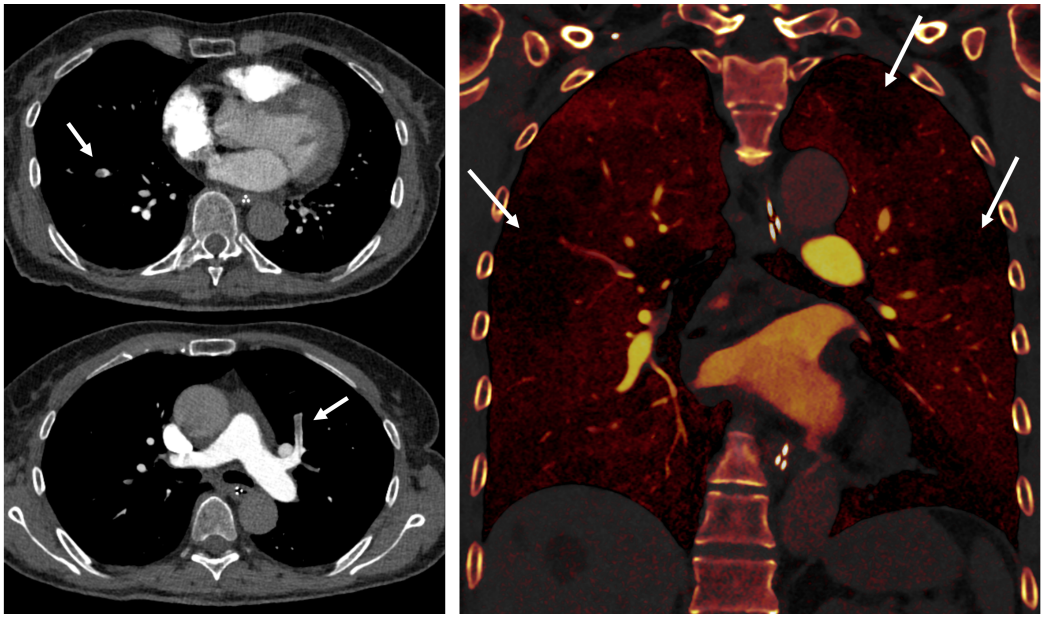

**Figure 4.33:** Pulmonary embolism shown on CTA in axial view (left) and on iodine map as overlay on VNC reconstruction in frontal view (right). Arrows indicate the occluded arteries and the resulting diffusion deficit.
CTA = CT angiography, VNC = virtual non-contrast.

characteristic to influence CACS.[97] We observed twice as large differences between $VNC_{pc}$ and TNC based calcium levels in patients with BMI above 28 kg/m$^2$, which supports the findings already made using the $VNC_{conv}$ algorithm.[104] Although the underestimation of $VNC_{pc}$ derived scores is not comparable to that observed with the conventional $VNC_{conv}$ algorithm, we still considered that 11% of the cohort may have received incorrect treatment due to misclassification of CAC risk category. On the other hand, volume quantification of epicardial adipose tissue performed on VNC reconstructions accurately reproduced measurements on TNC (refer to subsection 4.2.1). Nevertheless, volumes were evaluated based on segmentations requiring contrast rather than correct absolute CT values.

Besides the water basis material images, the corresponding iodine maps are of great value. In a feasibility study, we investigated the visibility of perfusion defects due to pulmonary embolism, as demonstrated in Figure 4.33. Previous studies of DECT evaluating its performance compared with single photon emission computed tomography (SPECT)-CT found a high sensitivity and specificity for identifying perfusion defects on iodine maps and concluded a potential for improving diagnostic accuracy for pulmonary embolism.[182,183] Further we could demonstrate the feasibility of precise quantification of contrast media density for concentrations ranging from 0 to 6 mgI/ml in our phantom study (refer to subsection 4.2.3). After intracranial endovascular procedures, this is useful in differentiating between acute hemorrhage and iodine that may have crossed the blood-brain barrier during the intervention. The lower limit of iodine quantifiability on different DECT scanners was measured to start from 0.5 mgI/ml in a phantom study.[184] In another study comparing PCD and EID performance in liver parenchyma, iodine quantification

on PCD-derived scans was found to be accurate regardless of radiation dose, iodine concentration and base attenuation.[31]

Overall, we have been able to demonstrate the potential but also the limitations of various applications of the basis material differentiation into iodine and water applied to PCD-CT data. In many cases the results were very convincing, in others we found a need for improvement. As J. Sosna concluded, PCD-CT is promising, but it is too early to say that VNC series are ready for daily clinical practice.[185]

CHAPTER 5

# Monoenergetic Imaging

Based on the information obtained from the material decomposition, which applications are discussed in more detail for the basis materials iodine and water in the previous chapter, virtual monoenergetic images can be synthesized that mimic the visual impression of a monoenergetic x-ray source. Although VM images show an increased level of image noise as a result of the necessary post-processing steps, the reconstruction is useful to either reduce or enhance specific contrasts. Higher keV levels have the potential to reduce beam hardening and scatter artifacts that occur in the presence of high x-ray attenuating material, such as metal prostheses. Their magnitude is energy dependent, with low keV amplifying the artifacts and high keV decreasing them.[3] Although unfavorable for imaging tissue including dense material, low keV VM reconstructions can improve the delineation of pathologies, especially in case of low contrast environments of CTA scans.[186] For both applications, high and low VM images, studies have been carried out which are presented and their results discussed in this chapter.

## 5.1 Metal Artifact Reduction

Materials used in medicine that are implanted in the human body for temporary or permanent fixation or replacement are mostly metal-based, ranging from rather small to quite substantial applications such as coils, clips and stents, dental fillings and artificial valves, bone fracture fixation (e.g. spine) and implants (e.g. hip). In terms of imaging with CT, metals present a challenge as beam hardening and scattering effects result in altered, reduced or missing projection data, which translates into bright or dark streak artifacts in the image domain.[187] The resulting problem is as obvious as it is problematic: Image quality is degraded and the tissue surrounding the metal cannot be reliably and diagnostically assessed. Approaches to metal artifact reduction and their appropriate application are similarly varied and adapted to their source. Gjesteby et al. differentiated between metal implant optimization, acquisition improvement, physics-based pre-processing, projection completion, iterative reconstruction and image post-processing.[187] The influence of CT scanner vendors on the first two groups of possibilities is rather limited, and the exact algorithm behind each customer's individual iterative metal artifact reduction (IMAR) application is not transparent, however, most likely consists of a mixture of the remaining options. The available 'iMAR' algorithm at our institute "[...] decreases

the influence of metal during image reconstruction by interpolating between boundaries of metal in a tissue-normalized sinogram".[188] Besides the advantages coming with PCD technology, such as higher spatial resolution and reduced noise (refer to subsection 2.2.2), the spectral sensitivity of the data can also be exploited for metal artifact reduction. With the 'spectral driven iterative reconstruction' an approach was proposed combining the differentiation into a material which is predominantly influenced by photoelectric effect and Compton scattering, plus gold as a third material with a k-edge, with iterative reconstruction, achieving good results.[189] The more common approach, however, is to use high keV VM levels, as they show reduced beam hardening artifacts, not only of metals, but also for contrast material influx and calcifications.[186] Whether high VM imaging and IMAR can be combined was evaluated in the following study for artifacts produced by dental material.

### 5.1.1 Dental Metal Artifacts

## Artifact Reduction from Dental Material in Photon-Counting Detector CT Datasets based on high-keV Monoenergetic Imaging and Iterative Metal Artifact Reduction Reconstructions - Can we combine the best of two worlds?

Franka Risch, Josua Decker, Daniel Popp, Andrea Sinzinger, Franziska Braun, Stefanie Bette, Bertram Jehs, Mark Härting, Claudia Wollny, Christian Scheurig-Münkler, Thomas Kröncke, Florian Schwarz

The study was presented by the author FR as a digital poster at the Radiological Society of North America Congress in Chicago, USA in 2022 and has been published in Investigative Radiology in September 2023.[17] The author FR performed the data collection, interpretation, statistical analysis and wrote the manuscript.

### Abstract

*Objective:* To compare the effectiveness of common strategies for artifact reduction of dental material in PCD-CT datasets.

*Materials and Methods:* Patients with dental material who underwent clinically indicated CT of the neck were enrolled. Image series were reconstructed using a standard and sharp kernel, with and without IMAR (Qr40, $\text{Qr40}_{\text{IMAR}}$, Qr60, $\text{Qr60}_{\text{IMAR}}$) at different VM levels (40 - 190 keV). On representative slice positions with and without dental artifacts, mean and SD of CT values were measured in all series at identical locations. The mean absolute error of CT values ($\Delta\overline{\text{HU}}$) and the artifact index (AIX) were calculated and analyzed focusing on three main comparisons: A) Different VM levels vs. 70 keV; B) Standard vs. sharp kernel; C) Non-use or use of IMAR reconstruction. The Wilcoxon test was used to assess differences for non-parametric data.

*Results:* The final cohort comprised fifty patients. Artifact measures decreased for VM levels $>$ 70 keV, yet only significantly so for reconstructions using IMAR (maximum reduction: 25%). The higher image noise of the sharp vs. standard kernel is reflected in higher AIX values and is more pronounced in IMAR series (maximum increase: 38%). The most profound artifact reduction was observed for IMAR reconstructions (maximum reduction $\Delta\overline{\text{HU}}$: 84%, AIX: 90%).

*Conclusions:* Metal artifacts caused by large amounts of dental material can be substantially reduced by IMAR, regardless of kernel choice or VM settings. Increasing the keV level of VM series, on the other hand, only slightly reduces dental artifacts. This effect, however, is additive to the benefit conferred by IMAR reconstructions.

### Introduction

Over the course of life, hardly anyone remains free of dental restorations such as fillings, crowns, implants, or orthodontic appliances. About half of the adult population in most European countries has received some type of dental prosthesis.[190] To facilitate radiographic assessments, materials used for dental restorations usually are radiopaque, containing elements with high

x-ray attenuation that are clearly distinguishable from dentin.[191] In CT, however, this becomes problematic, as these materials cause severe artifacts of varying appearance and extent.[192] Beam-hardening and photon starvation effects are the predominant cause and describe the absorption of low energy photons or complete absorption of the polychromatic x-ray beam by high atomic number materials.[6,193] In a multicenter study of image quality and artifacts on PET-CT by Stergar et al., 57% (201/353) of patients showed CT artifacts due to dental material.[194] These artifacts may affect image quality in the surrounding anatomic structures and compromise diagnostic value:[187,195,196] In the aforementioned study, misdiagnosis was considered possible in roughly one-third of all CTs with dental artifacts.
Several techniques have been developed to mitigate these artifacts, most commonly based on IR algorithms,[197,198] VM reconstructions from multi-energy imaging data,[3,6,143,193] or a combination thereof.[199–202] The recently introduced PCD-CT technology is especially promising in this regard because of its routine acquisition of spectral data.[9,116] From these, high-keV VM reconstructions can be derived which should reduce dental artifacts. This study investigates the extent to which dental artifacts are influenced by keV level choice in VM reconstructions, kernel choice, and the use or non-use of an IMAR reconstruction. To the best of our knowledge, this is the first study addressing the topic of dental artifacts combining VM imaging and IMAR on patient PCD-CT datasets.

## Materials and Methods

*Patients*

The local institutional review board approved this prospective study (NCT04989192), and all patients provided written informed consent. Between October 2021 and January 2022, consecutive patients scheduled for an oncological staging scan on a PCD-CT system were screened for study inclusion according to the following criteria: (1) Patient was scheduled to undergo a clinically indicated scan, including the neck with intravenous contrast material in venous phase and (2) is of a minimum age of 18 years. For this analysis, patients were excluded if no dental fillings/ implants were detected, if the neck was not scanned in venous contrast phase or if there was an error saving CT raw data. Patient characteristics such as BMI and past medical history were obtained from electronic medical records.

*CT Protocol*

All scans were performed on a novel PCD-CT (NAEOTOM Alpha, Siemens Healthcare GmbH, Erlangen, Germany), with the scan range extending from the base of the skull to the upper thoracic aperture in a supine patient position. The scan was acquired using a tube voltage of 120 kVp, image quality level 130, 0.5 s revolution time and using an acquisition mode with readout of the spectral information (Quantum Plus, Siemens Healthcare GmbH, with the following detector-based energy thresholds: 20, 35, 65 and 70 keV). Pitch was 0.8, and collimation was 144 x 0.4 mm. For all scans, 120 ml of intravenous contrast material (Ultravist 300, Iopromide, Bayer Vital GmbH, Leverkusen, Germany) was administered via an antecubital vein at an injection rate of 4.0 ml/s followed by a saline chaser of 50 ml injected at the same flow

rate. Scan delay for the acquisition of the neck was 120 s, and arms were in lowered position. Dose information, including DLP, $CTDI_{vol}$, and SSDE were extracted from the automatically generated structured dose report.

*Image Reconstruction*

All series were reconstructed on the scanner console using a quantitative regular (Qr) kernel optimized for spectral post-processing and a 'quantum iterative reconstruction' algorithm (QIR, Siemens Healthcare GmbH) at strength three. For each patient, four axial series were reconstructed using the 'SPP' DICOM file format ('Spectral Post-Processing', Siemens Healthcare GmbH), which fully preserves spectral information: Series 1 and 2 were generated using a medium soft-tissue kernel without and with IMAR (Qr40; $Qr40_{IMAR}$). Series 3 and 4 using a bone kernel without and with IMAR (Qr60; $Qr60_{IMAR}$). The IMAR algorithm ('iMAR', Siemens Healthcare GmbH) used in this study combines two methods, the normalized and frequency split metal artifact reduction[198] and has been published previously.[203,204] For all series, slice thickness and increment were 1.5 mm and 1.0 mm, respectively, matrix size was 512 pixels, and size and position of the FoV covered the whole head. From each spectral series, nine VM reconstructions were semi-automatically derived using syngo.via (version VB60A, Siemens Healthcare GmbH) at the following keV levels: 40, 50, 60, 70, 80, 100, 120, 140 and 190. This resulted in 36 series per patient.

*Image Analysis*

Image analyses were performed on a dedicated workstation using open-source software (ImageJ version 1.53k, https://imagej.nih.gov/ij/). Two slice positions with artifacts from dental implants and two without such artifacts were selected for each patient. Six circular ROIs were placed on each of the four slice positions, three in air (in front of, left of, and right of the jaw, with a diameter of 25 pixels, corresponding to a mean area of 147 $mm^2$ each), one within the tongue musculature (diameter of 40 pixels, corresponding to a mean area of 376 $mm^2$) and two in the subcutaneous fat layer of the cheeks (diameter of 15 pixels, corresponding to a mean area of 53 $mm^2$ each) and saved as a ROI set for each slice position, as exemplarily shown in Figure 5.1. To obtain mean and SD in CT values for each ROI, slice, keV level, and reconstruction (6 ROIs * 4 slices * 9 keV levels * 4 reconstruction settings = 864 measurements per patient), a python (version 3.9.7) script was written which works as follows: Iterate over patient cohort, load ROI set, read out slice positions, iterate over reconstructions, iterate over keV levels, load respective DICOM image, iterate over ROIs, measure mean and SD of CT values. For further statistical analyses, ROI measurements were averaged to three measurement regions for each patient: tongue, cheeks, and air, both for artifact and non-artifact slice-positions. The absolute difference of mean CT values between corresponding regions in artifact vs. non-artifact slice positions as a measure of artifact-induced CT value change and the artifact index were calculated as described before.[193,205]

$$\Delta\overline{HU} = \mid \overline{HU}_{artifact} - \overline{HU}_{non-artifact} \mid$$

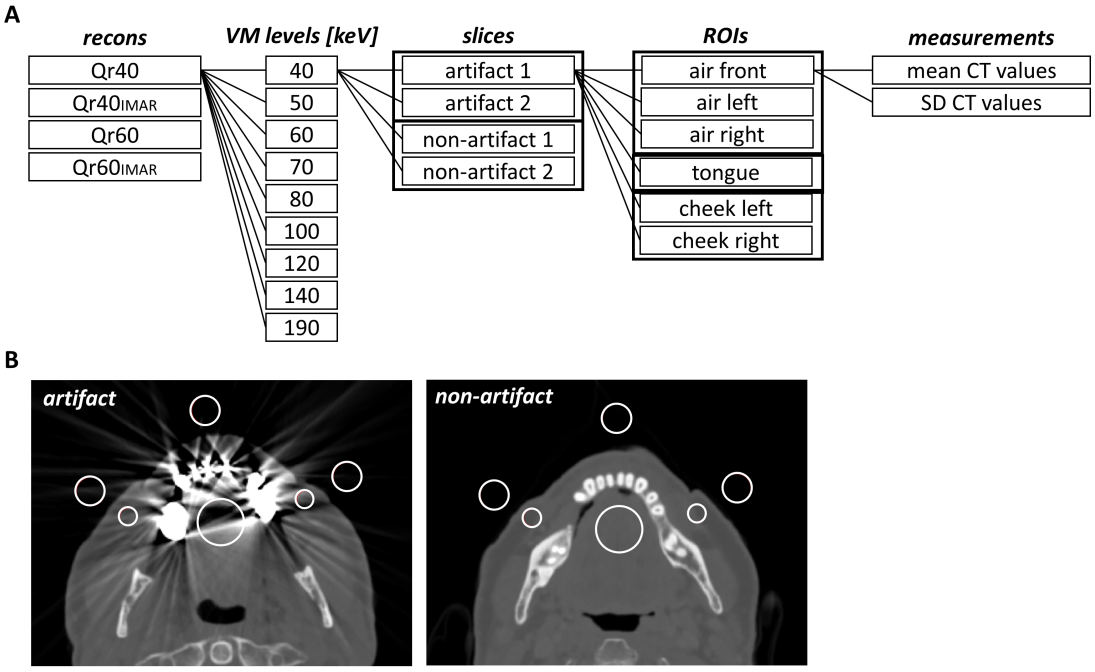


**Figure 5.1: A** Flowchart of the data collection procedure. Measurements framed (artifact/ non-artifact/ air/ cheek) were averaged for further analyses. **B** Exemplary slices with and without artifact as well as respective ROI positions (at Qr40, VM level 70 keV).
IMAR = iterative metal artifact reduction, ROI = region of interest, SD = standard deviation, VM = virtual monoenergetic.

$\overline{\text{HU}}$ denotes the mean measured CT value within the ROI, with ($\overline{\text{HU}}_{\text{artifact}}$) and without metal artifacts ($\overline{\text{HU}}_{\text{non-artifact}}$) from dental material. As a measure of differences in noise, defined as SD of CT values, in images exhibiting metal artifacts in comparison to images without artifacts, the metal artifact index was calculated as:

$$AIX = \sqrt{SD^2_{artifact} - SD^2_{non-artifact}}$$

SD denotes the standard deviation of CT values within a ROI on a slice position with appreciable dental artifacts ($\text{SD}_{\text{artifact}}$) vs. on a slice position without such artifacts ($\text{SD}_{\text{non-artifact}}$).
Our analyses focused on three aspects: A) Influence of keV level on artifacts (comparison of each keV level with the standard 70 keV level using identical kernels and identical IMAR settings, i.e. with or without IMAR):

$$A = \frac{art_r^k - art_r^{70}}{art_r^{70}}$$

With art $\in$ [$\Delta\overline{\text{HU}}$, AIX], k $\in$ [40, 50, 60, 70, 80, 100, 120, 140, 190] keV and r $\in$ [Qr40, Qr60, $\text{Qr40}_{\text{IMAR}}$, $\text{Qr60}_{\text{IMAR}}$]. B) Influence of kernel choice on artifacts (Qr40 vs. Qr60 and $\text{Qr40}_{\text{IMAR}}$

vs. $Qr60_{IMAR}$, at identical keV levels):

$$B = \frac{art^k_{r\ 60} - art^k_{r\ 40}}{art^k_{r\ 40}}$$

With art $\in$ [$\Delta\overline{HU}$, AIX], k $\in$ [40, 50, 60, 70, 80, 100, 120, 140, 190] keV, r 40 $\in$ [Qr40, $Qr40_{IMAR}$] and r 60 $\in$ [Qr60, $Qr60_{IMAR}$]. And C) influence of the use of IMAR on artifacts (Qr40 vs. $Qr40_{IMAR}$, Qr60 vs. $Qr60_{IMAR}$, at identical keV levels):

$$C = \frac{art^k_{r\ IMAR} - art^k_{r\ no\ IMAR}}{art^k_{r\ no\ IMAR}}$$

With art $\in$ [$\Delta\overline{HU}$, AIX], k $\in$ [40, 50, 60, 70, 80, 100, 120, 140, 190] keV, r IMAR $\in$ [$Qr40_{IMAR}$, $Qr60_{IMAR}$] and r no IMAR $\in$ [Qr40, Qr60]. The differences were calculated for all keV levels in each patient individually.

*Statistical Analyses*

Statistical analyses were performed using python (version 3.9.7). All data were tested for normal distribution using the Shapiro-Wilk test. Continuous parametric data are given as mean $\pm$ SD, non-parametric data as median with interquartile range, and binary data as frequencies with proportions. The two-sided Wilcoxon signed-rank test was used to test for differences in non-parametric data. In the case of multiple comparisons, p-values were corrected with the Bonferroni method. P-values $< .05$ were considered to indicate statistically significant differences.

## Results

*Patient Baseline Characteristics*

A total of 70 patients scheduled for a routine oncological staging scan including the neck were enrolled and underwent scanning on the PCD-CT system. Of these, 20 were excluded due to the following reasons: No dental material detected (n = 15), missing raw data (n = 4), and problems during contrast administration (n = 1). Thus, the final cohort consisted of 50 patients. Most scans were performed because of suspected or known lymphoma (n = 20, 40%), malignant melanoma (n = 10, 20%), or pharyngeal cancer (n = 6, 12%). 15 women and 35 men were enrolled, with an age of 71.7 $\pm$ 10.8 years and a BMI of 24.5 (23.4 - 27.8) kg/m$^2$. $CTDI_{vol}$ and DLP were 10.5 $\pm$ 1.4 mGy and 253.3 $\pm$ 46.9 mGy*cm, respectively, at an SSDE of 15.2 (14.6 - 15.9) mGy.

*Image Analysis*

Tables 5.1 and 5.2 show the results of $\Delta\overline{HU}$ and AIX for each ROI, kernel and VM level, respectively. Due to their predominant non-normal distribution, values are uniformly presented as median and interquartile range. Figure 5.2 demonstrates the different reconstructions of an 'artifact slice position' at VM level of 70 keV and the resulting calculations and comparisons for a tongue ROI. The differences calculated on the basis of the indices from Table 5.1 and 5.2 in the three main comparisons are plotted in Figure 5.3. The comparison of different VM levels to the

| | | 40 keV | 50 keV | 60 keV | 70 keV | 80 keV | 100 keV | 120 keV | 140 keV | 190 keV |
|---|---|---|---|---|---|---|---|---|---|---|
| cheeks | Qr40 | 122 (68-199) | 118 (56-191) | 112 (52-210) | 98 (31-241) | 99 (28-241) | 91 (34-237) | 92 (27-242) | 93 (24-244) | 94 (23-247) |
| | $Qr40_{IMAR}$ | 51 (26-86) | 38 (21-66) | 30 (16-57) | 28 (17-52) | 26 (16-50) | 26 (14-47) | 23 (12-45) | 23 (11-44) | 23 (9-43) |
| | Qr60 | 124 (70-221) | 118 (58-194) | 113 (52-202) | 97 (29-244) | 96 (28-241) | 96 (29-237) | 98 (25-239) | 101 (24-241) | 105 (27-243) |
| | $Qr60_{IMAR}$ | 49 (22-90) | 40 (21-71) | 32 (17-57) | 28 (17-54) | 27 (15-54) | 25 (12-48) | 24 (11-45) | 23 (11-43) | 23 (10-43) |
| tongue | Qr40 | 271 (110-488) | 291 (94-463) | 255 (89-470) | 247 (98-473) | 236 (86-424) | 217 (76-362) | 196 (74-350) | 187 (71-352) | 185 (75-354) |
| | $Qr40_{IMAR}$ | 70 (29-135) | 60 (26-110) | 47 (22-87) | 38 (16-80) | 36 (12-75) | 31 (19-66) | 33 (18-63) | 31 (19-65) | 29 (18-61) |
| | Qr60 | 258 (128-492) | 290 (89-460) | 255 (91-471) | 250 (95-474) | 241(84-429) | 212 (76-382) | 201 (72-379) | 194 (70-381) | 194 (73-385) |
| | $Qr60_{IMAR}$ | 62 (42-132) | 56 (30-89) | 43 (21-80) | 33 (12-76) | 29 (14-76) | 31 (10-66) | 28 (11-66) | 26 (11-65) | 25 (10-67) |
| air | Qr40 | 47 (17-101) | 39 (15-87) | 38 (15-85) | 31 (16-78) | 30 (17-71) | 29 (17-61) | 29 (15-59) | 31 (14-57) | 32 (15-55) |
| | $Qr40_{IMAR}$ | 25 (12-37) | 17 (11-33) | 17 (9-27) | 17 (8-26) | 15 (8-24) | 13 (6-23) | 13 (6-22) | 13 (6-21) | 13 (7-23) |
| | Qr60 | 50 (18-106) | 40 (14-86) | 38 (15-86) | 32 (17-79) | 30 (17-73) | 30 (18-63) | 31 (16-59) | 32 (15-57) | 34 (15-56) |
| | $Qr60_{IMAR}$ | 23 (10-40) | 16 (8-37) | 13 (7-33) | 12 (8-31) | 12 (6-25) | 13 (5-23) | 12 (5-23) | 13 (4-22) | 12 (4-22) |

**Table 5.1:** $\Delta\overline{HU}$ for each ROI, kernel and VM level.

Values are median (interquartile range) in Hounsfield Units. $\Delta\overline{HU}$ = absolute difference of mean CT values, IMAR = iterative metal artifact reduction, ROI = region of interest, Qr40/ Qr60 = quantitative regular standard/ sharp reconstruction kernel, VM = virtual monoenergetic.

| | | 40 keV | 50 keV | 60 keV | 70 keV | 80 keV | 100 keV | 120 keV | 140 keV | 190 keV |
|---|---|---|---|---|---|---|---|---|---|---|
| cheeks | Qr40 | 161 (103-234) | 168 (103-234) | 170 (99-246) | 177 (98-261) | 176 (95-269) | 178 (90-267) | 180 (92-273) | 181 (94-276) | 181 (95-280) |
| | $Qr40_{IMAR}$ | 40 (25-53) | 34 (20-44) | 29 (19-38) | 26 (18-37) | 24 (19-34) | 24 (18-30) | 23 (18-32) | 23 (18-33) | 23 (18-33) |
| | Qr60 | 208 (146-288) | 189 (123-259) | 188 (109-273) | 186 (112-293) | 186 (104-302) | 192 (103-312) | 192 (103-314) | 193 (103-316) | 193 (104-318) |
| | $Qr60_{IMAR}$ | 48 (32-71) | 37 (25-56) | 31 (22-51) | 29 (23-49) | 28 (21-44) | 26 (20-40) | 25 (19-43) | 25 (19-45) | 25 (18-48) |
| tongue | Qr40 | 592 (240-758) | 497 (241-672) | 449 (206-664) | 433 (181-672) | 393 (158-656) | 392 (147-651) | 398 (147-643) | 389 (149-639) | 381 (151-634) |
| | $Qr40_{IMAR}$ | 66 (42-119) | 54 (32-72) | 45 (29-60) | 38 (25-59) | 40 (24-64) | 42 (22-71) | 41 (23-82) | 41 (23-85) | 41 (22-90) |
| | Qr60 | 657 (273-830) | 545 (262-734) | 486 (238-718) | 472 (201-725) | 457 (198-715) | 431 (167-695) | 424 (167-687) | 421 (169-683) | 420 (171-679) |
| | $Qr60_{IMAR}$ | 104 (69-197) | 73 (42-123) | 59 (36-84) | 60 (36-85) | 61 (38-97) | 60 (30-110) | 59 (29-122) | 60 (28-128) | 59 (28-138) |
| air | Qr40 | 90 (71-133) | 90 (67-115) | 83 (65-121) | 81 (57-125) | 81 (61-126) | 79 (61-125) | 78 (60-128) | 78 (60-129) | 77 (59-131) |
| | $Qr40_{IMAR}$ | 61 (49-79) | 49 (40-64) | 44 (34-53) | 42 (32-49) | 39 (30-46) | 36 (28-44) | 36 (27-45) | 35 (27-44) | 35 (26-44) |
| | Qr60 | 106 (83-147) | 99 (75-132) | 90 (71-131) | 88 (61-135) | 87 (63-136) | 85 (63-135) | 85 (64-138) | 86 (64-140) | 86 (65-142) |
| | $Qr60_{IMAR}$ | 67 (51-83) | 51 (41-66) | 47 (37-55) | 43 (34-50) | 39 (30-46) | 37 (28-45) | 36 (28-46) | 36 (27-46) | 35 (27-47) |

**Table 5.2:** AIX for each ROI, kernel and VM level.

Values are median (interquartile range) in Hounsfield Units. AIX = artifact index, IMAR = iterative metal artifact reduction, ROI = region of interest, Qr40/ Qr60 = quantitative regular standard/ sharp reconstruction kernel, VM = virtual monoenergetic.

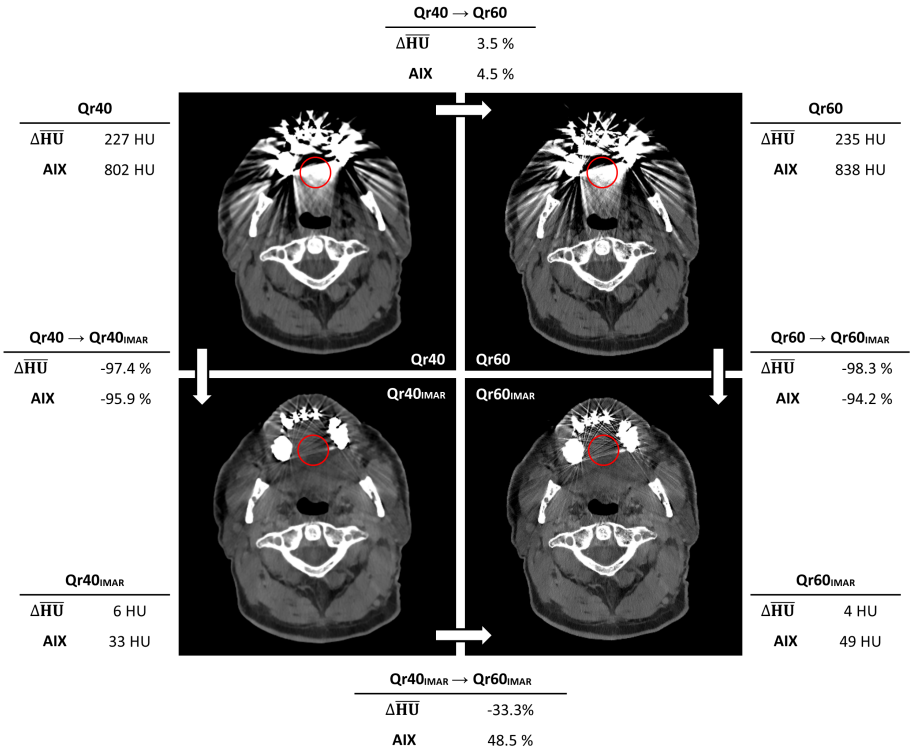


**Figure 5.2:** Demonstration of the four reconstructions of an artifact slice at VM level 70 keV and its respective measurements and calculations exemplarily shown for the tongue ROI.
AIX = artifact index, $\Delta\overline{HU}$ = absolute difference of mean CT values, IMAR = iterative metal artifact reduction, ROI = region of interest, VM = virtual monoenergetic.

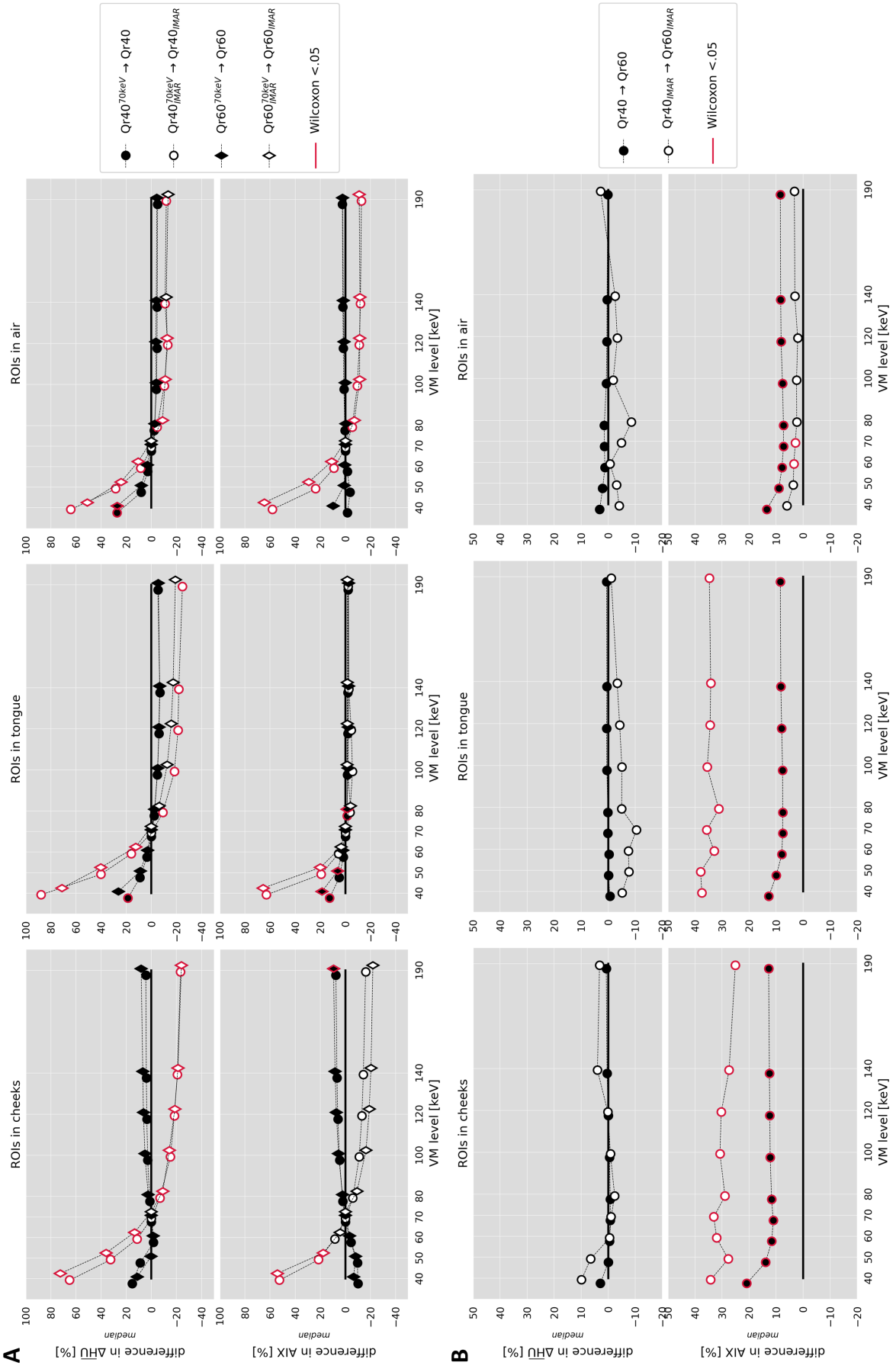
A
B
ROIs in cheeks
ROIs in tongue
ROIs in air
difference in ΔHU [%]
difference in AIX [%]
median
VM level [keV]
Qr40^70keV → Qr40
Qr40^70keV_IMAR → Qr40_IMAR
Qr60^70keV → Qr60
Qr60^70keV_IMAR → Qr60_IMAR
Wilcoxon <.05
Qr40 → Qr60
Qr40_IMAR → Qr60_IMAR
Wilcoxon <.05

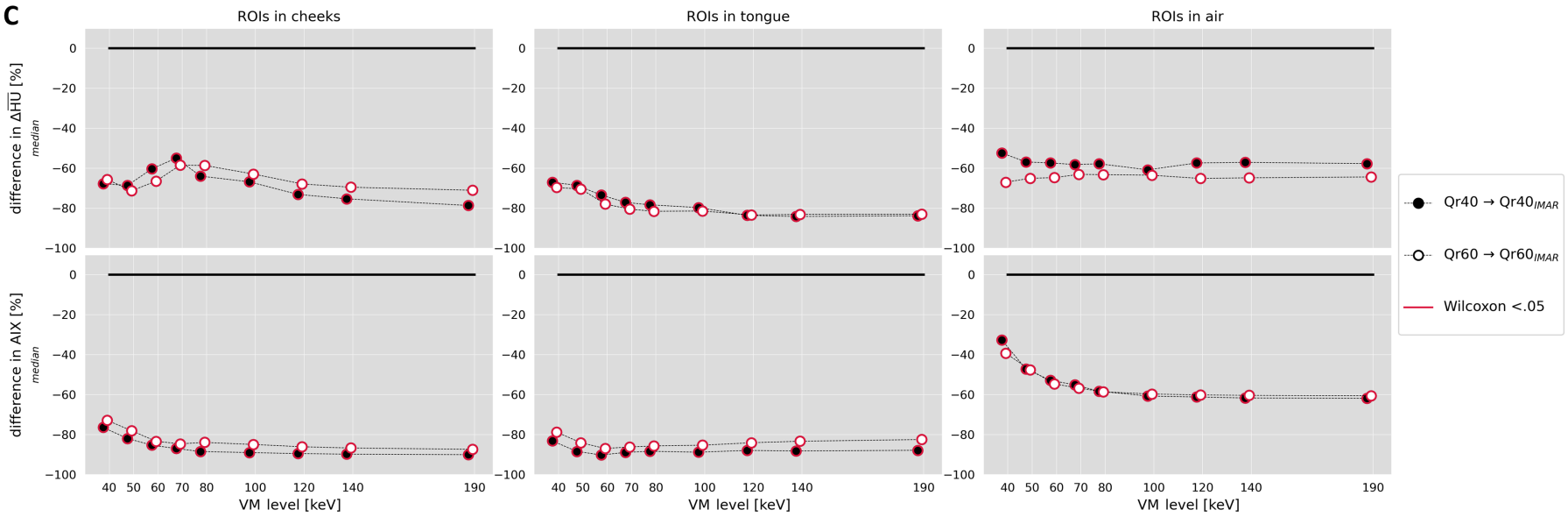


**Figure 5.3:** Results of the analysis concerning the three focused comparisons: artifact dependency on **A** keV selection (vs. standard 70 keV), **B** kernel selection (standard vs. sharp kernel), **C** use of IMAR. Significant differences are outlined in red (Wilcoxon $< .05$).

AIX = artifact index, $\Delta\overline{HU}$ = absolute difference of mean CT values, IMAR = iterative metal artifact reduction, ROI = region of interest, VM = virtual monoenergetic.

standard level of 70 keV showed an increase in $\Delta\overline{\text{HU}}$ for VM levels $< 70$ keV and a decrease for VM levels $> 70$ keV for most ROIs and reconstruction settings (Figure 5.3A). However, this change reached statistical significance only in combination with IMAR. The greatest differences were measured in the tongue ROI for $\text{Qr40}_{\text{IMAR}}$ with a decrease of 25% at VM level 190 keV, but also an increase of 88% at VM level 40 keV. AIX shows similar results to $\Delta\overline{\text{HU}}$, albeit to a smaller extent. There were no significant differences in $\Delta\overline{\text{HU}}$ comparing the standard vs. the sharp kernel, regardless of VM level or ROI region (air, tongue, cheeks) (Figure 5.3B). Regarding AIX, significant differences were observed for all ROI regions with higher AIX values in sharp kernel reconstructions. The most notable difference was registered for IMAR series, with an increase of AIX of 34% in cheeks and 38% in the tongue for the sharp kernel. The use of IMAR had the most profound effect on $\Delta\overline{\text{HU}}$ with significant reductions for all keV levels, ranging from 52% to 84% and 58% to 83%, for the standard and sharp kernel, respectively (Figure 5.3C). As for $\Delta\overline{\text{HU}}$, the use of IMAR reduced AIX by more than 33% in the air ROI's and by more than 73% in the cheek and tongue ROI's and was significant for all keV levels.

## Discussion

In this study, we quantified beam-hardening and photon-starvation artifacts caused by dental material in 50 patients who had undergone a CT scan of the neck on a novel PCD-CT and compared two strategies of mitigating these artifacts: A metal-specific IR technique and - using the spectral information inherent in PCD-CT datasets - VM reconstructions at higher keV levels. The most important finding of our study is that for severe artifacts caused by dental material, IR techniques (IMAR) lead to a much more pronounced artifact suppression than the use of VM images with higher keV levels.

Beam-hardening artifacts emanating from the jaw were quantified using ROI's in air, muscle, and subcutaneous fat in one or several predefined locations on series reconstructed using either a soft-tissue or bone kernel without or with IMAR. Utilizing the spectral information inherent in PCD-CT data, each of these series was reconstructed at nine distinct keV levels (40 - 190 keV), resulting in 36 series for each patient. By comparing ROI's from slice positions with artifacts vs. slice positions without artifacts, $\Delta\overline{\text{HU}}$ and AIX were derived as measures of artifact severity.

Several studies have demonstrated that higher keV levels reduce artifacts by simulating a monochromatic x-ray beam of higher photon energy, which is far less susceptible to partial or complete absorption in high atomic number materials.[186] In earlier dual-energy studies, this effect has been described not only for dental metals[193] but also for pedicle screws[205] and hip prostheses.[143]

In our study, this keV effect on dental artifacts was less pronounced and was statistically significant mainly for reconstructions also using IMAR. This implies that - with 70 keV VM reconstructions resembling the image impression of a standard polychromatic 120 kVp acquisition - little can be gained for dental artifact reduction by increasing keV levels over the standard settings in reconstructions without IMAR. Lower keV VM reconstructions, on the other hand, would be an unfavorable choice for any reconstruction of the neck due to the significant increase

in dental artifact severity.

It should be noted that in our study cohort, most patients had substantial amounts of dental material in situ. This might have been one reason for the weaker artifact suppression by high keV VM images than has previously been described and would concur with Zhu et al. who reported that higher keV VM images especially reduced artifacts caused by small dental fillings.[193] Anhaus et al. even tested multiple materials in their phantom study on a PCD-CT scanner and found no benefit by high-energy VM images on metal with high atomic number as used for dental restauration.[202] Kernel choice does not influence average CT values in ROI's of the size used in our analysis; yet, it affects image noise, resulting in higher AIX's for sharper reconstruction kernels, a trivial consequence of the higher spatial resolution.[206] In our study, the increase in AIX in the sharper kernel was significant for non-IMAR and IMAR reconstructions but in tissue more pronounced in the latter (with an increase in AIX of up to 38% in the sharper kernels).

The most profound dental artifact reduction was observed for the use of IMAR. This agrees with the findings reported by Weiß et al. who showed significant improvements for affected tissue, even distant from the dental artifact.[196] Hakim et al. observed a qualitative increase in diagnostic value while preserving image quality in regions not affected by the artifact.[198] The quantitative results of our study agree with these findings. The algorithm significantly reduced $\Delta\overline{\mathrm{HU}}$ and AIX for all analyzed VM levels and ROI regions regardless of kernel choice. In tissue, the reduction of AIX was even more pronounced, with well over 80%. These findings also agree with Hokamp et al. who described a substantially higher artifact suppression using an IR-based approach than high-keV VM levels, albeit in a smaller cohort and for artifacts caused by deep brain stimulation electrodes.[199] Our study extends these findings to the much more frequent artifacts caused by dental material and a new detector generation. Schmitt et al. found the IMAR algorithm to perform even better on PCD-CT compared to EID-CT datasets in their phantom study considering neurovascular platinum coils.[207]

This study has several limitations. First, we did not have information about the distinct dental materials used and therefore could not perform any subgroup analyses. Future studies could address this issue by including a phantom in which various dental materials can be tested. Second, we quantified artifacts only on two slice positions, however, we averaged across several ROI's - except for the central tongue ROI - and only performed intraindividual comparisons. Thus, even if our analysis of only two artifact slice positions per case might not fully encompass the entire extent of dental artifacts in a particular case, all analyses and comparisons are based exclusively on intraindividual comparisons of identically positioned ROI's. Changes observed will thus be valid even if they might have been more pronounced on some other slice position. Third, we do not address other aspects of image quality, such as soft tissue contrast, more objective parameters such as signal-to-noise ratio and a subjective image evaluation. This should be evaluated in future studies. Last, the used indices are based solely on ROI measurements and therefore have limited significance. In future, more elaborate methods for metal artifact evaluation might be available and should be preferred.

### Conclusion

In conclusion, increasing keV levels in VM reconstructions of PCD-CT datasets over 70 keV alone has little effect on the severity of dental artifacts in a cohort with large amounts of dental material. The highest benefit was observed for reconstructions who also used IMAR. However, lower keV VM images (40 - 60 keV) - frequently used to accentuate contrast enhancement in other body parts - should be handled with caution for the neck due to a substantial increase in dental artifact severity. The most profound artifact reduction was achieved by applying IMAR.

## 5.2 Conspicuity

The improvement of conspicuity at low keV VM images has been evaluated for several pathologies. For liver metastases,[36] breast cancer,[208] lesions of head and neck squamous cell carcinoma,[209] diagnosis of Crohn's disease,[210] vascular assessment in CTA[211] or pancreatic lesions,[212] an additive value could be demonstrated. All mentioned studies share the use of contrast enhanced spectral CT scans. Figure 2.3 shows the energy dependent x-ray mass attenuation coefficient for iodine, the main component of common CT contrast agents. The lowest possible pseudo-monoenergetic energy producible with the scanner-specific software at our institute is 40 keV, which is also the closest VM level to the k-edge of iodine at 33.2 keV and thus represents its highest achievable contrast. For this reason, conspicuity may benefit from a low keV level in low contrast enhancement scenarios. It was also shown that a 25% reduction in contrast volume for a thoracoabdominal aorta CTA on a PCD-CT is feasible and results in equivalent image quality compared to EID-based scans.[213] However, creating VM series introduces a significant increase in noise that should be taken into account.[186] Although the slope of the x-ray mass attenuation coefficient of soft tissue is not as steep as that of iodine (see Figure 2.3), its contrast is still enhanced at low VM reconstructions. In the study described below, it was investigated whether this could be exploited for the application of cryoablation. Cryoablation describes cancer treatment by freezing and therefore destroying the affected tissue optimally resulting in a shrinkage of the tumor and pain relief.[214] The procedure can be performed minimally invasively and on multiple organs, making it attractive for various types of cancer. Using CT guidance, not only can the precise placement of the probe be observed, but also the evolution of the ice ball. This raises the question of whether VM images at low keV may improve thermal sensitivity of CT values, resulting in earlier delineation and an additive value in percutaneous cryoablation.

### 5.2.1 Cryoablation

## Improved Thermal Sensitivity Using Virtual Monochromatic Imaging Derived from Photon Counting Detector CT Data Sets: Ex Vivo Results of CT-Guided Cryoablation in Porcine Liver

Josua Decker*, Franka Risch*, Florian Schwarz, Christian Scheurig-Münkler, Thomas Kröncke

* = contributed equally

The study was published in Cardiovascular and Interventional Radiology in September 2023.[215] The author FR participated in the data generation experiments, performed the data collection and statistical analysis, and contributed to the drafting of the manuscript.

### Abstract

*Purpose:* To investigate differences in thermal sensitivity of VM series generated from PCD-CT data sets, regarding their use to improve discrimination of the ablation zone during percutaneous cryoablation.

*Materials and Methods:* CT-guided cryoablation was performed using an ex vivo model of porcine liver on a PCD-CT system. The ablation zone was imaged continuously for 8 min by acquiring a CT scan every 5 seconds. Tissue temperature was measured using fiberoptic temperature probes placed parallel to the cryo probe. CT values and noise were measured at the tip of the temperature probes on each scan and on VM series from 40 -130 keV. Correlation of CT values and temperature were assessed using linear regression analyses.

*Results:* For the whole temperature range of [-40, +20]°C, we observed a linear correlation between CT values and temperature in reference 70 keV images ($r^2$ = 0.60, $p < 0.001$) with a thermal sensitivity of 1.4 HU/°C. For the most dynamic range of [-15, +20]°C, the sensitivity increased to 2.4 HU/°C ($r^2$ = 0.50, $p < 0.001$). Using VM reconstructions, the thermal sensitivity increased from 1.4 HU/°C at 70 keV to 1.5, 1.7 and 2.0 HU/°C at 60, 50 and 40 keV, respectively (range [-40, +20]°C). For [-15, +20]°C the thermal sensitivity increased from 2.4 HU/°C at 70 keV to 2.5, 2.6 and 2.7 HU/°C at 60, 50 and 40 keV, respectively. Both CT values and noise also increased with decreasing VM keV-levels.

*Conclusion:* During CT-guided cryoablation of porcine liver, low-keV VM reconstructions derived from PCD-CT data sets exhibit improved thermal sensitivity being highest between +20 and -15°C.

### Introduction

Percutaneous cryoablation plays an increasing role in the minimally invasive treatment of liver tumors and hepatic metastases.[216–219] In several studies, CT-guided percutaneous cryoablation has been reported to be a safe and efficacious treatment option for various liver lesions with low local recurrence rates.[220–225] During CT-guided cryoablation, the forming ice ball is visualized

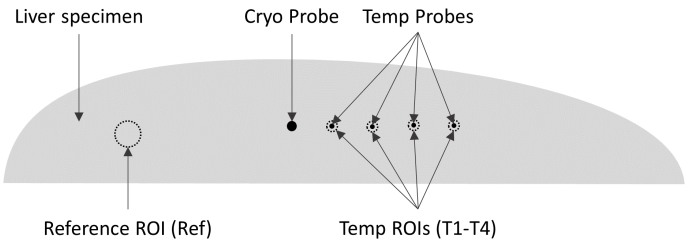


**Figure 5.4:** Schematic of the experimental setup with position of the cryo probe, the temperature probes, and the locations of the ROIs for CT value measurements in equidistance for T1-T4.
ROI = region of interest, temp = temperature.

by intraprocedural scanning of the growing hypoattenuating zone (phase transition front, i.e. interface between frozen and unfrozen liver tissue) around the cryoablation probes.[226–228] The temperature at the outer margin of the ice ball is 0°C.[229] The attenuation of the freezing liver tissue decreases with decreasing temperatures and partially shows a linear correlation.[226,230,231] Although CT is routinely used in guiding and placing cryo probes, its use for intraprocedural monitoring and visualization of the ice ball has known limitations.[229,232,233] To ensure complete ablation of the target lesion and to prevent injuring adjacent structures, it is important to strive for optimal discrimination of the ice ball and especially its outer margin.
Recently, CT systems with PCD have been introduced in clinical routine, which generate spectral information for every scan due to their inherent spectral sensitivity.[22,234] Using this spectral information, VM reconstructions can be generated, which show an increased soft-tissue contrast at low keV-levels.[36,235] Low-keV VM images improve the conspicuity of hypoattenuating liver metastases, however it is not yet known, if VM images can also be utilized to improve the visualization of the ice ball formation during percutaneous cryoablation.[36]
Therefore, in this study, we investigated if VM images generated from PCD-CT data sets exhibit differences in thermal sensitivity, and whether these VM reconstructions can be used to improve discrimination of the ice ball during percutaneous cryoablation.

## Materials and Methods

*Experimental Setup*
A healthy porcine liver was purchased from a local organic butchery and used on the same day. Three experiments were performed in separate liver segments carefully avoiding potential overlapping of puncture and ablation zones. The liver was placed on the CT table surrounded by air. A liquid argon cooled (Linde plc, Dublin, Ireland) cryoablation system (ICEfx, Icefx; Boston Scientific, Marlborough, Massachusetts, United States) was used for all experiments. The cryo probe (17 G, IceRod 1.5 CX, Boston Scientific) was placed parallel to the CT table centrally into the liver parenchyma. Four fiber-optic temperature probes (TS3 Sensor, Weidmann Technologies, Germany) were positioned parallel to the cryo probe in 5 mm intervals with distances of 5, 10, 15 and 20 mm (Figure 5.4). Positioning of the probes was checked by sequential CT acquisitions without table movement. The temperature measurements were obtained using a

four-channel thermometry-system (OEM-PLUS RS232, Weidmann Technologies) calibrated with 0.1°C accuracy from -100 to +200°C.

*Cryoablation Procedure and CT Protocol*

The cryoablation procedures were performed on a dual-source PCD-CT scanner (NAEOTOM Alpha, Siemens Healthcare GmbH, Erlangen, Germany) with the experimental setup placed in the isocenter. Correct positioning was again verified by a sequential reference CT scan. After starting continuous temperature measurements at four probe positions (in 0.25 s intervals) and acquisition of a reference CT scan, cryoablation was started with a freezing time of 8 minutes. During freezing, sequential CT scans without table movement were obtained in 5 second intervals adding up to a total of 97 scans (8*60 s/ 5 s + 1 at time point zero) for each of the three repetitions. The following scan parameters were applied: Total collimation of 144 x 0.4 mm resulting in 57.6 mm acquisition length in z-axis direction, reference tube potential of 70 kVp, reference tube current time product of 80 mAs, spectral acquisition mode (QuantumPlus, using thresholds at 20, 35, 65 and 70 keV, Siemens Healthcare GmbH).

*Image Reconstruction and Image Analysis*

The time resolved scans were reconstructed at the scanner console using a smooth body regular kernel (Br40) with IMAR at varying VM levels, ranging from 40 to 130 keV in 10 keV increments. Slice thickness and increment were both 1.0 mm and the matrix size was 512 pixels with a FoV identical for all three experiments. For image analysis, ROIs of 3 mm diameter were placed at the same axial slice position in front of the temperature probe endings (T1-T4) in most homogeneous and least artifact affected tissue using an open-source software (ImageJ version 1.53k, https://imagej.nih.gov/ij). A reference ROI (ref) with 8 mm diameter was placed at a distance where the tissue was not affected by the cryoablation. Mean and SD of CT values was automatically derived for all three experiments, the 97 points in time, the 10 VM levels and all five ROIs at three adjacent slices, respectively, using a python (version 3.9.7) script. For further analysis, ROIs were averaged across the three slices to increase robustness to local CT value inhomogeneities and noise. The signal to noise ratio was calculated from the ref ROI measurements, dividing the mean of the CT values by their standard deviation. For visualization, linear regression results were used to allocate temperatures to CT values creating 'temperature-coded' images.

*Statistical Analysis*

Statistical analyses were performed using python (version 3.9.7). The Shapiro-Wilk test was used to test for normal distribution of data. Continuous parametric data are given as mean $\pm$ SD, non-parametric data as median with interquartile range. To test for differences the paired t-test and the Wilcoxon signed rank test were used, for parametric and non-parametric data, respectively. Temperature measurements were correlated with the scan points of time and a linear regression performed. All p-values were corrected with the Bonferroni method, in case of multiple comparisons. P-values $< .05$ were considered to indicate statistical significance.

## Results

*Temperature Measurements*

Measured temperature shows an exponential decay with the lowest temperatures measured more closely to the tip of the cryo probe. The lowest measured temperature was -41.1°C in about 5 mm distance to the cryo probe after 8 min of cooling. During ablation we observed the characteristic low-attenuating area originating from the tip of the cryo probe. Figure 5.5 and Figure 5.6 illustrate grayscale images for different VM series over different time scales. Here, the ice ball formation can be observed with better delineation in lower VM series, which is especially pronounced during the first 120 s of the ablation procedure (see Figure 5.6).

*CT Value Measurements*

For analysis of the temperature-dependent changes of CT values, 34,920 ROI measurements were included. Figure 5.7 shows CT values over time for different distances to the cryo probe. In the ROIs more closely to the cryo probe, we observed a more rapid decrease in CT values compared to the more distant areas, where delayed decrease was observed. In the reference ROI, we observed no relevant changes in attenuation. Therefore, mean CT values were lower in close proximity to the cryo probe, which also results in a decreased SNR at these locations. Regarding VM levels, we observed an increase in image noise at lower keV-levels exemplarily increasing by 56.8% (SD: 17.6 to 27.6 HU; $p < 0.001$) between 70 to 40 keV series at temperature ROI T1 in closest proximity to the cryo probe. CT values also increased with decreasing keV, exemplarily in the reference ROI with a 117.4% increase (mean: 69.3 to 150.7 HU; $p < 0.001$) between 70 and 40 keV. Because CT values showed a disproportional increase at lower keV VM images, the overall SNR also increased at lower keV-levels. Exemplarily, SNR increased by 80% (1.0 to 1.8, $p < 0.001$) between 70 and 40 keV at T1. Due to the lower CT values at ROIs more closely to the cryo probe, overall noise and SNR were also lower in these locations.

*Correlation of Temperature and CT Values Measurements*

When comparing the measured CT values with the temperature, we found linear correlations for CT values and temperature for all VM levels. In regression analysis considering the full temperature range [-40, +20]°C, this yielded a linear correlation between CT values and temperature in reference 70 keV images ($r^2 = 0.60$, $p < 0.001$) with a slope of 1.4, which corresponds to a 1.4 HU decrease per °C. The slope, however, was steeper at lower keV-levels increasing to 1.5, 1.7 and 2.0 HU/°C for 60, 50 and 40 keV, respectively (Figure 5.8A). In the scatter plots, we observed only minor changes to a plateau-like configuration of CT values below -15°C. Therefore, we additionally assessed correlation of CT values and temperature for the dynamic range of [-15, 20]°C. Applying this range, we also found a linear correlation in reference 70 keV images ($r^2 = 0.50$, $p < 0.001$) with a steeper slope of 2.4 HU/°C increasing to 2.5, 2.6 and 2.7 HU/°C for 60, 50 and 40 keV, respectively (Figure 5.8B). Figure 5.9 shows temperature-coded images, where each voxel in each series was assigned the temperature according to the calculated linear correlation derived from regression analysis.

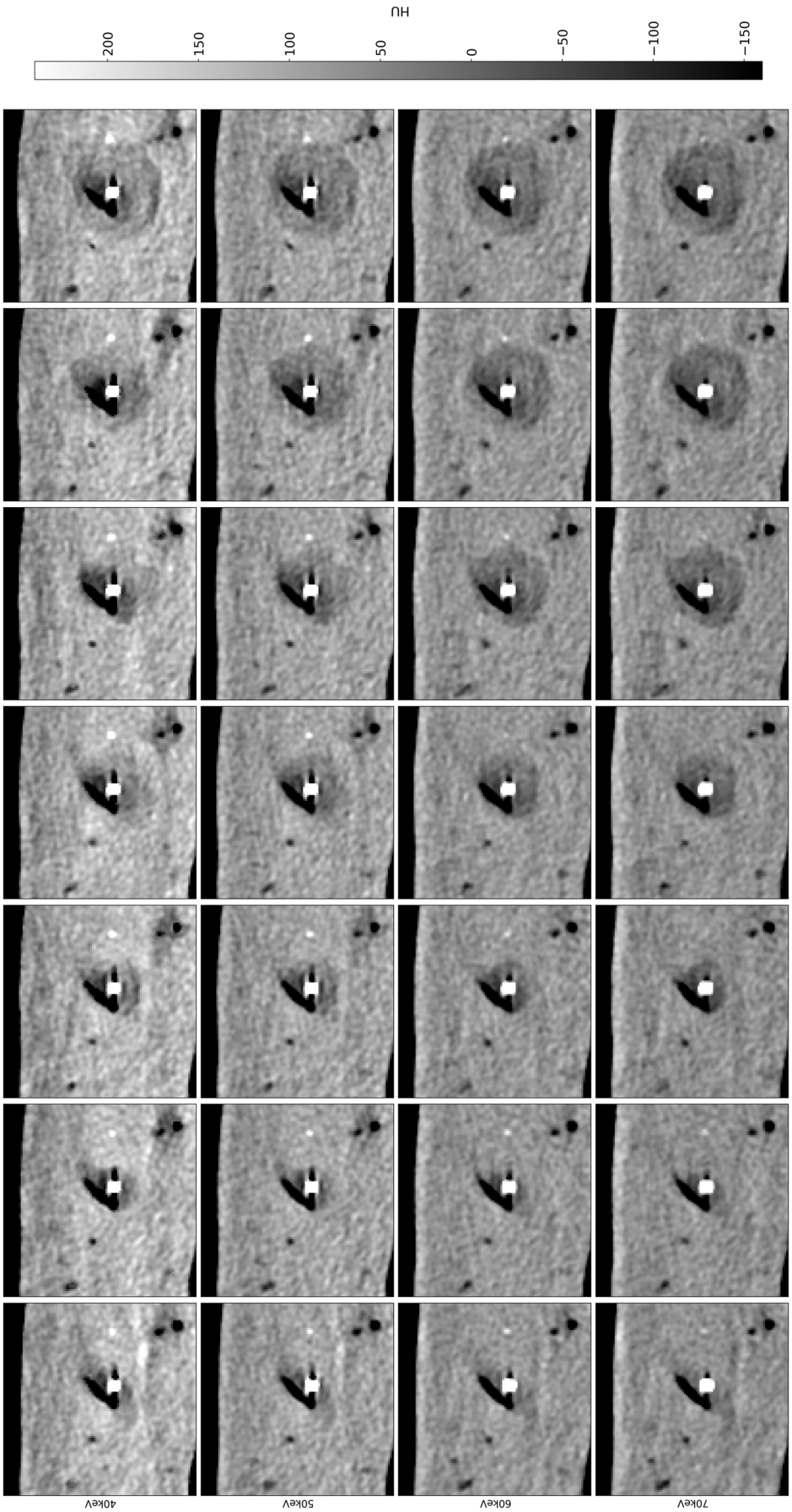


**Figure 5.5:** Visualization of the same axial slice during the cryoablation procedure at exemplary time points. On the horizontal axis, time varies from 0 to 480 s in 80 s intervals; On the vertical axis, the level of monoenergetic imaging varies from 40 to 70 keV in 10 keV intervals. HU values of all images are normalized to the grayscale shown on the right.

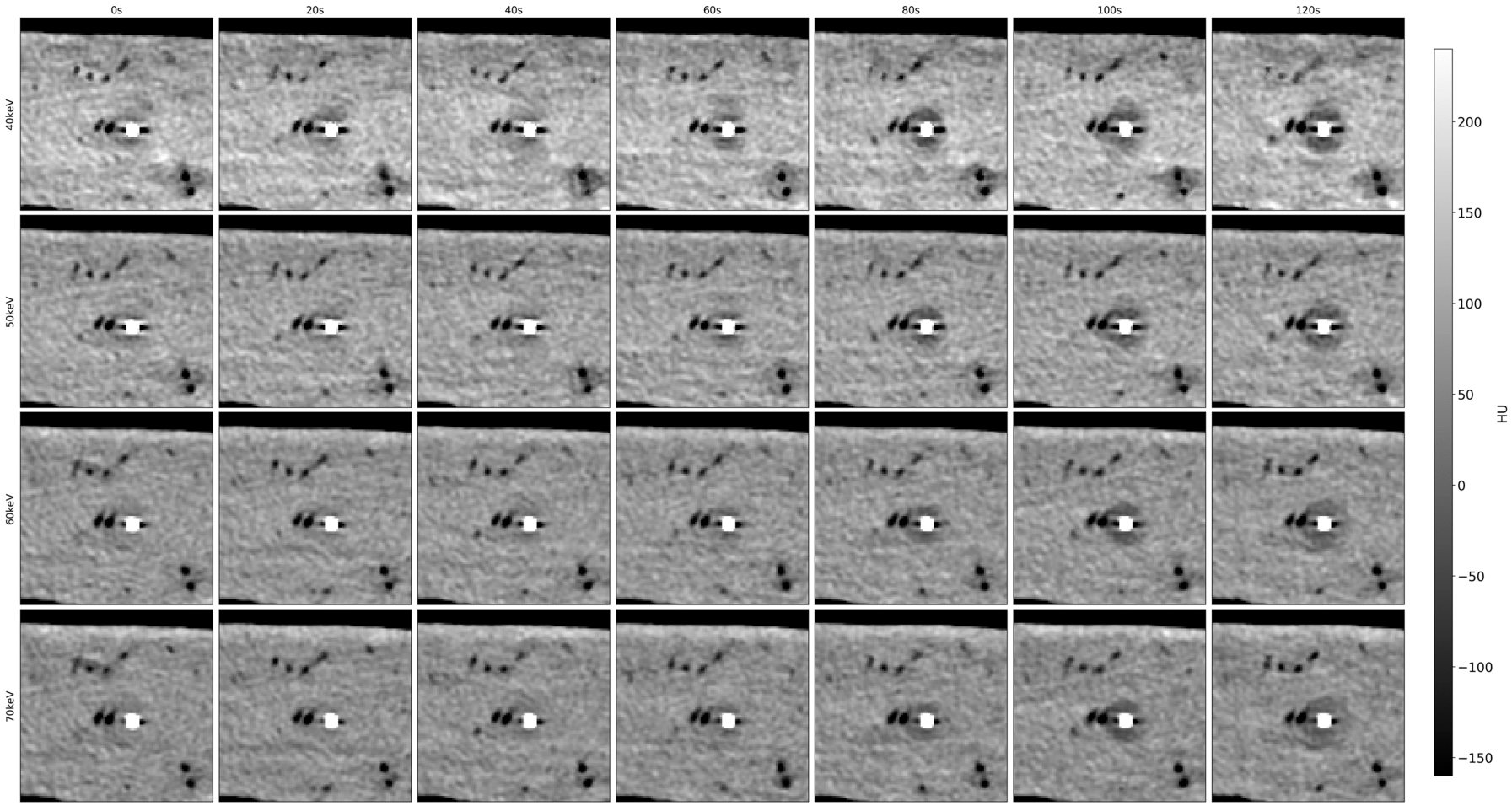


**Figure 5.6:** Visualization of the same axial slice during the cryoablation procedure at exemplary time points. On the horizontal axis, time varies from 0 to 120 s in 20 s intervals; On the vertical axis, the level of monoenergetic imaging varies from 40 to 70 keV in 10 keV intervals. HU values of all images are normalized to the grayscale shown on the right.

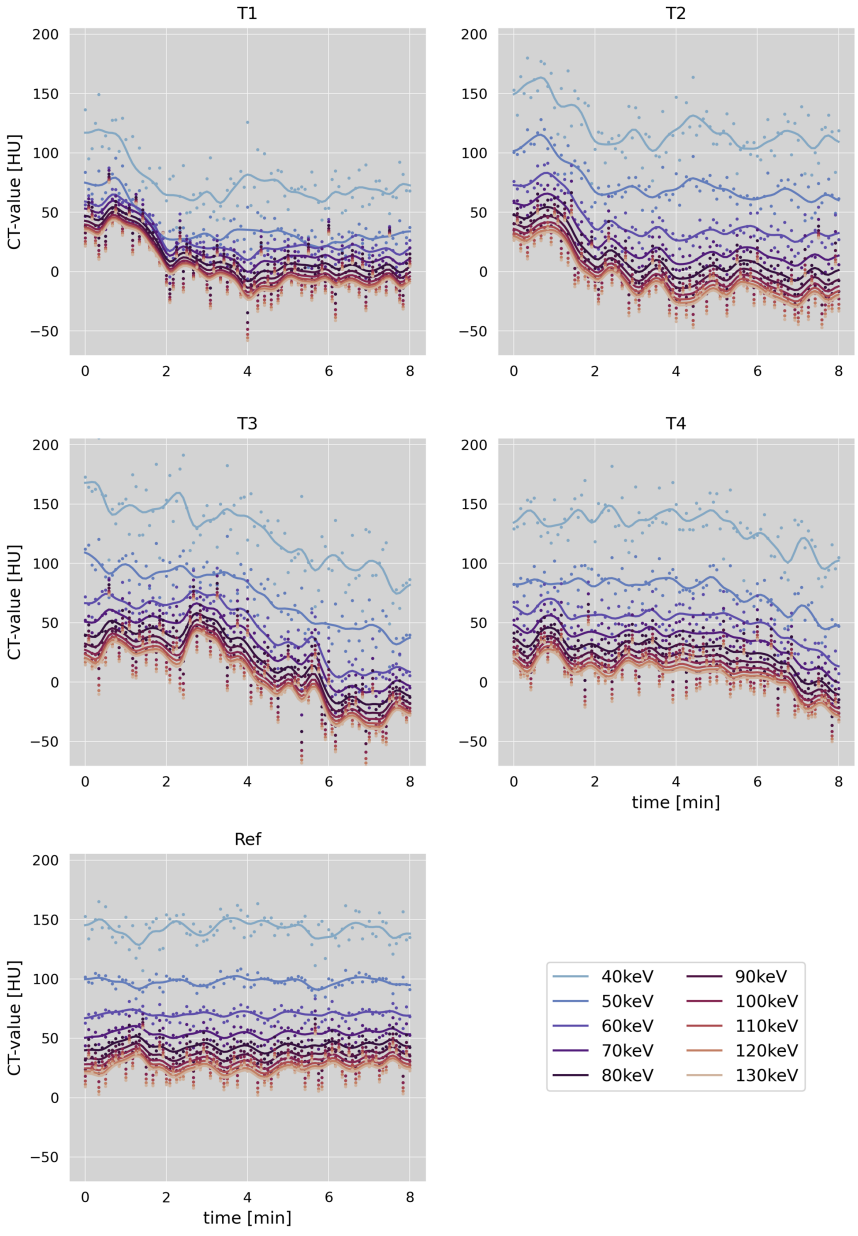


**Figure 5.7:** CT values over time for different ROIs.
ROI = region of interest, T1-T4 = ROIs of temperature probes 1-4 with increasing distance to the cryoprobe, Ref = reference ROI.

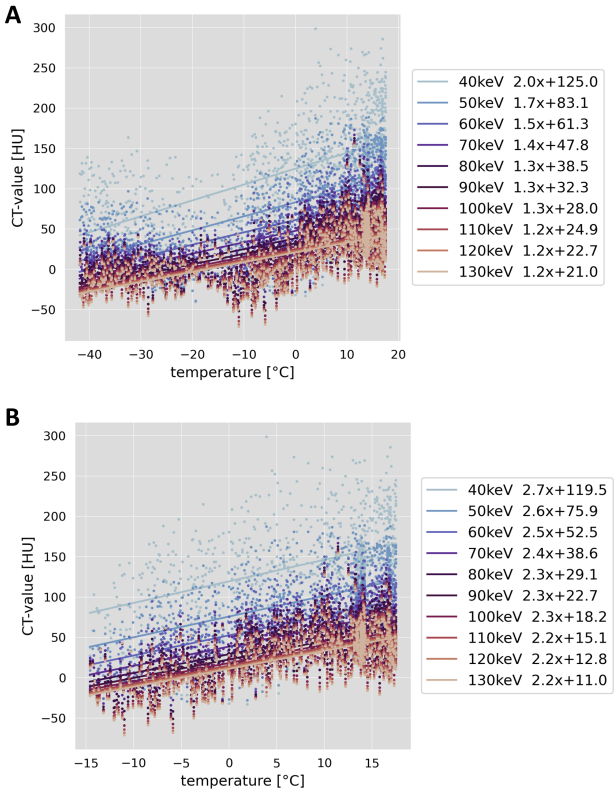


**Figure 5.8:** Scatter plots and linear correlation of CT values and temperatures measured during cryoablation of porcine liver tissue. **A** temperature range of [-45, +20]°C. **B** temperature range of [-15, +20]°C.

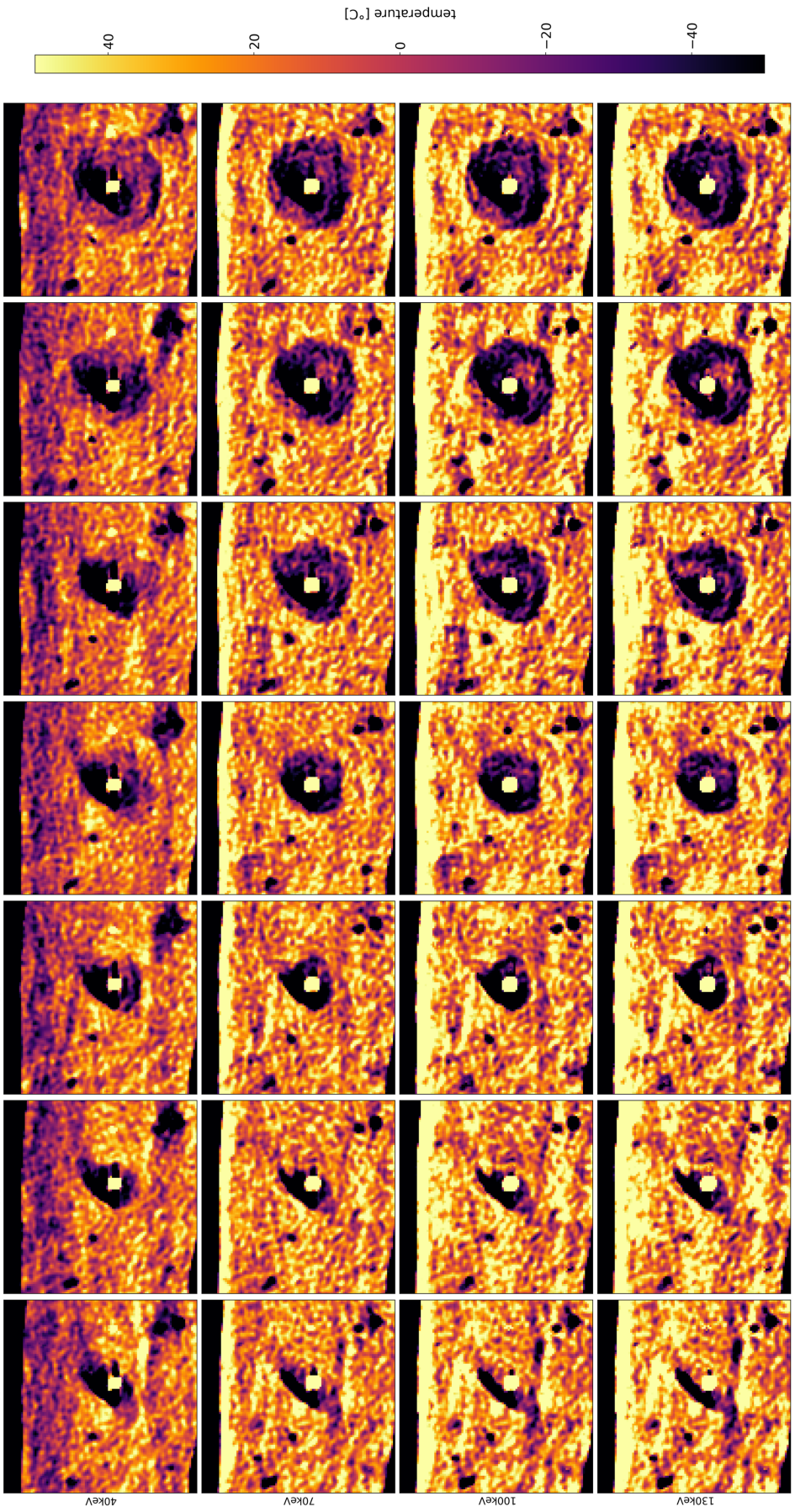


**Figure 5.9:** Temperature-coded images, where each voxel in each series was assigned the temperature according to the linear correlation or temperature range of [-45, +20]°C (see Figure 5.8A).

## Discussion

In this study, we investigated the thermal sensitivity of VM series of various keV-levels generated from PCD-CT data sets in an ex vivo porcine liver model during CT-guided cryoablation. The main findings are: (1) There is a linear correlation of tissue CT values and temperature especially between +20 and -15°C with formation of a plateau at lower temperatures; (2) VM reconstructions at lower keV-levels show higher image noise but also higher SNR; (3) With decreasing keV-levels, we observed a more pronounced linear correlation of CT values and temperature, which (4) results in an increased difference of CT values between the ablation zone and the surrounding tissue (especially at earlier time points, when the desired temperature has not yet been reached).

Image guidance in percutaneous cryoablation involves different steps such as planning, targeting, monitoring and assessment of treatment response.[236] Tissue changes that occur during the procedure can be monitored by CT to assess adequate tumor coverage, affection of nearby normal (non-target) structures and may also be used to perform intraprocedural modifications.[229] Careful observation of the hypoattenuating leading edge of the ice ball is required to achieve the best possible treatment and to avoid recurrences.[227,228] Evaluating the potential of dual-energy CT for cryoablation guidance in bone, Morris et al. reported an earlier ice ball visualization in the spine and pelvis.[28] But how can spectral information be used to improve discrimination of the ablation zone in hepatic tissue? Since recently introduced PCDs inherently provide spectral information for each scan, it is necessary to investigate, whether and how this additional and directly accessible information can be used to improve the peri-interventional control of the ablation zone in patients undergoing percutaneous cryoablation.

Using an ex vivo porcine liver, we observed a strong linear correlation of temperature and CT values that was even more distinct on VM series at low keV-levels. It is not unknown that there is a correlation between temperature and CT attenuation of hepatic tissue. Using a similar experimental setup, Huebner et al. reported a thermal sensitivity of 0.95 HU/°C ($r^2$ = 0.73) in an ex vivo porcine liver model.[230] Pohlan et al. reported a thermal sensitivity of even 2.11 HU/°C ($r^2$ = 0.55) using porcine liver placed on porcine ribs.[226] At comparable keV-levels, our experiments yielded a thermal sensitivity of 1.2 HU/°C ($r^2$ = 0.46) for the temperature range of [-40, 20]°C. An explanation for the observed deviations might be that Huebner et al. used temperatures as low as -75.4°C compared to -41.1°C in our study and about -35°C in Pohlan et al. Due to the plateau below -20°C, which can also be observed in the study of Huebner et al., the influence of even lower temperatures will most likely attribute to a flattening of the correlation line translating into a reduced thermal sensitivity. Additionally, we used a reference tube voltage of 70 kVp compared to 120 kVp of Huebner et al and Pohlan et al.[226,230] Due to the stagnating CT values at temperatures below -20°C, we decided to separately assess the thermal sensitivity of this range of transition, where we calculated a significantly higher value of 2.2 HU/°C ($r^2$ = 0.40) at 120 keV VM level. Utilizing the inherent spectral information of the PCD data sets, we showed that thermal sensitivity could be further improved (up to 2.7 HU/°C) by lowering keV-levels to 40 keV.

But how can these observations be utilized in clinical routine? First, it must be noted that low-keV VM reconstructions can directly be generated and displayed on the scanner during ablation. These low-keV VM reconstructions (with shown increased thermal sensitivity) could then be used during PCD-CT-guided cryoablation for a more precise delineation of the ice ball and subsequent ablation zone. This could help facilitating complete coverage of the target lesion and avoiding damage to adjacent structures. Furthermore, the highest thermometric sensitivity between 20 and -15°C in combination with VM reconstructions may be used for intraprocedural modification of the ablation zone by means of duty cycle setting adjustments at earlier time points - maybe also with the help of temperature-coded images. In consequence, the cryoablation of tumors could possibly be performed with greater confidence without additional effort, thanks to the routinely available VM reconstructions derived from the inherent spectral PCD-data.

This study has several limitations. First, we investigated an ex vivo porcine liver model without perfusion. Second, the experimental setup was surrounded by air and third, we performed the ablation on non-malignant tissue. Therefore, the results cannot simply be translated to an in vivo intervention. Fourth, we did not investigate the thermal sensitivity for increasing temperatures. Other studies also investigated the thermal sensitivity of CT for higher temperatures with the use of radiofrequency, microwave and laser ablation.[226,237–240] However, since heating is accompanied with fundamentally different changes of the affected tissue (such as gas building and irreversible protein denaturation and charring), we did not compare our findings to studies investigating CT thermal sensitivity by heating hepatic tissue.[240] Last, we did not investigate, whether these findings translate into an earlier visibility of the ablation zone in a real ablation scenario. This impact should be evaluated in future studies before VM reconstructions may be routinely used during hepatic cryoablation.

## Conclusion

In conclusion, this experimental study provides evidence that routinely and directly available low-keV VM reconstructions from inherently spectral PCD-CT data sets can be used to improve the thermal sensitivity of CT during cryoablation of liver tissue. Additional studies are necessary to assess, how these findings can be translated into an in vivo ablation and clinical routine.

## 5.3 Discussion

This chapter describes two applications of pseudo-monoenergetic images derived from PCD-CT spectral data, high keV levels for metal artifact reduction and low keV levels for improved conspicuity. In this discussion the results of the studies are recapitulated and supplemented with recent research.

70 keV roughly represents the mean energy of a typical 140 kVp x-ray spectrum and the same level VM images show favorable noise and image quality characteristics compared to other keV levels,[241] in coronary[242] or pulmonary[243] artery assessment or cardiomyopathy,[244] just to name a few. For this reason, 70 keV has been referred to as the reference or standard VM level in the studies presented in this chapter.

Although noise was not in the focus of analysis, for the cryoablation SD of CT values increased nearly 60% with a change from 70 keV to 40 keV VM level and otherwise constant reconstruction settings and ROI positioning. Because the enhancement of signal intensity exceeds this increase in noise, the SNR and CNR benefit from low keV levels, which is often viewed positively compared to polyenergetic visualization.[245–247] In general, the VM reconstruction-induced noise amplification is dependent on the quality of the separation of the dual-energy spectra used for the calculation and also affects high keV levels, but to a lesser extent.[3] An optimized VM algorithm, also known as mono+, counteracts the increase in noise through a frequency-split technique[248] and is now commonly used.

We observed greater differences between low compared to high adjacent VM levels. Regarding the reduction of dental metal artifacts, Figure 5.3A shows that the artifact indices are subject to a significantly greater change in the range of 40 to 70 keV compared to range of 70 to 130 keV. Similarly, Figure 5.8 demonstrates that the temperature sensitivity of CT values exhibited much more pronounced differences at low VM levels and varied only marginally at high. This observation leads to the conclusion that there is little to be gained by using high keV levels for dental metal artifact reduction, while low levels cause significant degradation. This result is consistent with a similar study on split-filter DECT.[201] Conversely, for maximum effect in improving ice ball conspicuity in cryoablation, the outer edge, i.e. 40 keV, should be used to take advantage of the highest temperature sensitivity.

Regarding spectral metal artifact suppression, in this study we considered only dental metals without knowledge of their composition, which naturally limits the applicability to other scenarios. Evaluating the effect of VM imaging on spinal fixation based artifacts, we could identify 110 keV as the most favorable in terms of artifact suppression.[35] This level of maximum artifact reduction without overcorrection was consistent with another study analyzing unilateral hip replacement artifacts.[249] Anhaus et al. investigated the potential of VM imaging on PCD-CT for artifact reduction in a phantom study for hip, dental, spine and neuro.[202] Their results are in line with our observations, as little improvement was found for large or high atomic number objects, such as dental material, while there is an optimum for spinal implants, which they experienced at 100 keV. Nevertheless, compared to polyenergetic imaging, the pseudo-monoenergetic visualiza-

tion already seems to significantly reduce the artifact impression, as Mellander et al. discovered retrospectively evaluating coils scanned with dual-layer (EID) technology.[250] However, when comparing the performance of PCD to EID-CT, Schmitt et al. found no superiority.[207] In fact, their EID-derived images showed a lower degree of coil artifacts compared to the total energy PCD images. With the introduction of IMAR, the results were reversed and PCD series were convincing with a higher degree of artifact reduction. Another approach with promising results was presented by Do et al., who used the high keV reconstructions of a PCD-CT and changed the threshold separating the high and the low bin instead of using a single VM keV level.[251] In our study, the use of IMAR had the most profound effect on the artifacts, that was slightly reduced for low keV and increased for high keV. Another recent study with a very similar setup and equivalent results by Patzer et al. demonstrates the reproducibility of our observations.[252] This suggests that, especially for dental implants, it is important to consider artifacts before image reconstruction and to choose the most appropriate settings, such as IMAR and a soft tissue rather than a bone kernel. Provided that reconstructions are available that inherit the full spectral information, the change to higher keV VM imaging can be applied without further effort, which is an indisputable advantage over IMAR.

The study on iceball visualization during cryoablation showed, that at the lowest possible VM level of 40 keV allows for the earliest delineation (see Figure 5.6) and provides the highest thermal sensitivity of CT values (see Figure 5.7B). Especially up to -15°C cooling, the CT values decreased linearly, followed by a plateau. One outlook is to translate this study to skeletal structures where the delineation of the iceball presents a significant challenge. Using dual-energy with EID-CT an earlier visualization could already be observed.[28] Again, this advantage can be used without additional effort and may increase the precision of cryoablation.

McCollough et al. recently highlighted the challenge of CT value inconsistency caused by different acquisition settings, such as choice of tube potential, and made a case for using VM imaging to standardize quantitative CT data.[34] This could facilitate technology comparisons and unify quantitative tasks. Furthermore, a tendency to more stable radiomics features was found compared to non-VM reconstructions.[253] It should be noted, however, that the comparability is only valid for identical reconstruction settings (algorithm, iteration strength, kernel, etc.), since they also strongly influence the CT values.

In conclusion, VM imaging has many advantages over polyenergetic visualization and may become the standard. The most adequate keV level is inevitably related to the underlying medical question and remains to be analyzed for many cases. However, by preserving the spectral information in the reconstructed image series, the adaptation of the keV level can be performed without additional time or effort using appropriate software, which is potentially helpful in patients with uncertain pathologies.

PART III

# Summary and Outlook

CHAPTER 6

# Summary and Outlook

Photon-counting detector CT overcomes many of the limitations associated with conventional energy-integrating detector CT. By counting each photon individually and directly measuring its energy without a required conversion step, electronic noise can be eliminated, high and low energy photons are given equal weight, smaller detector pixel sizes can be implemented, and bins can be delimited to allow spectral post-processing.[254] In summary, this new technology provides much more information about the object being scanned.

With PCD-CT, dual-energy applications can be performed with little effort, since the energy of each individual photon is known for each acquired scan and can be assigned to a high or low image, which in turn can be used for various post-processing algorithms. Unlike previous technologies, PCD-CT allows the combination of spectral evaluation with non-spectral ultra-high resolution reconstructions and the spectral information is also available for high temporal resolution acquisitions using both sources at the same tube voltage. The benefits generally associated with multi-energy imaging, including material differentiation or virtual monoenergetic imaging, which come with a reduction in radiation exposure, minimization of contrast material, time savings, and many others, have been widely appreciated. However, so far it has inevitably been associated with additional effort in acquisition, thinking of hardware requirements, such as dual-layer capabilities and dedicated imaging protocols, or quality limitations, such as the restriction in FoV[163] in dual-source scanners.

In the studies performed and presented in this dissertation, it has been demonstrated that several spectral imaging applications are equivalently feasible as previously evaluated using EID technology, and most of them even provide improved results, either due to the aforementioned hardware advances or to novel reconstruction algorithms. By material differentiation of iodine and water, contrast enhancement can either be quantified (iodine map) or effectively removed (water/ VNC image), promising to replace the TNC series in multi-phase acquisition. Iodine was shown to be accurately differentiated and quantified within a head phantom, and VNC reconstructions, especially the calcium-sensitive version $VNC_{pc}$, proved valuable in various scenarios, whether it being for calcium or other quantification tasks, conventionally performed on TNC. The VM visualization showed a positive impact on metal artifact reduction as well as ice ball visibility during cryoablation.

Of course, new technology rarely brings only opportunities, but also challenges. At the University Hospital of Augsburg, the system was introduced into clinical routine from the first day of installation. In addition to other new features and challenges which had to be mastered by the medical staff, the amount of raw and image data that needed to be processed was remarkable. Since the raw data is spectral sensitive for each individual scan, many more reconstructions are conceivable, which in turn produce a mass of image data. Not every reconstruction is useful for every medical question, and in some cases it may artificially increase the workload by requiring the radiologist to assess each piece of information presented. However, this evaluation is an ongoing process that takes time.

Photon counting detectors are an exciting milestone in the history of CT. The studies performed by our research group aim to exploit the full potential of this technology, but also to judge the results for their clinical relevance and translatability into routine practice. The logical next step is to integrate spectral data applications from photon-counting detector CT into clinical practice in a way that maximizes value for the medical staff and, ultimately, the patient.

# Bibliography


[1] Press release. https://www.nobelprize.org/prizes/medicine/1979/press-release/. Accessed: 2023-04-26.

[2] J. Hsieh and T. Flohr. Computed tomography recent history and future perspectives. *Journal of Medical Imaging*, 8(5):052109, August 2021.

[3] B. J. Heismann, B. T. Schmidt, and T. Flohr. *Spectral computed tomography*. SPIE Press, Bellingham, Wash, 2012.

[4] B. Krauss. Dual-Energy Computed Tomography: Technology and Challenges. *Radiologic Clinics*, 56(4):497–506, July 2018.

[5] K. Rajendran, M. Petersilka, A. Henning, et al. First Clinical Photon-counting Detector CT System: Technical Evaluation. *Radiology*, 303(1):130–138, December 2021.

[6] C. H. McCollough, K. Boedeker, D. Cody, et al. Principles and applications of multienergy CT: Report of AAPM Task Group 291. *Medical Physics*, 47(7):e881–e912, 2020.

[7] T. Emrich, G. Aquino, U. Schoepf, et al. Coronary Computed Tomography Angiography-Based Calcium Scoring: In Vitro and In Vivo Validation of a Novel Virtual Noniodine Reconstruction Algorithm on a Clinical, First-Generation Dual-Source Photon Counting-Detector System. *Investigative radiology*, March 2022.

[8] F. Risch, F. Schwarz, F. Braun, et al. Assessment of epicardial adipose tissue on virtual non-contrast images derived from photon-counting detector coronary CTA datasets. *European Radiology*, 33(4):2450–2460, 2023.

[9] J. Decker, S. Bette, C. Scheurig-Münkler, et al. Virtual Non-Contrast Reconstructions of Photon-Counting Detector CT Angiography Datasets as Substitutes for True Non-Contrast Acquisitions in Patients after EVAR-Performance of a Novel Calcium-Preserving Reconstruction Algorithm. *Diagnostics*, 12:558, February 2022.

[10] F. M. Braun, F. Risch, J. A. Decker, et al. Image Characteristics of Virtual Non-Contrast Series Derived from Photon-Counting Detector Coronary CT Angiography-Prerequisites for and Feasibility of Calcium Quantification. *Diagnostics*, 13(22):3402, January 2023.

[11] F. Risch, E. Harmel, K. Rippel, et al. Virtual non-contrast series of photon-counting detector computed tomography angiography for aortic valve calcium scoring. *The International Journal of Cardiovascular Imaging*, January 2024.

[12] Y. Choi, N.-Y. Shin, J. Jang, et al. Dual-energy CT for differentiating acute intracranial hemorrhage from contrast staining or calcification: a meta-analysis. *Neuroradiology*, 62(12):1617–1626, December 2020.

[13] V. Mergen, D. Racine, L. Jungblut, et al. Virtual Noncontrast Abdominal Imaging with Photon-counting Detector CT. *Radiology*, 305(1):107–115, October 2022.

[14] F. Risch, A. Berlis, T. Kroencke, et al. Discrimination of Hemorrhage and Contrast Media in a Head Phantom on Photon-Counting Detector CT Data. *American Journal of Neuroradiology*, (10), December 2023.

[15] E. Koons, P. VanMeter, K. Rajendran, et al. Improved quantification of coronary artery luminal stenosis in the presence of heavy calcifications using photon-counting detector CT. *Proceedings of SPIE–the International Society for Optical Engineering*, 12031:120311A, 2022.

[16] C. H. Suh, S. J. Yun, W. Jin, et al. Diagnostic performance of dual-energy CT for the detection of bone marrow oedema: a systematic review and meta-analysis. *European Radiology*, 28(10):4182–4194, October 2018.

[17] F. Risch, J. A. Decker, D. Popp, et al. Artifact Reduction From Dental Material in Photon-Counting Detector Computed Tomography Data Sets Based on High-keV Monoenergetic Imaging and Iterative Metal Artifact Reduction Reconstructions-Can We Combine the Best of Two Worlds? *Investigative Radiology*, 2023.

[18] T. Flohr and B. Schmidt. Technical Basics and Clinical Benefits of Photon-Counting CT. *Investigative Radiology*, 58(7):441, July 2023.

[19] R. Schofield, L. King, U. Tayal, et al. Image reconstruction: Part 1 - understanding filtered back projection, noise and image acquisition. *Journal of Cardiovascular Computed Tomography*, 14(3):219–225, May 2020.

[20] M. J. Willemink, P. A. de Jong, T. Leiner, et al. Iterative reconstruction techniques for computed tomography Part 1: Technical principles. *European Radiology*, 23(6):1623–1631, June 2013.

[21] X-Ray Mass Attenuation Coefficients - NIST Standard Reference Database 126. https://www.nist.gov/pml/x-ray-mass-attenuation-coefficients/. Accessed: 2023-07-06.

[22] T. Flohr, M. Petersilka, A. Henning, et al. Photon-counting CT review. *Physica Medica*, 79:126–136, November 2020.

[23] G. Hernández and F. Fernández. A model of tungsten anode x-ray spectra. *Medical Physics*, 43(8):4655–4664, 2016.

[24] T. Nowak, M. Eberhard, B. Schmidt, et al. Bone Mineral Density Quantification from Localizer Radiographs: Accuracy and Precision of Energy-integrating Detector CT and Photon-counting Detector CT. *Radiology*, 298(1):147–152, January 2021.

[25] S. Dahal, A. Y. Raja, E. Searle, et al. Components of carotid atherosclerotic plaque in spectral photon-counting CT with histopathologic comparison. *European Radiology*, 33(3):1612–1619, March 2023.

[26] M. J. Willemink, M. Persson, A. Pourmorteza, et al. Photon-counting CT: Technical Principles and Clinical Prospects. *Radiology*, 289(2):293–312, November 2018.

[27] Y. Watanabe, K. Uotani, T. Nakazawa, et al. Dual-energy direct bone removal CT angiography for evaluation of intracranial aneurysm or stenosis: comparison with conventional digital subtraction angiography. *European Radiology*, 19(4):1019–1024, April 2009.

[28] J. Morris, G. Michalak, S. Leng, et al. Dual-Energy CT Monitoring of Cryoablation Zone Growth in the Spinal Column and Bony Pelvis: A Laboratory Study. *Journal of vascular and interventional radiology: JVIR*, 30(9):1496–1503, September 2019.

[29] A. Ferrero, R. Gutjahr, A. F. Halaweish, et al. Characterization of Urinary Stone Composition by Use of Whole-body, Photon-counting Detector CT. *Academic Radiology*, 25(10):1270–1276, October 2018.

[30] R. P. Marcus, J. G. Fletcher, A. Ferrero, et al. Detection and Characterization of Renal Stones by Using Photon-Counting-based CT. *Radiology*, 289(2):436–442, November 2018.

[31] T. Sartoretti, V. Mergen, L. Jungblut, et al. Liver Iodine Quantification With Photon-Counting Detector CT: Accuracy in an Abdominal Phantom and Feasibility in Patients. *Academic Radiology*, 30(3):461–469, March 2023.

[32] R. Symons, D. S. Reich, M. Bagheri, et al. Photon-counting CT for vascular imaging of the head and neck: first in vivo human results. *Investigative Radiology*, 53(3):135–142, March 2018.

[33] S. Werner, B. Krauss, U. Haberland, et al. Dual-energy CT for liver iron quantification in patients with haematological disorders. *European Radiology*, 29(6):2868–2877, June 2019.

[34] C. H. McCollough, K. Rajendran, and S. Leng. Standardization and Quantitative Imaging With Photon-Counting Detector CT. *Investigative Radiology*, 58(7):451, July 2023.

[35] D. Popp, A. X. Sinzinger, J. A. Decker, et al. Spectral metal artifact reduction after posterior spinal fixation in photon-counting detector CT datasets. *European Journal of Radiology*, 165:110946, June 2023.

[36] S. Bette, J. Decker, F. Braun, et al. Optimal Conspicuity of Liver Metastases in Virtual Monochromatic Imaging Reconstructions on a Novel Photon-Counting Detector CT-Effect of keV Settings and BMI. *Diagnostics*, 12:1231, May 2022.

[37] L. Jungblut, T. Sartoretti, D. Kronenberg, et al. Performance of virtual non-contrast images generated on clinical photon-counting detector CT for emphysema quantification: proof of concept. *The British Journal of Radiology*, 95(1135):20211367, July 2022.

[38] G. Hu, K. Niepel, F. Risch, et al. Assessment of quantitative information for radiation therapy at a first-generation clinical photon-counting computed tomography scanner. *Frontiers in Oncology*, 12, 2022.

[39] H. Hecht, M. J. Blaha, D. S. Berman, et al. Clinical indications for coronary artery calcium scoring in asymptomatic patients: Expert consensus statement from the Society of Cardiovascular Computed Tomography. *Journal of Cardiovascular Computed Tomography*, 11(2):157–168, March 2017.

[40] M. J. Blaha, M. B. Mortensen, S. Kianoush, et al. Coronary Artery Calcium Scoring: Is It Time for a Change in Methodology? *JACC: Cardiovascular Imaging*, 10(8):923–937, August 2017.

[41] Z.-h. Hou, B. Lu, Y. Gao, et al. Prognostic value of coronary CT angiography and calcium score for major adverse cardiac events in outpatients. *JACC. Cardiovascular imaging*, 5(10):990–999, October 2012.

[42] T. K. M. Wang, S. D. Flamm, P. Schoenhagen, et al. Diagnostic and Prognostic Performance of Aortic Valve Calcium Score with Cardiac CT for Aortic Stenosis: A Meta-Analysis. *Radiology: Cardiothoracic Imaging*, 3(4):e210075, August 2021.

[43] A. W. Peng, M. Mirbolouk, O. A. Orimoloye, et al. Long-Term All-Cause and Cause-Specific Mortality in Asymptomatic Patients With CAC $\geq$1,000: Results From the CAC Consortium. *JACC: Cardiovascular Imaging*, 13(1, Part 1):83–93, January 2020.

[44] D. Han, R. Cordoso, S. Whelton, et al. Prognostic significance of aortic valve calcium in relation to coronary artery calcification for long-term, cause-specific mortality: results from the CAC Consortium. *European Heart Journal Cardiovascular Imaging*, 22(11):1257–1263, December 2020.

[45] H. Utsunomiya, H. Yamamoto, T. Kitagawa, et al. Incremental prognostic value of cardiac computed tomography angiography in asymptomatic aortic stenosis: significance of aortic valve calcium score. *International Journal of Cardiology*, 168(6):5205–5211, October 2013.

[46] A. S. Agatston, W. R. Janowitz, F. J. Hildner, et al. Quantification of coronary artery calcium using ultrafast computed tomography. *Journal of the American College of Cardiology*, 15(4):827–832, March 1990.

[47] J. Nadjiri, G. Kaissis, F. Meurer, et al. Accuracy of Calcium Scoring calculated from contrast-enhanced Coronary Computed Tomography Angiography using a dual-layer spectral CT: A comparison of Calcium Scoring from real and virtual non-contrast data. *PLOS ONE*, 13(12):e0208588, December 2018.

[48] I. Song, J. G. Yi, J. H. Park, et al. Virtual Non-Contrast CT Using Dual-Energy Spectral CT: Feasibility of Coronary Artery Calcium Scoring. *Korean Journal of Radiology*, 17(3):321–329, April 2016.

[49] F. G. Gassert, C. E. Schacky, C. Müller-Leisse, et al. Calcium scoring using virtual non-contrast images from a dual-layer spectral detector CT: comparison to true non-contrast data and evaluation of proportionality factor in a large patient collective. *European Radiology*, 31(8):6193–6199, August 2021.

[50] F. Schwarz, J. W. Nance, B. Ruzsics, et al. Quantification of Coronary Artery Calcium on the Basis of Dual-Energy Coronary CT Angiography. *Radiology*, 264(3):700–707, September 2012.

[51] S. Abbara, P. Blanke, C. D. Maroules, et al. SCCT guidelines for the performance and acquisition of coronary computed tomographic angiography: A report of the Society of Cardiovascular Computed Tomography Guidelines Committee: Endorsed by the North American Society for Cardiovascular Imaging (NASCI). *Journal of Cardiovascular Computed Tomography*, 10(6):435–449, November 2016.

[52] K. Nasir and M. Clouse. Role of Nonenhanced Multidetector CT Coronary Artery Calcium Testing in Asymptomatic and Symptomatic Individuals. *Radiology*, 264(3):637–649, September 2012.

[53] R. Detrano, A. D. Guerci, J. J. Carr, et al. Coronary Calcium as a Predictor of Coronary Events in Four Racial or Ethnic Groups. *New England Journal of Medicine*, 358(13):1336–1345, March 2008.

[54] A. A. Kelkar, W. M. Schultz, F. Khosa, et al. Long-Term Prognosis After Coronary Artery Calcium Scoring Among Low-Intermediate Risk Women and Men. *Circulation: Cardiovascular Imaging*, 9(4):e003742, April 2016.

[55] J. D. Mitchell, R. Paisley, P. Moon, et al. Coronary Artery Calcium and Long-Term Risk of Death, Myocardial Infarction, and Stroke: The Walter Reed Cohort Study. *JACC: Cardiovascular Imaging*, 11(12):1799–1806, December 2018.

[56] D. Rijlaarsdam-Hermsen, M. S. Lo-Kioeng-Shioe, D. Kuijpers, et al. Prognostic value of the coronary artery calcium score in suspected coronary artery disease: a study of 644 symptomatic patients. *Netherlands Heart Journal*, 28(1):44–50, January 2020.

[57] M. S. Lo-Kioeng-Shioe, D. Rijlaarsdam-Hermsen, R. T. van Domburg, et al. Prognostic value of coronary artery calcium score in symptomatic individuals: A meta-analysis of 34,000 subjects. *International Journal of Cardiology*, 299:56–62, January 2020.

[58] U. Hoffmann, J. M. Massaro, R. B. D'Agostino, et al. Cardiovascular Event Prediction and Risk Reclassification by Coronary, Aortic, and Valvular Calcification in the Framingham Heart Study. *Journal of the American Heart Association: Cardiovascular and Cerebrovascular Disease*, 5(2):e003144, February 2016.

[59] R. Kiani, H. Pouraliakbar, M. J. Alemzadeh-Ansari, et al. The significance of coronary artery calcium score as a predictor of coronary artery stenosis in individuals referred for CT angiography. *Journal of Cardiovascular and Thoracic Research*, 12(3):203–208, 2020.

[60] S. Winther, S. E. Schmidt, T. Mayrhofer, et al. Incorporating Coronary Calcification Into Pre-Test Assessment of the Likelihood of Coronary Artery Disease. *Journal of the American College of Cardiology*, 76(21):2421–2432, November 2020.

[61] J. Knuuti, W. Wijns, A. Saraste, et al. 2019 ESC Guidelines for the diagnosis and management of chronic coronary syndromes: The Task Force for the diagnosis and management of chronic coronary syndromes of the European Society of Cardiology (ESC). *European Heart Journal*, 41(3):407–477, January 2020.

[62] J. Narula, Y. Chandrashekhar, A. Ahmadi, et al. SCCT 2021 Expert Consensus Document on Coronary Computed Tomographic Angiography: A Report of the Society of Cardiovascular Computed Tomography. *Journal of Cardiovascular Computed Tomography*, 15(3):192–217, May 2021.

[63] P. Rajiah, A. Parakh, F. Kay, et al. Update on Multienergy CT: Physics, Principles, and Applications. *RadioGraphics*, 40(5):1284–1308, September 2020.

[64] D. Yamak, W. Pavlicek, T. Boltz, et al. Coronary calcium quantification using contrast-enhanced dual-energy computed tomography scans. *Journal of Applied Clinical Medical Physics*, 14(3):203–214, May 2013.

[65] Y. Yamada, M. Jinzaki, T. Okamura, et al. Feasibility of coronary artery calcium scoring on virtual unenhanced images derived from single-source fast kVp-switching dual-energy coronary CT angiography. *Journal of Cardiovascular Computed Tomography*, 8(5):391–400, September 2014.

[66] T. A. Fuchs, J. Stehli, S. Dougoud, et al. Coronary artery calcium quantification from contrast enhanced CT using gemstone spectral imaging and material decomposition. *The International Journal of Cardiovascular Imaging*, 30(7):1399–1405, October 2014.

[67] N. Fink, E. Zsarnoczay, U. J. Schoepf, et al. Impact of Cardiac Motion on coronary artery calcium scoring using a virtual non-iodine algorithm on photon-counting detector CT: a dynamic phantom study. *The International Journal of Cardiovascular Imaging*, July 2023.

[68] V. Mergen, S. Ghouse, T. Sartoretti, et al. Cardiac Virtual Noncontrast Images for Calcium Quantification with Photon-counting Detector CT. *Radiology: Cardiothoracic Imaging*, 5(3):e220307, June 2023.

[69] P. Blanke, J. R. Weir-McCall, S. Achenbach, et al. Computed Tomography Imaging in the Context of Transcatheter Aortic Valve Implantation (TAVI)/Transcatheter Aortic Valve Replacement (TAVR): An Expert Consensus Document of the Society of Cardiovascular Computed Tomography. *JACC. Cardiovascular imaging*, 12(1):1–24, January 2019.

[70] J. M. Kerl, J. G. Ravenel, S. A. Nguyen, et al. Right heart: split-bolus injection of diluted contrast medium for visualization at coronary CT angiography. *Radiology*, 247(2):356–364, May 2008.

[71] P. D. Deak, Y. Smal, and W. A. Kalender. Multisection CT protocols: sex- and age-specific conversion factors used to determine effective dose from dose-length product. *Radiology*, 257(1):158–166, October 2010.

[72] I. L. Langenbach, H. Wienemann, K. Klein, et al. Coronary calcium scoring using virtual non-contrast reconstructions on a dual-layer spectral CT system: Feasibility in the clinical practice. *European Journal of Radiology*, 159:110681, February 2023.

[73] N. Fink, E. Zsarnoczay, U. J. Schoepf, et al. Photon Counting Detector CT-Based Virtual Noniodine Reconstruction Algorithm for In Vitro and In Vivo Coronary Artery Calcium Scoring: Impact of Virtual Monoenergetic and Quantum Iterative Reconstructions. *Investigative Radiology*, 58(9):673, September 2023.

[74] M. N. D. Di Minno, P. Poggio, E. Conte, et al. Cardiovascular morbidity and mortality in patients with aortic valve calcification: A systematic review and meta-analysis. *Journal of Cardiovascular Computed Tomography*, 13(4):190–195, July 2019.

[75] M. E. Guillén Subirán, L. H. Ros Mendoza, E. Angulo Herviás, et al. Multidetector computed tomography evaluation of candidates for transcatheter aortic valve implantation. *Radiologia*, 60(1):24–38, 2018.

[76] H. Alkadhi and A. Euler. The Future of Computed Tomography: Personalized, Functional, and Precise. *Investigative Radiology*, 55(9):545–555, September 2020.

[77] P. Yang, R. Zhao, W. Deng, et al. Feasibility and accuracy of coronary artery calcium score on virtual non-contrast images derived from a dual-layer spectral detector CT: A retrospective multicenter study. *Frontiers in Cardiovascular Medicine*, 10:1114058, March 2023.

[78] T. Thonghong, O. De Backer, and L. Søndergaard. Comprehensive update on the new indications for transcatheter aortic valve replacement in the latest 2017 European guidelines for the management of valvular heart disease. *Open Heart*, 5(1):e000753, February 2018.

[79] A. Vahanian, F. Beyersdorf, F. Praz, et al. 2021 ESC/EACTS Guidelines for the management of valvular heart disease. *European Heart Journal*, 43(7):561–632, February 2022.

[80] O. Abdelkarim, A. Sinha, R. Barsoom, et al. Aortic valve calcium score in comparison to dobutamine stress echocardiography in the assessment of severe low flow low gradient aortic stenosis. *Journal of the American College of Cardiology*, 79:1232–1232, March 2022.

[81] J. van der Bie, S. P. Sharma, M. van Straten, et al. Photon-counting Detector CT in Patients Pre- and Post-Transcatheter Aortic Valve Replacement. *Radiology: Cardiothoracic Imaging*, 5(2):e220318, April 2023.

[82] F. M. Wang, A. Rozanski, Y. Arnson, et al. Cardiovascular and All-Cause Mortality Risk by Coronary Artery Calcium Scores and Percentiles Among Older Adult Males and Females. *The American Journal of Medicine*, 134(3):341–350.e1, March 2021.

[83] H. Mori, S. Torii, M. Kutyna, et al. Coronary Artery Calcification and its Progression. *JACC: Cardiovascular Imaging*, 11(1):127–142, January 2018.

[84] X. Ban, Z. Li, Y. Duan, et al. Advanced imaging modalities provide new insights into coronary artery calcification. *European Journal of Radiology*, 157:110601, December 2022.

[85] U. J. Schoepf, P. L. Zwerner, G. Savino, et al. Coronary CT Angiography. *Radiology*, 244(1):48–63, July 2007.

[86] N. R. van der Werf, M. J. Willemink, T. P. Willems, et al. Influence of heart rate on coronary calcium scores: a multi-manufacturer phantom study. *The International Journal of Cardiovascular Imaging*, 34(6):959–966, June 2018.

[87] K. Stepniak, A. Ursani, N. Paul, and H. Naguib. Novel 3D printing technology for CT phantom coronary arteries with high geometrical accuracy for biomedical imaging applications. *Bioprinting*, 18:e00074, June 2020.

[88] M. Toepker, G. Euller, E. Unger, et al. Stenosis Quantification of Coronary Arteries in Coronary Vessel Phantoms With Second-Generation Dual-Source CT: Influence of Measurement Parameters and Limitations. *American Journal of Roentgenology*, 201(2):W227–W234, August 2013.

[89] T. Allmendinger, T. Nowak, T. Flohr, et al. Photon-Counting Detector CT-Based Vascular Calcium Removal Algorithm : Assessment Using a Cardiac Motion Phantom. *Investigative Radiology*, 57(6):399–405, June 2022.

[90] O. Christianson, J. Winslow, D. P. Frush, and E. Samei. Automated Technique to Measure Noise in Clinical CT Examinations. *American Journal of Roentgenology*, 205(1):W93–W99, July 2015.

[91] A. A. Mahabadi, S. Achenbach, C. Burgstahler, et al. Safety, Efficacy, and Indications of $\beta$-Adrenergic Receptor Blockade to Reduce Heart Rate prior to Coronary CT Angiography. *Radiology*, 257(3):614–623, December 2010.

[92] R. Marano, G. Pontone, E. Agricola, et al. Recommendations in pre-procedural imaging assessment for TAVI intervention: SIC-SIRM position paper part 2 (CT and MR angiography, standard medical reporting, future perspectives). *La radiologia medica*, 127(3):277–293, March 2022.

[93] N. R. van der Werf, R. Booij, M. J. W. Greuter, et al. Reproducibility of coronary artery calcium quantification on dual-source CT and dual-source photon-counting CT: a dynamic phantom study. *The International Journal of Cardiovascular Imaging*, 38(7):1613–1619, February 2022.

[94] J. M. Groen, M. J. Greuter, B. Schmidt, et al. The Influence of Heart Rate, Slice Thickness, and Calcification Density on Calcium Scores Using 64-Slice Multidetector Computed Tomography: A Systematic Phantom Study. *Investigative Radiology*, 42(12):848, December 2007.

[95] C. Hong, K. T. Bae, T. K. Pilgram, and F. Zhu. Coronary Artery Calcium Quantification at Multi-Detector Row CT: Influence of Heart Rate and Measurement Methods on Interacquisition Variability-Initial Experience. *Radiology*, 228(1):95–100, July 2003.

[96] H. Brodoefel, C. Burgstahler, I. Tsiflikas, et al. Dual-Source CT: Effect of Heart Rate, Heart Rate Variability, and Calcification on Image Quality and Diagnostic Accuracy. *Radiology*, 247(2):346–355, May 2008.

[97] H. Alkadhi, H. Scheffel, L. Desbiolles, et al. Dual-source computed tomography coronary angiography: influence of obesity, calcium load, and heart rate on diagnostic accuracy. *European Heart Journal*, 29(6):766–776, February 2008.

[98] Cardiovascular diseases (CVDs). https://www.who.int/news-room/fact-sheets/detail/cardiovascular-diseases-(cvds). Accessed: 2023-06-23.

[99] J. M. Miller, C. E. Rochitte, M. Dewey, et al. Diagnostic Performance of Coronary Angiography by 64-Row CT. *New England Journal of Medicine*, 359(22):2324–2336, November 2008.

[100] M. Kidoh, D. Utsunomiya, Y. Funama, et al. The effect of heart rate on coronary plaque measurements in 320-row coronary CT angiography. *The International Journal of Cardiovascular Imaging*, 34(12):1977–1985, December 2018.

[101] A. C. Kwan, H. Gransar, E. Tzolos, et al. The accuracy of coronary CT angiography in patients with coronary calcium score above 1000 Agatston Units: Comparison with quantitative coronary angiography. *Journal of Cardiovascular Computed Tomography*, 15(5):412–418, 2021.

[102] Beauftragung IQWiG: Computertomographie-Koronarangiographie zur Diagnosestellung bei Patientinnen und Patienten mit Verdacht auf eine chronische koronare Herzkrankheit

- Anpassung - Gemeinsamer Bundesausschuss. https://www.g-ba.de/beschluesse/5511/. 2023-06-21.

[103] Q. Li, B. P. Berman, T. Hagio, et al. Coronary artery calcium quantification using contrast-enhanced dual-energy computed tomography scans in comparison with unenhanced single-energy scans. *Physics in medicine and biology*, 63(17):175006, August 2018.

[104] J. Perez-Cervera, J. Arce, M. Fattouh, et al. Influence of BMI on virtual coronary artery calcium scoring. *The International Journal of Cardiovascular Imaging*, December 2022.

[105] G. Mowatt, E. Cummins, N. Waugh, et al. Systematic review of the clinical effectiveness and cost-effectiveness of 64-slice or higher computed tomography angiography as an alternative to invasive coronary angiography in the investigation of coronary artery disease. *Health Technology Assessment (Winchester, England)*, 12(17):iii–iv, ix–143, May 2008.

[106] F. Hagen, J. Hofmann, R. Wrazidlo, et al. Image quality and dose exposure of contrast-enhanced abdominal CT on a 1st generation clinical dual-source photon-counting detector CT in obese patients vs. a 2nd generation dual-source dual energy integrating detector CT. *European Journal of Radiology*, 151:110325, June 2022.

[107] I. Tsiflikas, T. Drosch, H. Brodoefel, et al. Diagnostic accuracy and image quality of cardiac dual-source computed tomography in patients with arrhythmia. *International Journal of Cardiology*, 143(1):79–85, August 2010.

[108] G. Korosoglou, M. Marwan, S. Giusca, et al. Influence of irregular heart rhythm on radiation exposure, image quality and diagnostic impact of cardiac computed tomography angiography in 4,339 patients. Data from the German Cardiac Computed Tomography Registry. *Journal of Cardiovascular Computed Tomography*, 12(1):34–41, 2018.

[109] T. J. Stocker, J. Leipsic, M. Y. Chen, et al. Influence of Heart Rate on Image Quality and Radiation Dose Exposure in Coronary CT Angiography. *Radiology*, 300(3):701–703, September 2021.

[110] L. T. Rotkopf, M. F. Froelich, P. Riffel, et al. Influence of heart rate and heart rate variability on the feasibility of ultra-fast, high-pitch coronary photon-counting computed tomography angiography. *The International Journal of Cardiovascular Imaging*, 39(5):1065–1073, May 2023.

[111] J. P. Earls. How to use a prospective gated technique for cardiac CT. *Journal of Cardiovascular Computed Tomography*, 3(1):45–51, 2009.

[112] A. Sabarudin, Z. Sun, and A. K. M. Yusof. Coronary CT angiography with single-source and dual-source CT: Comparison of image quality and radiation dose between prospective ECG-triggered and retrospective ECG-gated protocols. *International Journal of Cardiology*, 168(2):746–753, September 2013.

[113] J. Hoe and K. H. Toh. First experience with 320-row multidetector CT coronary angiography scanning with prospective electrocardiogram gating to reduce radiation dose. *Journal of Cardiovascular Computed Tomography*, 3(4):257–261, 2009.

[114] M. J. Budoff, R. Young, G. Burke, et al. Ten-year association of coronary artery calcium with atherosclerotic cardiovascular disease (ASCVD) events: the multi-ethnic study of atherosclerosis (MESA). *European Heart Journal*, 39(25):2401–2408, July 2018.

[115] S. M. Grundy, N. J. Stone, A. L. Bailey, et al. 2018 AHA/ ACC/ AACVPR/ AAPA/ ABC/ ACPM/ ADA/ AGS/ APhA/ ASPC/ NLA/ PCNA Guideline on the Management of Blood Cholesterol. *Journal of the American College of Cardiology*, 73(24):e285–e350, June 2019.

[116] J. A. Decker, A. Huber, F. Senel, et al. Anemia Detection by Hemoglobin Quantification on Contrast-enhanced Photon-counting CT Data Sets. *Radiology*, page 220063, July 2022.

[117] J. A. Decker, A. Huber, F. Senel, et al. Anemia detection and quantification in contrast-enhanced CT scans on a novel photon-counting detector CT: A prospective proof-of-concept study. *European Journal of Radiology*, 166:110967, September 2023.

[118] M. Götz, M. Anders, E. Biecker, et al. S2k-Leitlinie Gastrointestinale Blutung: AWMF-Register Nr. 021-28. *Zeitschrift für Gastroenterologie*, 55(09):883–936, September 2017.

[119] E. Nagy, A. L. Jermendy, B. Merkely, and P. Maurovich-Horvat. Clinical importance of epicardial adipose tissue. *Archives of Medical Science : AMS*, 13(4):864–874, June 2017.

[120] A. M. Ansaldo, F. Montecucco, A. Sahebkar, et al. Epicardial adipose tissue and cardiovascular diseases. *International Journal of Cardiology*, 278:254–260, March 2019.

[121] V. Brandt, R. Bekeredjian, U. Schoepf, et al. Prognostic Value of Epicardial Adipose Tissue Volume in Combination with Coronary Plaque and Flow Assessment for the Prediction of Major Adverse Cardiac Events. *European Journal of Radiology*, 148:110157, January 2022.

[122] V. Brandt, J. Decker, U. J. Schoepf, et al. Additive value of epicardial adipose tissue quantification to coronary CT angiography-derived plaque characterization and CT fractional flow reserve for the prediction of lesion-specific ischemia. *European Radiology*, 32(6):4243–4252, June 2022.

[123] S. N. Hatem and P. Sanders. Epicardial adipose tissue and atrial fibrillation. *Cardiovascular Research*, 102(2):205–213, May 2014.

[124] G. Iacobellis and F. Leonetti. Epicardial Adipose Tissue and Insulin Resistance in Obese Subjects. *The Journal of Clinical Endocrinology & Metabolism*, 90(11):6300–6302, November 2005.

[125] P. M. Gorter, A. S. van Lindert, A. M. de Vos, et al. Quantification of epicardial and peri-coronary fat using cardiac computed tomography; reproducibility and relation with obesity

and metabolic syndrome in patients suspected of coronary artery disease. *Atherosclerosis*, 197(2):896–903, April 2008.

[126] M. Goeller, S. Achenbach, M. Marwan, et al. Epicardial adipose tissue density and volume are related to subclinical atherosclerosis, inflammation and major adverse cardiac events in asymptomatic subjects. *Journal of Cardiovascular Computed Tomography*, 12(1):67–73, February 2018.

[127] G. van Woerden, D. J. van Veldhuisen, T. M. Gorter, et al. Importance of epicardial adipose tissue localization using cardiac magnetic resonance imaging in patients with heart failure with mid-range and preserved ejection fraction. *Clinical Cardiology*, 44(7):987–993, 2021.

[128] V. Parisi, L. Petraglia, R. Formisano, et al. Validation of the echocardiographic assessment of epicardial adipose tissue thickness at the Rindfleisch fold for the prediction of coronary artery disease. *Nutrition, Metabolism and Cardiovascular Diseases*, 30(1):99–105, January 2020.

[129] B. Gaborit, C. Sengenes, P. Ancel, et al. Role of Epicardial Adipose Tissue in Health and Disease: A Matter of Fat? In *Comprehensive Physiology*, pages 1051–1082. John Wiley & Sons, Ltd, 2017.

[130] B. T. Franssens, H. M. Nathoe, T. Leiner, et al. Relation between cardiovascular disease risk factors and epicardial adipose tissue density on cardiac computed tomography in patients at high risk of cardiovascular events. *European Journal of Preventive Cardiology*, 24(6):660–670, April 2017.

[131] A. A. Mahabadi, B. Balcer, I. Dykun, et al. Cardiac computed tomography-derived epicardial fat volume and attenuation independently distinguish patients with and without myocardial infarction. *PLoS ONE*, 12(8):e0183514, August 2017.

[132] C. B. Monti, D. Capra, M. Zanardo, et al. CT-derived epicardial adipose tissue density: Systematic review and meta-analysis. *European Journal of Radiology*, 143:109902, October 2021.

[133] M. Marwan and S. Achenbach. Quantification of epicardial fat by computed tomography: Why, when and how? *Journal of Cardiovascular Computed Tomography*, 7(1):3–10, January 2013.

[134] M. Marwan, S. Koenig, K. Schreiber, et al. Quantification of epicardial adipose tissue by cardiac CT: Influence of acquisition parameters and contrast enhancement. *European Journal of Radiology*, 121:108732, December 2019.

[135] L. Xu, Y. Xu, R. Coulden, et al. Comparison of epicardial adipose tissue radiodensity threshold between contrast and non-contrast enhanced computed tomography scans: A cohort study of derivation and validation. *Atherosclerosis*, 275:74–79, August 2018.

[136] R. Nakazato, H. Shmilovich, B. K. Tamarappoo, et al. Interscan reproducibility of computer-aided epicardial and thoracic fat measurement from non-contrast cardiac CT. *Journal of Cardiovascular Computed Tomography*, 5(3):172–179, 2011.

[137] G. L. Wheeler, R. Shi, S. R. Beck, et al. Pericardial and visceral adipose tissues measured volumetrically with computed tomography are highly associated in type 2 diabetic families. *Investigative Radiology*, 40(2):97–101, February 2005.

[138] T. Yoshizumi, T. Nakamura, M. Yamane, et al. Abdominal fat: standardized technique for measurement at CT. *Radiology*, 211(1):283–286, April 1999.

[139] J. Kahn, U. Fehrenbach, G. Böning, et al. Spectral CT in patients with acute thoracoabdominal bleeding-a safe technique to improve diagnostic confidence and reduce dose? *Medicine*, 98(25):e16101, June 2019.

[140] A. P. Sauter, D. Muenzel, J. Dangelmaier, et al. Dual-layer spectral computed tomography: Virtual non-contrast in comparison to true non-contrast images. *European Journal of Radiology*, 104:108–114, July 2018.

[141] J. H. Niehoff, M. M. Woeltjen, K. R. Laukamp, et al. Virtual Non-Contrast versus True Non-Contrast Computed Tomography: Initial Experiences with a Photon Counting Scanner Approved for Clinical Use. *Diagnostics*, 11(12):2377, December 2021.

[142] M. H. Choi, Y. J. Lee, Y. J. Choi, and S. Pak. Dual-energy CT of the liver: True noncontrast vs. virtual noncontrast images derived from multiple phases for the diagnosis of fatty liver. *European Journal of Radiology*, 140:109741, July 2021.

[143] R. H. H. Wellenberg, M. F. Boomsma, J. A. C. van Osch, et al. Quantifying metal artefact reduction using virtual monochromatic dual-layer detector spectral CT imaging in unilateral and bilateral total hip prostheses. *European Journal of Radiology*, 88:61–70, March 2017.

[144] T. Sartoretti, V. Mergen, L. Jungblut, et al. Liver Iodine Quantification With Photon-Counting Detector CT: Accuracy in an Abdominal Phantom and Feasibility in Patients. *Academic Radiology*, May 2022.

[145] F. Risch, S. Bette, A. Sinzinger, et al. Multiphase photon counting detector CT data sets - Which combination of contrast phase and virtual non-contrast algorithm is best suited to replace true non-contrast series in the assessment of active bleeding? *European Journal of Radiology*, 168:111125, September 2023.

[146] A. J. Stanley and L. Laine. Management of acute upper gastrointestinal bleeding. *BMJ*, 364:l536, March 2019.

[147] V. García-Blázquez, A. Vicente-Bártulos, A. Olavarria-Delgado, et al. Accuracy of CT angiography in the diagnosis of acute gastrointestinal bleeding: systematic review and meta-analysis. *European Radiology*, 23(5):1181–1190, May 2013.

[148] M. Maegele. The Diagnosis and Treatment of Acute Traumatic Bleeding and Coagulopathy. *Deutsches ärzteblatt International*, 116(47):799–806, November 2019.

[149] G. Ndrepepa, F.-J. Neumann, M. Menichelli, et al. Prognostic value of haemoglobin drop in patients with acute coronary syndromes. *European Journal of Clinical Investigation*, 51(12):e13670, 2021.

[150] J.-Z. Ren, M.-F. Zhang, A.-M. Rong, et al. Lower gastrointestinal bleeding: Role of 64-row computed tomographic angiography in diagnosis and therapeutic planning. *World Journal of Gastroenterology : WJG*, 21(13):4030–4037, April 2015.

[151] M. Martí de Gracia, J. Artigas, G. Garzón, et al. Acute Lower Intestinal Bleeding: Feasibility and Diagnostic Performance of CT Angiography. *Radiology*, 262:109–16, November 2011.

[152] Y. Geffroy, M. Rodallec, I. Boulay-Coletta, et al. Multidetector CT Angiography in Acute Gastrointestinal Bleeding: Why, When, and How. *Radiographics : a review publication of the Radiological Society of North America, Inc*, 31:E35–46, May 2011.

[153] S. B. Raniga, A. K. Mittal, M. Bernstein, et al. Multidetector CT in Vascular Injuries Resulting from Pelvic Fractures: A Primer for Diagnostic Radiologists. *RadioGraphics*, 39(7):2111–2129, November 2019.

[154] M. Maegele. The European Perspective on the Management of Acute Major Hemorrhage and Coagulopathy after Trauma: Summary of the 2019 Updated European Guideline. *Journal of Clinical Medicine*, 10(2):362, January 2021.

[155] J. M. Artigas, M. Martí, J. A. Soto, et al. Multidetector CT Angiography for Acute Gastrointestinal Bleeding: Technique and Findings. *RadioGraphics*, 33(5):1453–1470, September 2013.

[156] Y. Kim, Y. K. Kim, B. E. Lee, et al. Ultra-Low-Dose CT of the Thorax Using Iterative Reconstruction: Evaluation of Image Quality and Radiation Dose Reduction. *American Journal of Roentgenology*, 204(6):1197–1202, June 2015.

[157] L. Yu, J. G. Fletcher, K. L. Grant, et al. Automatic Selection of Tube Potential for Radiation Dose Reduction in Vascular and Contrast-Enhanced Abdominopelvic CT. *American Journal of Roentgenology*, 201(2):W297–W306, August 2013.

[158] M. K. Kalra, M. Woisetschläger, N. Dahlström, et al. Radiation Dose Reduction With Sinogram Affirmed Iterative Reconstruction Technique for Abdominal Computed Tomography. *Journal of Computer Assisted Tomography*, 36(3):339–346, June 2012.

[159] D. J. Brenner and H. Hricak. Radiation exposure from medical imaging: time to regulate? *JAMA*, 304(2):208–209, July 2010.

[160] E. J. Hall and D. J. Brenner. Cancer risks from diagnostic radiology. *The British Journal of Radiology*, 81(965):362–378, May 2008.

[161] S. S. Walter, S. Schneeweiß, M. Maurer, et al. Virtual non-enhanced dual-energy CT reconstruction may replace true non-enhanced CT scans in the setting of suspected active hemorrhage. *European Journal of Radiology*, 109:218–222, December 2018.

[162] H. Sun, X.-Y. Hou, H.-D. Xue, et al. Dual-source dual-energy CT angiography with virtual non-enhanced images and iodine map for active gastrointestinal bleeding: image quality, radiation dose and diagnostic performance. *European Journal of Radiology*, 84(5):884–891, May 2015.

[163] H. Huflage, A. S. Kunz, R. Hendel, et al. Obesity-Related Pitfalls of Virtual versus True Non-Contrast Imaging-An Intraindividual Comparison in 253 Oncologic Patients. *Diagnostics*, 13(9):1558, January 2023.

[164] A. Estler, K. Nikolaou, S. O. Schönberg, et al. Is There Still a Role for Two-Phase Contrast-Enhanced CT and Virtual Monoenergetic Images in the Era of Photon-Counting Detector CT? *Diagnostics*, 13(8):1454, January 2023.

[165] L. Jungblut, F. Abel, D. Nakhostin, et al. Impact of photon counting detector CT derived virtual monoenergetic images and iodine maps on the diagnosis of pleural empyema. *Diagnostic and Interventional Imaging*, 104(2):84–90, February 2023.

[166] L. Lehti, M. Söderberg, P. Höglund, and J. Wassélius. Comparing Arterial- and Venous-Phase Acquisition for Optimization of Virtual Noncontrast Images From Dual-Energy Computed Tomography Angiography. *Journal of Computer Assisted Tomography*, 43(5):770–774, 2019.

[167] C. J. Eskey, P. M. Meyers, T. N. Nguyen, et al. Indications for the Performance of Intracranial Endovascular Neurointerventional Procedures: A Scientific Statement From the American Heart Association. *Circulation*, 137(21):e661–e689, May 2018.

[168] N. Lummel, G. Schulte-Altedorneburg, C. Bernau, et al. Hyperattenuated Intracerebral Lesions after Mechanical Recanalization in Acute Stroke. *American Journal of Neuroradiology*, 35(2):345–351, February 2014.

[169] J.-T. Kim, S.-H. Heo, B.-H. Cho, et al. Hyperdensity on non-contrast CT immediately after intra-arterial revascularization. *Journal of Neurology*, 259(5):936–943, May 2012.

[170] U. Neuberger, P. Kickingereder, S. Schönenberger, et al. Risk factors of intracranial hemorrhage after mechanical thrombectomy of anterior circulation ischemic stroke. *Neuroradiology*, 61(4):461–469, April 2019.

[171] I. Riederer, A. A. Fingerle, C. Zimmer, et al. Potential of dual-layer spectral CT for the differentiation between hemorrhage and iodinated contrast medium in the brain after endovascular treatment of ischemic stroke patients. *Clinical Imaging*, 79:158–164, November 2021.

[172] B. Gibney, C. E. Redmond, D. Byrne, et al. A Review of the Applications of Dual-Energy CT in Acute Neuroimaging. *Canadian Association of Radiologists Journal*, 71(3):253–265, August 2020.

[173] I. Nakagawa, H. S. Park, M. Kotsugi, et al. Enhanced Hematoma Membrane on DynaCT Images During Middle Meningeal Artery Embolization for Persistently Recurrent Chronic Subdural Hematoma. *World Neurosurgery*, 126:e473–e479, June 2019.

[174] Y. Zaouak, N. Sadeghi, N. Sarbu, et al. Differentiation between Cerebral Hemorrhage and Contrast Extravasation Using Dual Energy Computed Tomography after Intra-Arterial Neuro Interventional Procedures. *Journal of the Belgian Society of Radiology*, 104(1):70, November 2020.

[175] U. Bodanapally, K. Shanmuganathan, Y. Gunjan, et al. Quantification of Iodine Leakage on Dual-Energy CT as a Marker of Blood-Brain Barrier Permeability in Traumatic Hemorrhagic Contusions: Prediction of Surgical Intervention for Intracranial Pressure Management. *AJNR: American Journal of Neuroradiology*, 40(12):2059–2065, December 2019.

[176] S. Kim, H. Lim, H. Lee, et al. Dual-Energy CT in the Evaluation of Intracerebral Hemorrhage of Unknown Origin: Differentiation between Tumor Bleeding and Pure Hemorrhage. *AJNR: American Journal of Neuroradiology*, 33(5):865–872, May 2012.

[177] T. Sartoretti, V. Mergen, K. Higashigaito, et al. Virtual Noncontrast Imaging of the Liver Using Photon-Counting Detector Computed Tomography : A Systematic Phantom and Patient Study. *Investigative Radiology*, 57(7):488–493, July 2022.

[178] M. Diwakar and M. Kumar. A review on CT image noise and its denoising. *Biomedical Signal Processing and Control*, 42:73–88, April 2018.

[179] T. Sartoretti, A. Landsmann, D. Nakhostin, et al. Quantum Iterative Reconstruction for Abdominal Photon-counting Detector CT Improves Image Quality. *Radiology*, 303(2):339–348, May 2022.

[180] M. Eberhard, V. Mergen, K. Higashigaito, et al. Coronary Calcium Scoring with First Generation Dual-Source Photon-Counting CT-First Evidence from Phantom and In-Vivo Scans. *Diagnostics*, 11(9):1708, September 2021.

[181] S. Ulzheimer and W. A. Kalender. Assessment of calcium scoring performance in cardiac computed tomography. *European Radiology*, 13(3):484–497, March 2003.

[182] S. Si-Mohamed, C. Moreau-Triby, P. Tylski, et al. Head-to-head comparison of lung perfusion with dual-energy CT and SPECT-CT. *Diagnostic and Interventional Imaging*, 101(5):299–310, May 2020.

[183] S. F. Thieme, V. Graute, K. Nikolaou, et al. Dual Energy CT lung perfusion imaging-Correlation with SPECT/CT. *European Journal of Radiology*, 81(2):360–365, February 2012.

[184] M. C. Jacobsen, E. N. K. Cressman, E. P. Tamm, et al. Dual-Energy CT: Lower Limits of Iodine Detection and Quantification. *Radiology*, 292(2):414–419, August 2019.

[185] J. Sosna. Photon-counting Detector CT: Initial Analysis of Virtual Noncontrast Imaging. *Radiology*, 305(1):116–117, October 2022.

[186] T. D'Angelo, G. Cicero, S. Mazziotti, et al. Dual energy computed tomography virtual monoenergetic imaging: technique and clinical applications. *The British Journal of Radiology*, 92(1098):20180546, June 2019.

[187] L. Gjesteby, B. De Man, Y. Jin, et al. Metal Artifact Reduction in CT: Where Are We After Four Decades? *IEEE Access*, 4:5826–5849, 2016.

[188] Reducing metal artefacts in photon-counting CT. https://physicsworld.com/?p=101628. Accessed: 2023-08-16.

[189] R. A. Nasirudin, K. Mei, P. Panchev, et al. Reduction of Metal Artifact in Single Photon-Counting Computed Tomography by Spectral-Driven Iterative Reconstruction Technique. *PLOS ONE*, 10(5):e0124831, May 2015.

[190] N. U. Zitzmann, E. Hagmann, and R. Weiger. What is the prevalence of various types of prosthetic dental restorations in Europe? *Clinical Oral Implants Research*, 18(s3):20–33, 2007.

[191] W. Dukic, B. Delija, D. Derossi, and I. Dadic. Radiopacity of composite dental materials using a digital X-ray system. *Dental Materials Journal*, 31(1):47–53, 2012.

[192] T. Klinke, A. Daboul, J. Maron, et al. Artifacts In Magnetic Resonance Imaging and Computed Tomography Caused By Dental Materials. *PLoS ONE*, 7(2):e31766, February 2012.

[193] L. Zhu, Y. Chen, J. Yang, et al. Evaluation of the dental spectral cone beam CT for metal artefact reduction. *Dentomaxillofacial Radiology*, 48(2):20180044, February 2019.

[194] H. Stergar, B. J. Krause, S. M. Eschmann, et al. Lesion concordance, image quality and artefacts in PET/CT. *Nuklearmedizin - NuclearMedicine*, 49(4):129–137, 2010.

[195] S. Arya, P. Rane, and A. Deshmukh. Oral cavity squamous cell carcinoma: Role of pretreatment imaging and its influence on management. *Clinical Radiology*, 69(9):916–930, September 2014.

[196] J. Weiß, C. Schabel, M. Bongers, et al. Impact of iterative metal artifact reduction on diagnostic image quality in patients with dental hardware. *Acta Radiologica*, 58(3):279–285, March 2017.

[197] J. Aissa, J. Boos, L. M. Sawicki, et al. Iterative metal artefact reduction (MAR) in postsurgical chest CT: comparison of three iMAR-algorithms. *The British Journal of Radiology*, 90(1079):20160778, November 2017.

[198] A. Hakim, J. Slotboom, O. Lieger, et al. Clinical evaluation of the iterative metal artefact reduction algorithm for post-operative CT examination after maxillofacial surgery. *Dentomaxillofacial Radiology*, 46(4):20160355, April 2017.

[199] N. Große-Hokamp, A. Hellerbach, A. Gierich, et al. Reduction of Artifacts Caused by Deep Brain Stimulating Electrodes in Cranial Computed Tomography Imaging by Means of Virtual Monoenergetic Images, Metal Artifact Reduction Algorithms, and Their Combination. *Investigative Radiology*, 53(7):424–431, July 2018.

[200] S. Winklhofer, E. Benninger, C. Spross, et al. CT metal artefact reduction for internal fixation of the proximal humerus: Value of mono-energetic extrapolation from dual-energy and iterative reconstructions. *Clinical Radiology*, 69(5):e199–e206, May 2014.

[201] A. M. A. Schmidt, J.-P. Grunz, B. Petritsch, et al. Combination of Iterative Metal Artifact Reduction and Virtual Monoenergetic Reconstruction Using Split-Filter Dual-Energy CT in Patients With Dental Artifact on Head and Neck CT. *American Journal of Roentgenology*, 218(4):716–727, April 2022.

[202] J. A. Anhaus, S. Schmidt, P. Killermann, et al. Iterative metal artifact reduction on a clinical photon counting system-technical possibilities and reconstruction selection for optimal results dependent on the metal scenario. *Physics in Medicine & Biology*, 67(11):115018, June 2022.

[203] E. Meyer, R. Raupach, M. Lell, et al. Frequency split metal artifact reduction (FSMAR) in computed tomography. *Medical Physics*, 39(4):1904–1916, 2012.

[204] E. Meyer, R. Raupach, M. Lell, et al. Normalized metal artifact reduction (NMAR) in computed tomography. *Medical Physics*, 37(10):5482–5493, 2010.

[205] Y. Dong, A. J. Shi, J. L. Wu, et al. Metal artifact reduction using virtual monochromatic images for patients with pedicle screws implants on CT. *European Spine Journal*, 25(6):1754–1763, June 2016.

[206] J. von Spiczak, M. Mannil, B. Peters, et al. Photon Counting Computed Tomography With Dedicated Sharp Convolution Kernels: Tapping the Potential of a New Technology for Stent Imaging. *Investigative Radiology*, 53(8):486–494, August 2018.

[207] N. Schmitt, L. Wucherpfennig, L. T. Rotkopf, et al. Metal artifacts and artifact reduction of neurovascular coils in photon-counting detector CT versus energy-integrating detector CT - in vitro comparison of a standard brain imaging protocol. *European Radiology*, August 2022.

[208] Y. Metin, N. O. Metin, O. Özdemir, et al. The role of low keV virtual monochromatic imaging in increasing the conspicuity of primary breast cancer in dual-energy spectral thoracic CT examination for staging purposes. *Acta Radiologica*, 61(2):168–174, February 2020.

[209] D. Zopfs, S. Lennartz, N. Große Hokamp, et al. Head and neck squamous cell carcinoma: evaluation of iodine overlay maps and low-energy virtual mono-energetic images acquired with spectral detector CT. *Clinical Radiology*, 77(6):e425–e433, June 2022.

[210] S. M. Lee, S. H. Kim, S. J. Ahn, et al. Virtual monoenergetic dual-layer, dual-energy CT enterography: optimization of keV settings and its added value for Crohn's disease. *European Radiology*, 28(6):2525–2534, June 2018.

[211] N. F. Majeed, S. M. Ali, J. Therrien, et al. Virtual Monoenergetic Spectral Detector CT for Preoperative CT Angiography in Liver Donors. *Current Problems in Diagnostic Radiology*, 51(4):517–523, July 2022.

[212] K. R. Laukamp, S. H. Tirumani, S. Lennartz, et al. Evaluation of equivocal small cystic pancreatic lesions with spectral-detector computed tomography. *Acta Radiologica*, 62(2):172–181, February 2021.

[213] K. Higashigaito, V. Mergen, M. Eberhard, et al. CT Angiography of the Aorta Using Photon-counting Detector CT with Reduced Contrast Media Volume. *Radiology: Cardiothoracic Imaging*, 5(1):e220140, February 2023.

[214] J. P. Erinjeri and T. W. Clark. Cryoablation: Mechanism of Action and Devices. *Journal of vascular and interventional radiology : JVIR*, 21(8 Suppl):S187–S191, August 2010.

[215] J. A. Decker, F. Risch, F. Schwarz, et al. Improved Thermal Sensitivity Using Virtual Monochromatic Imaging Derived from Photon Counting Detector CT Data Sets: Ex Vivo Results of CT-Guided Cryoablation in Porcine Liver. *CardioVascular and Interventional Radiology*, 46(10):1385–1393, October 2023.

[216] C. Pusceddu, L. Mascia, C. Ninniri, et al. The Increasing Role of CT-Guided Cryoablation for the Treatment of Liver Cancer: A Single-Center Report. *Cancers*, 14(12):3018, June 2022.

[217] J. Ma, F. Wang, W. Zhang, et al. Percutaneous cryoablation for the treatment of liver cancer at special sites: an assessment of efficacy and safety. *Quantitative imaging in medicine and surgery*, 9(12):1948–1957, December 2019.

[218] G. Rong, W. Bai, Z. Dong, et al. Long-Term Outcomes of Percutaneous Cryoablation for Patients with Hepatocellular Carcinoma within Milan Criteria. *PLOS ONE*, 10(4):e0123065, April 2015.

[219] L.-Z. Niu, J.-L. Li, J.-Y. Zeng, et al. Combination treatment with comprehensive cryoablation and immunotherapy in metastatic hepatocellular cancer. *World Journal of Gastroenterology*, 19(22):3473–3480, June 2013.

[220] P. J. Littrup, H. D. Aoun, B. Adam, et al. Percutaneous cryoablation of hepatic tumors: long-term experience of a large U.S. series. *Abdominal Radiology (New York)*, 41(4):767–780, April 2016.

[221] D. I. Glazer, S. Tatli, P. B. Shyn, et al. Percutaneous Image-Guided Cryoablation of Hepatic Tumors: Single-Center Experience With Intermediate to Long-Term Outcomes. *AJR. American journal of roentgenology*, 209(6):1381–1389, December 2017.

[222] X. Chang, Y. Wang, H.-P. Yu, et al. CT-guided percutaneous cryoablation for palliative therapy of gastric cancer liver metastases. *Cryobiology*, 82:43–48, June 2018.

[223] N. Kalra, P. Gupta, T. Jugpal, et al. Percutaneous Cryoablation of Liver Tumors: Initial Experience from a Tertiary Care Center in India. *Journal of Clinical and Experimental Hepatology*, 11(3):305–311, 2021.

[224] S. Y. Cha, T. W. Kang, J. H. Min, et al. RF Ablation Versus Cryoablation for Small Perivascular Hepatocellular Carcinoma: Propensity Score Analyses of Mid-Term Outcomes. *Cardiovascular and Interventional Radiology*, 43(3):434–444, March 2020.

[225] J. Xu, C. Noda, A. Erickson, et al. Radiofrequency Ablation *vs*. Cryoablation for Localized Hepatocellular Carcinoma: A Propensity-matched Population Study. *Anticancer research*, 38(11):6381–6386, November 2018.

[226] J. Pohlan, W. Kress, K.-G. Hermann, et al. Computed Tomography Thermography for Ablation Zone Prediction in Microwave Ablation and Cryoablation: Advantages and Challenges in an Ex Vivo Porcine Liver Model. *Journal of Computer Assisted Tomography*, 44(5):744–749, 2020.

[227] F. T. Lee, S. G. Chosy, P. J. Littrup, et al. CT-monitored percutaneous cryoablation in a pig liver model: pilot study. *Radiology*, 211(3):687–692, June 1999.

[228] J. L. Hinshaw and F. T. Lee. Cryoablation for liver cancer. *Techniques in Vascular and Interventional Radiology*, 10(1):47–57, March 2007.

[229] S. Permpongkosol, R. E. Link, L. R. Kavoussi, and S. B. Solomon. Temperature measurements of the low-attenuation radiographic ice ball during CT-guided renal cryoablation. *Cardiovascular and Interventional Radiology*, 31(1):116–121, 2008.

[230] F. Hübner, R. Schreiner, B. Panahi, and T. J. Vogl. Evaluation of the thermal sensitivity of porcine liver in CT-guided cryoablation: an initial study. *Medical Physics*, 47(10):4997–5005, October 2020.

[231] G. A. Sandison, M. P. Loye, J. C. Rewcastle, et al. X-ray CT monitoring of iceball growth and thermal distribution during cryosurgery. *Physics in Medicine and Biology*, 43(11):3309–3324, November 1998.

[232] M. Reiser, A. K. Drukier, B. Ultsch, and S. Feuerbach. The use of CT in monitoring cryosurgery. *European Journal of Radiology*, 3(2):123–128, May 1983.

[233] F. Popken, J. K. Seifert, R. Engelmann, et al. Comparison of iceball diameter and temperature distribution achieved with 3-mm accuprobe cryoprobes in porcine and human liver tissue and human colorectal liver metastases in vitro. *Cryobiology*, 40(4):302–310, June 2000.

[234] T. Flohr, S. Ulzheimer, M. Petersilka, and B. Schmidt. Basic principles and clinical potential of photon-counting detector CT. *Chinese Journal of Academic Radiology*, 3(1):19–34, March 2020.

[235] K. Higashigaito, A. Euler, M. Eberhard, et al. Contrast-Enhanced Abdominal CT with Clinical Photon-Counting Detector CT: Assessment of Image Quality and Comparison with Energy-Integrating Detector CT. *Academic Radiology*, 29(5):689–697, May 2022.

[236] M. Ahmed, L. Solbiati, C. L. Brace, et al. Image-guided tumor ablation: standardization of terminology and reporting criteria–a 10-year update. *Radiology*, 273(1):241–260, October 2014.

[237] G. D. Pandeya, M. J. W. Greuter, B. Schmidt, et al. Assessment of thermal sensitivity of CT during heating of liver: an *ex vivo* study. *The British Journal of Radiology*, 85(1017):e661–e665, September 2012.

[238] G. D. Pandeya, M. J. W. Greuter, K. P. de Jong, et al. Feasibility of noninvasive temperature assessment during radiofrequency liver ablation on computed tomography. *Journal of Computer Assisted Tomography*, 35(3):356–360, 2011.

[239] E. Schena, F. Giurazza, C. Massaroni, et al. Thermometry based on computed tomography images during microwave ablation: Trials on ex vivo porcine liver. In *2017 IEEE International Instrumentation and Measurement Technology Conference (I2MTC)*, pages 1–6, May 2017.

[240] F. Fani, E. Schena, P. Saccomandi, and S. Silvestri. CT-based thermometry: an overview. *International Journal of Hyperthermia: The Official Journal of European Society for Hyperthermic Oncology, North American Hyperthermia Group*, 30(4):219–227, June 2014.

[241] N. Große Hokamp, R. Gilkeson, M. K. Jordan, et al. Virtual monoenergetic images from spectral detector CT as a surrogate for conventional CT images: Unaltered attenuation characteristics with reduced image noise. *European Journal of Radiology*, 117:49–55, August 2019.

[242] R. Symons, Y. Choi, T. E. Cork, et al. Optimized energy of spectral coronary CT angiography for coronary plaque detection and quantification. *Journal of Cardiovascular Computed Tomography*, 12(2):108–114, 2018.

[243] P. Apfaltrer, S. Sudarski, D. Schneider, et al. Value of monoenergetic low-kV dual energy CT datasets for improved image quality of CT pulmonary angiography. *European Journal of Radiology*, 83(2):322–328, February 2014.

[244] S. Chang, K. Han, J.-C. Youn, et al. Utility of Dual-Energy CT-based Monochromatic Imaging in the Assessment of Myocardial Delayed Enhancement in Patients with Cardiomyopathy. *Radiology*, 287(2):442–451, May 2018.

[245] L. Beer, M. Toepker, A. Ba-Ssalamah, et al. Objective and subjective comparison of virtual monoenergetic vs. polychromatic images in patients with pancreatic ductal adenocarcinoma. *European Radiology*, 29(7):3617–3625, July 2019.

[246] A. E. Michael, J. Boriesosdick, D. Schoenbeck, et al. Photon Counting CT Angiography of the Head and Neck: Image Quality Assessment of Polyenergetic and Virtual Monoenergetic Reconstructions. *Diagnostics*, 12(6):1306, June 2022.

[247] R. Booij, N. R. van der Werf, M. L. Dijkshoorn, et al. Assessment of Iodine Contrast-To-Noise Ratio in Virtual Monoenergetic Images Reconstructed from Dual-Source Energy-Integrating CT and Photon-Counting CT Data. *Diagnostics*, 12(6):1467, June 2022.

[248] K. L. Grant, T. G. Flohr, B. Krauss, et al. Assessment of an Advanced Image-Based Technique to Calculate Virtual Monoenergetic Computed Tomographic Images From a Dual-Energy Examination to Improve Contrast-To-Noise Ratio in Examinations Using Iodinated Contrast Media. *Investigative Radiology*, 49(9):586, September 2014.

[249] J. Schreck, K. R. Laukamp, J. H. Niehoff, et al. Metal artifact reduction in patients with total hip replacements: evaluation of clinical photon counting CT using virtual monoenergetic images. *European Radiology*, July 2023.

[250] H. Mellander, V. Fransson, K. Ydström, et al. Metal artifact reduction by virtual monoenergetic reconstructions from spectral brain CT. *European Journal of Radiology Open*, 10:100479, January 2023.

[251] T. D. Do, S. Sawall, S. Heinze, et al. A semi-automated quantitative comparison of metal artifact reduction in photon-counting computed tomography by energy-selective thresholding. *Scientific Reports*, 10(1):21099, December 2020.

[252] T. S. Patzer, A. S. Kunz, H. Huflage, et al. Combining virtual monoenergetic imaging and iterative metal artifact reduction in first-generation photon-counting computed tomography of patients with dental implants. *European Radiology*, June 2023.

[253] H. Tharmaseelan, L. T. Rotkopf, I. Ayx, et al. Evaluation of radiomics feature stability in abdominal monoenergetic photon counting CT reconstructions. *Scientific Reports*, 12(1):19594, November 2022.

[254] C. H. McCollough, K. Rajendran, F. I. Baffour, et al. Clinical applications of photon counting detector CT. *European Radiology*, 33(8):5309–5320, August 2023.

APPENDIX A

# Acknowledgement

I would like to express my deepest gratitude to the Director of the Department of Diagnostic and Interventional Radiology and my supervisor, Prof. Dr. med. Thomas Kröncke. He not only encouraged me to take advantage of the opportunity to gain a clinical perspective on medical technology and delve deeper into scientific medical research, but also provided me with resources, trust, and plenty of rope that allowed me to translate ideas into experiments and studies and helped me achieve my goals. In addition, this work would not have been possible without the support of my medical colleagues, especially Dr. med. Florian Schwarz, and Dr. med. Josua Decker, who co-supervised me, gave me an insight into the daily challenges faced by radiologists and never lacked enthusiasm, creativity and vision, inspiring and motivating me for each and every study performed. Thank you for all your input, criticism and backing that helped me grow into this position. I feel fortunate to be part of such a collaborative and supportive research team that values everyone's contribution and perspective. Thanks to the many co-authors who have shared their knowledge and expertise in our collaborative projects. Very important roles in our team were played by Dr. rer. nat. Claudia Wollny and Luca Canalini, who kept the overview and always had an open ear for me, whether it was brainstorming about current topics or whining about issues. I could not ask for better colleagues to share the office with - thank you. I would like to thank Dr. Bernhard Schmidt from Siemens Healthineers, who not only arranged my position at the University Hospital, but also supported me with advice. His colleagues, especially Dr. Markus Jürgens, always took the time to explain software, technical or physical backgrounds and never tired of my questions. My family, my mom, my dad, my sister, my partner and my friends were not spared and had to endure endless monologues about current projects, challenges and excitement. Thank you for never leaving me with doubts, believing in my strengths and sharing my goals.